Construction of Rotaxanes and Their Biological Applications

THESIS SUBMITTED FOR

THE DEGREE OF DOCTOR OF PHILOSOPHY (SCIENCE)

OF

JADAVPUR UNIVERSITY

MAY, 2023

By

RABI SANKAR DAS, M.Sc.

DEPARTMENT OF CHEMISTRY

INDEX NO: 34/19/CHEM/26.

DATE OF REGISTRATION: 22nd AUGUST, 2019

JADAVPUR UNIVERSITY,

KOLKATA-700032, WEST BENGAL, INDIA

I would like to dedicate this thesis to my beloved parents and all of my teachers.

Jadavpur University
Department of Chemistry
Organic Chemistry Section
Kolkata-700032, India

Dr. Samit Guha
Assistant Professor
Mobile: +91 9163750994
E-mail: samitfsu@gmail.com;
samit.guha@jadavpuruniversity.in

11th ,May, 2023

CERTIFICATE FROM THE SUPERVISOR

This is to certify that the thesis entitled "Construction of Rotaxanes and Their Biological Applications" submitted by Sri Rabi Sankar Das, who got his name registered on 22nd August, 2019 for the award of Ph. D. (Science) degree of Jadavpur University, is absolutely based upon his own work under the supervision of Dr. SAMIT GUHA and that neither this thesis nor any part of it has been submitted for either any degree/diploma or any other academic award anywhere before.

Samit Guha 11th May 2023

(Signature of the Supervisor)

Dr. Samit Guha
Assistant Professor
Department of Chemistry
Jadavpur University
Kolkata-700032, India

Construction of Rotaxanes and Their Biological Applications

INDEX NO: 34/19/CHEM/26.

Abstract: Development of organelle targeting rotaxane-based fluorophores that can selectively stain specific intracellular compartments such as mitochondria, lysosome, Golgi apparatus, endoplasmic reticulum, etc., has become an emerging field of contemporary research. Nevertheless, due to the extremely intricate cellular milieu, rational control for selective targeting of cellular organelles using organic fluorescent probes has remained challenging. Among the intracellular organelles, mitochondria are unique and indispensable, playing the crucial role in regulating cellular protein homeostasis, oxidative metabolism, and intracellular redox balance. Unlike other cellular organelles, mitochondria are difficult to target due to their unusual double-layer membrane and extremely negative inner mitochondrial membrane (IMM) potential ($\Delta\Psi_m$ −150 to −180 mV for normal cell and $\Delta\Psi_m$ ~ −220 mV for cancer cell). Lysosomes are also a significant target for all malignant cells. Lysosomes are membrane-bound acidic organelles that have a pH value of 4-5. They include a range of enzymes that are responsible for the degradation of nucleic acids, fats, proteins, and so on. In my research work, I have utilized the microwave-assisted template-directed clipping reaction on low-loading 2-chlorotrityl chloride resin to create NIR unsymmetrical mechanically interlocked molecules. These squaraine rotaxane compounds have a high potential for selective targeting and NIR imaging of mitochondria. This is the first report of an NIR unsymmetrical 1,3,3-trimethyl indoline squaraine-rotaxane-based mitochondria targeting and staining agent. The rotaxane molecule conjugated with TPP^+ functionality might be useful for mitochondrial treatment with NIR imaging diagnostics. MW-assisted SPPS protocol is also used for the effective synthesis of RGDS peptide. Two N_3-RGDS peptides are conjugated at the terminal alkyne residue of the macrocycle

using CuAAC on the Wang resin to synthesize rotaxane/RGDS conjugates. RGDS peptide is incorporated to target the $\alpha v\beta_3$ integrin which is overexpressed at the tumor site. A morpholine moiety is conjugated at the axle to selectively target the lysosomes. This dual targeting rotaxane has been used for live cancer cell specific active targeting followed by selective internalization and tracking of malignant lysosomes. I have also presented a multifunctional rotaxane molecule composed of a lipophilic TPP^+ for mitochondrial targeting and dopamine-containing catechol groups for the surface coating of the superparamagnetic Fe_3O_4 NPs. TPP^+ and dopamine residues are both attached to the axle of the NIR rotaxane molecule. Two carbohydrate moieties are attached at the tetralactam macrocycle to enhance the water solubility of MitoSQRot-DOPA. Click chemistry has been used to conjugate carbohydrates into the tetralactam macrocycle of the rotaxane. TBDMS-protected MitoSQRot-(Carb-$OH)_2$-DOPA is deprotected with TBAF/THF and capped with our synthesized magnetic nanoparticles to produce Fe_3O_4 NPs surface coated with the rotaxane molecules [MitoSQRot-(Carb-$OH)_2$-DOPA-Fe_3O_4]. Water-soluble rotaxane capped superparamagnetic Fe_3O_4 NPs could be a promising candidate for the targeted multimodal imaging applications.

Samit Guha
11th May 2023
Signature with seal of the supervisor

Rabi Sankar Das
11/05/2023
Full Signature of the Candidate

Dr. Samit Guha
Assistant Professor
Department of Chemistry
Jadavpur University
Kolkata-700032, India

Acknowledgements

I would like to express my sincere gratitude and deep appreciation to my supervisor Dr. Samit Guha, Department of Chemistry, Jadavpur University, for stimulating discussions, constructive ideas, expert criticism and valuable guidance throughout the progress of this research work. Without his guidance and enthusiasm completion of the thesis would not be possible. I would also like to mention that Dr. Samit Guha has not only been an excellent supervisor but also a great human being to me in this long journey. Building a positive relationship with a supervisor can make a significant difference in the overall experience of completing a research project, The scientific discussions those I had with him motivated me a lot. Besides being an excellent supervisor, He also helped me in the improvement of my writing skill.

I am grateful to our collaborators Dr. Arunima Sengupta (Department of Life Sciences and Biotechnology, Jadavpur University) for their spontaneous help in biological studies related to my research work.

I would also like to thank my friends Ms. Paramita Saha (Department of Inorganic Chemistry, IACS), Mr. Sanu Saha (Department of Organic Chemistry, IACS), Mr. Pradip Sheet (Department of Organic Chemistry, Bose Institution) and Shreya Das (Department of Life Sciences and Biotechnology, Jadavpur University) for their extensive help and valuable suggestions regarding biological work.

I am obliged to the Authorities of Jadavpur University and Department chemistry for providing me laboratory, library and proper atmosphere for carrying out my research work. I also thankful to all the teachers of Organic chemistry section, Jadavpur University and all the supporting staff-members of the department.

It is my pleasure to thank Dr. Nayim Sepay for helping me in Docking study and providing valuable suggestions throughout my research work.

I am also thankful to Indian Institute of Chemical Biology (CSIR-IICB, Kolkata) and Bose Institute, Kolkata for allowing me to use confocal microscopy instrument for my research work.

I take pride in thanking my group members, Mr.Pranab Chandra Saha, Mr.Ayan Mukherjee, Mr. Tapas Bera, and Mr. Samiran Kar, Mr. Aniruddha Mondal for their kind support and

encouragement. I am also thankful to Project students Mr. Deepak Kumar Bhunia, for their support in my research work.

I am also thankful to UGC-NET-JRF, Govt. of India for financial assistance during the course of my research work.

It is my pleasure to thank Prof Rina Ghosh (Jadavpur University, Department of Chemistry), Prof Umesh Chandra Halder (Jadavpur University, Department of Chemistry), Prof Gourhari Maiti (Jadavpur University, Department of Chemistry), Prof Sanjay Bhar (Jadavpur University, Department of Chemistry), Prof Tapan Kumar Mondal (Jadavpur University, Department of Chemistry), Mr. Sounak Bhattacharya (Technical Assistance, confocal microscopy section, CSIR-IICB, Kolkata), Mr. Gopal Krishna Manna (Drawing Section, IACS, Kolkata), Mr. Prantik Saha (confocal microscopy section, Bose Institute) and all the fellow friends of Department of chemistry, Jadavpur University for their overwhelming help and support throughout my research work.

I think this is the best opportunity to convey my heartiest regards to all of my teachers, especially Ms. Mamata Maity for his support in my early school days.

My thanks to all of my friends (especially Mr. Hasan Parvej, Mr. Pravat Kumar Ghorai and Mr. Niladri Hazra, Mr. Arghadip Choudhury), for their spontaneous help throughout my research work.

Last but not least, I embrace the pleasure of expressing my deep regards and love for my parents (Baba and Ma), for their valuable guidance, encouragement, and mental support. Their blessings and well-wishes always guide me to select the right pathway in life.

Rabi Sankar Das
11/05/2023
.....

(Rabi Sankar Das)

11th May, 2023

Department of Chemistry
Jadavpur University,
188, Raja S.C. Mallick Road,
Jadavpur, Kolkata, West Bengal-700032

PREFACE

The research embodied in the present thesis entitled *"Construction of Rotaxanes and Their Biological Applications"* deals with the synthesis and characterization of near-infrared (NIR) symmetrical as well as unsymmetrical squarine rotaxanes and their conjugates along with their application in selective targeting and imaging of cellular mitochondria/lysosome of fixed and live cells using confocal laser scanning microscopy. Moreover, these fluorophores are found to be useful in cellular imaging.

The present investigation described in this thesis have been carried out by the author in the Department of Chemistry, Jadavpur university, Kolkata, during the period April, 2018 to May, 2023 under the supervision of Dr. Samit Guha, Department of Chemistry, Organic section, Jadavpur University, Kolkata-700032, India.

The thesis has been presented in six chapters:

Chapter-1 consists of a brief discussion on the synthetic strategies of mechanically interlocked molecules and their applications in molecular shuttles, chemical sensors, and drug delivery vehicles. Mitochondria and lysosome targeting structural scaffolds, confocal laser scanning microscopy (CLSM) for live and fixed cell imaging, and multicolor cellular imaging have been discussed. Iron-Oxide NPs have unique properties that make them useful in a variety of applications such as magnetic resonance imaging (MRI) contrast agents, catalysts, drug delivery systems, magnetic data storage, and cancer therapy have been discussed.

Chapter-2 describes the chemicals utilized and the experimental techniques required to complete the whole work of this thesis.

Chapter-3 deals with the development of near-infrared (NIR) mechanically interlocked molecules for selective targeting of mitochondria. Solid phase method on resin is used to synthesize the rotaxane molecule MSQRot. This novel MSQRot is particularly appealing to stain fixed epithelioid cervix carcinoma HeLa cell line. High photostability, intense and narrow NIR absorption/emission bands with good quantum yield and brilliant NIR fluorescence of MSQRot make it suitable for mitochondria imaging as proven from the Confocal images of MSQRot colocalized with MTG in HeLa cells.

Chapter-4 describes the red fluorescent dual targeting mechanically interlocked molecules with dual targeting functionality. Two RGDS peptides functionalized with azide are conjugated with the alkyne containing macrocycle and a morpholine moiety is coupled at the axle for live cancer cell-specific active targeting followed by selective internalization and tracking of malignant lysosomes. This solid phase click chemistry on the Wang resin allows easy purification with a decent yield of rotaxane/RGDS conjugates. Live cancer cell-selective lysosome targeting and red fluorescence imaging using rotaxane [LysoSQRot-$(RGDS)_2$] is demonstrated and compared with control rotaxane molecules using confocal laser scanning microscopy for lysosomal staining and multicolor cellular imaging application.

Chapter-5 describes a dual functional stopper containing unsymmetrical NIR squaraine dye interlocked within a sugar conjugated macrocycle to construct water soluble multifunctional mechanically interlocked molecules with enhanced NIR fluorescence efficiency and durability. One of the stoppers of the axle is composed of a lipophilic cationic TPP^+ functionality to target mitochondria and the other stopper comprising of a dopamine-containing catechol group to anchor with the synthesized superparamagnetic Fe_3O_4 NPs. Fe_3O_4 NPs surface coated with dopamine conjugated TPP^+ tethered targeted NIR rotaxane help to specifically deliver 15 nm size magnetic NPs inside the mitochondria. Two carbohydrate moieties are conjugated with the macrocycle of the rotaxane via click chemistry to improve the water solubility of MitoSQRot-$(Carb\text{-}OH)_2$-DOPA-Fe_3O_4 NPs. The water soluble rotaxane capped Fe_3O_4 NPs has been used for live-cell mitochondria targeted NIR fluorescence confocal imaging, 3D and multicolor imaging in combination with T_2-weighted magnetic resonance imaging with high relaxation rate (r_2) of 180.7 $mM^{-1}\ s^{-1}$. Biocompatible ultra-bright NIR rotaxane capped superparamagnetic Fe_3O_4 NPs could be a promising candidate for the targeted multimodal imaging applications.

Chapter-6 includes the summary and outlook of all the chapters covered in this thesis. The relevance of the investigation's findings is also examined in this chapter.

Chapter 3-5 begins with a brief introduction, then moves on to Experimental Methodology, Results & Discussion, and Conclusions.

The list of Publications has been incorporated at the end of this thesis.

Abbreviations

Abbreviations used for amino acids, peptides, amino acid derivatives, substituents, reagents are largely in accordance with the recommendations of IUPAC–IUB commission on Biochemical Nomenclature, 1974, Pure and Applied Chemistry, 40, 315–331. Other symbols and nomenclature, etc. are based on the list in J. Biol. Chem. 1989, 669–671. Standard three letter coding is used for all the amino acids. Additional abbreviations used in this thesis are listed below–

ACN	Acetonitrile
AFM	Atomic Force Microscopy
AIE	Aggregation-induced emission
ATP	Adenosine triphosphate
CAC	Critical aggregation concentration
CLSM	Confocal laser scanning microscopy
2-CTC	2-chloro tritylchloride
DBU	1,8-diazabicyclo[5.4.0]undec-7-ene
DCM	Dichloromethane
DIPEA	N,N-Diisopropylethylamine
DMSO	Dimethyl sulfoxide
DMF	N, N – dimethylformamide
DQF COSY	Double Quantum Filtered Correlation Spectroscopy
d	doublet
FBS	Fetal Bovine Serum
Fmoc	9-Fluorenylmethoxycarbonyl
FACS	Fluorescence-activated cell sorting

GSH	Glutathione
HATU	1-Bis(dimethylamino)methylene]-1H-1,2,3-triazolo[4,5-b]pyridinium 3-oxide hexafluorophosphate
HRMS	High-resolution mass spectrometry
HRMS-ESI	High-resolution electrospray ionisation mass spectrometry
HOBT	1- hydroxybenzotriazole
IMM	Inner mitochondrial membrane
IMS	Intermembrane space
J	Coupling constant
LTG	Lyso Tracker Green
LySQ	Lysosome Targeting Squarine
LySQRot	Lysosome Targeting Squarine Rotaxane
MeOH	Methanol
MSQ	Mitochondria Targeting Squarine
MSQRot	Mitochondria Targeting Squarine Rotaxane
MTDR	Mitotracker Deep Red FM
MTG	MitoTracker Green FM
MTT	3-(4,5-dimethyl-2-thiazolyl)-2,5-diphenyltetrazolium bromide
MW	Microwave
m	Multiplate
NMR	Nuclear Magnetic Resonance
NIR	Near-infrared
NPs	Nanoparticle

PDT	Photodynamic therapy
PTT	Photothermal therapy
ROS	Reactive oxygen species
SQ	Squarine
SQRot	Squarine Rotaxane
SPPS	Solid phase peptide synthesis
s	singlet
t	triplet
TCSPC	Time-correlated single photon counting
TLC	Thin layer chromatography
TEM	Transmission Electron Microscopy
TPP^+	Triphenylphosphonium cation

Contents

Chapter 1

General Introduction

GENERAL INTRODUCTION

What is a mechanical bond?

A mechanical bond is a type of bond that results from the interlocking of two or more molecular components in a way that is similar to how puzzle pieces fit together.[1] Unlike a covalent or ionic bond, which involves the sharing or transfer of electrons between atoms, respectively, mechanical bonds rely on shape complementarity and topology to hold the components together. Supramolecular chemistry, which investigates chemical systems composed of multiple components held together by non-covalent interactions like hydrogen bonding, van der Waals forces, and electrostatic interactions, is where mechanical bonds are most frequently encountered. Examples of molecules that exhibit mechanical bonding include rotaxanes, catenanes, and molecular knots.[2] Mechanical bonding can also be found in materials such as fabrics, where interlocking fibers create a strong, cohesive structure.[3] Overall, mechanical bonding represents an important way in which molecular components can be assembled into functional systems, with potential applications in areas such as drug delivery, catalysis, and molecular machines.[4] For their groundbreaking contributions in the "design and synthesis of molecular machines," Jean-Pierre Sauvage, Sir J. Fraser Stoddart, and Bernard L. Feringa were jointly awarded the Nobel Prize in Chemistry in 2016.[1,5-6] Their revolutionary research has paved the way for the development of complex molecular systems that can perform mechanical tasks and respond to external stimuli.

MECHANICALLY INTERLOCKED MOLECULES (MIMs)

According to the definition proposed via way of means of 2016 chemistry Nobel laureate Fraser Stoddart, mechanically interlocked molecules

(MIMs) involve two or more distinct components that can only be separated by breaking covalent bonds.

In 1971, Gottfried Schill published a monograph-titled "Catenanes, Rotaxanes, and Knots" which focused on two typical examples of MIMs - catenanes and rotaxanes(**Figure 1**).[2] A catenane is a molecule containing two or more macrocyclic components that are interlocked through mechanical bonds. The name catenane derived from the Latin word "catena" meaning chain. On the other hand, a rotaxane gets its name from the Latin words "rota" for wheel and "axis" for axle. Rotaxanes are dumbbell shaped molecular architecture composed of at least one macrocyclic ring(s) threaded through a linear axle(s) and capped with bulky end-groups (stoppers) that prevent dethreading of the axle. It is important to note that catenanes and rotaxanes are molecules rather than supramolecular entities or supermolecules, even though they contain intramolecular noncovalent bonds. While catenanes have trivial topologies of links, rotaxanes are topologically non-trivial as their components can be separated by continuous deformation such as expanding the diameter of a ring or shrinking the cross-section of a stopper, which have been demonstrated chemically.[7]

(A) 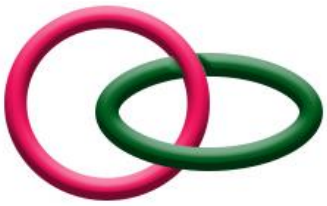 (B) 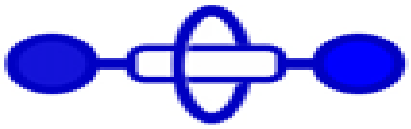

Figure 1. Graphical representations of (A) a catenane and (B) a rotaxane.[2]

STRATEGY FOR THE SYNTHESIS OF ROTAXANE MOLECULES:

In 1967, the first suggested synthesis of a rotaxane relied on the statistical probability that when halves of a dumbbell-shaped molecule were reacted in the presence of a macrocycle, a small percentage of the newly formed axle was incorporated inside the macrocycle.[8] To achieve a reasonable yield of rotaxane, solid-phase support was utilized. The macrocycle was attached to the support and treated with both halves of the dumbbell 70 times before being severed from the support to yield only 6%.[9] However, the synthesis of rotaxanes has undergone significant revolution and efficient yields can now be obtained through the reorganization of components using hydrogen bonding, metal coordination, hydrophobic forces, covalent bonds, or coulomb interactions.[10] The three most commonly used pathways for rotaxane synthesis are "threading and stoppering","clipping", and "slipping" (**Figure 2**).[11] Recently, Leigh and co-workers have described a new pathway for the synthesis of mechanically interlocked architectures that involves a transition-metal catalyzed reaction through inside the cavity of a macrocycle.[12]

Threading and Stoppering (Capping):

The capping approach for synthesizing rotaxane is predominantly based on a thermodynamically driven template effect. In this method, the "thread" is held inside the "macrocycle" through non-covalent interactions, resulting in the formation of pseudo rotaxane. The rotaxane is then formed by reacting the ends of the threaded guest with bulky groups that prevent it from slipping out from the macrocycle (**Figure 2**).

Clipping:

The clipping method is analogous to the capping approach, with the difference being that in this case, the complete dumbbell-shaped molecule is bound to a partial macrocycle. The partial macrocycle then undergoes a template directed ring-closing reaction such as amidation with suitable residue of the macrocycle across the formed dumbbell-shaped molecule, resulting in the formation of the rotaxane molecule.

Slipping:

The slipping technique is based on the thermodynamic equilibrium of the rotaxane. By utilizing bulky end groups of appropriate size, the dumbbell molecule can reversibly thread through the macrocycle at higher temperatures. However, upon cooling, the dynamic complex becomes kinetically trapped as a rotaxane.

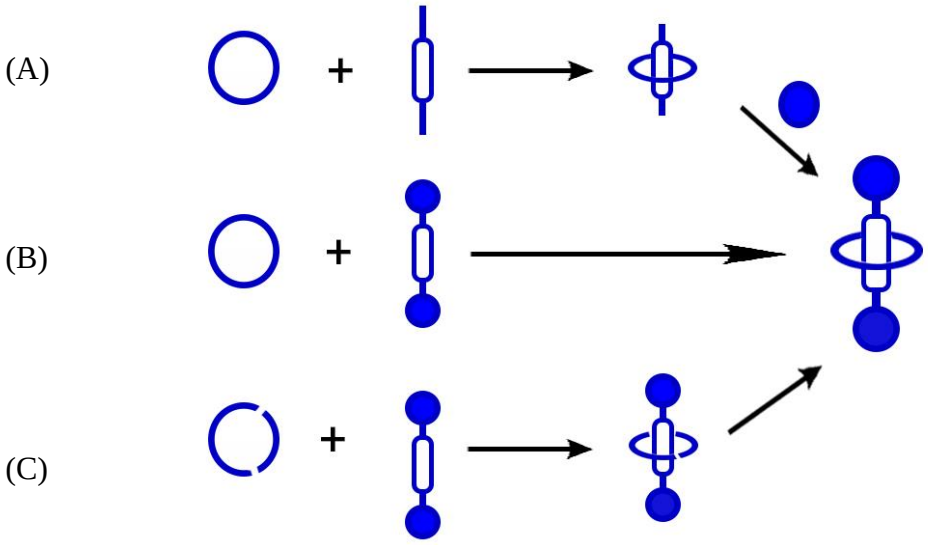

Figure 2: Graphical representations of (A) threading and stoppering (capping) (B) slipping and (C) clipping methods for the synthesis of rotaxane molecules.[11]

APPLICATION OF ROTAXANE MOLECULES:

Interesting topology and synthetic variation are the two facets for which rotaxane molecules gained significant interest. On top of this, recent efforts have proven that they can be used in many important applications. Rotaxanes have been utilized as (a) molecular shuttles, (b) chemical sensors, (c) biomarkers and (d) drug delivery vehicles.

MOLECULAR SHUTTLE:

A molecular shuttle is a unique molecular device with the potential of shuttling molecules or ions from one place to another. Molecular shuttles are relevant in the field of nanotechnology and biology with their huge array of aligning applications in biomedical functions. In addition, there is academic interest in synthetic molecular shuttles, which was first reported in 1991 and based on a rotaxane prototype.[13]

Stoddart et al. first developed an acid-base catalyzed molecular shuttle based on compound $1\cdot[PF_6]_4$, that can reversibly switch between two states by altering pH (**Figure 3**).[14] The switching of the ring from one station to the other was carried out using acid and base. To characterize the dynamics of the bead's movement along the thread before and after switching, ^{1}H NMR and UV/vis spectroscopy were employed. The addition of excess deuterated trifluoroacetic acid (TFA-d_1) to the solution of compound $l\cdot[PF_6]_4$ in CD_3CN resulted in significant changes in the NMR spectrum. In presence of pyridine-d_5 (base) which effectively regenerated the ^{1}H NMR spectrum due to the protonation of the benzidine nitrogens and hence the macrocycle was shifted from the benzidine station to the biphenol station. In presence of pyridine-d_5 (base) which effectively regenerated the ^{1}H NMR spectrum obtained prior to TFA-d_1 (acid) addition via diprotonation of the ammonium group of the

benzidine residue and hence the macrocycle was shifted from the biphenol station to the benzidine station. This finding confirmed the reversible nature of the structural changes resulting from the protonation and deprotonation of the benzidine residue.

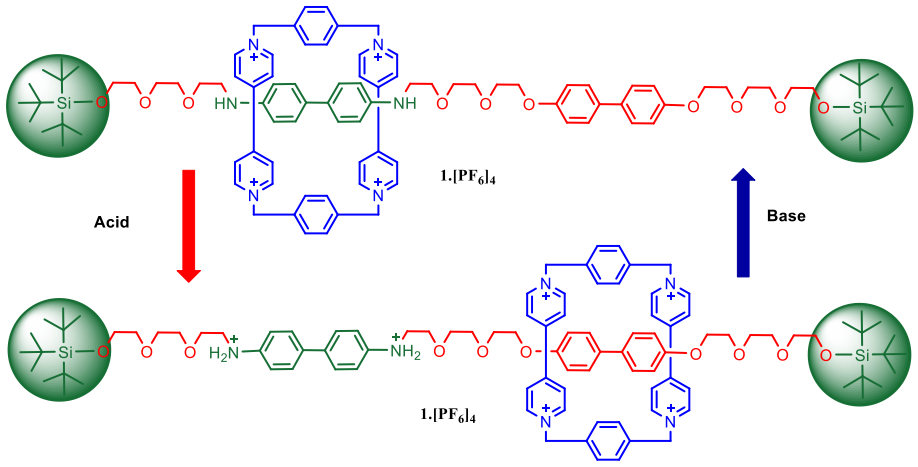

Figure 3. Rotaxane based pH sensitive molecular shuttle.[14]

Liu et al. published a report in 2013 on a double-leg donor-acceptor molecular elevator that allowed for controlled separation between two aromatic platforms by utilizing translational motion of macrocycles along a bis-threaded axle (**Figure 4**).[15] At the protonated state 2, the bis-crown ether interacts with the ammonium molecular stations via non-covalent interactions. The naphthalene diimide residue interacts with the anthracene moiety through charge transfer, which quenches the fluorescence of the interlocked molecule 2. Semi-rotaxane formation is enhanced by the charge transfer, and the molecule can be efficiently assembled with only a stoichiometric amount of each component.[16] Deprotonation of rotaxane 2 was performed by a strong base phosphazene. The shuttling of the bis-crown ether towards the triazolium stations was induced by base. Consequently, the anthracene and naphthalene diimide residues were

separated which helps to restore the fluorescence intensity of the anthracene and function as a molecular elevator.[17]

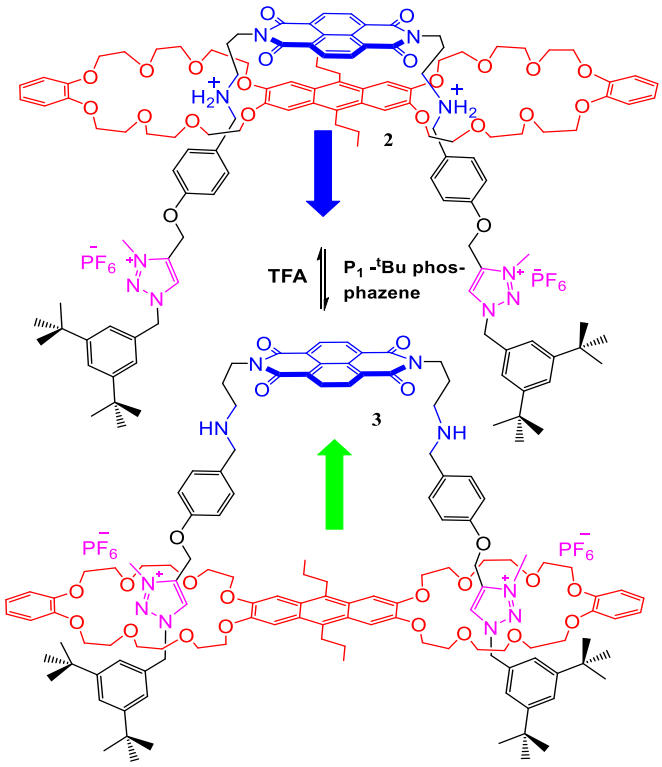

Figure 4. Actuation of a triazolium-containing double-leg molecular elevator.[15]

Chen et al. reported a novel example of "chemical design" in 2014, which was inspired by bionic machines. They utilized copper catalyzed azide/alkyne cycloaddition (CuAAC) and methylation of triazoles to synthesize a 2-rotaxane featuring a pentiptycene-derived bis(crown ether), ammonium stations, and N-methyltriazolium stations (**Figure 5**).[18] This doubly-threaded molecule exhibited pH sensitivity and mimicked the flapping motion of butterfly wings. Upon deprotonation of the ammonium-containing rotaxane, the DB24C8 rings moved to the triazolium stations, and the twist of the host was necessary for the

DB24C8 to reside around the triazolium units due to the steric hindrance and constraints. The reversed process was induced by the TFA. The sequential pH-dependent approach and distancing of the related DB24C8 moieties was simulated the wing-flapping motion of a butterfly, where the DB24C8 moieties represented the wings.

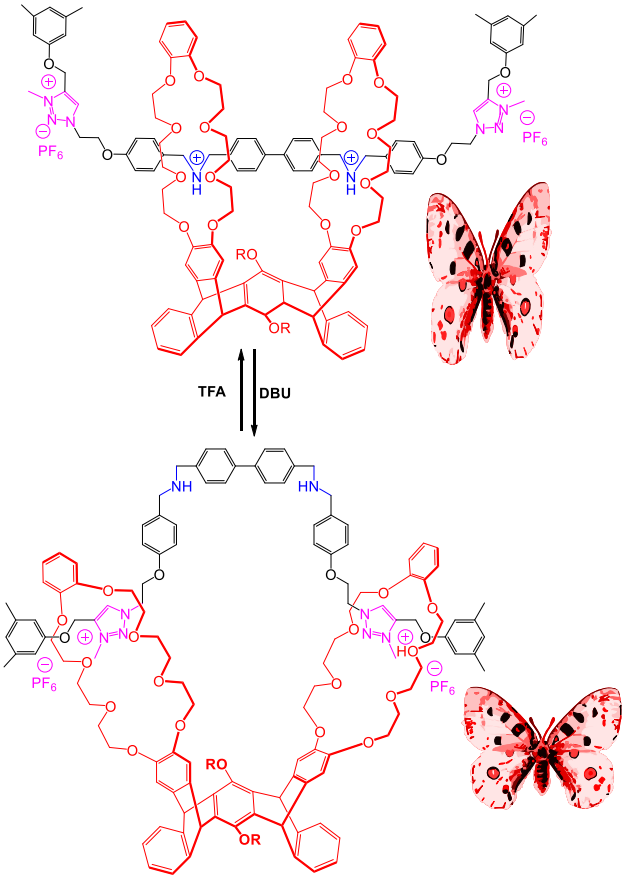

Figure 5. Mimicking the wing-flapping motion of a butterfly using a triazolium-containing pentiptycene bis(crown ether)-based [2](2)rotaxane.[18]

Houk and Ho at UCLA have synthesized a redox-switchable donor-acceptor [2] rotaxane (**Figure 6**).[19] Chemical oxidation of tetrathiafulvalene (TTF) to TTF^{+2} generated a strong charge-charge repulsion between the cyclo bis(paraquat-p-phenylene) {$CBPQT^{+4}$} ring and TTF^{+2}, caused the macrocycle to shuttle to the electron-rich 1,5-dihydroxynapthalene moiety. The AFM experiment revealed that more force was required on average to pull the cyclophane off from the dumbbell in A^{6+} (145 pN) compared to A^{4+} (66 pN). This indicates that the force generated along the pathway of the away movement of donor-acceptor [2] rotaxane from TTF^{2+} on oxidation could reach 79 pN. This force was quite large for a single rotaxane molecule compared to the forces (5-60 pN) produced in many biological machines. [20]

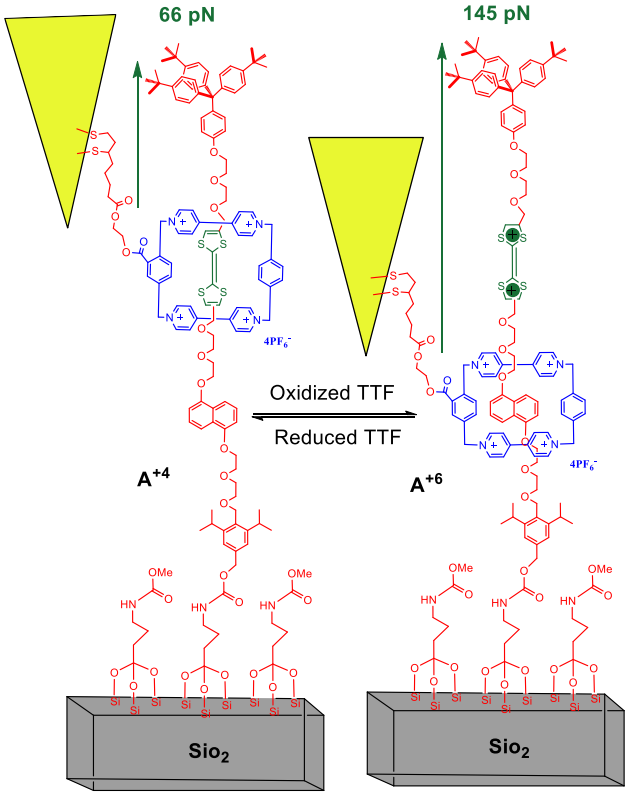

Figure 6. Redox-switchable donor-acceptor [2] rotaxane.[19]

Chemical sensor:

Rotaxane molecules have been studied for their potential applications as chemical sensors due to their unique properties. The threaded ring component of a rotaxane molecule can move along the molecular axle in response to external stimuli such as pH, temperature, or the presence of specific analytes. This movement can be used to detect and quantify the analytes.

There was a report of a rotaxane-based fluorescent chemical sensor for metal ions.[21] A crown ether macrocycle was tethered to a rotaxane molecule that can selectively bind to metal ions, and a fluorescent dye that was quenched in the absence of the metal ion. When the metal ion was bound to the macrocycle, the ring component of the rotaxane moved along the axle and released the fluorescent dye, as a result fluorescence was enhanced. This approach has been used to detect metal ions such as copper and chloride in aqueous solutions.

In addition to metal ion sensing, rotaxane molecules have also been explored for their potential applications as sensors for other analytes such as glucose, pH, and biomolecules. With their high sensitivity, selectivity, and reversibility, rotaxane-based chemical sensors are ideal for a variety of applications including environmental monitoring, medical diagnostics, and industrial process control.

A fundamental area of modern supramolecular chemistry research is to develop anion induced molecular shuttles. Synthetic receptors that can transduce anion binding events into detectable optical signals is one of the aims of developing a molecular shuttle with high chemical stability. In this quest Smith *et al.* has developed a squaraine rotaxane-based molecular shuttle (**Figure 7**) which acts as deep-red fluorescent and colorimetric sensor for Cl^- anion.[22] This synthetic feat has been achieved by converting pseudorotaxanes into permanently interlocked rotaxanes through Cu(I) catalyzed click chemistry. In this much

coveted rotaxane when titrated with tetrabutyl ammonium chloride and the absorption, fluorescence spectroscopy has been monitored, it has been established that the color changes due to the movement of absorption maxima from 663 nm to 647 nm. On top of this, concurrently, the Cl^- association process was restored by incorporating Cl^- precipitating reagent which restores the rotaxanes' inherent property.

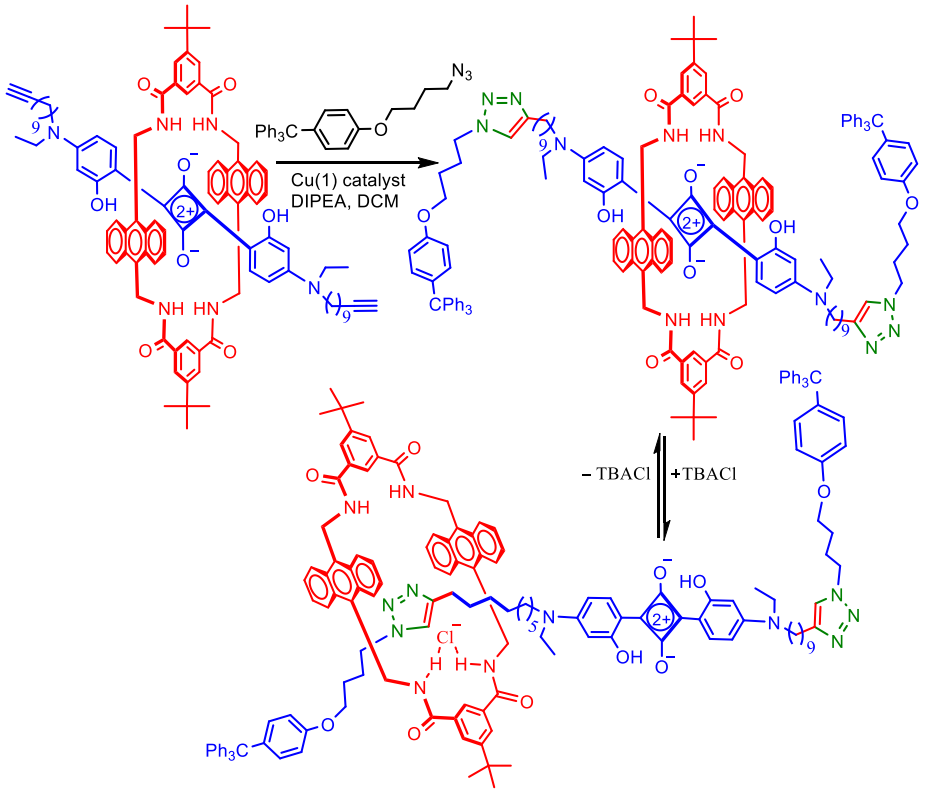

Figure 7: Squaraine rotaxane shuttle for ratiometric Cl^- sensing.[22]

Another work in the field of molecular shuttle was the development of anion and pH-dependent molecular motion by halogen bonding and other external stimuli. In the area of developing synthetic receptors capable of transducing anion binding events into detectable optical signals, the pioneering work has been made by Paul D. Beer and his group. They achieved this through the

origination of a [2]-rotaxane, which features a halogen binding benzimidazole-iodotriazole station directly conjugated to a naphthalimide station axle component.[23] This overall system was driven by anion induced external stimuli and as a result naked-eye detectable colorimetric response has been observed. Both the stimuli in the form of protonation of the benzimidazole moiety and addition of co-ordinating anion for instance chloride was essential in order to facilitate the molecular shuttling effect of macrocycle translocation.

For synthesizing the half axle precursors, Beer and co-workers have chosen to follow two separate pathways. These pathways involve the creation of a naphthalimide-based benzimidazole-iodotriazole stoppered azide, as well as a stoppered alkyne. (**Figure 8**).[23] CuAAC stoppering reaction has been performed after protonation of the benzimidazole azide and subsequent addition of isophthalamide macrocycle to produce [2]-rotaxane. The translocation of macrocycle from naphthalimide platform towards the benzimidazole platform has been confirmed by HCl addition which displays naked-eye color change which was further established through the significant shift in the region $\lambda > 340$ nm with the disappearance of broad absorbance band at 380 nm. Both ^{1}H NMR and ^{1}H-^{1}H ROSEY NMR spectra of each compound upon HCl addition intensified the fact that MIM co-conformational difference has indeed taken place.

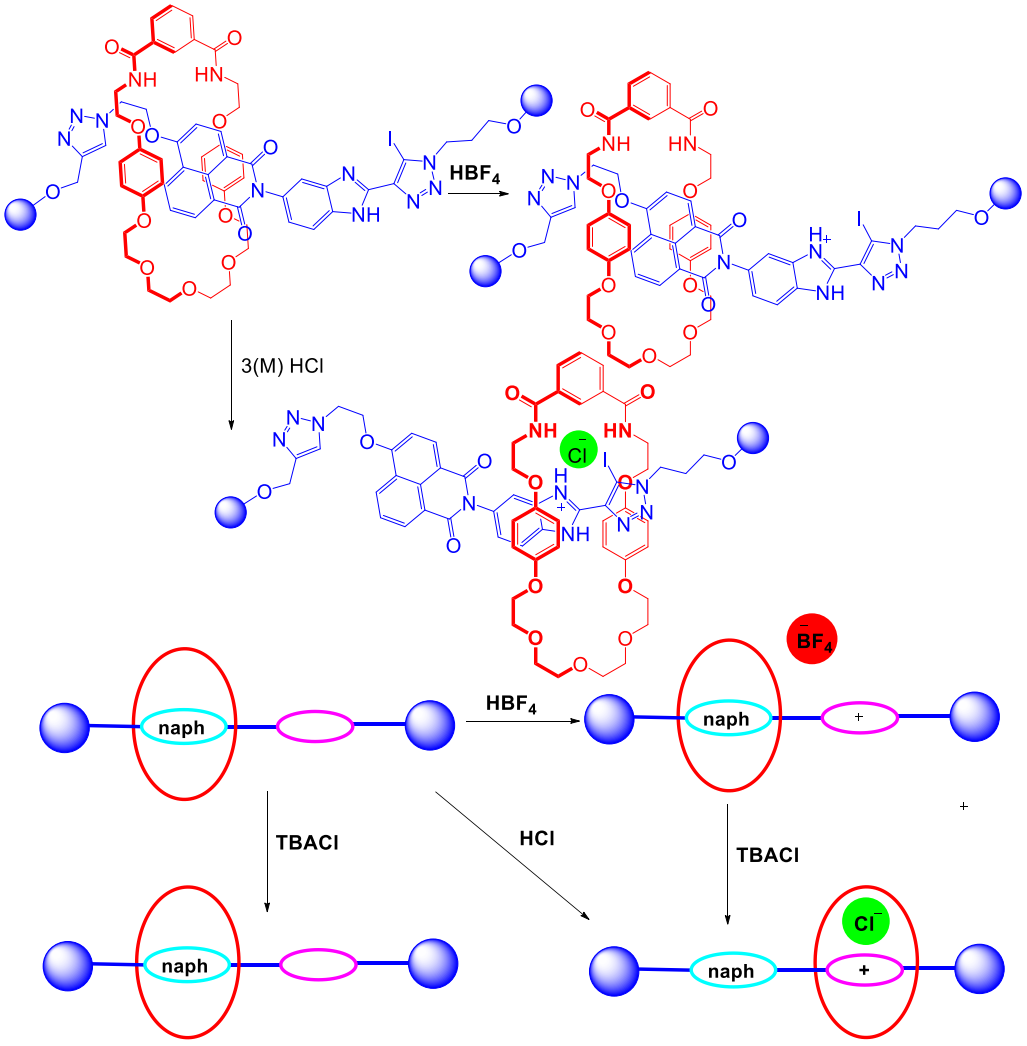

Figure 8: Synthesis of a Cl^- sensitive [2]rotaxane.[23]

In a corresponding work, Beer *et al.* has reported the synthesis of the first halogen bonding based [3]-rotaxane system (**Figure 9**).[24] The uniqueness of this system lies in comprising of four station axle components, consisting of bis-iodotriazole-bis-naphthalene diimide motifs. These varieties of stations enabled the system to display co-operative halogen binding and hydrogen binding which provided selectivity in nitrate anion binding over other oxoanions and chloride. This [3]-rotaxane system operated in a pincer like molecular motion in which both macrocycles show shuttling movement from periphery of the axle component towards the central halogen bonding bis-iodo-triazolium station upon exposure to anion. The translational molecular shuttle nature of the system has been verified by introducing $TBANO_3$ to rotaxane in $CDCl_3$ solution. The ^1H NMR spectra depicts that the macrocycle undergoes a concerted molecular pincer like movement from the peripheral NDI stations into the bis-triazolium station located at the center of the [3]-rotaxane system. The ^1H-^1H ROESY NMR ensured the movement via cross coupling between macrocyclic protons and the axle protons associated with the bis-triazolium station.

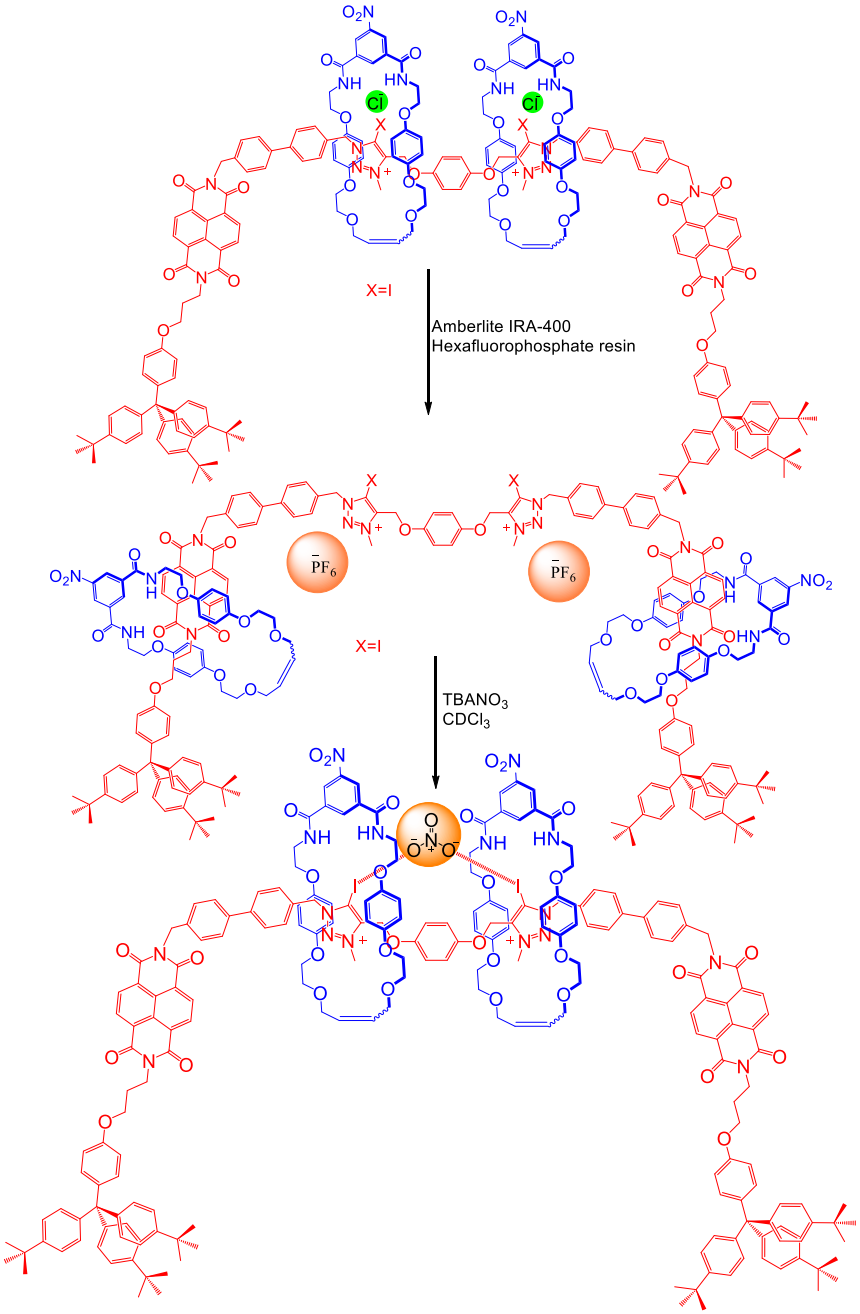

Figure 9: Synthesis of a halogen bond forming [3]rotaxane. Nitrate recognition by a halogen bond forming four station [3]rotaxane molecular shuttle.[24]

BIOLOGICAL ACTIVITY AND DRUG DELIVERY SYSTEM:

In biological systems, rotaxanes have been studied for their potential applications as drug delivery vehicles. Rotaxanes can be functionalized with suitable targeting moieties such as antibodies or peptides, which can selectively bind to specific cells or tissues.[25] This can enhance the efficacy of the drug by delivering it directly to the affected area while minimizing its exposure to healthy tissues.[26-27] Rotaxane formation improves the stability of drugs, especially those that are prone to degradation or have low solubility. The macrocyclic ring can protect the drug from premature degradation, while the dumbbell-shaped molecule can enhance the solubility of the hydrophobic drugs. Overall, the unique properties of rotaxanes make them promising candidates for a wide range of applications in the field of biological activity and drug delivery. While there is still much research to be done, to improve the efficacy and safety of drugs based on rotaxanes.

Choudhary and co-workers have reported a [2]pseudorotaxane based on maleimide-functionalized naphthalene diimide (NDI) guest and thiol functionalized stopper (**Figure 10**).[28] In the biological system, such rotaxane molecule opens the possibility of using stimuli-responsive moieties for allosteric control over the protein and enzymes.

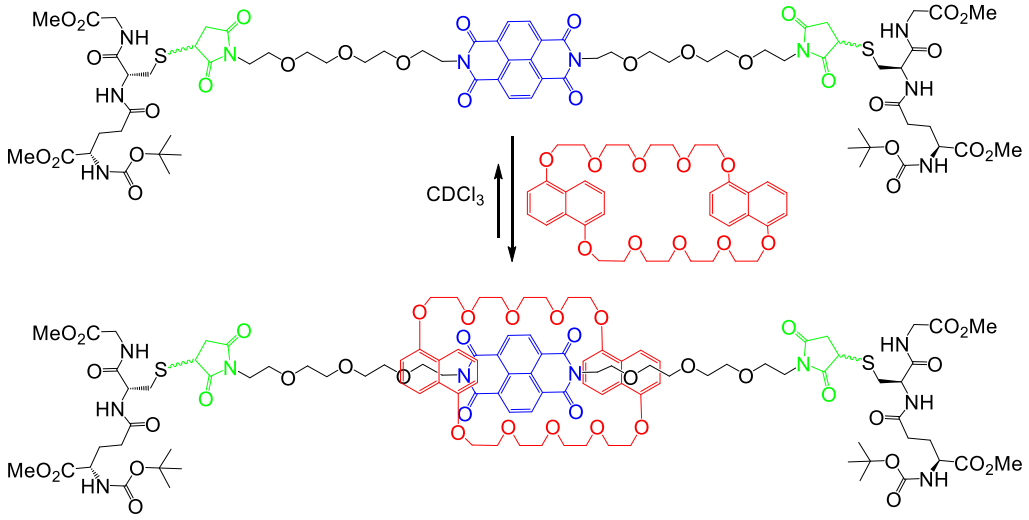

Figure 10. Glutathione-functionalized [2]pseudo rotaxane.[28]

Apart from being poorly able to cross cell membranes, many bioactive peptides are also prone to in-vivo instability due to fast degradation by the enzymes present in the biological milieu. For example, met-enkephalin, the pentapeptide (YGGFM), which has a critical response against proliferative activities in many cancer cell lines, [25-27] is not suitable as an anticancer drug because of its degradation in human plasma in less than 5 min. Leigh and co-workers demonstrated that the release of this met-enkephalin can be stimuli-responsive when attached to a galactoside trigger, self-immolative stopper and caged inside a benzylic amide macrocycle, forming a mechanically interlocked rotaxane (**Figure 11**).[29] The macrocycle acted as a transient defender against the plasmatic enzymes, thus protecting the peptide bonds of met-enkephalin from being hydrolyzed. *β*-Galactosidase, which is overexpressed in tumor tissues, can now cause the active peptide to be released quickly by forming an unstable phenolate intermediate that underwent 1,6-elimination followed by rapid decarboxylation.

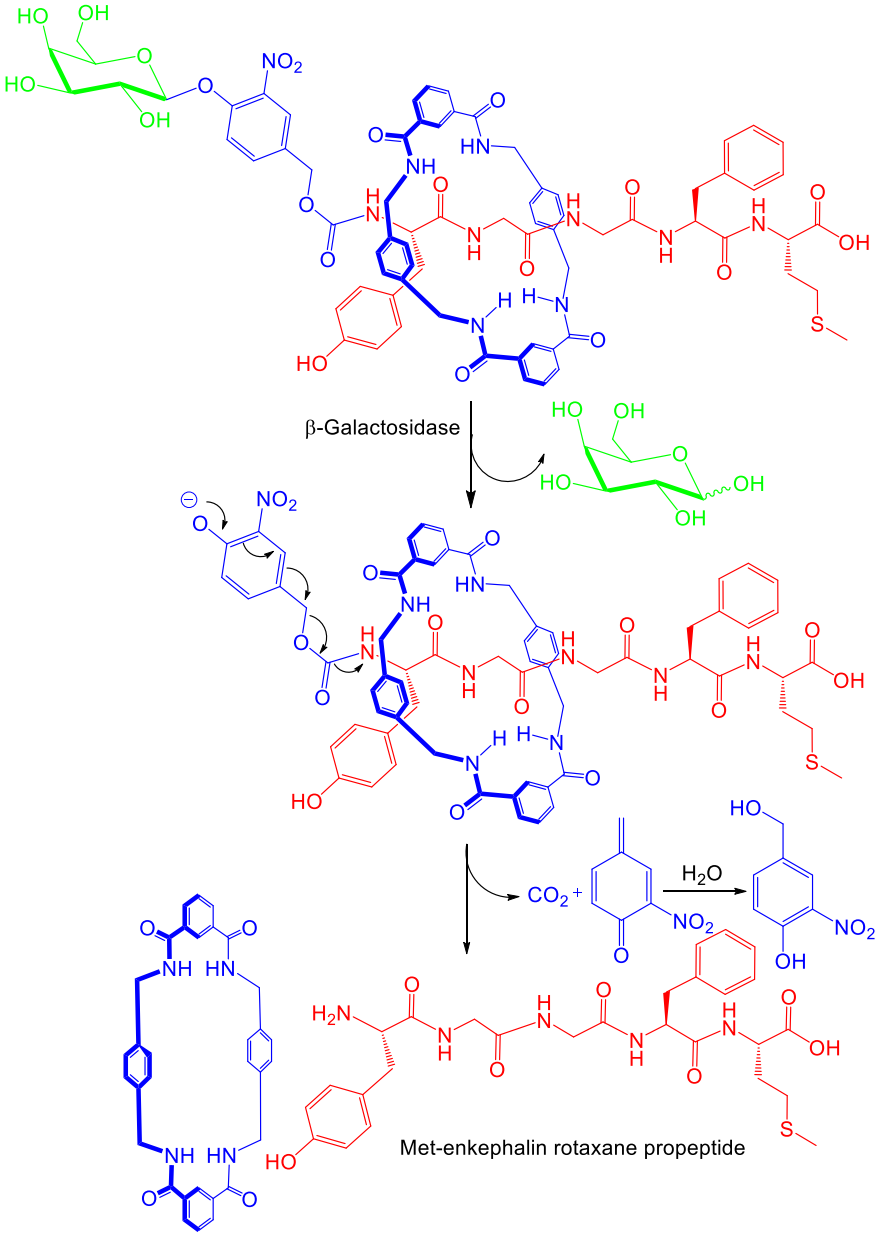

Figure 11. Met-enkephalin rotaxane for the enzyme trigger release of the pentapeptide.[29]

Mitochondria Targeting Pseudorotaxane:

Liu and co-workers have reported two-photon supramolecular ternary assembly with NIR emission for mitochondria-targeted imaging built from TPE moiety comprising methoxyl and vinyl pyridinium cation (TPE-2SP), *β*-cyclodextrin containing hyaluronic acid (HA-CD), and cucurbit[8]uril (CB[8]) (**Figure 12)**.[30] TPE-2SP exhibited very weak λ_{em} at 650 nm, however, in presence of CB[8] has a great binding affinity with cationic pyridinium residue, it forms supramolecular netlike pseudorotaxane (TPE2SP/CB[8]) which showed enhanced and red-shifted NIR λ_{em} at 680 nm in H_2O because of restricted rotation of the C=C bond. The pseudorotaxane TPE2SP/CB[8] was further assembled with HA-CD (cancer cell targeting agent) to form nanoparticles (β-CD can participate in host–guest complexation with the methoxyphenyl unit of TPE-2SP), causing assembling-induced augmentation of NIR emission. Amazingly, pseudorotaxane based supramolecular nanoparticles possess the two-photon character, and were effectively used for targeted NIR imaging of mitochondria in A549 cancer cells.

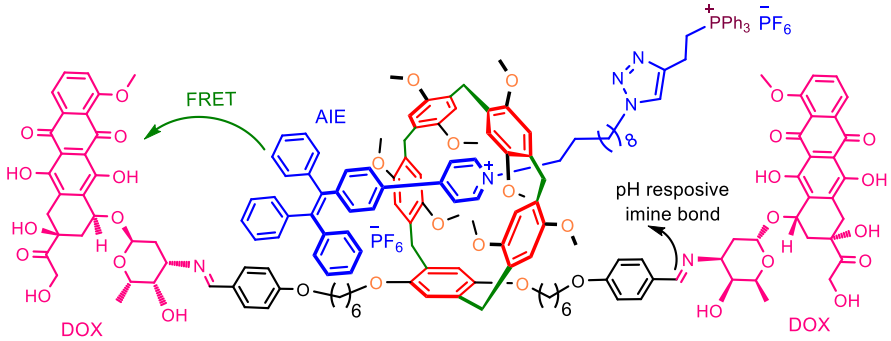

Figure 12. Mitochondria targeted DOX conjugated pillar[5]arene-based [2]rotaxane molecule.[30]

pH-Activated Photothermal Heating and Ratiometric Photoacoustic Imaging of Acidic pH based on Rotaxane:

Photothermal heating and ratiometric imaging techniques have immerged as great tools in modern-day medical applications. Towards this end, Guha et al. developed a ratiometric pH-sensitive croconaine rotaxane (pK_a= 6.0) (**Figure 13**).[31] The basic form of the dye has an absorbance at around 660 nm. A large red shift of 134 nm in absorbance is observed in the acidic pH, at a zwitterionic form of the dye (794 nm). The marcocycle prevents nucleophilic attack on croconaine thus stopping photobleaching. Photothermal heat generation was mainly turned on at acidic pH and turned off at physiological pH when irradiated with an 808 nm laser. Multiple photothermal heating cycles with unquantifiable change in absorbance as well as photothermal heating were observed when this croconaine rotaxane doped stealth liposomes were irradiation using an 808 nm laser. This NIR pH-responsive ratiometric photoacoustic imaging probe could easily detect the weakly acidic (6-6.5) pH region in deep tissue locations, including a living mouse.

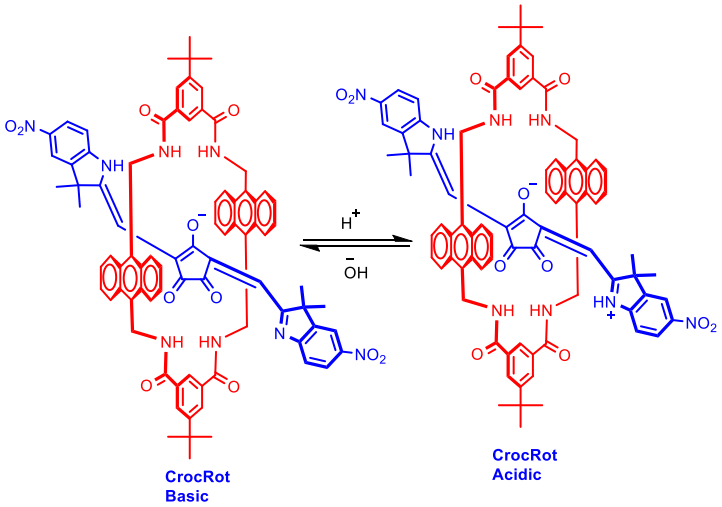

Figure 13. pH sensitive croconaine rotaxane.[31]

Viral Neuraminidase Cleavage Assay based on Rotaxane:

An enzymatic cleavage experiment sensitive to viral neuraminidase, an indicator of influenza infection, has been developed recently by Smith et al. The technique was based on capture of deep red fluorescent squaraine dye **SQ1'**, inside a tetralactam macrocycle, **M**, by threading after the bulkier sialic acid group stoppers of the bis(4-amino-3-hydroxyphenyl) squaraine dye, **SQ1**, was being cleaved by the viral neuraminidase **(Figure 14)**.[32] **SQ1** showed a very weak fluorescence emission at 660 nm and low photostability. The results change drastically with neuraminidase activity, and there was a red shift with a high intensity fluorescence signal at 720 nm, indicating the formation of the rotaxane structure and the dye showed high photostability. With the use of affinity capture beads to localize the liberated SQ1', the authors demonstrated the usefulness of the assay in quantitative estimation through automated heterogeneous procedures such as fluorescence microscopy, microfluidics, or flow cytometry. In addition of fluorescent neuraminidase assay, the assay can determine quickly between the two accepted antiviral medicines, Oseltamivir (Tamiflu) or Zanamivir (Relenza), would be the utmost potent therapeutics for a particular patient.

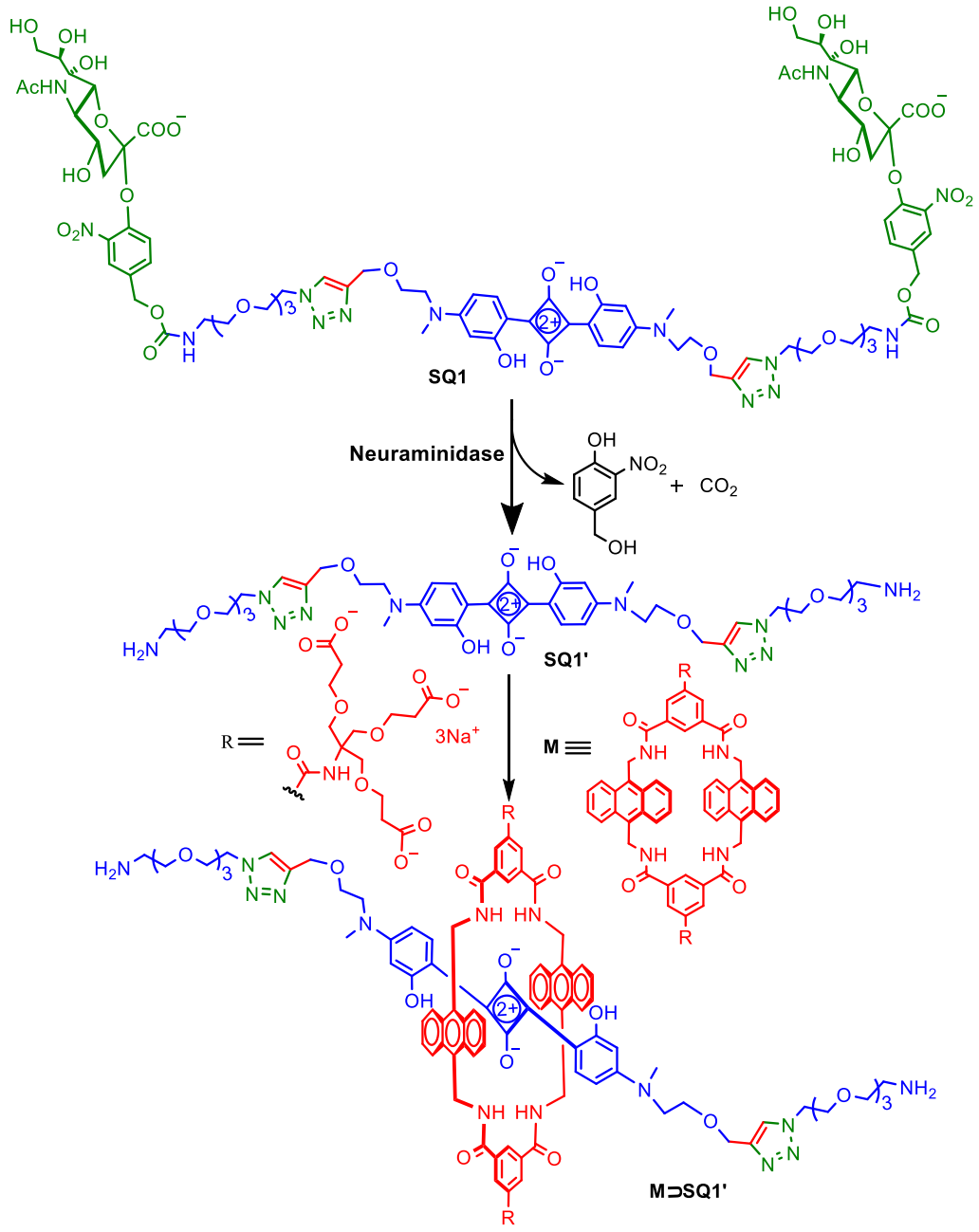

Figure 14. Neuraminidase cleavage assay by in situ capture of the fluorescent dye by a macrocycle.[32]

Synthetic peptides often qualify as a popular choice for biological imaging. Some of the major limitations by opting naturally occurring linear polypeptides are a) less targeting ability, b) lesser cell permeability and c) minimal resistance towards proteolytic enzymes. In order to mitigate these drawbacks, structural modifications were done to synthesize peptidomimetics with better properties. Smith *et al.* has reported a covalently connected squaraine figure eight like molecular structure with better stability, permeability and target specificity (**Figure 15**).[33] In such covalently connected molecules, the squaraine fluorochrome is buried deeply inside the macrocycle resulting in better stability as well as less probability of self-aggregation. Squaraine core has been often used for fluorescence microscopy because in the deep red and NIR region endogenous cell biomolecules absorb minimally with significantly lowered auto fluorescence. The group has developed a deep-red fluorescent peptide for high-performance bioimaging with self-threaded molecular figure eight architecture. This synthetic feat has been achieved by starting with a mechanically interlocked squaraine rotaxane molecule along with side-chain protected peptide attached by amide bond to each end of squaraine rotaxane. Lastly, a double macrocyclization step was carried out using CuAAC reaction. The advantages of the covalently bonded peptidyl squaraine figure eight (SF8) over the mechanically bonded squaraine rotaxane predecessor were as follows: (a) the peptidyl design element of the SF8 molecules induces high water solubility compared to its mechanically interlocked counterparts, (b) the scope for self-aggregation was significantly lower for the self-threaded peptidyl structure; as a result the emission peak remains narrower with high intensity. In addition to this, squaraine figure eight molecules show higher withstanding capability in proteolytic enzyme medium compared to the mechanically interlocked squaraine rotaxane molecules.

Imaging studies of this SF8 probe established the fact that these molecular architectures have huge advantages in biological imaging. The peptidyl loops in these SF8 molecules specifically help in targeting biomedically relevant biomolecules such as cell surface receptors which inevitably can open up new avenues in imaging techniques.

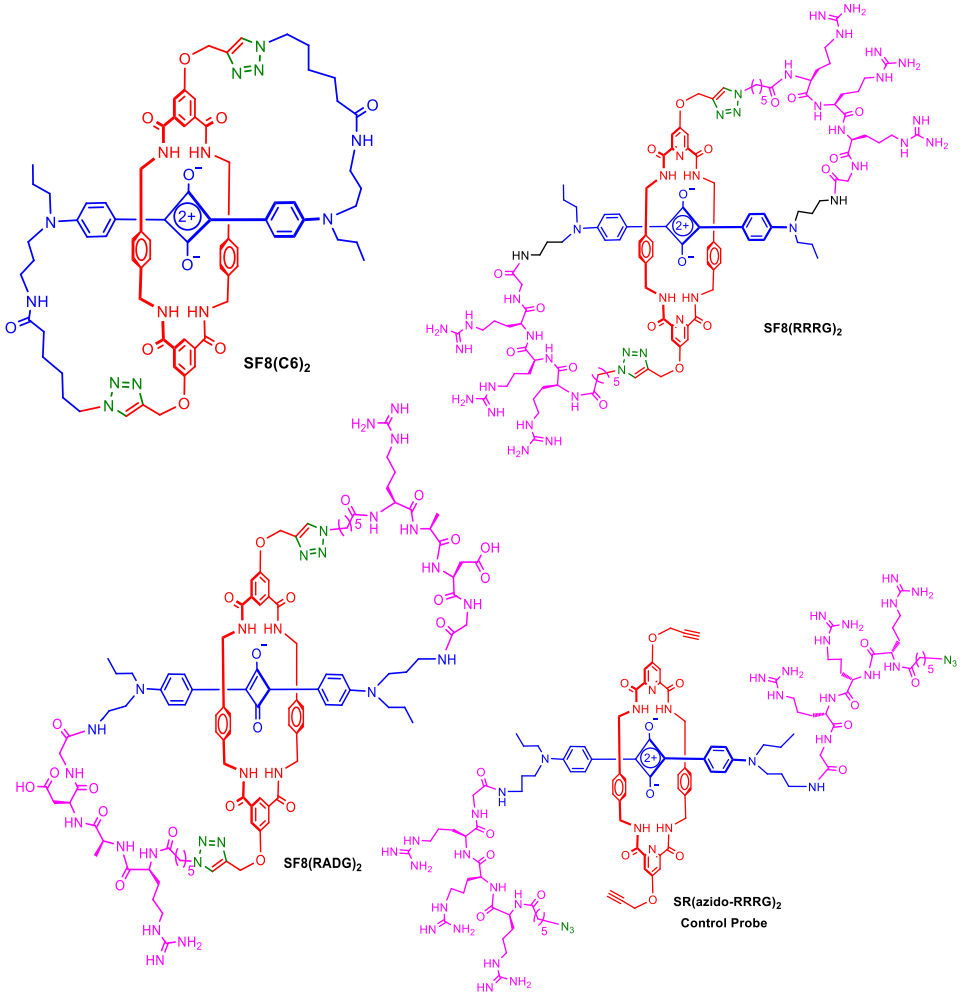

Figure 15. Peptidyl SF8 probes and linear control probe.[33]

Why mitochondria are an important target for all cells:

Amongst the innumerable cellular organelle's mitochondria are an important target for all cells. Mitochondria are the powerhouse of cells and control cellular function and fate.[34] Mitochondria play a key role in programmed cell death such as apoptosis.[35] So, mitochondria targeting and staining are the key methods for the diagnosis of mitochondria associated diseases. However, it is very difficult to target mitochondria due to the double layer membrane and highly negative inner mitochondrial membrane (IMM) potential [$(\Delta \Psi_m)_{normal}$ − 150 to –180 mV and $(\Delta \Psi_m)_{cancer}$ –220 mV].[36-37] The shape of mitochondria can vary from spherical to elongated, and can be tubular, rod-shaped, or even branched and found in most eukaryotic cells. The shape of mitochondria is often influenced by the cell type and its metabolic needs. For example, muscle cells have more elongated mitochondria to support the high energy demands of muscle contractions, while liver cells may have more spherical mitochondria to efficiently process nutrients. The size of the mitochondria is usually 0.5–1 μm in diameter, 1–10 μm in length.[38] Mitochondrial size and shape can also be influenced by environmental factors such as stress, disease, and aging. For example, mitochondria may become more fragmented or swollen in response to cellular stress or damage, which can affect their function and lead to disease. Mitochondria are frequently altering their shape, size, and position due to mitochondrial dynamics by undergoing fission, fusion, and motility. Overall, the size and shape of mitochondria are important factors that contribute to their function and are influenced by a variety of genetic and environmental factors.

Design of Mitochondria Targeting Organic Molecules:

Lipophilicity and delocalized cationic charge of the molecule are the two most important biophysical parameters considered for constructing effective mitochondria targeting agents. Additionally, in order to successful localization towards mitochondria, molecules also required to cross the barrier of both the plasma membrane as well as mitochondrial membranes. Typically, IMM possesses more negative membrane potential ($\Delta\Psi_m$ −150 to −180 mV) in contrast to plasma membrane ($\Delta\Psi_p$ −30 to −60 mV) which allows higher accumulation of lipophilic cation inside the mitochondrial matrix. In comparison to normal healthy cells, malignant cells mitochondria maintain hyperpolarised IMM potential [$(\Delta\Psi_m)_{cancer}$ ~ −220 mV], exploiting this over negative potential, probes can be designed to specifically target cancerous cell mitochondria over non-cancerous mitochondria. However, complex biological environment makes it challenging to target mitochondria.

Over the span of last few decades, convenient synthetic protocol and the higher specificity makes the covalently modified lipophilic cationic compounds appropriate as mitochondria-targeting agents. Higher lipophilicity and the positive charge density eventually make it easier to cross the hydrophobic phospholipid bilayers and to accumulate inside the mitochondrial matrix. The delocalised lipophilic cationic mitochondriotropics has the ability to dissipate the positive charge across the large surface area either via shielding the charge or delocalising it while passing through the inner mitochondrial membrane space and these results dropping of the activation energy for transportation through the phospholipid bilayer. The Nernst equation depicts that for every ~61.5 mV increases in $\Delta\Psi_m$, the concentration of the lipophilic molecules increases ten folds; thus, in response to the $\Delta\Psi_p$ of −30 to −60 mV these compounds first concentrate in the cytosol 5–10 times more than that in the

extracellular matrix. Thereafter, based on the hypernegative IMM potential, there occurs 100-1000-fold higher accumulation within the mitochondrial matrix compared to cytosol.[39] Inspired by the TPP^+, ammonium, pyridinium, isoquinolinium and other mitochondria targeting agents having comparable characteristics have also been developed (**Figure 16**).[40-47] Guanidinium containing arginine, oligomers comprising of chiral bicyclic guanidinium moieties, nonpeptidic oligoguanidinium, octa-arginine oligomers for mitochondria targeting have also been constructed (**Figure 16**).[48-50] Delocalized cationic rhodamine, cyanine, dequalinium, and berberinium have also been utilized (**Figure 16**).[51-57]

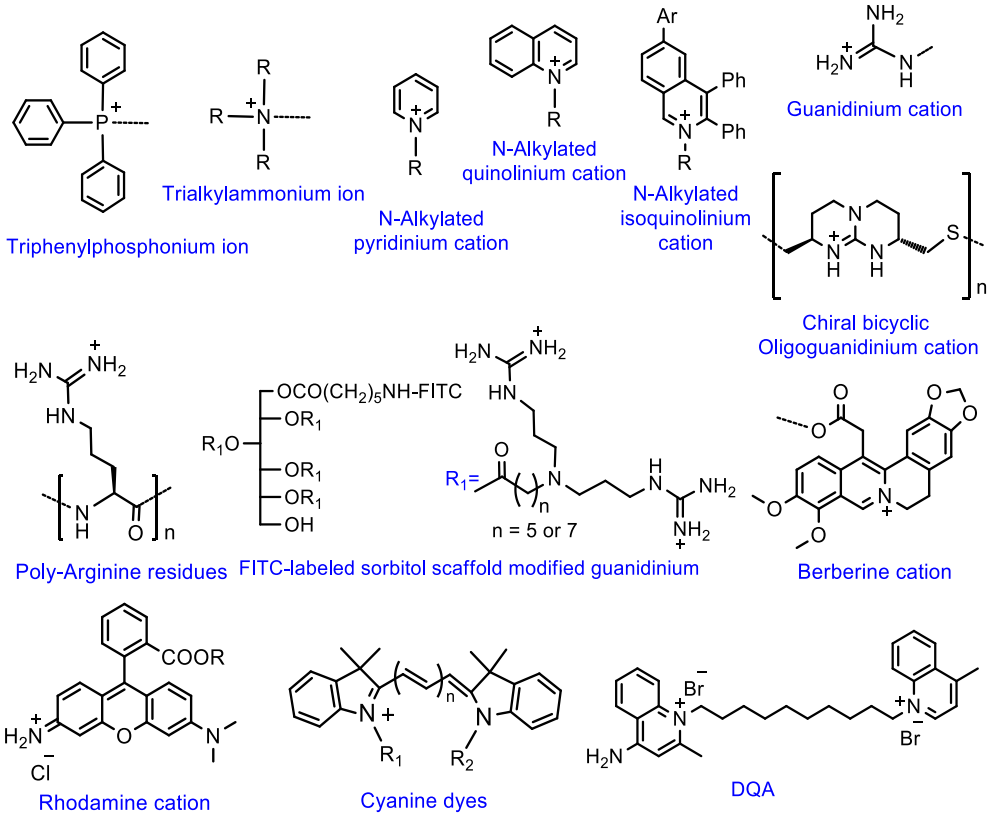

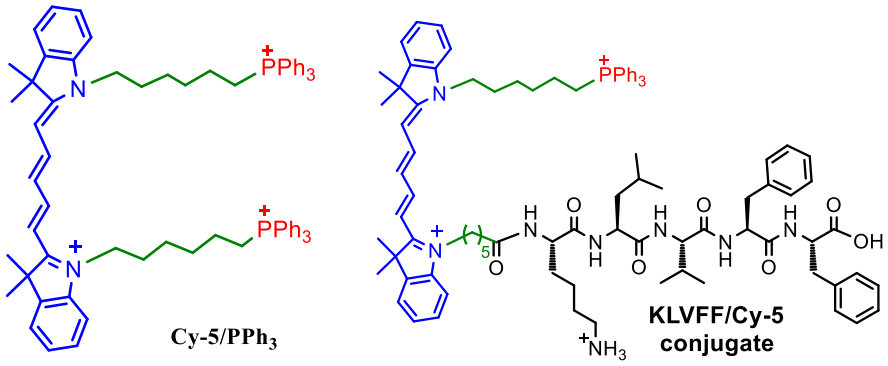

Figure 16. Mitochondria targeting structural scaffolds.[40-57]

Lysosome:

Lysosomes are crucial cellular organelles that play a critical role in maintaining the cellular environment.[58] Christian de Duve, a Belgian biochemist, and cell biologist is credited with the discovery of the lysosome in 1955. His ground-breaking research on insulin in pancreatic cells led him to observe the presence of tiny structures containing enzymes that could break down and digest cellular waste. De Duve named these structures "lysosomes". In recognition of his pioneering work, de Duve shared the Nobel Prize for Physiology or Medicine in 1974 with Albert Claude and George Palade.

Functions of the Lysosome:

Lysosomes are essential organelles within cells that digest a variety of complex molecules, such as carbohydrates, lipids, proteins, and nucleic acids. They achieve this by using hydrolytic enzymes that are optimally active in an acidic environment with a pH of around 4.0-5.0.[59] This pH is in contrast to the physiological pH of the cell, and it ensures that the enzymes are functional and effective in their role. Similar to the digestive system of the human body, lysosomes can be thought of as the “digestive system” of the cell, as they break down molecules into smaller pieces using hydrolytic enzymes. This breakdown

process is called hydrolysis and involves the addition of a water molecule, which cleaves the larger molecule. A range of enzymes, including proteases, amylases, nucleases, lipases, and acid phosphatases, can be found in lysosomes. The presence of lysosomes within cells is essential for the proper degradation and recycling of complex molecules.[60] By breaking down these molecules, the lysosome helps to maintain the health and function of the cell, allowing it to carry out its many essential processes.

Lysosomes perform several different functions within the cell. They can digest food molecules that have entered the cell, as well as degrade and recycle cellular components that are no longer functional. This process is called autophagy and helps to maintain the health and function of the cell.[61]

Lysosomes also have a crucial role in phagocytosis, which is the process by which a cell engulfs a molecule or particle to break it down. For example, white blood cells called phagocytes ingest invading bacteria by enclosing them in a vesicle, which then fuses with a lysosome. The lysosome then breaks down the bacteria, destroying it in the process. This function is essential in the body's defense against infection and disease.

Structure of Lysosome:

Lysosomes are tiny spherical organelles found within cells, typically ranging in size from 0.1-0.5 µm, although they can occasionally reach up to 1.2 µm. These structures consist of a simple lipid bilayer enclosing fluid that contains various hydrolytic enzymes. Phospholipids are the primary components of this bilayer, and they arrange themselves in a double-layered membrane due to the properties of their hydrophilic phosphate head groups and hydrophobic fatty

acid tails. The endoplasmic reticulum is responsible for the synthesis of the hydrolytic enzymes found in lysosomes, which are then transported to the Golgi apparatus. At this point, they are tagged with a molecule called mannose-6-phosphate and packaged into lysosomes. The Golgi apparatus is also responsible for the formation of lysosomes, which bud off from this organelle.

Design of Lysosome targeting functional groups:

Lysosomes are known for their acidic nature, with a pK_a ranging from 4.0-5.0. This property has led to the development of lysosome-targeting groups that are able to easily uptake protons and accumulate in higher concentrations within lysosomes. To enable visualization of lysosomes inside living cells under a fluorescent microscope, fluorescent moieties have been attached to these functional groups.

Secondary and tertiary amines have similar pK_a values to lysosomes and are thus ideal candidates for lysosome-specific groups.[62] Several such groups have been developed, including morpholine, piperazine, N-ethyl-N-methyl ethanamine, and mannose 6-phosphate.[63-66] Overall, the ability to target lysosomes with specific functional groups and fluorescent markers has opened up new avenues of research into the behaviour and function of these important cellular organelles.

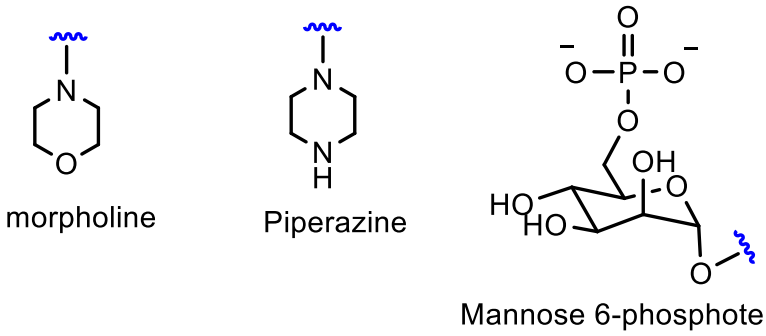

Figure 17. Lysosome targeting structural scaffolds.[63-66]

Mitochondrial-lysosome interaction, cross talk and contact site between two organelles:

Mitochondria and lysosomes are two important organelles in eukaryotic cells, each with unique functions. Recent studies have shown that these two organelles also interact with each other, forming contact sites that facilitate cross-talk between them.

One important aspect of mitochondrial-lysosome interaction is the regulation of cellular energy balance. Mitochondria produce ATP, which is the primary source of energy for the cell.[67] However, in conditions of nutrient deprivation or stress, lysosomes can break down cellular components to generate amino acids and other nutrients that can be used by the mitochondria to produce energy. This process is known as macro pinophagy or lysosomal-mitochondrial axis (LYMA).

Another important aspect of mitochondrial-lysosome interaction is the regulation of cellular metabolism.[68] Lysosomes contain enzymes that can break down lipids and amino acids, and recent studies have shown that these metabolites can be transported to the mitochondria through contact sites

between the two organelles. This metabolic cross-talk can regulate mitochondrial function and influence cellular processes such as autophagy, apoptosis, and cellular signaling.

The contact sites between mitochondria and lysosomes are dynamic structures that are regulated by a variety of proteins and signaling pathways. One key protein involved in the formation of these contact sites is the lipid transfer protein, VPS13D,[69] which is present on both organelles and facilitates lipid transfer between them. Other proteins involved in mitochondrial-lysosome interaction include the lysosomal protein LAMP-2A, the mitochondrial protein MFN2, and the protein kinase ULK1.[70]

Confocal Laser Scanning Microscopy:

Confocal laser scanning microscopy (CLSM) is a specialised fluorescence imaging technique which caters in multiple bioimaging applications. It operates on the same principle as a conventional fluorescence microscope to generate an image, on the contrary instead of a lamp or LED lights; a focused beam of laser light is opted for CLSM. CLSM uses various wavelength laser excitation sources or white light laser. Laser light illuminates the small portion of a specimen, and emitted light is passed through a pinhole (placed right in front of the detector), which eradicates out-of-focus light from the neighbouring planes to mitigate the background noise and significantly enhance the quality of the image. Initially, a photomultiplier tube (PMT) was used in CLSM to detect and amplify the fluorescence signal from the specimen, but technological advancements and the introduction of the HyD hybrid detector provide improved contrast with enhanced image quality. In contrast to traditional fluorescence microscopy, the evident advantages of CLSM are followed as reduction of out-of-focus blurring effects using spatial filtering techniques, enhancement of the contrast, sharpness, and optical resolution of the captured

images. The significant advantage of CLSM is the construction of 3D cellular images using suitable dyes by harvesting several Z-stack slices collected at various depths of the specimen. This provides better structural details of cellular organelles. Betzi, Hell and Moerner were received the Nobel Prize in Chemistry in 2014 for the creation of super-resolved fluorescence microscopy.

Fixed cell and live cell confocal imaging:

Cellular uptake of a probe is ensured often by both fixed cell and live cell confocal imaging techniques. However, live cell imaging is quite different and more challenging than fixed cell imaging technique. In case of fixed cell imaging, cells are first cultured on the coverslip and then fixed with 4% paraformaldehyde solution.[71] The unchanged shape and contents of the cells are usually preserved during the process and additional staining of the fixed cell makes the imaging process much easier as compared to live cells. However, while fixed cell protocol, the integrity of the cell membrane can be compromised and fixed cells become more permeabilized to external substances. On top of this, the dynamic behaviour of the cells, which is imperative biological data, is missing from the images obtained after cell fixation. On the other hand, live cell imaging is just like it sounds; cells are alive in the phenol red free growth media and images are captured over time (time-lapse imaging) at 37°C, 5% CO_2 incubation depicting the dynamic nature of cellular organelles. [72] Live cell imaging is more complex in contrast to fixed cell imaging and requires a special set up (**Figure 18**). Low cytotoxicity and excellent photophysical properties are two important facets of fluorophores which is essential for live cell imaging in order to withstand longer duration of laser exposure.

Multicolor cellular imaging:

A multicolor live cell confocal imaging technique has become an emerging and contemporary field of research to understand and visualize complex and dynamic biological events. However, lack of suitable dyes is a relevant problem which makes the process of tracking various cellular organelles of the same cell simultaneously, much more challenging. For multicolour cellular imaging, fluorophores conjugated with organelle selective functional groups and having specific narrow excitation and emission bands are required. Multicolor imaging reveals different cellular events of the same cell in a single image by visualising the morphological and structural changes of different organelles that take place under various pathological events. Recently, Kai Johnsson and Collot groups have reported NIR fluorophores with narrow absorption and emission bands for multicolor imaging purposes.[73-75]

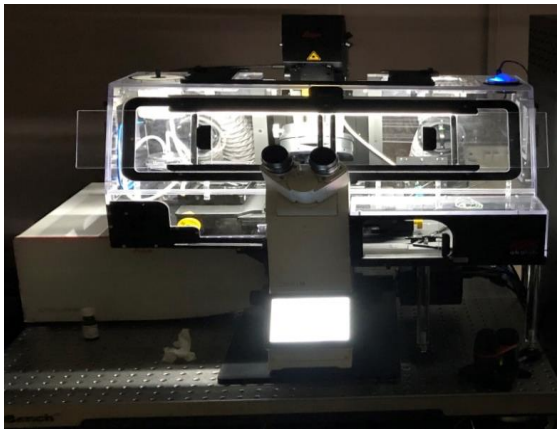

Figure 18. Special instrumental set up for live cell confocal imaging.[72]

Healthy or Normal Cells:

A healthy or normal cell can be defined as a unit of living matter that is capable of carrying out its essential functions, such as metabolism, growth, and division, in a regulated and controlled manner. In a healthy cell, the genetic

information stored in the DNA is properly replicated and transmitted to the daughter cells during cell division.[76] Healthy cells also have mechanisms to repair any damage to their DNA, protein, or lipid cell death, or apoptosis, when necessary to maintain tissue homeostasis and prevent the development of abnormal growths, such as tumors.[77-79] Overall, a healthy or normal cell is a complex and dynamic entity that is capable of carrying out its specialized functions and communicating with other cells to maintain the proper functioning of the structures, and to undergo programmed organism as a whole.

Cancer Cells:

Cancer cells are defined as cells that have undergone genetic alterations that result in uncontrolled cell growth and division, leading to the formation of a tumor or tumors. These cells often have defects in their DNA repair mechanisms, [80-83] which can lead to the accumulation of further mutations and genomic instability. They may also be able to evade normal cellular processes that would normally lead to cell death or apoptosis,[84-86] allowing them to survive and proliferate even in adverse conditions. The characteristics of cancer cells can vary depending on the type of cancer, but they all share the common feature of uncontrolled growth and proliferation.

Difference Between Cancer Cells and Normal Cells:

There are several key differences between normal cells and cancer cells:

1. Growth and division: Normal cells have a regulated process of growth and division, which is tightly controlled by a complex network of signaling pathways. [87-89] This allows them to maintain the appropriate number of cells in a tissue or organ. In contrast, cancer cells have lost the ability to control their growth and division and continue to divide uncontrollably, even when there is no need for additional cells. Healthy

cells follow a typical cell cycle: They grow, divide and die. Cancer cells, on the contrary, don't follow this cycle. Instead of dying, they multiply and continue to reproduce other abnormal cells.

2. DNA repair mechanisms: Normal cells have a robust system for repairing DNA damage that occurs as a result of normal cellular processes or environmental factors.[80,90] These repair mechanisms help to maintain the integrity of the genome and prevent mutations from accumulating. In contrast, cancer cells often have defects in their DNA repair mechanisms, which can lead to the accumulation of mutations and genomic instability.

3. Cell death: Normal cells have the ability to undergo programmed cell death or apoptosis, which helps to remove damaged or unwanted cells from the body. In contrast, cancer cells often have defects in the pathways that control apoptosis, which allows them to survive and proliferate even in adverse conditions. [91-94]

4. Contact inhibition: Normal cells exhibit contact inhibition, which means that they stop dividing when they come into contact with other cells. This helps to maintain the appropriate spatial organization of cells within a tissue or organ. [93,95] In contrast, cancer cells often lack contact inhibition and continue to divide even when they are in contact with other cells.

5. Angiogenesis: Cancer cells have the ability to induce the formation of new blood vessels (angiogenesis),[96] which helps to supply the growing tumour with nutrients and oxygen. In contrast, normal cells do not induce angiogenesis.

6. Metastasis: Cancer cells have the ability to invade nearby tissues and spread to other parts of the body (metastasis), which can lead to the formation of secondary tumours.[97] In contrast, normal cells do not exhibit metastatic behaviour.

7. Certain receptors and enzymes are overexpressed at the tumor site such as $\alpha_v\beta_3$ integrin, folate, EGFR, leucine aminopeptidase (LAP), β-galactosidase etc.

Cell-penetrating peptides (CPPs):

Cell-penetrating peptides (CPPs) are short peptides that can penetrate the cell membrane and deliver various molecules, including proteins, drugs, diagnostic agents and nucleic acids, into cells. [98-101] The trans activator of transcription (TAT) peptide is a well-known example of a CPP. The TAT peptide, (**Figure 19)** in particular, is derived from the protein of the human immunodeficiency virus (HIV) and has been extensively studied for its ability to deliver therapeutic molecules to various cell types.[102-103] The mechanism of cellular uptake by CPPs like TAT involves various mechanisms, including direct translocation through the lipid bilayer or receptor-mediated endocytosis.

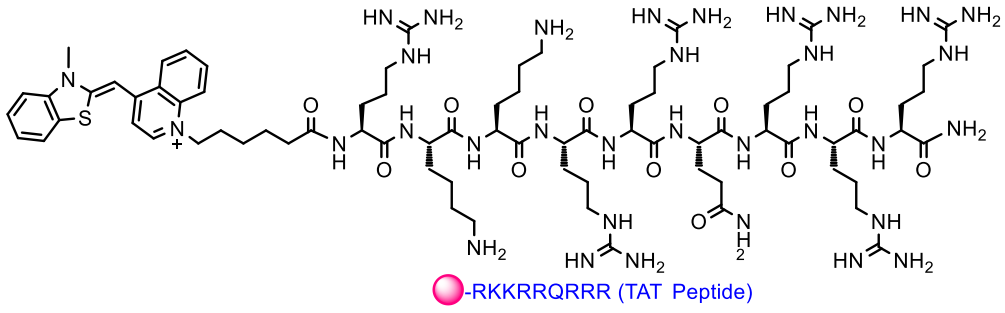

Figure 19. Fluorophore conjugated trans activator of transcription (TAT) peptide.[98-101]

CPPs have a number of potential applications in the fields of biomedicine and biotechnology. Here are a few examples:

1. Drug delivery: CPPs can be used to deliver drugs directly into cells, which may increase their efficacy and reduce side effects compared to traditional drug delivery methods.
2. Gene therapy: CPPs can be used to deliver therapeutic genes into cells, which may help to treat genetic diseases and certain types of cancer.
3. Protein delivery: CPPs can be used to deliver therapeutic proteins into cells, which may help to treat a variety of diseases, including autoimmune diseases and certain types of cancer.
4. Diagnostics: CPPs can be used to deliver diagnostic agents into cells, which may help to detect diseases at an early stage and monitor their progression.

Despite their potential, the use of CPPs is still in the early stages of development and there are many challenges that need to be overcome, including improving their specificity and efficacy, and reducing their toxicity. However, the development of CPPs is an active area of research and there is great potential for their use in a variety of medical applications in the future.

Different type of receptors which are over expressed at the cancer calls:

Certain receptors are overexpressed at the tumor site such as $\alpha_v\beta_3$ integrin, folate, EGFR, etc.[104-105] There are several types of receptors that are

overexpressed on cancer cells, and $\alpha_V\beta_3$ integrin is one of them. $\alpha_v\beta_3$ integrin is involved in cell adhesion and migration, and it binds to a specific sequence of amino acids known as the RGD peptide.

The overexpression of $\alpha_V\beta_3$ integrin in cancer cells plays a role in tumor angiogenesis, invasion, and metastasis. [106-107] Therefore, targeting this receptor with RGD-containing molecules has been explored as a potential approach for cancer imaging and therapy.

One example of an RGD-containing molecule that targets $\alpha_V\beta_3$ integrin is the radiopharmaceutical ^{18}F-fluciclatide, which is used for positron emission tomography (PET) imaging of various types of cancer. Another example is the drug cilengitide, which is a cyclic RGD-containing peptide that is being investigated as a potential anti-cancer therapy.[108-110] Cilengitide has been shown to inhibit tumor angiogenesis and invasion in preclinical models and is currently being tested in clinical trials for the treatment of various types of cancer, including glioblastoma, non-small cell lung cancer, and melanoma.

Overall, the targeting of $\alpha_V\beta_3$ integrin with RGD-containing molecules holds promise as a potential strategy for cancer diagnosis and treatment.

Applications of Iron oxide Nanoparticles:

Iron oxide nanoparticles are tiny particles that are less than 100 nm in size and composed of iron and oxygen. Magnetite (Fe_3O_4), maghemite (γ-Fe_2O_3), and hematite (Fe_2O_3) are the three types of iron oxides that occur most frequently in nature.[111-113] These nanoparticles have interesting properties that make them useful in a variety of applications such as magnetic resonance imaging (MRI) contrast agents, catalysts, drug delivery systems, and magnetic data storage.[114] In addition, iron oxide nanoparticles have been explored for their potential in environmental remediation and cancer therapy due to their magnetic and catalytic properties. [112,115-117]

Iron oxide nanoparticles have a wide range of applications due to their unique properties and versatility. Here are a few of the most common applications of iron oxide nanoparticles:

1. Magnetic Resonance Imaging (MRI): Iron oxide nanoparticles can be used as contrast agents in MRI to enhance the imaging of tissues and organs.

2. Drug Delivery: Iron oxide nanoparticles can be used to deliver drugs and therapeutic agents directly to diseased tissues, making treatment more effective and minimizing side effects.

3. Environmental Remediation: Iron oxide nanoparticles can be used to remove heavy metals and other contaminants from water and soil due to their magnetic properties.

4. Cancer Therapy: Iron oxide based magnetic nanoparticles can be targeted to cancer cells and used as a heat source to destroy the cells through a process known as magnetic hyperthermia.

5. Data Storage: Iron oxide nanoparticles can be used as magnetic bits in hard disk drives and other data storage devices due to their magnetic properties.

6. Catalysis: Iron oxide nanoparticles can be used as catalysts in chemical reactions, improving the efficiency and selectivity of the reaction.

T_2 relaxation:

T_2 relaxation refers to the decay of transverse magnetization in magnetic resonance imaging (MRI) and nuclear magnetic resonance (NMR) spectroscopy. In MRI, T_2 relaxation is an important contrast mechanism that

enables the differentiation of tissues based on their water content and mobility.[118]

During an MRI scan, the patient is placed in a strong magnetic field, which aligns the spins of protons in the water molecules of the body. A brief pulse of radiofrequency energy is then applied to the patient, which tips the protons out of alignment with the magnetic field. As the protons return to their original alignment, they emit a signal that can be detected by the MRI machine. [119-120]

However, the signal emitted by the proton's decays rapidly due to interactions with their surrounding environment, such as other water molecules and tissue structures. This decay is characterized by T_2 relaxation time, which is the time constant for the decay of transverse magnetization.

Different tissues in the body have different T_2 relaxation times, depending on their water content and mobility. For example, tissues with high water content and mobility, such as cerebrospinal fluid, have longer T_2 relaxation times and appear bright on T_2-weighted MRI images. In contrast, tissues with low water content and mobility, such as bone, have shorter T_2 relaxation times and appear dark on T_2-weighted images.[121-123] T_2 relaxation is an important contrast mechanism in MRI and is used to diagnose various conditions, such as multiple sclerosis, brain tumors, and joint injuries. By manipulating T_2 relaxation times through various imaging sequences, radiologists can obtain detailed images of different tissues and structures in the body.

References:

[1] Stoddart, J. F. *Angew.Chem.Int.Ed*. **2017**, *56*, 11094–11125.

[2] Schill, G. *Academic press*.**1971.**

[3] C, Shaokang; L, Zixing; Y, Zhenyu. *Compos Struct.* **2019**, *226*, 1112602.

[4] Neal, E. A.; Goldup, S. M. *Chem. Commun.* **2014**, *50*, 5128−5142.

[5] Sauvage, J.-P. *Angew. Chem. Int. Ed.* **2017**, *56*, 11080−11093.

[6] Feringa, B. L. *Angew. Chemie. Int. Ed.* **2017**, *56*, 11060−11078.

[7] *Aucagne, V.; Berná, J.; Crowley, J. D.; Goldup, S. M.; Hänni, K. D.; Leigh, D. A.; Lusby, P. J.; Ronaldson, V. E.; Slawin, A. M. Z.; Viterisi, A.; Walker, D. B. J. Am. Chem. Soc.* **2007**, *129*, 11950–11963.

[8] Harrison, I. T.; Harrison. S. *J. Am. Chem. Soc.* **1967**, *89*, 5723-5724.

[9] P. Waelès, M; Gauthier, F. Coutrot. *Angew. Chem. Int. Ed*. **2020**, *60*,16778–16799.

[10] Mooibroek, T. J. *Molecules.* **2019**, *24*, 3370.

[11] Aricó, F.; Badjic, J. D.; Cantrill, S. J.; Flood, A. H.; Leung, K C F.; Liu, y.; Stoddart, J. F. *Templates in Chemistry II. Topics in Current Chemistry.* **2005,** *249*, 203–259.

[12] *Aucagne, V.; Berná, J.; Crowley, J. D.; Goldup, S. M.; Hänni, K. D.; Leigh, D. A.; Lusby, P. J.; Ronaldson, V. E.; Slawin, A. M. Z.; Viterisi, A.; Walker, D. B. J. Am. Chem. Soc.* **2007**, *129*, 11950–11963.

[13] Anelli, P. L.; Spencer, N.; Stoddart, J. F. *J. Am. Chem. Soc.* **1991**, *113*, 5131−5133.

[14] Bissell, R. A.; Córdova, E.; Kaifer , A. E.; Stoddart, J. F. *Nature*. **1994,** *369*, 133–137.

[15] Zhang, Z.-J.; Han, M.; Zhang, H.-Y.; Liu, Y. *Org. Lett.* **2013,** *15*, 1698−1701.

[16] Jiang, W.; Han, M.; Zhang, H.-Y.; Zhang, Z.-J.; Liu, Y. *Chem.- Eur. J.* **2009**, *15*, 9938− 9945.

[17] Zhang, Z.-J.; Han, M.; Zhang, H.-Y.; Liu, Y. *Org. Lett.* **2013,** *15*, 1698−1701.

[18] Ma, Y.-X.; Meng, Z.; Chen, C.-F. *Org. Lett.* **2014,** *16*, 1860−1863.

[19] Brough, B.; Northrop, B.H.; Schmidt, J. J.; Tseng, H.-R.; Houk, K. N.; Stoddart, J. F.; Ho, C.-M. *Proc. Natl. Acad. Sci. U.S.A.* **2006,** *103*, 8583−8588.

[20] Bustamante, C.; Chemla, Y. R.; Forde, N. R.; Izhaky, D. *Annu. Rev. Biochem***. 2004**, *73*, 705−748.

[21] Denis, M.; Pancholi, J.; Jobe, K.; Watkinson, M.; Goldup, SM. *Angew. Chem. Int. Ed.* **2018**, *57*, 5310−5314.

[22] Collins, C. G.; Peck, E. M.; Kramer, P. J.; Smith, B. D. *Chem. Sci*. **2013**, *4*, 2557−2563.

[23] Klein, H. A.; Kuhna, H.; Beer, P. D. *Chem. Commun.* **2019**, *55*, 9975−9978.

[24] Barendt, T. A.; Docker, A.; Marques, I.; Felix, V.; Beer, P. D. *Angew. Chem.*,**2016**, *55*, 11069−11076.

[25] Zagon, I. S.; McLaughlin, P. J. *Neuropeptides.* **2003**, *37*,79-88.

[26] Cheng, F.; Zagon, I.S.; Verderame, M.F.; McLaughlin, P.J. *Cancer Res*. **2007**, *67*, 10511–10518.

[27] Cheng, F.; McLaughlin, P.J.; Verderame, M.F.; Zagon, I.S. *Mol Biol Cell.* **2009**, *20*, 319–327.

[28] Choudhary, U.; Northrop, B. H. *Org. Lett*. **2012**, *14*, 2082−2085.

[29] Fernandes, A. E.; Viterisi, A.; Coutrot, F.; Potok, S.; Leigh, D. A.; Aucagne, V.; Papot, S. *Angew. Chem., Int. Ed.* **2009**, *48*, 6443 –6447.

[30] Yu, G.; Wu, D.; Li, Y.; Zhang, Z.; Shao, L.; Zhou, J.; Hu, Q.; Tang, G.; Huang, F. *Chem. Sci.* **2016**, *7*, 3017−3024.

[31] Guha, S.; Shaw, G. K.; Mitcham, T. M.; Bouchard, R. R.; Smith, B. D. *Chem. Commun*. **2016**, *52*, 120−123.

[32] Liu, W.; Gómez-Durán, C. F. A.; Smith, B. D. *J. Am. Chem. Soc.* **2017**, *139*, 6390−6395.

[33] Zhai, C.; Schreiber, C. L.; Padilla-Coley, S.; Oliver, A. G.; Smith, B. D. *Angew. Chem., Int. Ed.* **2020**, *59*, 23740.

[34] Anderson, A. J.; Jackson, T. D.; Stroud, D. A.; Stojanovski, D. *Open Biol.* **2019,** *9*, 190126.

[35] Jeong, S. Y.; & Seol, D. W. *BMB reports*, **2008**, *41*, 11–22.

[36] Chen, L. B. *Annu. Rev. Cell Biol.* **1988**, *4*, 155−181.

[37] Davis, S.; Weiss, M. J.; Wong, J. R.; Lampidis, T. J.; Chen, L. B. *J. Biol. Chem*. **1985**, *260*, 13844−13850.

[38] Friedman, J. R.; Nunnari, J. *Nature.* **2014**, *505*, 335-43.

[39] Cho, H.; Cho, Y-Y.; Shim, M. S.; Lee, J. Y.; Lee, H. S.; Kang, C. K. *BBA - Molecular Basis of Disease*. **2020**, *1866*, 1658082.

[40] Jiang, M.; Gu, Xi.; Kwok, R. T. K.; Li, Y.; Sung, H. H. Y.; Zheng, X.; *Funct. Mater*. **2018**, *28*, 1704589.

[41] Chalmers, S.; Caldwell, S. T.; Quin, C.; Prime, T. A.; James, A. M.; Cairns, A. G.; Murphy, M. P.; McCarron, J. G.; and Hartley, R. C. *J. Am. Chem. Soc.* **2012**, *134*, 758−761.

[42] Prag, H. A.; Kula-Alwar, D.; Pala, L.; Caldwell, S. T.; Beach, T. E.; James, A. M.; Saeb-Parsy, K.; Krieg, T.; Hartley, and R. C.; Murphy, M. P. *Mol. Pharmaceutics* **2020**, *17*, 3526−3540.

[43] Chen, H.; Wang, J.; Feng, X.; Zhu, M.; Hoffmann, S.; Hsu, A.; Qian, K.; Huang, D.; Zhao, F.; Liu, W.; Zhang, H.; and Cheng, Z. *Chem. Sci.* **2019**, *10*, 7946–7951.

[44] Zhang, R.; Niu, G.; Li, X.; Guo, L.; Zhang, H.; Yang, R.; Chen, Y.; Yu, X.; and Tang, B. Z. *Chem. Sci.* **2019**, *10*, 1994–2000.

[45] Tian, M.; Ge, E.; Dong, B.; Zuo, Y.; Zhao, Y.; and Lin, W. *Anal. Chem.* **2021**, *93*, 3602−3610.

[46] Chen, W.-H.; Luo, G.-F.; and Zhang. X.-Z. *Adv. Mater*. **2019**, *31*, 1802725.

[47] Wu, S.; Cao, Q.; Wang, X.; Chenga, K.; and Cheng, Z. *Chem. Commun.* **2014**, *50*, 8919–8922.

[48] Maiti, K. K.; Lee, W. S.; Takeuchi, T.; Watkins, C.; Fretz, M.; Kim, D. C.; Futaki, S.; Jones, A.; Kim, K. T.; and Chung, S. K. *Angew. Chem., Int. Ed.* **2007**, *46*, 5880−5884.

[49] Ferna´ndez-Carneado, J.; Gool, M. V.;Vera, M.; Castel, S.; Prados, P.; de Mendoza, J.; and Giralt., E. *J. Am. Chem. Soc.* **2005**, *127*, 869–874.

[50] Valero, J.; Van Gool, M.; Perez-Fernandez, R.; Castreno, P.; Sanchez-Quesada, J.; Prados, P.; and de Mendoza, J. *Org. Biomol. Chem.* **2012**, *10*, 5417−5430.

[51] Shi, M.; Zhang, J.; Li, X.; Pan, S.; Li, J.; Yang, C.; Hu, H.; Qiao, M.; Chen, D.; and Zhao, X. *Int. J. Nanomed.* **2018**, *13*, 4209–4226.

[52] Nodling A. R.; Mills, E. M.; Li, X.; Cardella, D.; Sayers, E. J.; Wu, S.-H.; Jones, A.T.; Luk, L. Y. P.; and Tsai, Y.-H. *Chem. Commun.* **2020**, *56*, 4672−4675.

[53] Paul, A.; Mengji, R.; Bera, M.; Ojha, M.; Jana, A.; and Singh, N. D. P. *Chem. Commun.* **2020**, *56*, 8412−8415.

[54] D'Souza, G. G. M.; Rammohan, R.; Cheng, S. M.; Torchilin, V. P.; and Weissig, V. *J. Controlled Release*. **2003**, *92*, 189–197.

[55] Cheng, Y.; and Ji, Y. *J. Controlled Release.* **2020**, *318*, 38–49.

[56] Saha, P. C.; Chatterjee, T.; Pattanayak, R.; Das, R. S.; Mukherjee, A.; Bhattacharyya, M.; Guha, S. *ACS Omega*. **2019**, *4*, 14579−14588.

[57] Saha, P. C.; Das, R. S.; Chatterjee, T.; Bhattacharyya, M.; Guha, S. *Bioconjugate Chem.* **2020**, *31*, 1301−1306.

[58] Trivedi PC, Bartlett JJ, Pulinilkunnil T. *Cells.* **2020**, *9*, 1131.

[59] Xue, Z.; Zhao, H.; Liu, J.; Han, J.; Han, S. *Anal. Chem.* **2020**, *92*,15059–15068

[60] Zhang, Z.; Yue, P.; Lu, T.; Wang, Y.; Wei, Y.; Wei, X. *J Hematol Oncol*. **2021**, *14*, 79.

[61] Trivedi, P.C.; Bartlett, J.J.; Pulinilkunnil, T. Lysosomal Biology and Function: Modern View of Cellular Debris Bin. *Cells.* **2020**, *9*, 1131.

[62] Goldman, S. D.; Funk, R, S.; Rajewski, R, A.; Krise, J, P. *Bioanalysis.***2009,** *1*,1445-59.

[63] Yu, H. B.; Xiao, Y.; Jin, L. J. *J. Am. Chem. Soc.* **2012**, *134*, 17486−17489.

[64] Shi, X.; Yan, N.; Niu, G.; Sung, S. H. P.; Liu, Z.; Liu, J.; Kwok, R. T. K.; Lam, J. W.Y.; Wang, W.; Sung, H.H.;Williams, I. D.; Tang, B. Z. Chem. Sci. **2020**, *11*, 3152−3163.

[65] Hoogendoorn, S.; van Puijvelde, G. H. M.; Kuiper, J.; van der Marel, G. A.; Overkleeft, H. S. A. *Angew. Chem., Int. Ed.* **2014,** *53*, 10975−10978.

[66] Jethava, K. P.; Prakash,P.; Manchanda, P.; Arora, H.; Chopra, G. *ChemBioChem.* **2022**, *23*, e2021003.

[67] Bonora, M.; Patergnani, S.; Rimessi, A.; De Marchi, E.; Suski, JM.; Bononi, A.; Giorgi, C.; Marchi, S.; Missiroli, S.; Poletti, F.; Wieckowski, MR.; Pinton, P. *Purinergic Signal.* **2012**, *8*, 343-57.

[68] Wong, Y. C.; Kim, S.; Peng, W.; Krainc, D. *Trends Cell Biol.* **2019**, *29*, 500-513.

[69] Wang, J.; Fang, N.; Xiong, J.; Du, Y.; Cao, Y.; Ji, W. K. *Nat. Commun.* **2021**, *12*, 1252.

[70] Liu, X..; Liao, X.; Rao, X.; Wang, B.; Zhang, J.; Xu, G.; Jiang, X.; Qin, X.; Chen, C.; Zou, Z. *FEBS letters*, **2020**, *594*, 823–840.

[71] Qin, Y.; Jiang, W.; Li, A.; Gao, M.; Liu, H.; Gao, Y.; Tian, X.; Gong, G. *Biomolecules*. **2021**, 11, 711.

[72] Tsubone, T. M.; Martins, W. K.; Baptista, M. S. *Yale J Biol Med.* **2019**, *92*, 413−422.

[73] Wang, L.; Tran, M.; D'Este, E.; Roberti, J.; Koch, B.; Xue, L.; and Johnsson, K. *Nat. Chem.* **2020**, *12*, 165–172.

[74] Lukinavicius, G.; Reymond, L.; Umezawa, K.; Sallin, O.;ˇ D'Este, E.; Gottfert, F.; Ta, H.; Hell, S. W.; Urano, Y.; and Johnsson, K. *J. Am. Chem. Soc.* **2016**, *138*, 9365−9368.

[75] Collot, M.; Fam, T. K.; Ashokkumar, P.; Faklaris, O.; Galli, T.; Danglot, L.; and Klymchenko, A. S. *J. Am. Chem. Soc.* **2018**, *140*, 5401−541.

[76] Nishitani, H.; Lygerou, Z. *Genes to Cells.* **2002**, *7*, 523 –534.

[77] Salazar, N.; Zabel, B.A. *Front Immunol.* **2019**, *10*, 147.

[78] Dudley, A.C. *Cold Spring Harb Perspect Med*. **2012**, *2*, a006536.

[79] Aird, W.C. *Cell Tissue Res* **2019**, *335*, 271–281.

[80] Aas, P. A.; Otterlei, M.; Falnes, P. O.; Vågbø, C. B.; Skorpen, F.; Akbari, M.; Sundheim, O.; Bjørås, M.; Slupphaug, G.; Seeberg, E.; Krokan, H.E. *Nature.* **2003**, *421*, 859–863.

[81] Bakkenist, C. J.; Kastan, M. B. *Nature.* **2003**, *421*, 499−506.

[82] Bonate, P. L.; Arthaud, L.; Cantrell, W. R.; Stephenson, K.; Secrist, J. A.; Weitman, S. *Nat. Rev. Drug Discov.* **2006**, *5*, 855–863.

[83] Cerbinskaite, A.; Mukhopadhyay, A.; Plummer, E. R.; Curtin, N. J.; Edmondson, R. J. *Cancer Treat. Rev.* **2012**, *38*, 89–100.

[84] Elmore S. *Toxicol.Pathol*. **2007**, *35*, 495−516.

[85] Yang, E.; Zha, J.; Jockel, J.; Boise, L. H.; Thompson, C. B.; Korsmeyer, S. J. *Cell.* **1995**, *80*, 285–91.

[86] Hoeppner, D. J.; Hengartner, M. O.; Schnabel, R. *Nature.* **2001**, *412*, 202–6.

[87] Hitoshi, Y.; Lorens, J.; Kitada, S. I.; Fisher, J.; LaBarge, M.; Ring, H. Z.; Francke, U.; Reed, J. C.; Kinoshita, S.; Nolan, G. P. *Immunity*. **1998**, *8*, 461–71.

[88] Barry, M.; Bleackley, R. C. *Nat Rev Immunol.* **2002**, *2*, 401–9.

[89] Freude, B.; Masters, T. N.; Robicsek, F.; Fokin, A.; Kostin, S.; Zimmermann, R.; Ullmann, C.; Lorenz-Meyer, S.; Schaper, J. *J Mol Cell Cardiol.* **2000**, *32*, 197–208.

[90] Torgovnick, A.; Schumacher, B. *Front Genet.* **2015**, *6*, 157.

[91] Wong, R.S. *J Exp Clin Cancer Res.* **2011**, *30*, 87.

[92] Vikhanskaya, F.; Lee, M. K.; Mazzoletti, M.; Broggini, M.; Sabapathy, K. *Nucl Acids Res.* **2007**, *35*, 2093–2104.

[93] Vucic, D.; Stennicke, H. R.; Pisabarro, M.T.; Salvesen, G. S.; Dixit, V. M. *Curr Biol.* **2000**, *10*, 1359–1366.

[94] Kang, M. H.; Reynolds, C, P. *Clin Cancer Res.* **2009**, *15*, 1126–1132.

[95] Raffo, A. J.; Perlman, H.; Chen, M. W.; Day, M. L.; Streitman, J. S.; Buttyan, R. *Cancer Res.***1995**, *55*, 4438.

[96] Nishida, N.; Yano, H.; Nishida, T.; Kamura, T.; Kojiro, M. *Vasc Health Risk Manag.* **2006**, *2*, 213–219.

[97] Fares, J.; Fares, M. Y.; Khachfe, H. H.; Salhab, H. A.; Fares, Y. *Signal Transduct Target Ther.* **2020**, *5*, 28.

[98] Mäe, M.; Langel, U. *Current Opinion in Pharmacology.* **2006**, *6*, 509–514.

[99] Biswas, S.; Torchilin, V. P. *Adv. Drug Deliv. Rev.* **2014**, *66*, 26–41.

[100] Cai, W.; Chen, X. *Small.* **2007**, *3*, 1840–1854.

[101] Carnevale, K. J. F.; Muroski, M. E.; Vakil, P. N.; Foley, M. E.; Laufersky, G.; Kenworthy, R.; Zorio, D. A. R.; Morgan, T. J. Jr.; Levenson, C. W.; Strouse, G. F. *Bioconjugate Chem.* **2018**, *29*, 3273–3284.

[102] Grunwald, J.; Rejtar, T.; Sawant, R.; Wang, Z.; Torchilin, V. P. *Bioconjugate Chem.* **2009**, *20*, 1531−1537.

[103] Mishra, A.; Lai, G. H.; Schmidt, N. W.; Sun, V. Z.; Rodriguez, A. R.; Tong, R.; Tang, L.; Cheng, J.; Deming, T. J.; Kamei, D. T.; Wong, G. C. *Proc Natl Acad Sci U S A.* **2011**, *108*, 16883−16888.

[104] Liu, S. *Bioconjugate Chem.* **2009**, *20*, 2199−2213.

[105] Dechantsreiter, M. A.; Planker, E.; Matha, B.; Lohof, E.; Holzemann, G.; Jonczyk, A.; Goodman, S. L.; Kessler, H. *J. Med. Chem.* **1999**, *42*, 3033−3040.

[106] Liu, Z.; Yu, L.; Wang, X.; Zhang, X.; Liu, M.; Zeng, W. *Curr Protein Pept Sci.* **2016**, *17*, 570−81.

[107] Danhier, F.; Le Breton, A.; Preat, V. *Mol. Pharmaceutics.* **2012**, *9*, 2961−73.

[108] Ruoslahti, E.; Pierschbacher, M. D. *Science.* **1987**, *238*, 491−497.

[109] Reinmuth, N.; Liu, W.; Ahmad, S. A.; Fan, F.; Stoeltzing, O.; Parikh, A. A.; Bucana, C. D.; Gallick, G. E.; Nickols, M. A.; Westlin, W. F.; Ellis, L. M. *Cancer Res.* **2003**, *63*, 2079−2087.

[110] Chen, X.; Conti, P. S.; Moats, R. A. *Cancer Res.* **2004**, *64*, 8009−8014.

[111] Fortin, J. P.; Wilhelm, C.; Servais, J.; Ménager, C.; Bacri, J. C.; Gazeau, F. *J Am Chem Soc*. **2007**, *129*, 2628–2635.

[112] Laurent, S.; Forge, D.; Port, M.; Roch, A.; Robic, C.; Vander Elst, L.; Muller, R. N. *Chem. Rev*. **2008**, *108*, 2064−2110.

[113] Ling D, Hyeon T. *Small*. **2013**, *9*, 1450–1466.

[114] Thompson, D. A.; Best, J. S. *IBM Journal of Research and Development*, **2000,** *44*, 311−322.

[115] Tavakoli A, Sohrabi M, Kargari A. *Chem Papers*. **2007**, *61*, 151–170

[116] Parsons, J.; Luna, C.; Botez, C. E.; Elizalde, J.; Gardea-Torresdey, J. L. *J Phys Chem Solids*. **2009**, *70*, 555–560.

[117] Soenen, S. J.; Himmelreich, U.; Nuytten, N.; De Cuyper, M. *Biomaterials*. **2011**, *32*, 195–205.

[118] Gahramanov, S.; Muldoon, L. L.; Varallyay, C. G.; Li, X.; Kraemer, D. F.; Fu, R.; Hamilton, B. E.; Rooney, W. D.; Neuwelt, E. A. *Radiology*. **2013**, *266*, 842− 852.

[119] Rooney, W. D.; Johnson, G.; Li, X.; Cohen, E. R.; Kim, S.-g.; Ugurbil, K.; Springer, C. S. *Magn. Reson. Med.* **2007**, *57*, 308−318.

[120] De Leon-Rodríguez, L. M.; Martins, A. F.; Pinho, M. C.; Rofsky, N. M.; Sherry, A. D. *J. Magn. Reson. Imaging.* **2015**, *42*, 545−565.

[121] chellenberger, E. A.; Bogdanov, A., Jr.; Hogemann, D.; Tait, J.; Weissleder, R.; Josephson, L. *Mol. Imaging.* **2002**, *1*, 102−107.

[122] Na, H. B.; Song, I. C.; Hyeon, T. *Adv. Mater*. **2009**, *21*, 2133−2148.

[123] Bannas, P.; Graumann, O.; Balcerak, P.; Peldschus, K.; Kaul, M. G.; Hohenberg, H.; Haag, F.; Adam, G.; Ittrich, H.; Koch-Nolte, F. *Mol. Imaging*. **2010**, *9*, 211−222.

Chapter 2

Materials and Methods

Introduction:

This chapter contains thorough information on basic materials as well as a brief overview of the experimental processes used in this thesis to synthesize rotaxane-based SQ dyes for selective targeting and imaging of mitochondria /Lysosome. The chapter also includes detailed information on all spectroscopic measurements and microscopic methods, as well as various biological investigations pertinent to this topic. Confocal laser scanning microscopy (CLSM) has also received specific attention for imaging fixed and live cell organelles, as well as multicolor imaging. All of the chapters gave a detailed overview of the synthetic techniques used to create the compounds reviewed in this thesis, as well as the biological studies that were pertinent to this research.

Experimental Procedures

General Materials:

Wang resin LL (100-200 mesh), Fmoc-amino acid building blocks: Fmoc-Arg(Pbf)-OH, Fmoc-Gly-OH, Fmoc-Asp(OtBu)-OH, Fmoc-Ser(tBu)-OH, 2-(1HBenzotriazole-1-yl)-1,1,3,3tetramethyluroniumhexafluorophosphate (HBTU), 1-Hydroxybenzotriazole (HOBt) hydrate, Ethanol, and TLC silica gel 60 F254 were purchased from Merck. 3-methyl-2-butanone, phenylhydrazine hydrochloride, iodomethane, 3,4-Dihydroxy-3-cyclobutene-1,2-dione (squaric acid), 5-tert-butylisophthalic acid, 5-hydroxyisophthalic acid, propargyl bromide, paraformaldehyde, hexamethylenetetramine, HBr, N,N-diisopropylethylamine (DIPEA), DMF (anhydrous, 99.8%), trifluoroacetic acid (TFA), triisopropylsilane (TIS), D- Glucose, 2-Chloroethanol, BF_3-Et_2O, oleic acid (90%), 1-octadecene (90%), and $FeCl_3 \cdot 6H_2O$ (98%) piperidine, and Hoechst 33342 were procured from Sigma-Aldrich. Appropriate deuterated

NMR solvents were acquired from Cambridge Isotope Laboratories, Inc. Spectroscopic grade solvents and commercially accessible solvents were used for the spectroscopy and reaction, respectively without further purification. Before opening the container of Fmoc amino acids the chemicals were warmed to room temperature. Human lung adenocarcinoma A549, human breast adenocarcinoma MDA-MB-231 (MD Anderson Metastatic Breast-231), epithelioid cervix carcinoma HeLa, normal human embryonic kidney (HEK293) cell line and noncancerous mouse myoblast C2C12 cell lines were procured from The National Centre for Cell Science, India. 3-(4,5-dimethyl-2thiazolyl)-2,5-diphenyltetrazolium bromide (MTT), Dulbecco's modified eagle medium (DMEM), Trypsin EDTA mixture, Fetal Bovine Serum (FBS), and Antibiotic Antimycotic Solution were achieved from Himedia. LysoTracker Green DND-26 and MitoTracker Green were obtained from Thermo Fisher Scientific.Tetrakis(acetonitrile)copper(I) hexafluorophosphate, 2,6-lutidine, anthracene, hexadecyltrimethylammonium bromide (CTAB), sodium oleate (95%), Tert-butyldimethylsilyl chloride (TBDMSCl), Zinc phthalocyanine, Tetra-n-butylammonium fluoride (TBAF), 4-aminobenzoic acid, NaN_3, and $NaNO_2$ were obtained from TCI Chemicals.

Purification of rotaxane-based SQ dyes required solvents:

Dry chloroform is required for the synthesis of both symmetrical and unsymmetrical rotaxane-based SQ dyes. All intermediate and final stapes require a solvent combination of EtOAc/Hexn and DCM/MeOH for column purification.

Microwave Synthesizer: Both symmetrical and unsymmetrical rotaxane-based SQ dyes, as well as their associated precursor molecules, were synthesized using a manual microwave synthesiser (CEM corporation, USA make), whereas SQ rotaxane-peptide conjugates were synthesised using a

microwave peptide synthesiser and a manual microwave-assisted Fmoc-SPPS protocol (CEM, Discover Bio). Peptides and SQ rotaxane-peptide conjugates were synthesized using 2-CTC (2-chloro trityl chloride) resin (LL, 0.85 mmol/g loading density) and Wang resin (LL, 0.60 mmol/g loading density).

Characterization of rotaxane-based SQ dyes and their precursors:

Spectroscopic Measurements:

NMR Spectroscopy: 1D (1H, 13C, 31P) and 2D NMR (1H-1H DQF COSY) spectroscopy were used to characterised all of the cyanine dyes as well as their precursor compounds. All NMR investigations were performed at room temperature using Bruker DPX300 MHz and Bruker DPX400 MHz spectrometers in suitable deuterated solutions.

Mass spectrometry: A Q-TofmicroTM (Waters Corporation) mass spectrometer was used for high-resolution electrospray ionisation mass spectrometry (HRMS-ESI).

Absorption Spectroscopy: Absorption spectra were recorded using a Shimadzu UV-1800 spectrometer in a quartz cuvette with a path length of 1 cm.

Fluorescence Spectroscopy: Fluorescence measurement was obtained on a Horiba Jobin Yvon FluoroMax-4 spectrofluorometer.

Time-correlated single photon counting (TCSPC) experiment: Fluorescence lifetime (τ) of the rotaxane-based SQ dyes were measured by time-correlated single photon counting (TCSPC) technique on Horiba DeltaFlex lifetime instrument (Horiba Jobin Yvon IBH Ltd, Glasgow, Scotland, UK). 510 nm (Model: DD-510L, Horiba Scientific) and 650 nm (Model: DD-650L, Horiba Scientific) Delta diode laser excitation source was used to determine the

fluorescence lifetime of rotaxane-based SQ dyes in various solvents. Lifetime measurements and data analysis were obtained using Horiba EzTime decay analysis software.

FT-IR Spectroscopy: FT-IR spectrum of peptide conjugated cyanine probes were recorded on a PerkinElmer Spectrum Two FT-IR spectrometer.

Microscopic Studies:

Transmission Electron Microscopy (TEM): 10 μL of freshly prepared aqueous stock solution of respective SQ rotaxane-Fe_3o_4 NPs conjugates were separately drop casted on a carbon coated copper grid (300 mesh) and waited for 2 m followed by blotting with filter paper to remove the excess fluid. Finally, for negative staining 10 μL of 2 % (w/v) uranyl acetate in H_2O solution was drop casted on the grid and waited for 30 s followed by blotting with filter paper. The grid was allowed to dry completely in air then vacuum drying for 1 day. TEM images of respective compounds were acquired on JEM-2100F Field Emission Electron microscope (JEOL) instrument with acceleration voltage 200 kV.

Magnetic Measurement: The magnetic measurements were carried out using a vibrating sample magnetometer (VSM) of quantum design. In the presence of a zero magnetic field, the sample was placed in the sample holder in powder form, and the magnetic hysteresis curves were recorded by sweeping the external field between 2kOe at room temperature.

Biological Studies:

Cell culture: Both malignant and noncancerous cell lines were grown in DMEM (pH 7.4) growth medium supplemented with 10% Fetal Bovine Serum (FBS) and antibiotic-(6H, m) antimycotic solution 100 (containing 10,000 units penicillin, 10 mg streptomycin, and 25 g amphotericin B per mL in 0.9%

normal saline). All cell lines were kept at 37°C in an incubator with 5% CO2 passages on a regular basis.

Cell viability assay: MTT test was used to assess the cytotoxicity of all produced rotaxane-based SQ derivatives on malignant and noncancerous cell lines.

Cellular uptake and mitochondrial localization study: Confocal laser scanning microscopy techniques were employed to validate the cellular uptake and organelle selectivity of rotaxane-based SQ dye conjugates, as well as for multicolor imaging in fixed and living cells.

Magnetic Resonance Imaging (MRI): MRI measurements were performed at 25ºC in a 9.4 T MR system (BioSpec 94/20USR, Bruker cryo platform, TX, USA). The MitoSQRot-(Carbo-OH)$_2$-DOPA-Fe_3O_4 NPs was dispersed in 600 µL of D-PBS (-) in microtubes with different concentrations of Fe (0.33, 0.165, 0.083, 0.041, 0.021, and 0 mM; Fe concentrations were determined from the ICP-OES experiment on a PerkinElmer instrument, Optical Emission Spectrometer Avio 200). The tubes were placed on a sample holder followed by putting into the MR scanner. Image acquisition was performed in the spin echo mode to determine T_2 of each sample with parameters, echo time (TE=24 ms), repetition time (TR=500 ms), resolution 192 × 192, field of view (FOV) = 4.80 cm, thickness =2.0 mm. Signal intensities were measured from region of interest (ROI) and the T_2 relaxation time was calculated by linear fitting as function of TE. The r_2 relaxivity value was obtained from the slope of linear fitting curve of $1/T_2$ values (y-axis) with Fe concentrations (x-axis).

Chapter 3

Design and Synthesis of Near-Infrared Mechanically Interlocked Molecules for Specific Targeting of Mitochondria

Design and Synthesis of Near-Infrared Mechanically Interlocked Molecules for Specific Targeting of Mitochondria

---

Introduction:

Using smart near-infrared (NIR) fluorescence imaging probes constructed from organic molecules to target specific cellular organelles is an emerging field of contemporary research.[1] NIR fluorescent biomarkers (650−900 nm) for intracellular locations are indispensable in contrast with visible and other fluorescent dyes because NIR light can permeate deep tissues and offers a meaningful bioimaging method with negligible autofluorescence background.[2] Mitochondria are crucial targets within the numerous cellular organelles.[3] Mitochondria are the powerhouse of cells, and they control cellular functions. The high negative inner mitochondrial membrane potential ($\Delta\Psi_m$ −150 to −180 mV) is distinctive because it does not exist in other cellular organelles, and this offers a design opportunity to target mitochondria. So far, squaraine (SQ) has been overlooked when building probes for the selective staining of mitochondria.[4] We envision that the electrophilic SQ chromophore could be susceptible to nucleophilic attack by the reactive thiols (SH) present in various mitochondrial proteins as well as mitochondrial glutathione (GSH), and hence NIR fluorescence could be quenched after the accumulation of SQ inside the mitochondria.[5] Moreover, SQ has a propensity to form nonfluorescent aggregates in an aqueous environment; this leads to substantial broadening of its absorption as well as emission bands, which is undesired for cellular organelle imaging.[6] These could be potential downsides for the development of SQ-based mitochondria tracking agents. We propose that the entrapment of a mitochondria-targeting SQ probe inside a container molecule to form mechanically interlocked molecules (rotaxane) that are stabilized through noncovalent interactions could be a method of improving the dye performance inside the mitochondria.[7] Smith and co-workers have made seminal contributions toward the development of squaraine rotaxane for various

applications.[8] However, the synthesis of mitochondria targeting NIR unsymmetrical 1,3,3-trimethylindolin squaraine rotaxane is a challenging task. The synthesis of unsymmetrical SQRot can be achieved by the conventional oil bath heating method, which takes days and often requires prolonged and difficult column chromatographic purification due to unwanted side products. Therefore, a fast, effective methodology with a high yield and product purity is required for the synthesis of unsymmetrical SQRot. We propose that microwave (MW)-assisted solid-phase synthesis on low-loading resin could be an effective way to construct an unsymmetrical rotaxane molecule. Moreover, the synthesized SQRot can be further bioconjugated with various target specific functional groups, including organelle-selective targeting moieties. To the best of our knowledge, this is the first report of an NIR unsymmetrical 1,3,3-trimethylindoline squaraine-rotaxane-based mitochondria targeting and imaging agent.

Experimental Methods

General Methods and Materials

Synthesis, Purification, and Characterization of MSQRot, and SQRot molecules:

The compounds 2,3,3-trimethyl-3*H*-indolenene and 2,3,3-trimethylindolenine 5-carboxylic acid are synthesized by the Fischer indole synthesis and the N of the indolenine residue is alkylated using methyl iodide. Unsymmetrical SQ and their precursor molecules were constructed by a proficient way using MW protocol with practical overall yield from effortlessly available starting materials. 9,10-Bis(aminomethyl)anthracene and 5-(*tert*-butyl)isophthaloyl dichloride were constructed by literature reported procedures. Analytical TLC was achieved on TLC silica gel 60 F254 with suitable solvent systems and

spotted by naked eye or UV lamp. The desired compounds were purified using column chromatography (silica gel 100-200 mesh). The distilled solvents were used for the column chromatography.

Then the rotaxane molecule was synthesized using manual MW-assisted solid-phase synthesis protocol on 2-CTC resin. All the compounds were characterised by 1D (^{1}H, ^{13}C and ^{31}P) and 2D (^{1}H-^{1}H DQF-COSY) NMR spectroscopy, as well as high resolution ESI-MS.

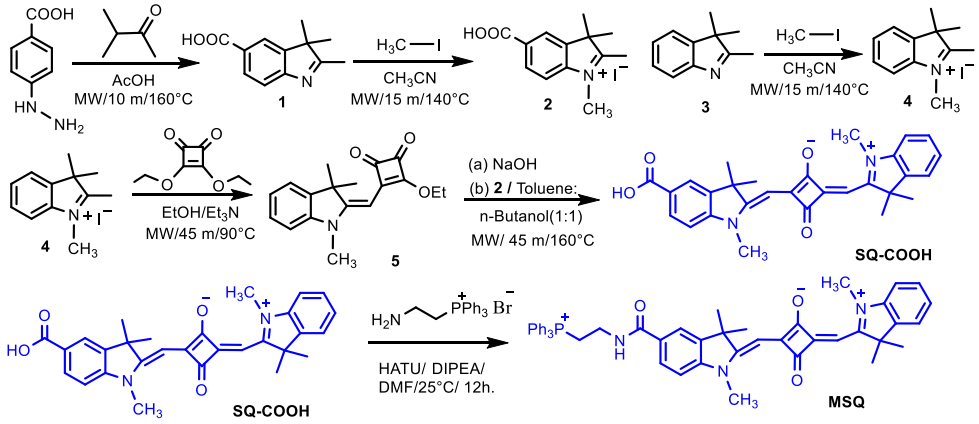

Scheme 1. Synthesis of SQ-COOH and MSQ dyes.

Synthesis of 2,3,3-trimethyl-3*H*-indole-5-carboxylic acid (1) 3-Methyl-2-

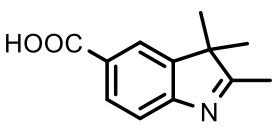

butanone (2 ml, 19 mmol), 4-hydrazinobenzoic acid (1.67 g, 11 mmol), and glacial AcOH (6 mL) was introduced in the reaction vial, which was sealed and heated in MW system at 160ºC for 10 min. The reaction mixture was cooled to room temperature. The solvent was removed under reduced pressure and the crude product was purified by column chromatography (40-45% EtOAc/Hexane) to get a yellow product. Yield: 1.82 g (81%)

^{1}H NMR (400 MHz, DMSO-d_6, 25°C): δ = 12.76 (1H, br), 7.97 (1H, s), 7. 90 (1H, d, J = 8.7 Hz), 7.48 (1H, d, J = 8.0 Hz), 2.23 (3H, s), 1.25 (6H, s) ppm. ^{13}C NMR (100 MHz, DMSO-d_6, 25°C): δ = 192.2, 168.0, 157.9, 146.6, 129.8, 127.8, 123.2, 119.5, 53.8, 22.8, and 15.8 ppm.

HRMS (ESI +ve) *m/z*: Observed for $C_{12}H_{13}NO_2$ $[M+H]^+$ = 204.1017, $[M+H]^+$ calcd = 204.1019.

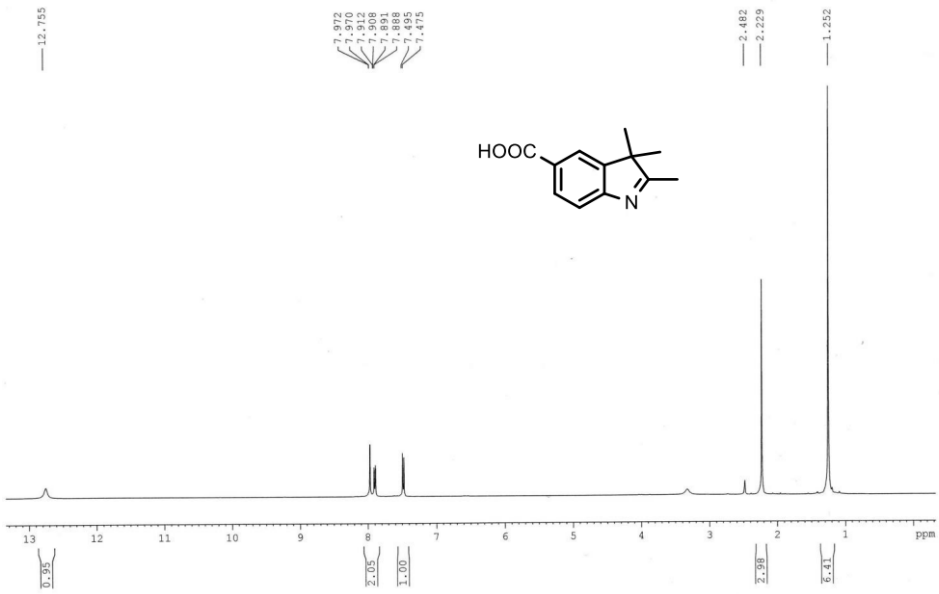

Figure 1.^{1}H NMR (400 MHz, DMSO-d_6, 25°C) spectrum of compound 1.

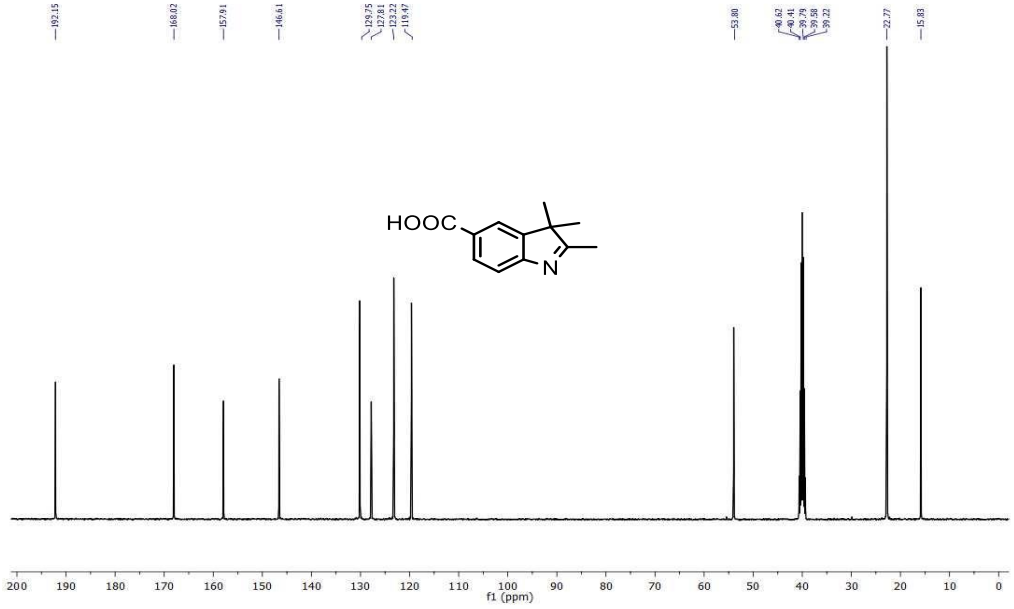

Figure 2.[1]H NMR (100 MHz, DMSO-d_6, 25°C) spectrum of compound 1.

Synthesis of 5-carboxy-1,2,3,3-tetramethyl-*3H*-indol-1-ium iodide (2)

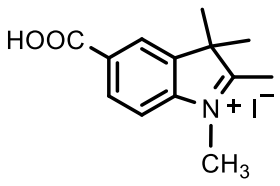

Iodomethane (1 mL, 16.06 mmol), 2,3,3-trimethyl-*3H*-indole-5-carboxylicacid (1 g, 4.92 mmol) and CH_3CN (4 mL) were introduced in a reaction vial, which was sealed and heated in MW system at 140ºC for 10 min. Then the reaction mixture was cooled to room temperature, 10 mL Et_2O was added to get a precipitate. The precipitate was filtered off and washed with Et_2O for several times to get a yellow product.

Yield: 1.56 g (92%).

[1]H NMR (400 MHz, DMSO-d_6, 25°C): δ = 8.35 (1H, s), 8.16 (1H, d, J = 8.0 Hz), 8.00 (1H, d, J = 8.4 Hz), 3.99 (3H, s), 2.81 (3H, s), 1.56 (6H, s) ppm. [13]C

NMR (100 MHz, DMSO-d_6, 25°C): δ = 199.5, 167.1, 145.7, 142.4, 132.2, 130.8, 124.7, 116.0, 55.1, 35.7, 22.0, and 15.4 ppm.

HRMS (ESI +ve) *m/z*: Observed for $C_{13}H_{16}NO_2^+$ $[M]^+$ = 218.1179, $[M]^+$ calcd = 218.1176.

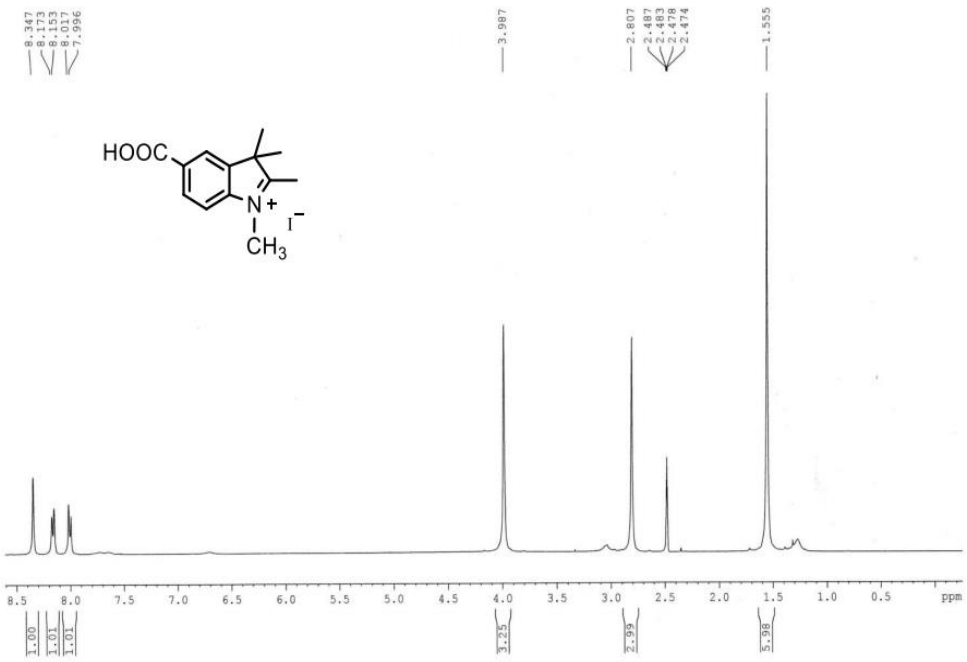

Figure 3.[1]H NMR (400 MHz, DMSO-d_6, 25°C) spectrum of compound 2.

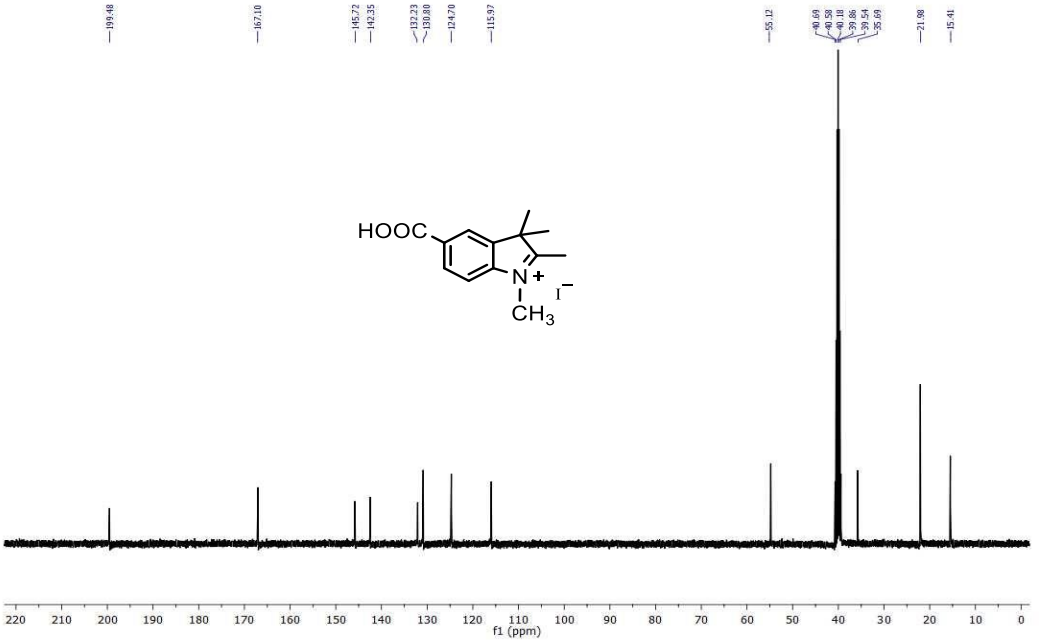

Figure 4 .^{13}C NMR (100 MHz, DMSO-d_6, 25°C) spectrum of compound 2.

Synthesis of 2,3,3-Trimethylindolenine (3): 2,3,3-Trimethylindolenine was

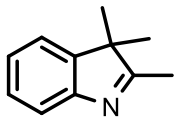

synthesized by the Fischer indole synthesis from 3-methyl-2-butanone (5 mL, 46.8 mmol) and phenylhydrazine hydrochloride (2.46 g, 17 mmol) in glacial AcOH (30 mL) was introduced in the reaction vial, which was sealed and heated in MW system at 140ºC for 15 min. The reaction mixture was cooled to room temperature. The solvent was removed under reduced pressure and the crude product was purified by column chromatography using 25-35% EtOAc/Hexane to get yellowish brown colored liquid product of 2,3,3-trimethylindolenine [R_f= 0.5, Hexane:EtOAc (2:1)].

Yield: 2.40 g (90%)

^{1}H NMR (400 MHz, $CDCl_3$, 25°C): δ = 7.49 (1H, d, J = 7.6 Hz), 7.25–7.19 (2H, m), 7.14–7.11 (1H, m), 2.20 (3H, s), 1.22 (6H, s) ppm. ^{13}C NMR (100 MHz, $CDCl_3$, 25°C): δ = 187.7, 153.6, 145.5, 127.4, 124.9, 121.1, 119.7, 53.4, 22.9, and 15.2 ppm.

HRMS (ESI +ve) *m/z*: Observed for $C_{11}H_{13}N$ $[M]^+$ = 159.1039, $[M]^+$ calcd = 159.1048.

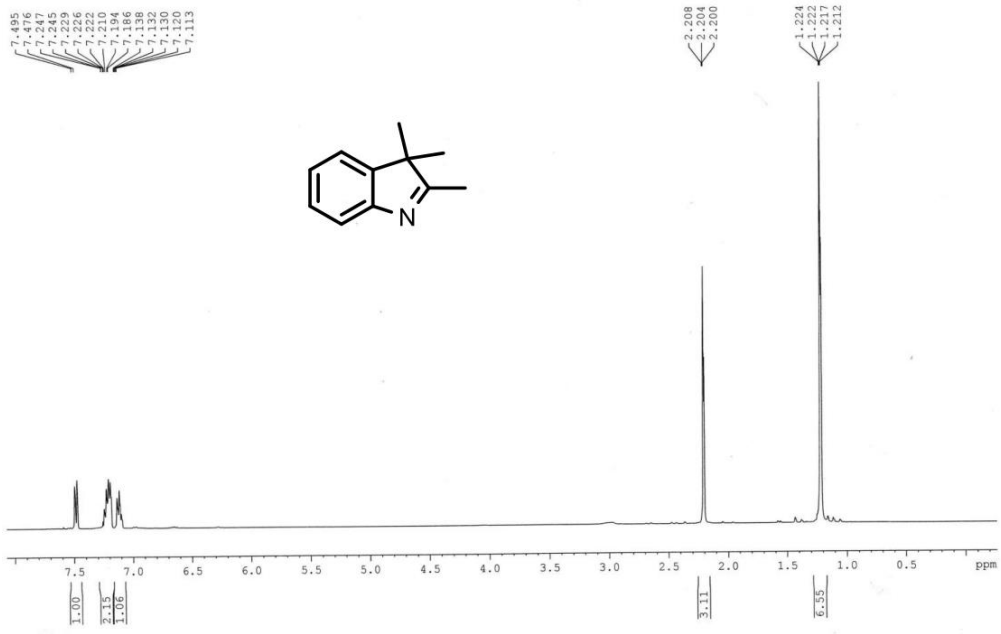

Figure 5 .^{1}H NMR (400 MHz, $CDCl_3$, 25°C) spectrum of compound 3.

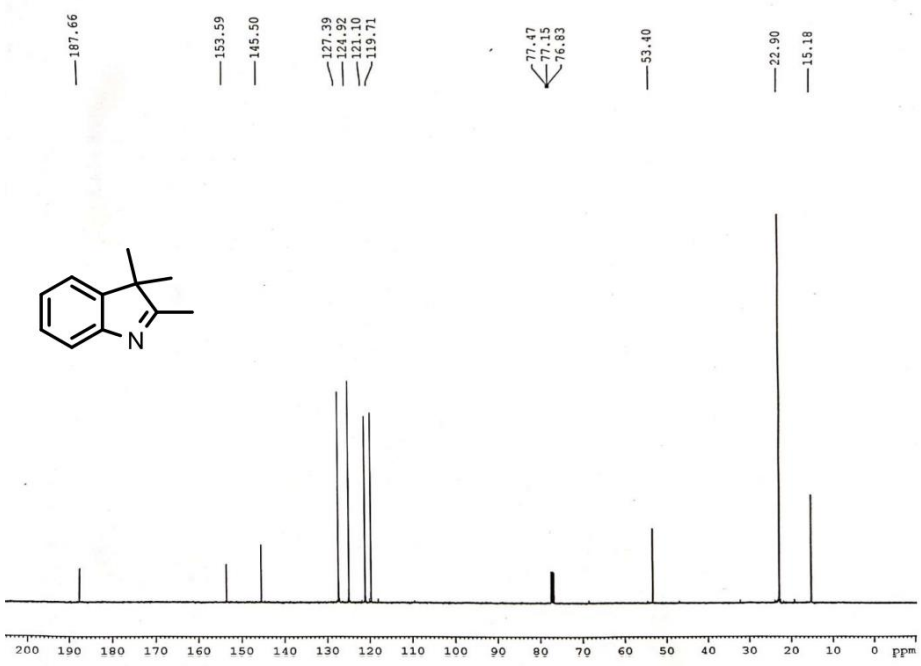

Figure 6 .^{13}C NMR (100 MHz, $CDCl_3$, 25°C) spectrum of compound 3.

Synthesis of 1,2,3,3-tetramethyl-3*H*-indol-1-ium iodide (4): Iodomethane (1 mL, 16.06 mmol), 2,3,3-trimethylindolenine (0.78 g, 4.92 mmol) and CH_3CN (4 mL) was introduced in a MW vessel equipped with a magnetic stir bar. The reaction mixture was sealed with a cap and subjected to MW irradiation at 140ºC for 10 m. Then the reaction mixture was cooled to room temperature and 10 mL Et_2O was added to get a brown precipitate. The precipitate was filtered off and washed with Et_2O (3 × 20 mL) to get a brownish solid pure product.

Yield: 1.34 g (91%).

^{1}H NMR (400 MHz, DMSO-d_6, 25°C): δ = 7.90 (1H, d, J = 8.4 Hz), 7.82 (1H, d, J = 8.4 Hz), 7.62-7.59 (2H, m), 3.98 (3H, s), 2.78 (3H, s), 1.53 (6H, s) ppm.

^{13}C NMR (100 MHz, DMSO-d_6, 25°C): δ = 196.5, 142.7, 141.9, S8 129.8, 129.2, 123.9, 115.5, 54.5, 35.5, 22.3, and 15.0 ppm.

HRMS (ESI +ve) *m/z*: Observed for $C_{12}H_{16}N^+$ $[M]^+$ = 174.1263, $[M]^+$ calcd = 174.1277.

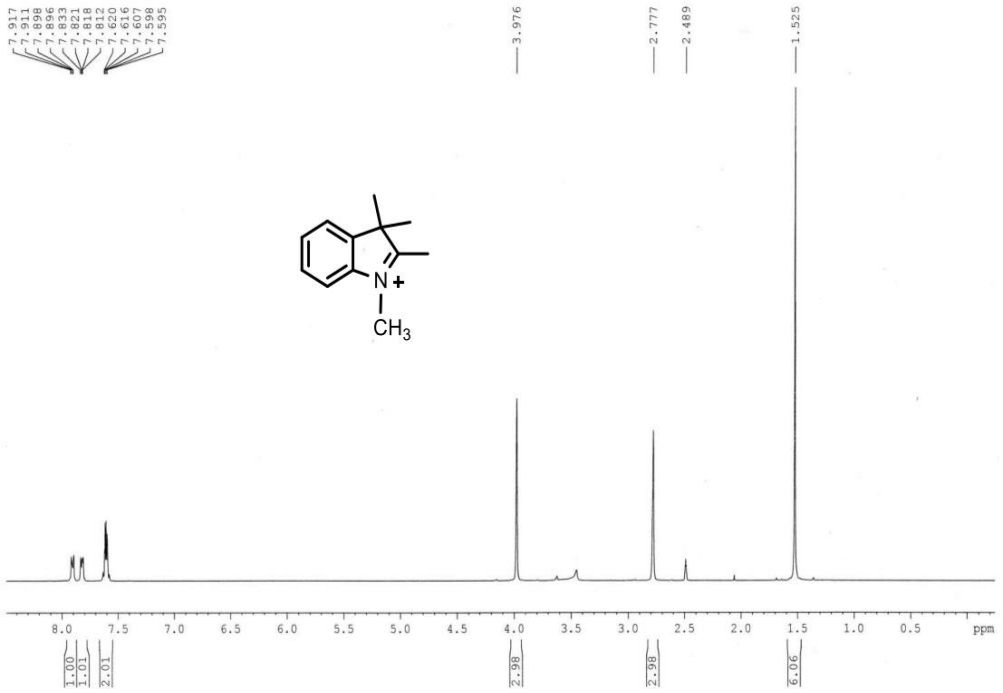

Figure 7. ^{1}H NMR (400 MHz, DMSO-d_6, 25°C) spectrum of compound 4.

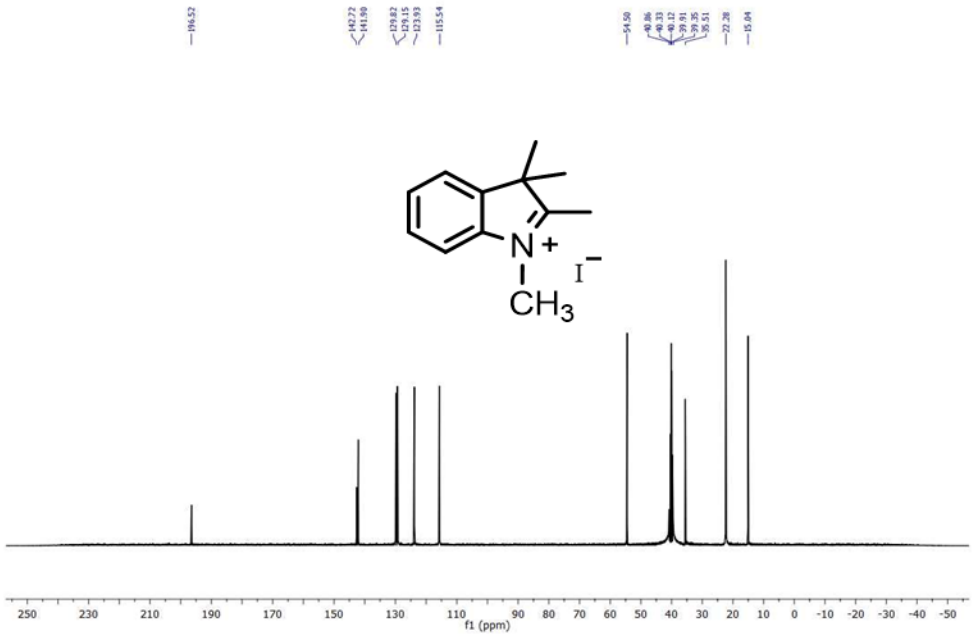

Figure 8 .^{13}C NMR (100 MHz, DMSO-d_6, 25°C) spectrum of compound 4.

Synthesis of 3,4-diethoxycyclobut-3-ene-1,2-dione: 3,4-dihydroxycyclobut-3-ene-1,2-dione (1 g, 8.77 mmol) was dissolved in 15 mL EtOH and reflux for 3 hr. The solvent was removed under reduced pressure. The resulting white slurry was re-dissolved in 15 mL EtOH and the resulting mixture was reflux for an additional 1 hr. The solvent was removed under reduced pressure and same procedure was repeated 4 times to obtain yellow oil as a pure product.

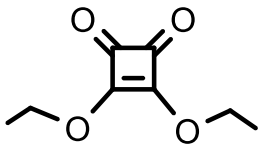

Yield: 1.48 g (99%).

^{1}H NMR (400 MHz, $CDCl_3$, 25°C): δ = 4.65 (4H, q, J = 7.2 Hz), 1.39 (6H, t, J = 6.8 Hz) ppm. ^{13}C NMR (100 MHz, $CDCl_3$, 25°C): δ = 189.3, 184.2, 70.6, and 15.5 ppm.

HRMS (ESI +ve) *m/z*: Observed for $C_8H_{10}O_4Na$ $[M+Na]^+$ = 193.0479, $[M+Na]^+$ calcd = 193.0472.

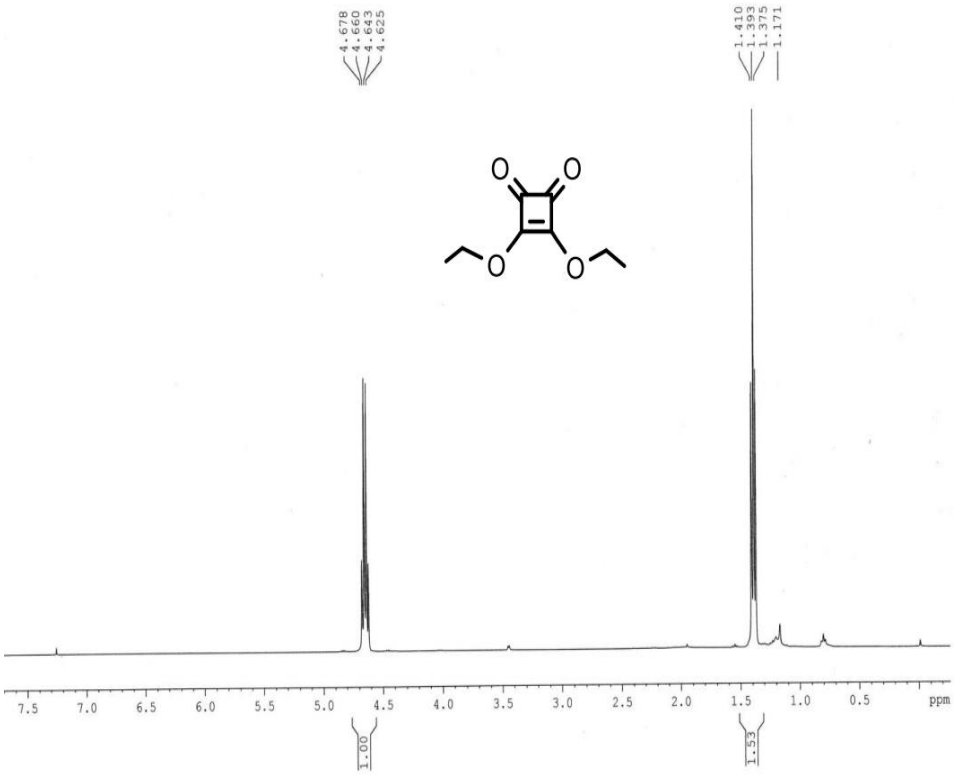

Figure 9.^{1}H NMR (400 MHz, $CDCl_3$, 25°C) spectrum of 3,4-diethoxycyclobut-3-ene-1,2-dione.

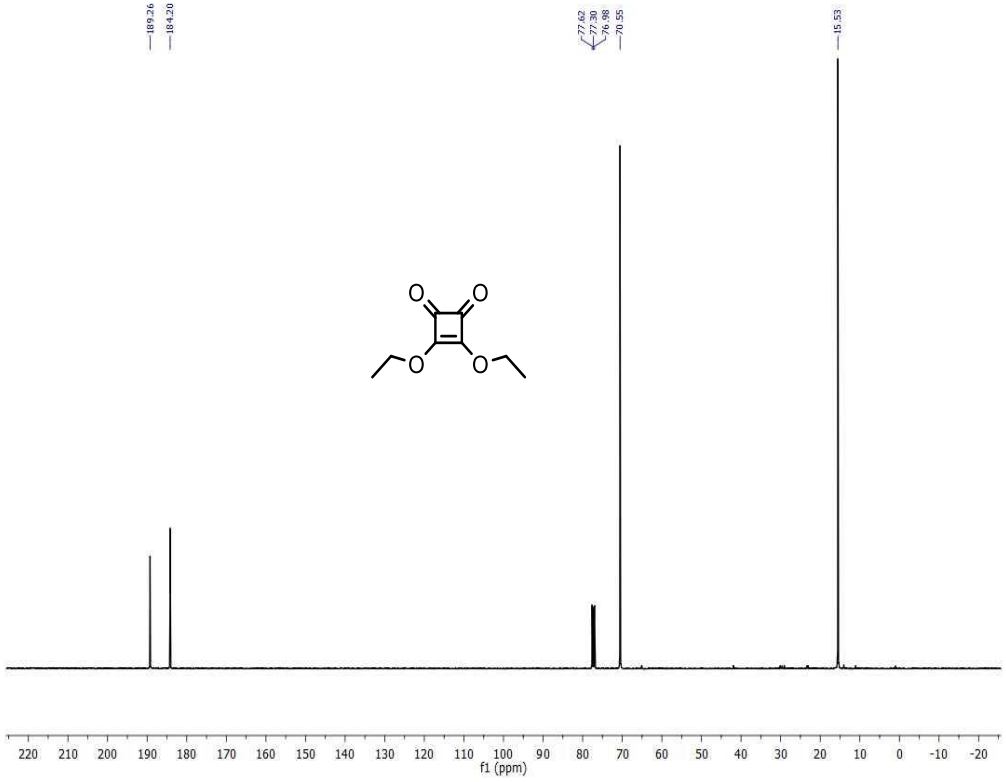

Figure 10.^{13}C NMR (100 MHz, $CDCl_3$, 25°C) spectrum of 3,4-diethoxycyclobut-3-ene-1,2-dione.

Synthesis of (*E*)-3-ethoxy-4-((1,3,3-trimethylindolin-2-ylidene) methyl) cyclobut-3-ene-1,2-dione (5): 1,2,3,3-Tetramethyl-3*H*-indol-1-ium iodide (1.2 g, 3.98 mmol), 3,4-diethoxycyclobut-3- ene-1,2-dione (0.57 g, 3.32 mmol), Et_3N (1.23 mL, 8.96 mmol), and 6 mL EtOH were introduced in a reaction vial, which was sealed and heated in MW system at 90ºC for 45 min. Then the reaction mixture

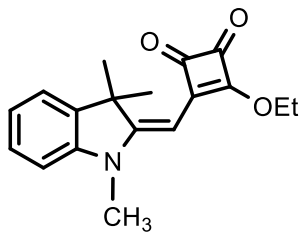

was cooled to room temperature. The solvent was removed under reduced pressure and the crude product was purified by column chromatography with 50% EtOAc / Hexane (R_f = 0.3) to get an orange solid.

Yield: 0.92 g (78%).

^{1}H NMR (300 MHz, $CDCl_3$, 25°C): δ = 7.30-7.24 (2H, m), 7.06 (1H, t, J = 7.2 Hz), 6.88 (1H, d, J = 8.4 Hz), 5.38 (1H, s), 4.88 (2H, q, J = 7.2), 3.36 (3H, s), 1.63 (6H, s), 1.53 (3H, t, J = 7.0 Hz) ppm. ^{13}C NMR (75 MHz, $CDCl_3$, 25°C): δ = 192.4, 187.7, 173.8, 169.3, 143.1, 140.8, 128.2, 127.8, 123.0, 122.8, 121.9, 109.0, 108.1, 81.6, 70.0, 47.8, 30.0, 28.3, 27.0, and 15.9 ppm.

HRMS (ESI +ve) *m/z*: Observed for $C_{18}H_{19}NO_3$ $[M]^+$ = 297.1325, $[M]^+$ calcd = 297.1365.

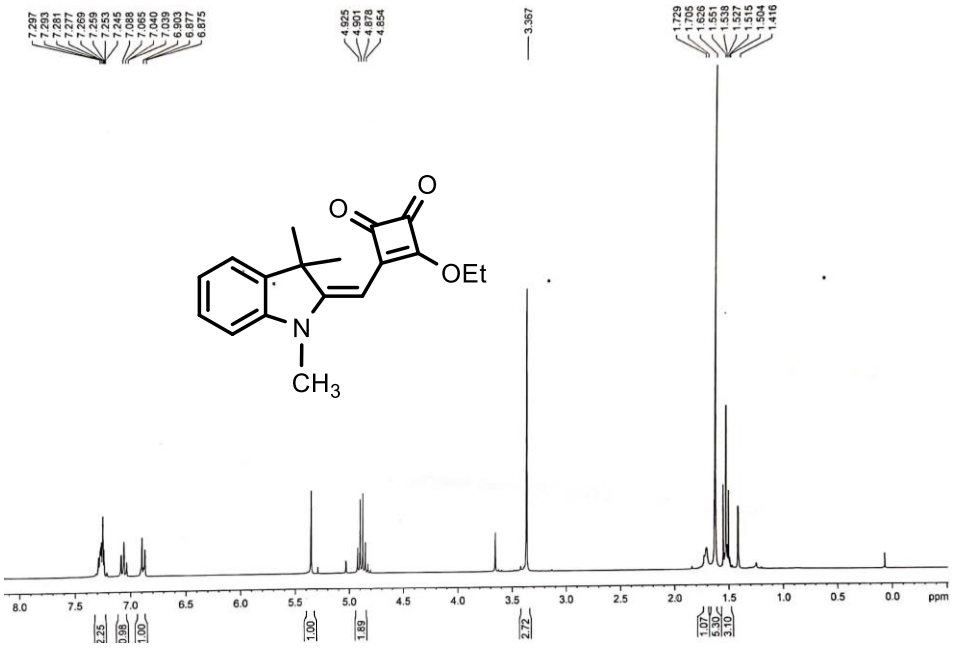

Figure 11 .^{1}H NMR (300 MHz, $CDCl_3$, 25°C) spectrum of compound 5.

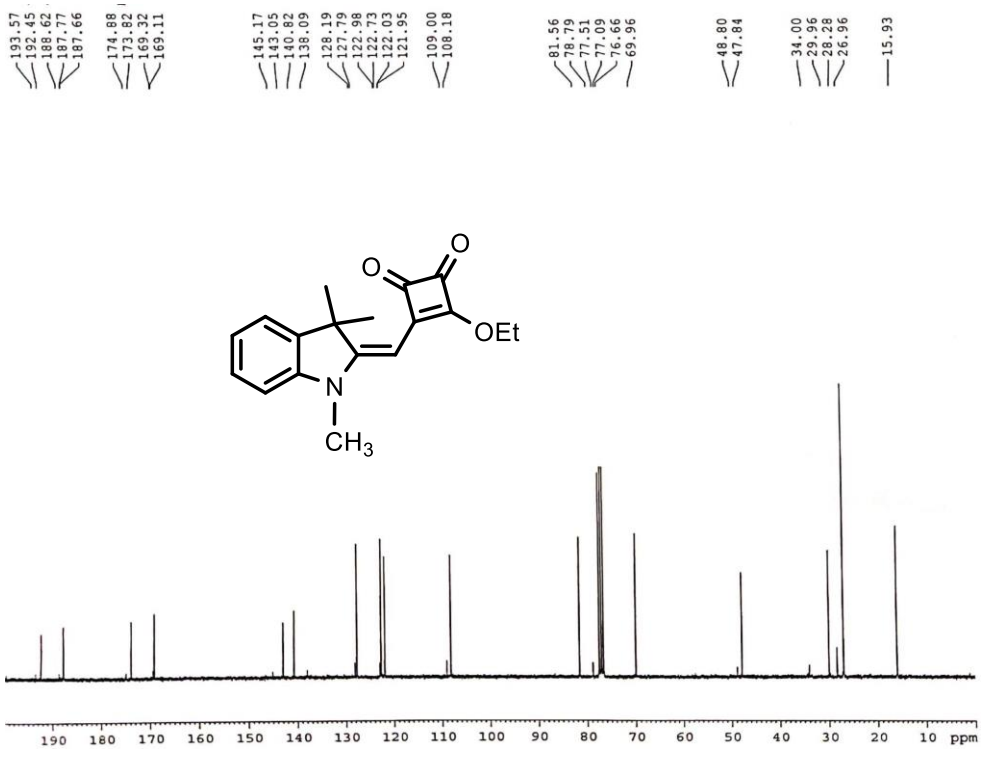

Figure 12 .^{1}H NMR (300 MHz, $CDCl_3$, 25°C) spectrum of compound 5.

Synthesis of (*E*)-3-hydroxy-4-((1,3,3-trimethylindolin-2-ylidene)methyl) cyclobut-3-ene-1,2-dione: Compound 5 (0.60 g, 2.02 mmol) was dissolved in 10 mL EtOH. Under refluxing condition 0.4 mL of 40% aq NaOH solution was added and stirred for 10 min. The reaction mixture was cooled to room temperature and neutralized with 2 ml 2(N) HCl. The reaction mixture was concentrated and 5 mL cold EtOH was added to get a precipitate. The precipitate was filter off and washed with cold EtOH to get an orange solid (0.32 g, 1.19 mmol). No further purification was required and used directly in the next step.

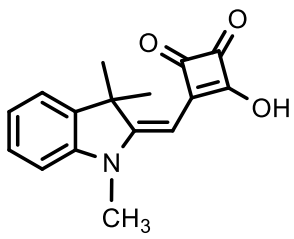

Synthesis of SQ-COOH: The hydrolysis product of 5 (0.32 mg, 1.20 mmol) and compound 2 (0.42 g, 1.20 mmol) were taken in a reaction vial containing a mixture of n-butanol (1 mL) and toluene (1 mL), which was sealed and heated in MW system at 160ºC for 55 min. Then the reaction mixture was cooled to room temperature. Deep blue colored solution was concentrated under vacuum and the crude product was purified by 5% MeOH/DCM (R_f = 0.3) to get a deep blue colored solid.

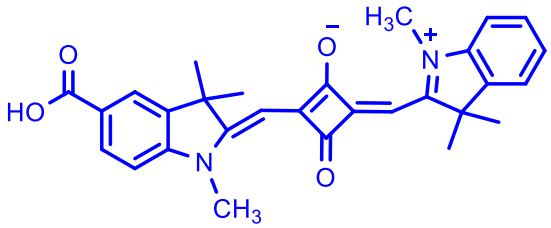

Yield: 0.46 g (81%).

^{1}H NMR (300 MHz, DMSO-d_6, 25°C): δ = 7.98 (1H, s), 7.95-7.92 (1H, m), 7.57 (1H, d, J = 7.2 Hz), 7.45-7.39 (2H, m), 7.34 (1H, d, J = 8.4 Hz), 7.23 (1H, t, J = 7.2 Hz), 5.86 (1H, s), 5.76 (1H, s), 3.65 (3H, s), 3.54 (3H, s), 1.70 (12H, s) ppm. ^{13}C NMR (75 MHz, DMSO-d_6, 25°C): δ = 182.4, 181.1, 177.4, 172.3, 168.4, 167.6, 143.1, 142.2, 130.7, 128.5, 125.4, 124.9, 123.5, 122.7, 111.4, 109.7, 87.7, 49.6, 48.2, 31.4, 27.1, and 26.6 ppm.

HRMS (ESI +ve) *m/z*: Observed for $C_{29}H_{28}N_2O_4$ $[M+H]^+$ = 469.2127, $[M+H]^+$ calcd = 469.2122.

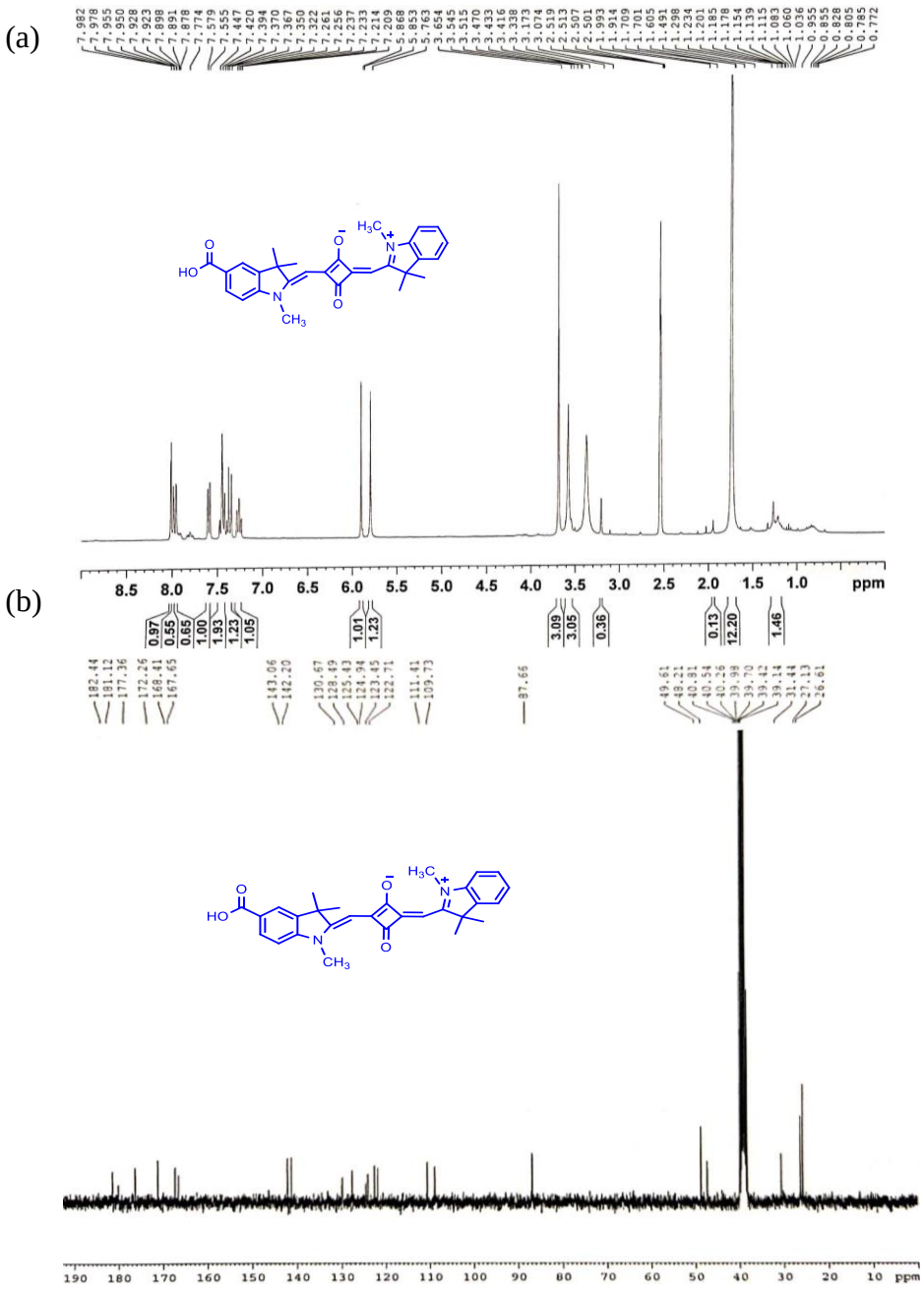

Figure 13. (a)^{1}H NMR (300 MHz, DMSO-d_6, 25°C) spectrum of SQ-COOH. (b)^{13}C NMR (75 MHz, DMSO-d_6, 25°C) spectrum of SQ-COOH.

Synthesis of MSQ: The compound SQ-COOH (0.20 g, 0.43 mmol), HATU

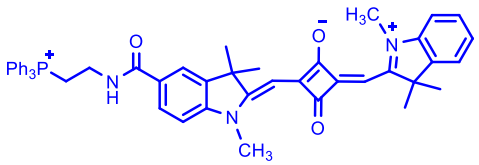

(0.18 g, 0.47 mmol) was dissolved in 3 mL DMF followed by 298 µL DIPEA was added to the reaction mixture and stirred for 15 min at 0°C. Then the synthesized compound (2-aminoethyl)triphenylphosphonium bromide (0.18 g, 0.47 mmol) was added and stirred for 12 hr at room temperature. The reaction mixture was concentrated under reduced pressure to get the crude product. The crude product was subjected to column chromatography by 3% MeOH/DCM (R_f=0.4) to get a deep blue colored solid product MSQ.

Yield: 0.19 g (53.5%).

^{1}H NMR (400 MHz, $CDCl_3$, 25°C): δ = 9.44 (1H, t, J = 4.8 Hz), 8.02 (1H, d, J = 7.1 Hz), 7.91 (1H, s), 7.83-7.67 (15H, m), 7.37-7.31 (2H, m), 7.17 (1H, t, J = 7.3 Hz), 7.04-6.98 (2H, m), 5.96 (1H, s), 5.93 (1H, s), 3.98-3.92 (2H, m), 3.86-3.80 (2H, m), 3.61 (3H, s), 3.50 (3H, s), 1.77 (12H, s) ppm. ^{13}C NMR (100 MHz, $CDCl_3$, 25°C): δ = 178.0, 167.7, 162.7, 142.8, 142.0, 135.4, 133.4, 133.3, 130.8, 130.6, 128.0, 127.7, 124.5, 122.3, 121.6, 118.2, 117.0, 109.8, 87.3, 65.8, 49.6, 48.7, 36.6, 34.3, 31.5, 31.1, 27.0, 26.8, 22.7, 22.0, and 21.0 ppm.

HRMS (ESI +ve) *m/z*: Observed for $C_{49}H_{47}N_3O_3P^+[M]^+$ = 756.3343, $[M]^+$ calcd = 756.3350.

Photophysical properties in $CHCl_3$ λ_{abs}= 640 nm, λ_{em}= 659 nm, Stokes shift ($\Delta\lambda$) = 19 nm, ε = 2.26 ×10^5 M $^{-1}$ cm^{-1}, Φ_f = 0.15 in DMSO (Φ_f of Zinc phthalocyanine as reference = 0.20 in DMSO).

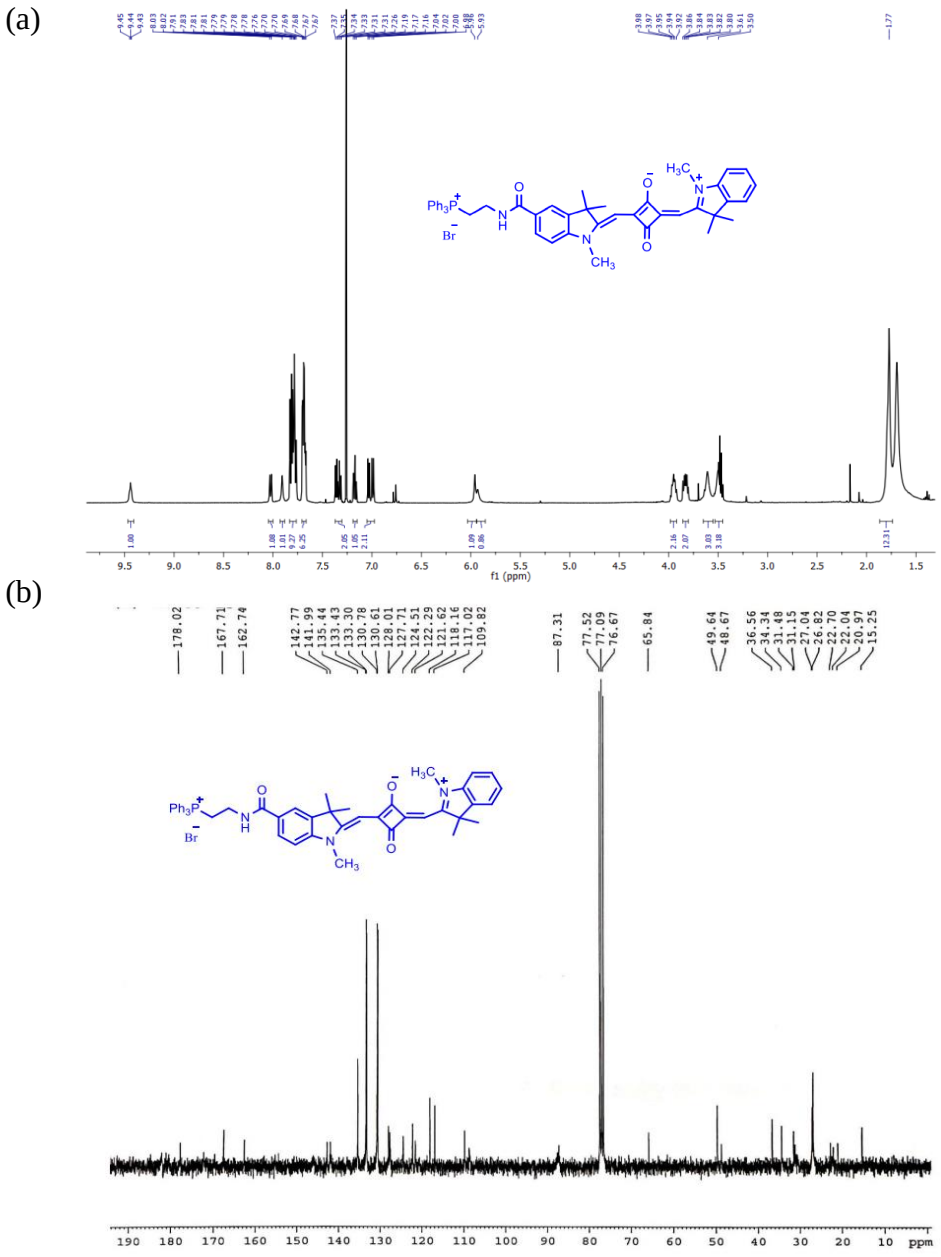

Figure 14. (a) ^{1}H NMR (400 MHz, $CDCl_3$, 25°C) spectrum of MSQ. (b) ^{13}C NMR (100 MHz, $CDCl_3$, 25°C) spectrum of MSQ.

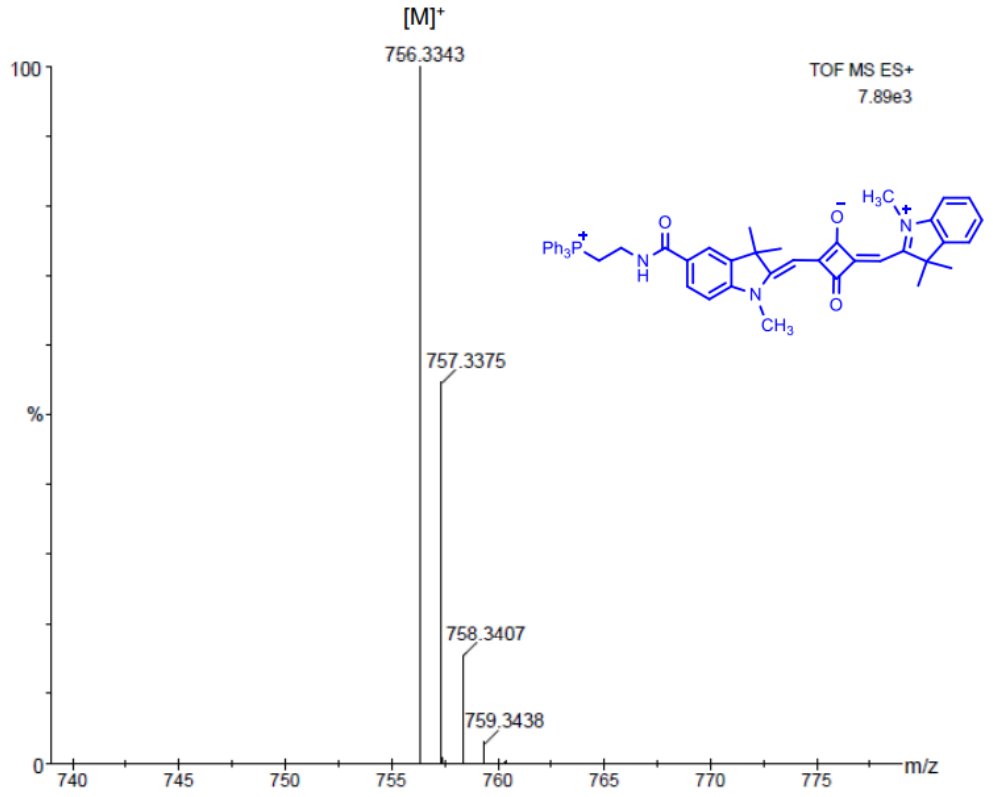

Figure 15. HRMS (ESI +ve) spectrum of MSQ

Synthesis of Macrocycle: 9,10-Bis(aminomethyl)anthracene (0.19 g, 0.81 mmol) and 5-(*tert*-butyl)isophthaloyl dichloride (0.21 g, 0.81 mmol) were

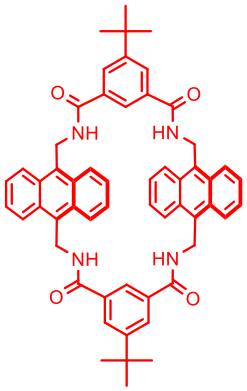

separately dissolved in 20 mL anhydrous $CHCl_3$.Each solution was taken into separate 50 mL syringes. Et_3N (0.5 mL) was added to the syringe containing 9,10-bis(aminomethyl)anthracene. The two solutions were added simultaneously drop wise to a stirred solution of 40 mL anhydrous $CHCl_3$ over 6 hr. After stirring overnight, the solution was concentrated under reduced pressure to obtain the crude product. The crude product was purified by column chromatography using 2% MeOH/$CHCl_3$ to get a pale yellow coloured solid.

Yield: 0.19 g (27.9%).

^{1}H NMR (400 MHz, $CDCl_3$, 25°C): δ = 8.38 (4H, s), 8.21 (8H, dd, J = 6.8 Hz, J = 3.2 Hz), 7.47 (8H, dd, J = 6.8 Hz, J = 3.2 Hz), 7.22 (2H, s), 6.40 (4H, br), 5.51 (8H, d, J = 4.8 Hz), 1.45 (18H, s) ppm. ^{13}C NMR (100 MHz, $CDCl_3$, 25°C): δ = 166.6, 153.9, 133.2, 130.4, 129.8, 129.3, 126.8, 126.1, 124.2, 37.3, and 29.7 ppm.

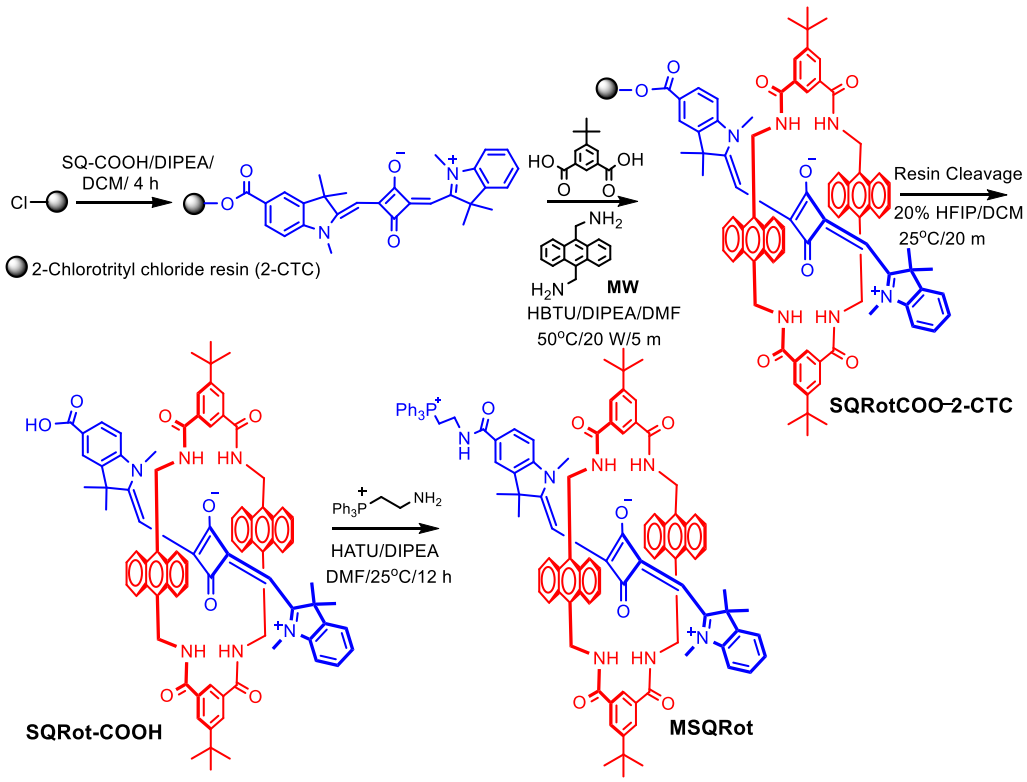

Scheme 2. Synthesis of MSQRot molecule.

Synthesis of Rotaxane using Manual MW-Assisted Solid-Phase Synthesis Protocol on 2-CTC Resin: SQRot-COOH was synthesized by manual microwave-assisted SPPS protocol on a microwave peptide synthesizer (CEM, Discover Bio). We use 2-chloro tritylchloride (2-CTC) resin (LL, 0.85 mmol/g loading density) to synthesize SQRot-COOH.

SQ-COOH Loading on 2-CTC Resin: SQ-COOH (0.32 g, 0.68 mmol, 2 eq), DCM (5 mL), and DIPEA (0.24 mL, 1.36 mmol, 4 eq) were added in a solid phase extraction (SPE) cartridge with frit and shaken to dissolve under N_2. 2-CTC resin (0.4 g, 0.34 mmol, 1eq) was taken into the SQ-COOH solution and shaken for 4 h under N_2 bubbling. Dry MeOH (2 mL) was added into the 2-

CTC resin solution and shaken for another 30 min for the capping of any unreacted 2-CTC resin and then washes with DCM (2×), DMF (2×), isopropanol (2×), DMF (2×), MeOH (3×).

Estimation of the SQ-COOH Loading on 2-CTC Resin: The resin loading was estimated by measuring the absorption using UV/vis spectroscopy. The resin (5 mg) was taken in a 5 mL vial and 2 mL 20% HFIP in DCM was added. It was shaken for 20 min at 25°C. The resin was filtered off and the solvent was removed under the reduced pressure. It was then transferred to a 25 mL graduated flask quantitatively using DCM. The absorption experiment was performed using a UV cuvette with a path length of 1 cm. The absorption of the cleaved SQ-COOH from resin was detected at 640 nm ($\varepsilon_{640} = 2.1 \times 10^5$ L mol^{-1} cm^{-1}) in DCM. The resin loading was calculated based on Lambert-Beer's law. 91% loading of SQ-COOH on 2-CTC resin was obtained.

Microwave-Assisted Solid Phase Rotaxane Synthesis (SQRot-COOH) on 2-CTC Resin: SQRot-COOH was synthesized in 0.1 mmol scale on SQ-COOH loaded 2-CTC resin. We particularly choose low loading 2-CTC resin for the template-directed rotaxane synthesis. Special care was taken for the template-directed clipping reaction on 2-CTC resin. The temperature was maintained to 50°C and no HOBt was added to the coupling step. 5-*tert*-Butylisophthalic acid (5 eqv.) and 9,10-bis(aminomethyl)anthracene (5 eqv.) were each dissolved in 3 mL anhydrous DMF in presence of DIPEA. Coupling (0.5 M HBTU/2 M DIPEA/DMF; 300 sec, 50°C, 20 W) were performed under MW condition at 50°C. Double coupling using same protocol was performed. The resin was transferred into a SPE cartridge with frit and washed manually with DMF (5×), DCM (5×), DMF (5×), isopropanol (2×), DMF (5×), and finally with MeOH

(5×). The rotaxane loaded resins were dried in vacuum and stored at −18°C. Cleavage of SQRot-COOH from 2-CTC Resin: SQRot-COO-2CTC resin was taken in a sample vial and 20% HFIP in DCM (extremely mild acidic conditions) was added and stirred for 20 min at 25°C. The resin beads were filtered off and evaporate the solvent to get the blue colored solid. The product was easily purified by column chromatography using 10% MeOH/$CHCl_3$ to get a see green colored solid SQRot-COOH with free carboxyl (–COOH) group. Yield: 0.09 g (69.4%).

HRMS (ESI +ve) *m/z*: observed for $C_{85}H_{80}N_6O_8$ $[M]^+$ = 1313.6049, $[M]^+$ calcd = 1313.6110.

Protocol for Microwave-Assisted Solid-Phase Synthesis of SQRot-COOH

Working Step	Reagents	Reaction condition
Coupling	HBTU/DIPEA/DMF	300 sec/50°C/20W
Washing after coupling	DMF (5×), DCM (5×), DMF (5×), isopropanol (2×), DMF (5×), MeOH (5×)	
Resin Cleavage	20%HFIP/DCM (extremely mild acidic conditions)	20 min/25°C

Standard Protocols for Manual MW-Assisted Solid Phase Synthesis using 2-CTC Resin:

1. Bubbling during the MW-assisted synthesis for all steps: on 3 sec; off 7 sec
2. Coupling: 2-CTC resin- time 300 sec, power 20 W, temperature: 50ºC, delta temperature: 5ºC Double coupling was performed.

Synthesis of MSQRot: The compound SQRot-COOH (0.066 g, 0.05 mmol), HATU (0.023 g, 0.06 mmol) was dissolved in 2 mL DMF followed by 38 µL

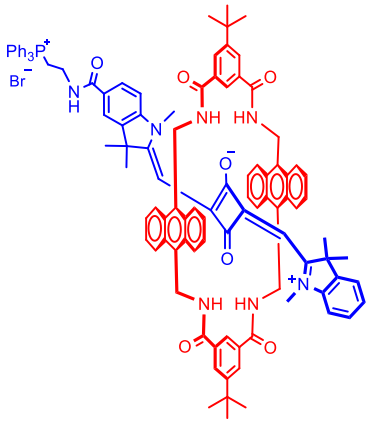

DIPEA was added to the reaction mixture and stirred for 15 min at 0°C. Then the synthesized compound (2-aminoethyl)triphenylphosphonium bromide (0.024 g, 0.06 mmol) was added and stirred for 12 hr at 25°C. The reaction mixture was concentrated under reduced pressure to get the crude product. The crude product was purified by column chromatography using 3% MeOH/$CHCl_3$ to get a see green colored solid.

Yield: 0.034 g (42%).

^{1}H NMR (400 MHz, $CDCl_3$, 25°C): δ = 9.47 (1H, s), 9.45 (1H, s), 8.59 (4H, s), 8.06 (4H, d, J = 8.8 Hz), 7.86-7.73 (25H, m), 7.43 (1H, t, J = 8.0 Hz), 7.25-7.23 (2H, m), 7.06-7.00 (7H, m), 6.66-6.60 (4H, m), 5.55-5.46 (4H, m), 5.12-5.07 (4H, m), 4.58 (1H, s), 4.49 (1H, s), 3.85-3.83 (2H, m), 3.64-3.57 (2H, m), 2.71 (3H, s), 2.62 (3H, s), 1.57 (18H, s), and 1.25 (12H, s) ppm. ^{13}C NMR (100 MHz, $CDCl_3$, 25°C): δ = 181.9, 167.0, 166.9, 153.9, 147.1, 139.6, 135.7, 133.6, 133.4, 131.0, 130.9, 130.5, 129.8, 128.9, 126.0, 125.5, 124.8, 122.2, 118.5, 117.6, 109.1, 84.5, 59.1, 50.5, 49.9, 38.2, 35.8, 34.5, 31.6, 29.8, 28.3, and 28.0 ppm. ^{31}P NMR (202 MHz, $CDCl_3$, 25°C): δ = 24.8 ppm.

HRMS (ESI +ve) *m/z*: observed for $C_{105}H_{99}N_7O_7P^+$ $[M]^+$ = 1601.7362, $[M]^+$ calcd = 1601.7372.

Photophysical properties in $CHCl_3$ λ_{abs}= 652 nm, λ_{em}= 670 nm, Stokes shift ($\Delta\lambda$) = 18 nm, ε = 1.50 ×10^5 M^{-1} cm^{-1}, Φ_f = 0.53 in DMSO (Φ_f of Zinc phthalocyanine as reference = 0.20 in DMSO).

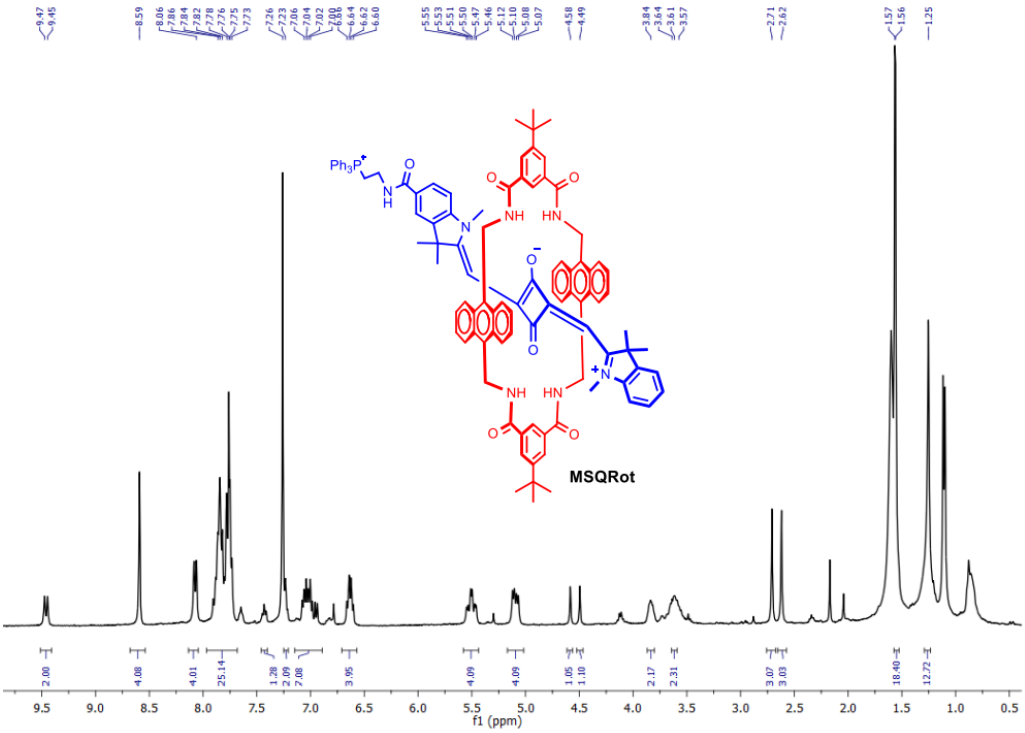

Figure 16. ^{1}H NMR (400 MHz, $CDCl_3$, 25°C) spectrum of MSQRot.

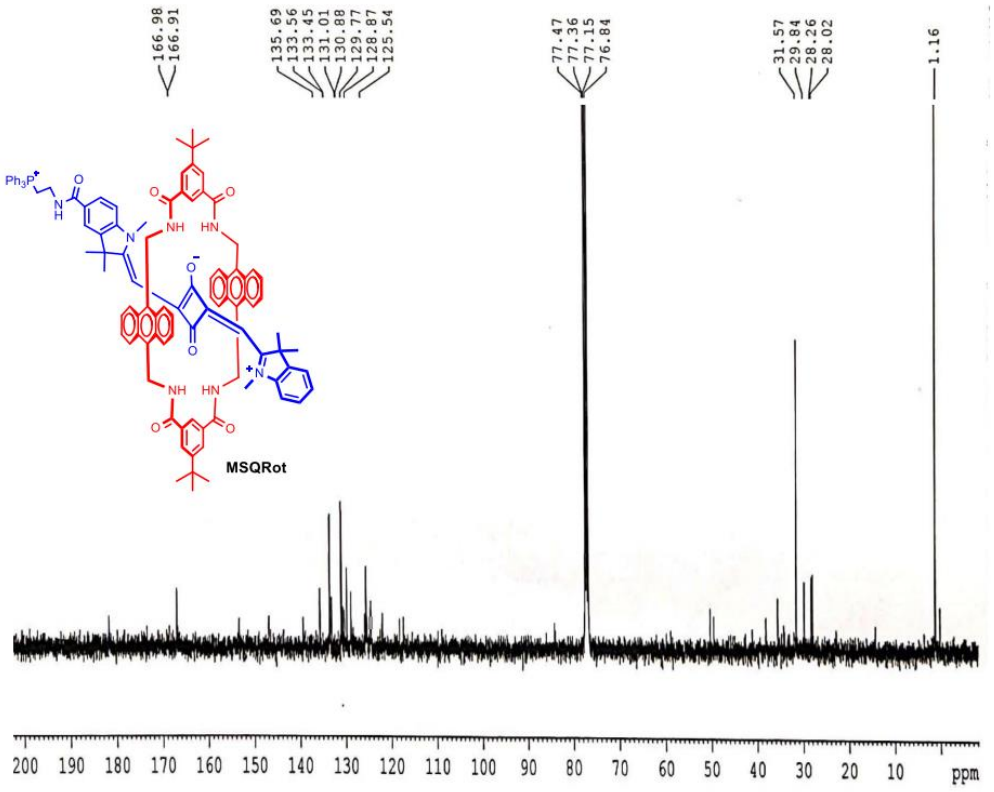

Figure 17. ^{13}C NMR (100 MHz, $CDCl_3$, 25°C) spectrum of MSQRot.

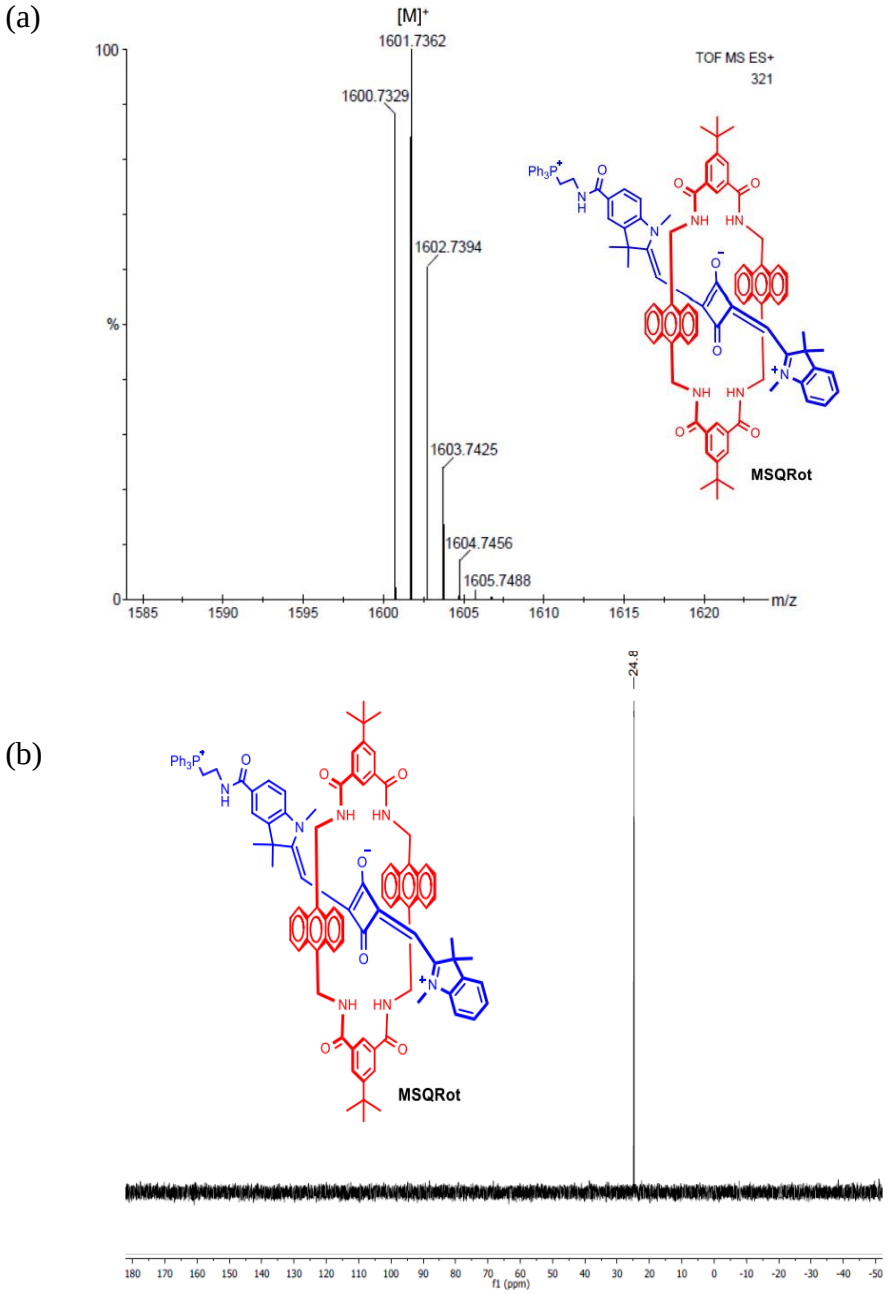

Figure 18. (a) HRMS (ESI +ve) spectrum of MSQRot. (b) ^{31}P-NMR of MSQRot.

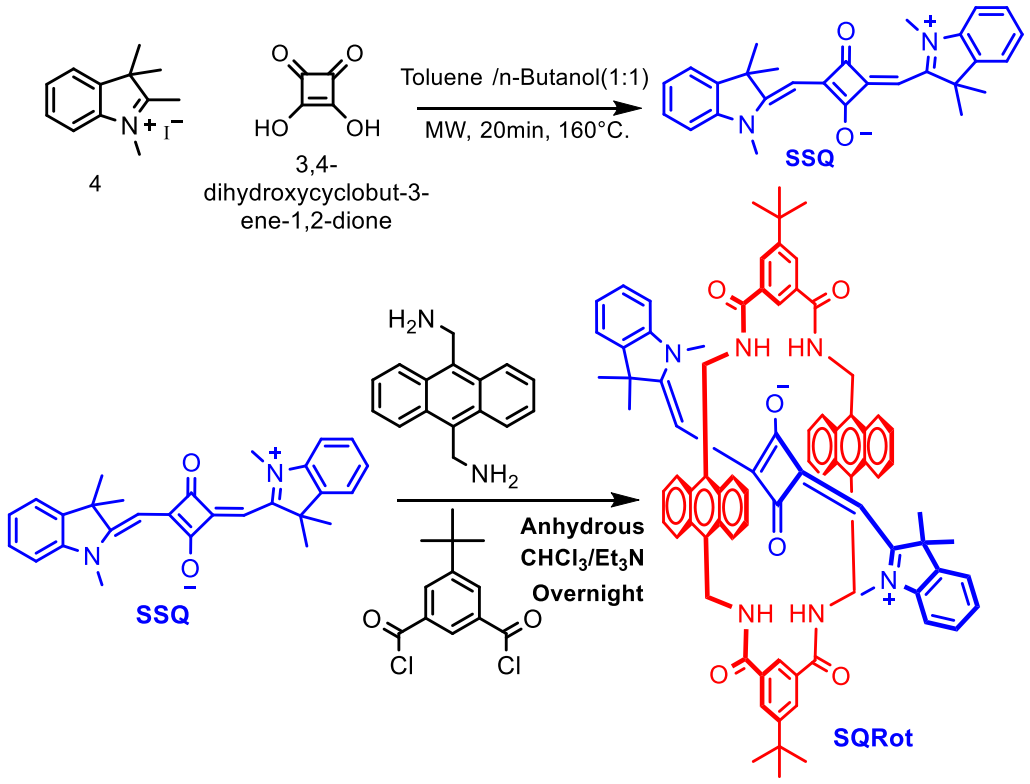

Scheme 3. Synthesis of SSQ and SQRot molecules.

Synthesis of Symmetrical SQ Dye: 1,2,3,3-tetramethyl-3*H*-indol-1-ium iodide (4) (0.50 g, 1.66 mmol) and squaric acid (0.10 g, 0.83 mmol) was introduced in

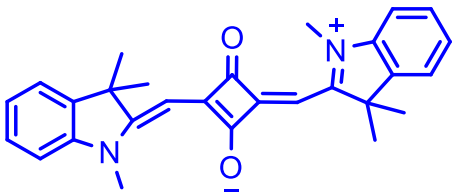

a reaction vial containing a mixture of n-butanol (1 mL) and toluene (1 mL). The vial was sealed and heated in a MW system at 160ºC for 20 min. Then the reaction mixture was cooled to room temperature. The deep blue colored solution was concentrated under vacuum and washed with Et_2O (3 × 10 mL) to get a pure deep blue product (R_f = 0.3 in 1% MeOH/ DCM).

Yield: 0.62 g (87%).

^{1}H NMR (400 MHz, $CDCl_3$, 25°C): δ = 7.36-7.30 (4H, m), 7.15 (2H, t, J = 7.5 Hz), 7.0 (2H, d, J = 8.0 Hz), 5.92 (2H, s), 3.56 (6H, s), 1.78 (12H, s) ppm. ^{13}C NMR (100 MHz, $CDCl_3$, 25°C): δ = 182.5, 180.1, 170.8, 143.1, 127.8, 123.8, 122.3, 109.2, 86.8, 49.3, and 27.1 ppm.

HRMS (ESI +ve) *m/z*: observed for $C_{28}H_{28}N_2O_2Na$ $[M+Na]^+$ = 447.2011, $[M+Na]^+$ calcd = 447.2043.

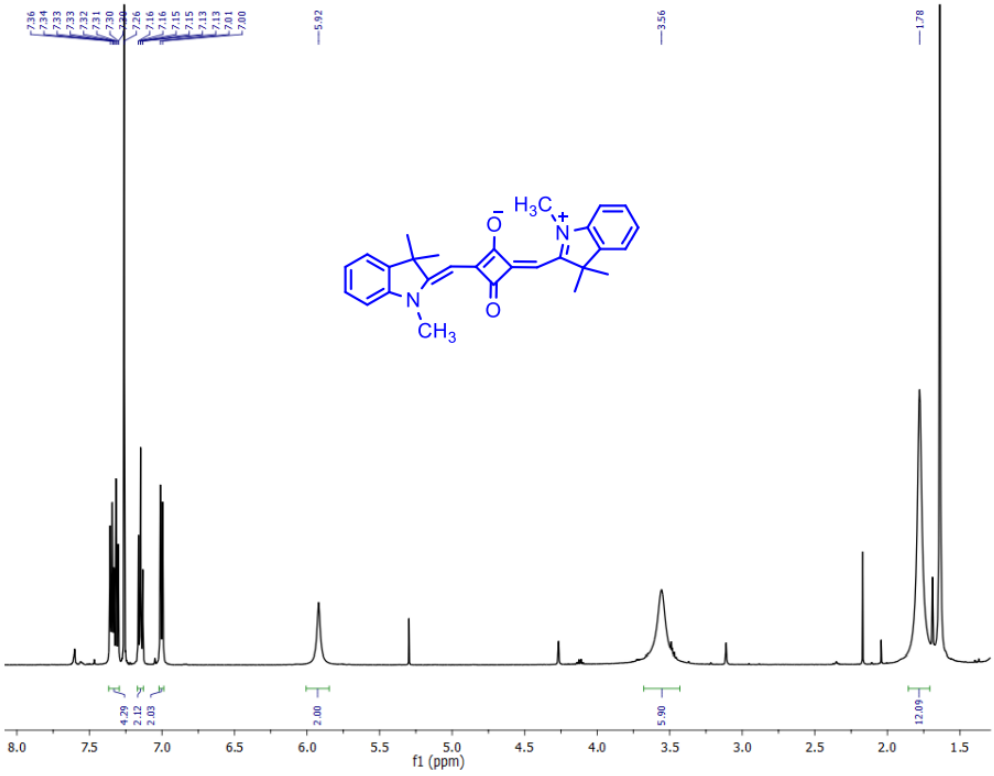

Figure 19. ^{1}H NMR (400 MHz, $CDCl_3$, 25°C) spectrum of SQ.

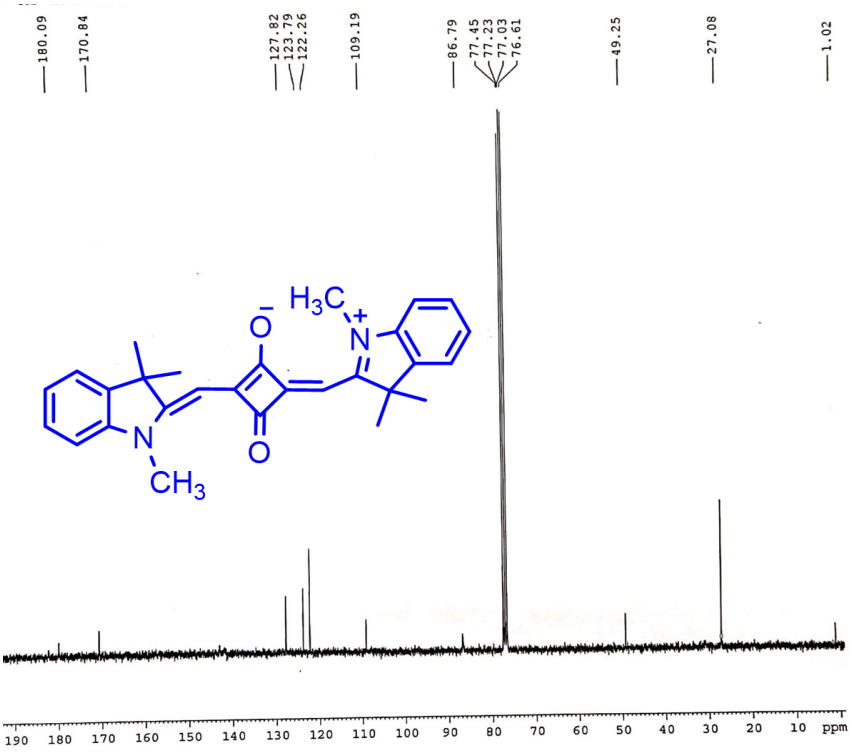

Figure 20. ^{13}C NMR (100 MHz, $CDCl_3$, 25°C) spectrum of SQ.

Synthesis of Symmetrical SQ Rotaxane (SQRot): 5-(*tert*-butyl)isophthaloyl dichloride (0.23 g, 0.89 mmol) and 9,10-bis(aminomethyl)anthracene (0.21 g, 0.89 mmol) were dissolved separately in 20 mL anhydrous $CHCl_3$. Each solution was taken into separate 50 mL syringe. Et_3N (0.5 mL) was added to the syringe containing 9,10-bis(aminomethyl)anthracene. The two solution was added simultaneously drop wise to a stirred solution of symmetrical SQ (0.09 g, 0.22 mmol) in 40 mL anhydrous $CHCl_3$ over 6 hr. After stirring 24 hr, the resulting solution was concentrated under vacuum to get the crude product. The crude product was purified by column chromatography using 2% MeOH/$CHCl_3$ to get a see green colored SQRot solid.

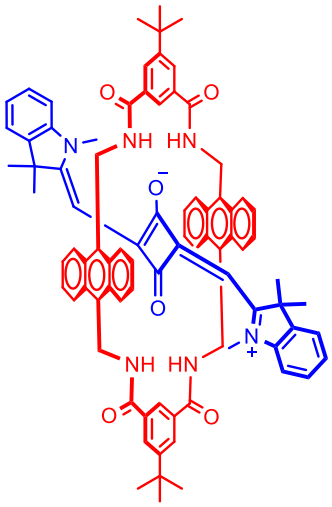

Yield: 0.039 g (14%).

^{1}H NMR (400 MHz, $CDCl_3$, 25°C): δ = 9.48 (2H, s), 8.58 (4H, s), 8.04 (4H, d, J = 8.0 Hz), 7.88 (4H, br), 7.81 (4H, d, J = 9.0 Hz), 7.41-7.39 (2H, m), 7.23-7.20 (4H, m), 7.03 (4H, t, J = 8.0 Hz), 6.95-6.93 (2H, m), 6.62 (4H, d, J = 8 Hz), 5.49-5.44 (4H, m), 5.08-5.04 (4H, m), 4.50 (2H, s), 2.64 (6H, s), 1.55 (18H, s), and 1.11 (12H, s) ppm. ^{13}C NMR (100 MHz, $CDCl_3$, 25°C): δ = 181.8, 171.6, 167.6, 167.0, 153.3, 143.8, 139.1, 133.1, 130.6, 130.4, 130.2, 130.0, 129.7, 128.7, 128.2, 128.0, 125.6, 124.8, 124.5, 122.3, 109.4, 83.4, 49.9, 38.2, 35.6, 34.0, S13 31.6, 29.9, 29.2, 28.2, 27.4, 25.8, and 22.8 ppm.

HRMS (ESI +ve) *m/z*: observed for $C_{84}H_{80}N_6O_6$ $[M]^+$ = 1268.6194, $[M]^+$ calcd = 1268.6139.

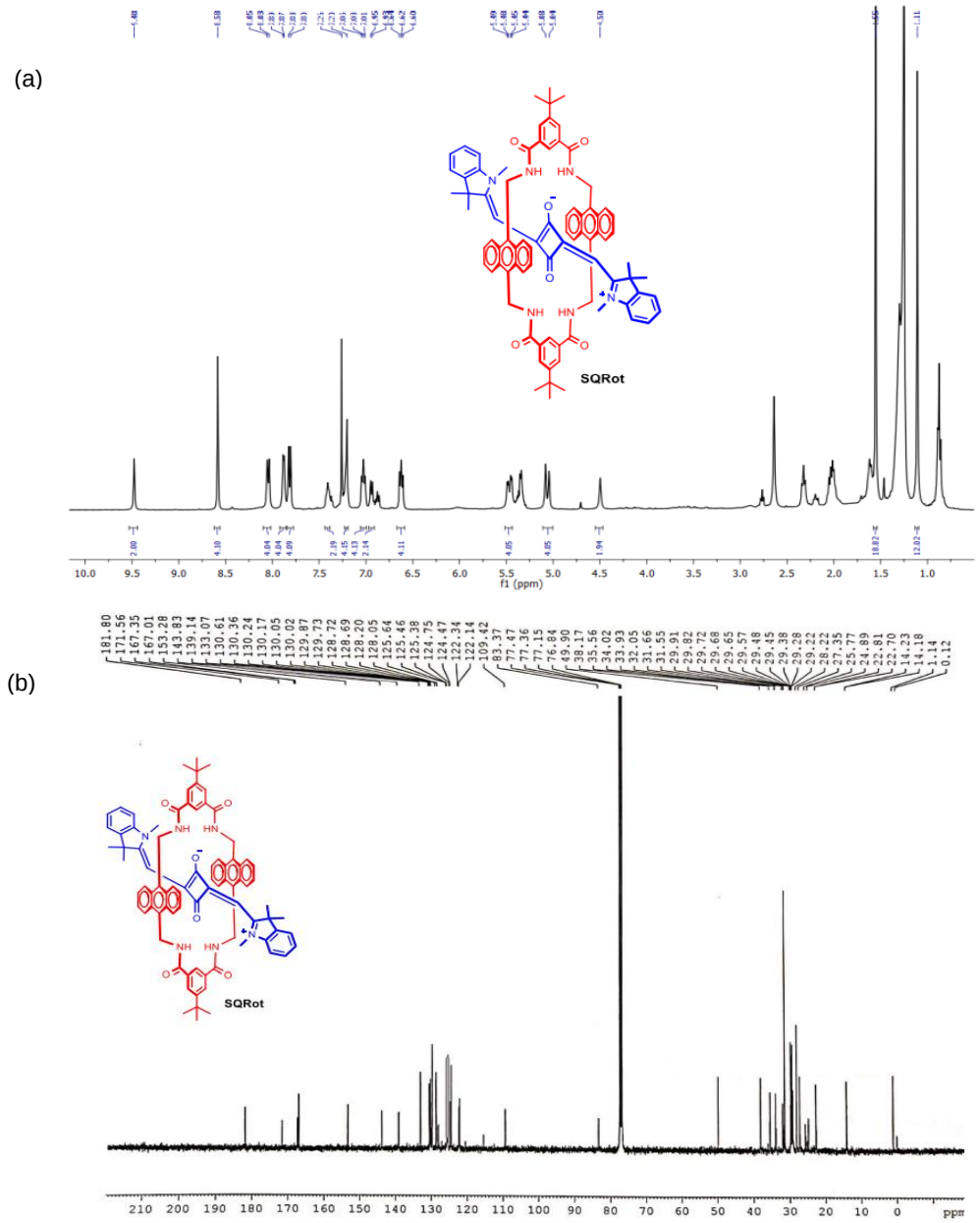

Figure 21. (a) ^{1}H NMR (400 MHz, $CDCl_3$, 25°C) spectrum of SQRot. (b) ^{13}C NMR (100 MHz, $CDCl_3$, 25°C) spectrum of SQRot.

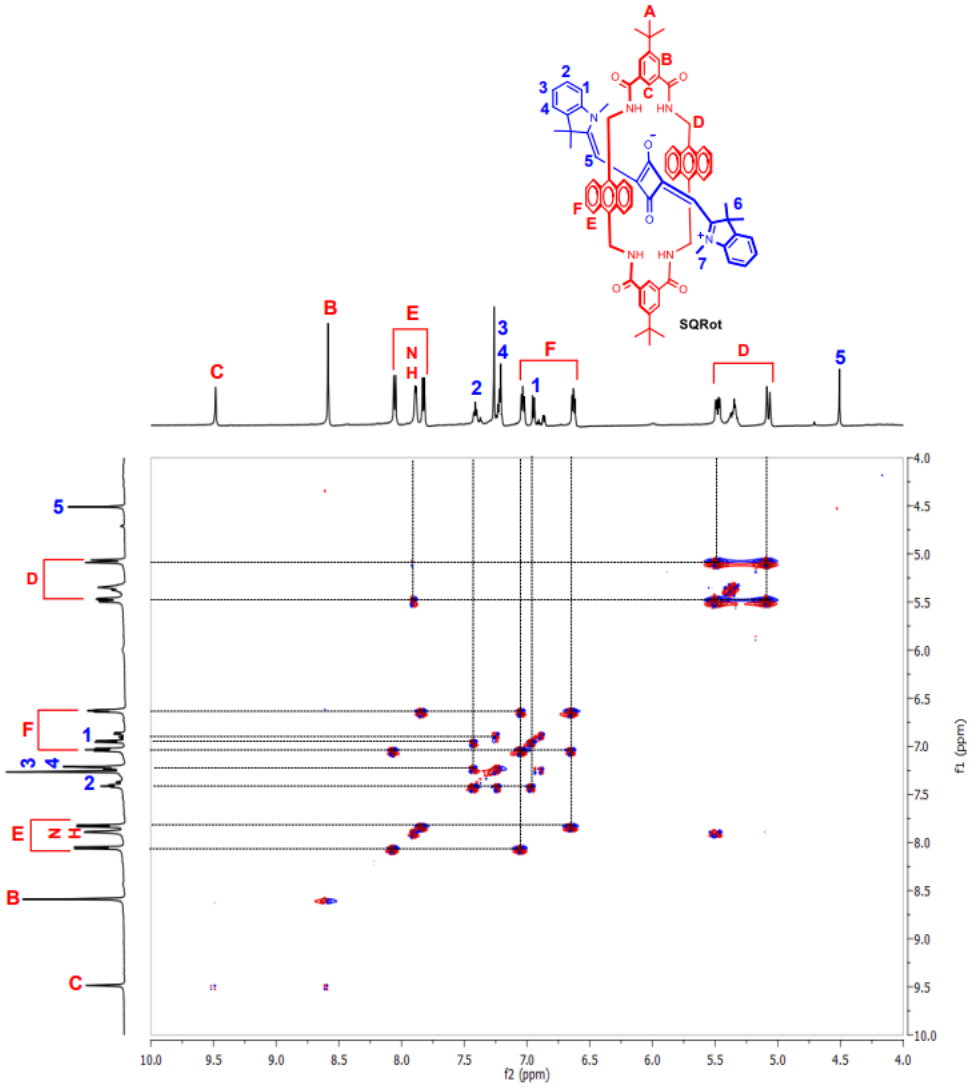

Figure 22. Partial ^{1}H-^{1}H DQF COSY NMR spectrum of control SQRot (400 MHz, $CDCl_3$, 25°C).

METHODS

NMR Spectroscopy: 1D (^{1}H, ^{13}C, ^{31}P) and 2D NMR (^{1}H–^{1}H DQF COSY) were measured on Bruker DPX500 MHz, Bruker DPX400 MHz, and Bruker DPX300 MHz spectrometers at 25°C in appropriate deuterated solvents.

HRMS (ESI): High-resolution electrospray ionisation mass spectrometry (HRMS-ESI) was recorded using a Q-TofmicroTM (Waters Corporation) mass spectrometer.

Absorption Spectroscopy: Absorption spectra were recorded in various solvents on a Shimadzu UV-1800 spectrometer. All measurements were carried out in a quartz cuvette with a path length of 1 cm. Stabilities of the MSQRot were measured in mitochondrial pH 8.0, 37°C, over 48h using a peltier temperature controlling unit attached with the UV/vis instrument.

Fluorescence Spectroscopy: Fluorescence experiment was performed on a Horiba Jobin Yvon FluoroMax-4 spectrofluorometer in various solvents.

Calculation of Relative Quantum Yield of MSQ and MSQRot: Fluorescence quantum yields (Φ_f) of MSQ and MSQRot were determined by relative method. The integrated fluorescence intensity of the MSQ and MSQRot was compared with respect to fluorescence intensity of a reference compound [Φ_f (st) of Zinc phthalocyanine in DMSO = 0.20] using the following equation:

$$\Phi_f(x) = \Phi_f(st) \times [(A_{st} \times F_x \times \eta_x^2) / (A_x \times F_{st} \times \eta_{st}^2)]$$

Φ_f (st) and Φ_f (x): fluorescence quantum yield of the reference and sample compounds, respectively.

A_{st} and A_x: Absorbance of reference and sample at the excitation wavelength, respectively.

F_{st} and F_x: Integrated fluorescence areas under the corrected fluorescence spectra for the reference and sample compound, respectively.

η_{st} and η_x: Refractive indices of the solvent in which the reference and sample compounds are measured, respectively [here, both the sample and reference compound were dissolved in DMSO; so $(\eta_x^2 / \eta_{st}^2) = 1$].

"x" refers to the unknown sample and "st" stands for the standard.

The relative Quantum yields (Φ_f) of MSQ and MSQRot were measured as 0.15 and 0.53, respectively, in DMSO.

Single Crystal X-Ray Diffraction: Single crystals suitable for X-ray diffraction was obtained by vapor diffusion method. A solution of SQRot in $CHCl_3$ was placed in a 2 mL vial and put inside a 20 mL vial filled with EtOAc. The larger vial was capped and allow to slow diffusion of EtOAc into $CHCl_3$ solution of the compound. Diffraction data of SQRot was measured with MoK_α radiation (a graded multilayer mirror monochromator, λ = 0.71073 Å) at 273 K on a micro focus Single Crystal X-ray Diffraction instrument (Make: Bruker, Model: D8 Quest). A PHOTON-100 CMOS detector is used. Structures were solved by direct methods using the SHELXT 2014/5 program.[9-10] Refinements were carried out with a full-matrix least squares method against F 2 using SHELXL-2018/3,[11] incorporated in Olex2 crystallographic collective package. The non-hydrogen atoms were refined with anisotropic thermal parameters. Formula sum = $C_{97.24}H_{84}N_6O_{12}$, formula weight = 1528.58, crystal system = triclinic, space group = *P* -1, *a* = 11.1202(11) Å, *b* = 11.6727(12) Å, *c* = 16.8575(17) Å, α = 94.197(3)°, β = 100.651(3)°, γ = 111.900(3)°, *V* = 1970.9(3) $Å^3$, *Z* = 1, D_{calcd} = 1.288 g cm^{-3}, μ = 0.085 mm^{-1}. The final R value was R_1 = 0.0688 and wR_2 = 0.1875 for reflections with I > 2ζ(I). Despite our best efforts, we were unable to obtain high quality crystals of the rotaxane molecule. The best piece of crystal of this compound was found to be weak

scatterers of X-rays and thus the quality of the structure is not very high. Nevertheless, the structural analysis of the compound suffices to establish the identity and gross features of the system. Crystallographic data was deposited at Cambridge Crystallographic Data Centre (CCDC) with reference number CCDC 1998840. These data can be obtained free of charge from the Cambridge Crystallographic Data Centre, www.ccdc.cam.ac.uk/structures.

Energy Minimized Structures of MSQ and MSQRot: The energy minimized structure of MSQ and MSQRot were obtained from density functional theory (DFT) combines the Becke 3-parameter exchange functional with the gradient-corrected correlation functional of Lee, Yang, and Parr (B_3LYP) by the 6-31+G** [or 6-31G(d,p)] basis set [B3LYP/6-31+G**] using Gaussian 09W Revision D.01.B3LYP/6-31+G**[12] energy minimized structure displayed that the two 1,3,3-trimethylindolin rings of MSQ were in trans configuration in the mechanically interlocked rotaxane (MSQRot). Macrocycle N–H′s was forming hydrogen bond with O′s of squaraine residue. Two C–H′s of aryl ring macrocycle was forming hydrogen bond with squaraine O′s. The central four-membered core of MSQ was extremely electron deficient and inserted between the sidewalls of electron rich two anthracene residues. The centroid-to-centroid distance among the anthracene moieties to four membered ring was 3.9 Å and stabilized by D-A-D kind interaction.

Docking Studies: The docking calculation was performed using AutoDock 4.2 with the standard method described in the user manual. Here, genetic algorithm with 90 x 90 x 90 grid box were used for the calculations. For visualization of the docking results the Discovery Studio Client 2017 was utilized. Molecular docking of MSQ with exposed thiol containing proteins ATP synthase subunit beta 1 (PDB: 4Q4L), Nit2 (PDB: 4H5U), and human peroxiredoxin 5 (PDB: 1H4O) help to understand the interaction of exposed thiol of Cys residues in

these proteins with MSQ dye. MSQ is an unsymmetrical molecule with electrophilic SQ chromophore. All these proteins contain more than one Cys amino acid residues which may attack to the SQ chromophore. MSQ shows binding affinity with ATP synthase subunit beta 1, Nit2, and human peroxiredoxin 5 with ΔG = –6.25, –7.78, and –5.62 kcal/mol, respectively. Remarkably, for all these exposed thiol proteins it was observed that the Cys residue was very close to the electrophilic conjugated C_4O_2 core and the distance were 3.8 Å (C35 of ATP synthase subunit beta 1), 3.6 Å (Cys14 of Nit2), and 5.8 Å (C47 of human peroxiredoxin 5), respectively, whereas, the C-S bond length was 1.83 Å. In these three proteins, the addition reaction with exposed SH was favoured at the side of the unsymmetrical MSQ where TPP+ group was attached. The cationic TPP^+ moiety also play an important role in the binding of MSQ with mitochondrial proteins through π-π stacking and electrostatic interactions with various amino acid residues.

Cell Culture: HeLa, A549, and HEK293 cells were cultured in DMEM (pH 7.4) with 10% fetal bovine serum (FBS) and antibiotic-antimycotic solution 100×(containing 10000 units penicillin, 10 mg streptomycin, and 25μg amphotericin B per mL in 0.9% normal saline). The cell lines were preserved at 37°C in an air-jacketed 5% CO_2 incubator and were routinely passaged.

Cell Viability Assay: The cell viability of HeLa and HEK293 cell lines were determined by 3-(4,5-dimethyl-2- thiazolyl)-2,5-diphenyltetrazolium bromide (MTT) assay using freshly harvested cells. HeLa and HEK293 cells were separately seeded at a density of ~10^3 cells on a 96-well plate by DMEM for 24 h incubation. Subsequently 24 h incubation, MSQ or MSQRot was treated at different doses (5, 10, 15, and 20 μM per well) at 37°C for 24 h. The HeLa and HEK293 cells were then individually incubated with 10 μL of MTT solution (5 mg mL^{-1} in PBS) at 37°C for 4 h in darkness.

The outcomes (performed the assay in triplicates) were determined as the percentages of the viable cells by the succeeding equation:

Viable cells (%) = (*A* of treated cells / *A* of untreated cells) × 100.

Confocal Microscopy: Confocal laser scanning microscopic images were obtained from Leica TCS SP8 Confocal Microscope furnished with a 60× and 100× oil plan apochromatic objective. HeLa and A549 cells were individually seeded on a cover slip and developed in DMEM. Cells were fixed with 4% paraformaldehyde for 30 m and subjected to confocal fluorescence microscopic assay. Fixed cells were incubated with 2 μM concentration of MSQ or MSQRot for 10 m at 37°C in darkness and then washed twice with 1x PBS. The samples were incubated with 0.2 μM MitoTracker Green and placed in the dark for 15 m, and washed three times with 1x PBS. HeLa cells were then incubated for 15 m with DAPI. Afterward, washing by the same protocol, cells were mounted with antiquench agent *n*-propyl gallate for microscopic slide preparation and imaged by confocal microscope. Higher magnification confocal images were acquired from Leica microscope and were analyzed by Leica Application Suite X (LAS X) software. For DAPI: laser excitation wave length = 359 nm, emission wavelength = 461 nm, MitoTracker Green: laser excitation wave length = 490 nm, emission wavelength = 516 nm, For MSQ and MSQRot: laser excitation wave length = 645 nm, emission wavelength = 664 nm.

Determination of Pearson's Correlation Coefficient: Values of Pearson's correlation (PC) coefficient was obtained by comparing the confocal images of MSQRot or SQRot with MitoTracker Green (MTG). PC coefficients were determined by the examination of confocal micrographs with the LAS X software using Quantify tool. PC coefficient is one of the classic procedures (standard statistical analysis) in pattern recognition for matching one confocal

image (green channel designates MitoTracker Green staining) with another (red channel designates MSQRot or SQRot staining) and can be used to depict the extent of overlapping between two patterns in a dual-color image. To calculate PC for confocal images, all of the pixels having the same image coordinates were paired.

PC coefficient (R_r) was calculated (image consisting of red and green channels) according to the equation:

$$R_r = \frac{\sum_i (S1_i - S1_{avg}) * (S2_i - S2_{avg})}{[\sum_i (S1_i - S1_{avg})^2 * \sum_i (S2_i - S2_{avg})^2]^{(1/2)}}$$

S1 = signal intensity of pixels (pixel i) in the first (green) channel.

S2 = signal intensity of pixels (pixel i) in the second (red) channel.

$S1_{avg}$ = mean values of pixels in the first (green) channel.

$S2_{avg}$ = mean values of pixels in the second (red) channel.

The average pixel intensity ($S1_{avg}$) of an image was subtracted from the intensity of each pixel within the image (S1), and the value obtained for each pixel was multiplied by the value from the pixel's partner in the complement image ($S2–S2_{avg}$) to generate the product of the difference from the average. It was summed for the entire dataset and divided by the utmost probable sum of the product of the difference from the mean. PC is independent of signal levels and background because it subtracts the average intensity from each pixel's intensity value. PC coefficient was measured for colocalization area within the area foreground by LAS X software.

Concentration of MSQRot Inside the Mitochondria of HeLa Cells: To determine the concentration of MSQRot inside the mitochondria, HeLa cells were seeded in a 24 well plate and allowed to develop at 37°C for 24 h,

10% CO_2. The culture media was waste and fresh medium comprising 2 μM and 5 μM MSQRot was added and incubated at 37°C for 3 h to ensure adequate cellular uptakes. After discarding the media, the HeLa cells were washed with cold 1X PBS for three times. The cells were harvested with trypsin solution and taken in an eppendorf tube. The average cell number was determined by using Hemocytometer. The HeLa cells were then centrifuged for 5 min at 1400 rpm and the supernatant was waste to gather the cells as pellet. The centrifugation procedure was repeated (×2) with PBS and supernatant was discarded. Ripa lysis buffer (200 μL) was injected to the pellet of HeLa cells and paused for 30 min to confirm complete lysis. MeOH (200 μL) was inserted in the lysate and after centrifugation supernatant was collected and λ_{em} at 670 nm were recorded (λ_{ex} = 650 nm). Concentration of the MSQRot was calculated from the fluorescence vs concentration calibration curve. Primarily, fluorescence vs concentration calibration plot was obtained with known concentrations of MSQRot in a mixture of Ripa buffer:MeOH (1:1). Concentration of MSQRot inside the HeLa cells was measured by the following equation: Intracellular concentration = Cellular uptake (μmol) / (Cell number × Volume of the cell). The average size and average cell volume of the HeLa cells were measured as 20 μm and 4000 μm^3, respectively. Inner mitochondrial concentration of MSQRot in HeLa cells was determined using the following relation: Volume ratio of HeLa cell to the cell mitochondria as 0.06.

Accumulation of MSQRot molecules inside the mitochondria of HeLa cells were 1.3±0.3 mM and 4.2±0.6 mM than the original exterior concentration in the culture medium 2 μM and 5 μM, respectively, and it was determined by fluorescence spectroscopy.

Results and discussion

Design and synthesis of MSQRot and SQRot: We have designed and constructed an unsymmetrical 1,3,3- trimethylindoline SQ appended with triphenylphosphonium (TPP^+) functionality (MSQ) to target mitochondria (**Scheme 1**).[13] A screening inspection is carried out under MW conditions to optimize the yield of the hemisquarate intermediate (5) from diethyl squarate (**Table 3**).[14] Compound 5 is hydrolyzed with NaOH and treated with 2 under MW irradiation to obtain unsymmetrical SQ with one −COOH functionality (SQ-COOH) (**Table 4**). The SQ-COOH is further conjugated with a TPP^+ functionality to get MSQ. The MSQ (blue colored powder) is characterized by ^1H, ^{13}C NMR and high -resolution ESI-MS (**Figures 14, 15**).

Stability of MSQ Dye:

The absorption and emission of MSQ are observed in the NIR region (**Figure 23**). A cellular uptake and imaging assay was performed by a confocal laser scanning microscope on an epithelioid cervix carcinoma HeLa cell line. In the case of mitochondria targeting MSQ, we observed a weak NIR fluorescence signal inside the mitochondria [**Figure 24 a, b**].

We hypothesize that the MSQ is selectively incorporated inside the mitochondria; however, the chromophore is vulnerable to nucleophilic attack by the exposed Cys-containing mitochondrial proteins as well as mitochondrial GSH. This leads to a discontinuity in conjugation, and thus the NIR fluorescence of MSQ is dropped. To understand the fluorescence turn-off of MSQ by the nucleophilic attack of the −SH group, we used 2-mercaptoethanol with 1 equiv of Hunig's base in DMSO as well as GSH in mitochondrial pH 8.0 as model systems. We treated a DMSO/pH 8.0 buffer solution (1:10) of MSQ with GSH. Within a few minutes, the blue color of MSQ disappeared after

the addition of GSH or 2-mercaptoethanol. UV/vis and fluorescence titration of MSQ in the presence of GSH and 2-mercaptoethanol showed bleaching of the λ_{abs} as well as λ_{em} (**Figure 25**). The molecular docking of MSQ with Cys exposed mitochondrial protein ATP synthase subunit beta1(PDB: 4Q4L), and other SH-exposed proteins showed interactions between the SH moieties and MSQ [**Figure 26a**]. The encapsulation of MSQ dye inside a molecular container has been shown to greatly improve the MSQ chemical stability and also alter the fluorescence spectroscopic and microscopic properties.

Table 1. Synthesis of compound **1** under MW conditions in AcOH

Compound	Temperature (ºC)	Time (min)	Yield (%)
1	140	7	62
1	155	10	71
1	160	10	81

Table 2. Synthesis of compounds **2** and **4** under MW conditions in ACN

Compound	Temperature (ºC)	Time (min)	Yield (%)
2	110	7	52
2	140	7	71
2	140	10	92
4	110	7	55
4	140	7	75
4	140	10	94

Table 3. Synthesis of (*E*)-3-ethoxy-4-((1,3,3-trimethylindolin-2-ylidene) methyl) cyclobut-3-ene-1,2-dione (**5**) under MW method in EtOH/Et_3N

Compound	Temperature (ºC)	Time (min)	Yield (%)
5	80	30	52
5	90	40	67
5	90	45	73

Table 4. Synthesis of unsymmetrical SQ-COOH under MW conditions in Toluene : n-BuOH(1:1)

Compound	Temperature (ºC)	Time (min)	Yield (%)
SQ-COOH	110	1440	59
SQ-COOH	140	30	42
SQ-COOH	160	40	72
SQ-COOH	160	55	75

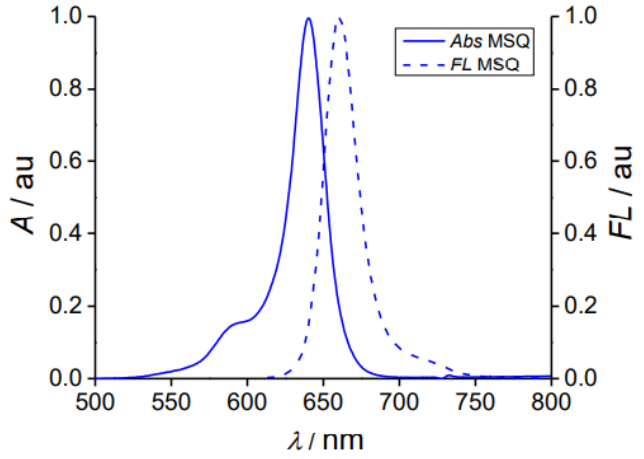

Figure 23. Normalized absorption and emission plot of MSQ (2 μM) in $CHCl_3$.

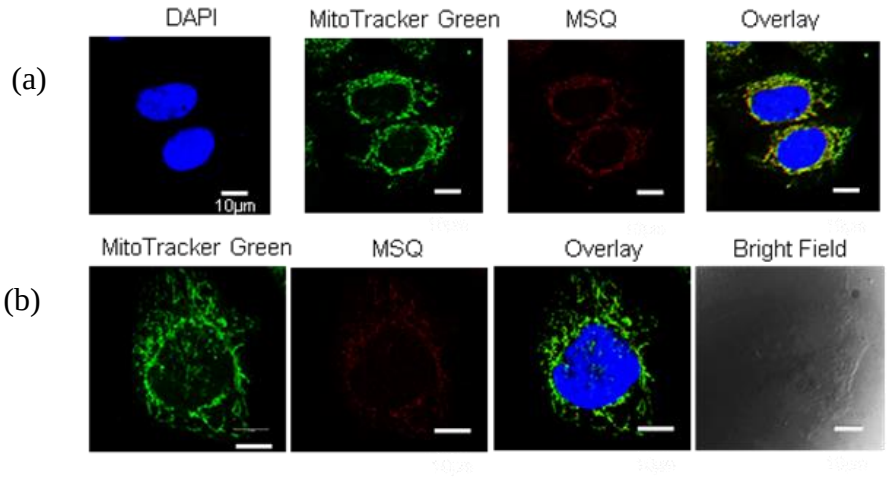

Figure 24. (a,b) Confocal microscopic images of MSQ colocalized with Mito Tracker Green (MTG) in fixed HeLa carcinoma cells. DAPI (blue channel), MTG (green channel), and MSQ (red channel) are recorded using laser excitation wavelengths at 359 nm, 490 nm, and 645 nm, respectively.

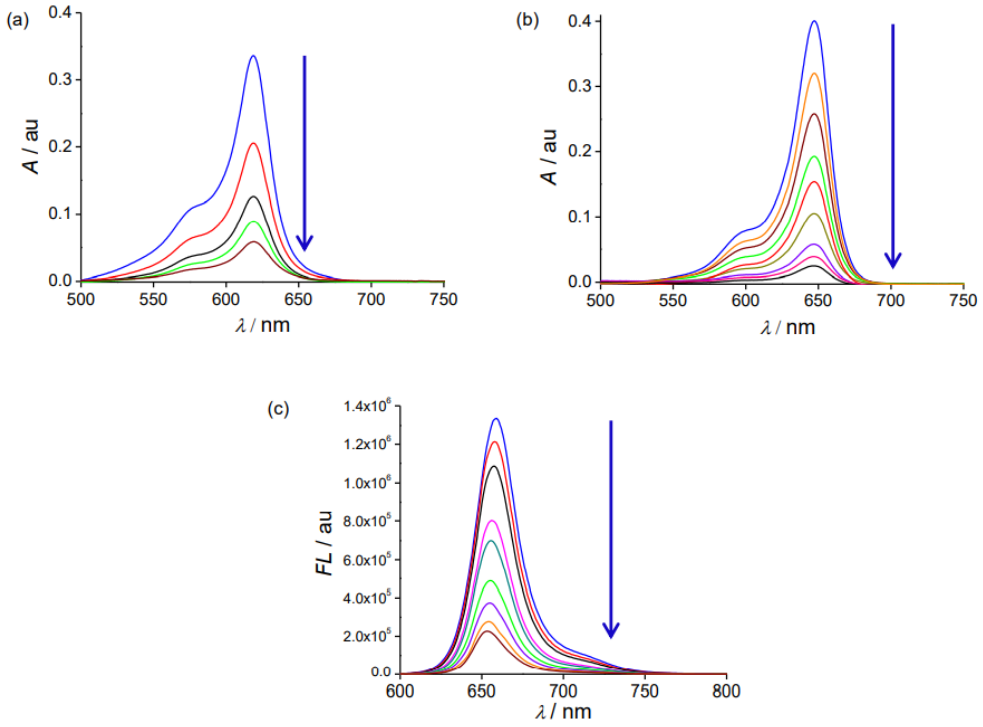

Figure 25. (a) Titration of MSQ (2 μM) in DMSO:pH 8.0 buffer solution (1:10) with GSH in mitochondrial pH 8.0. Decrease in absorption was observed on gradual addition of GSH solution. (b) UV/vis absorption plot of MSQ (2 μM, DMSO) titrated with 2-mercaptoethanol in DMSO in presence of Hunig's base. A gradual decrease in absorption was observed on sequential addition of 2-mercaptoethanol solution. (c) Fluorescence bleaching of MSQ (2 μM in DMSO) is noticed on progressive addition of 2-mercaptoethanol (2.5 μM) in presence of Hunig's base in DMSO.

(a)

(b)

(c)

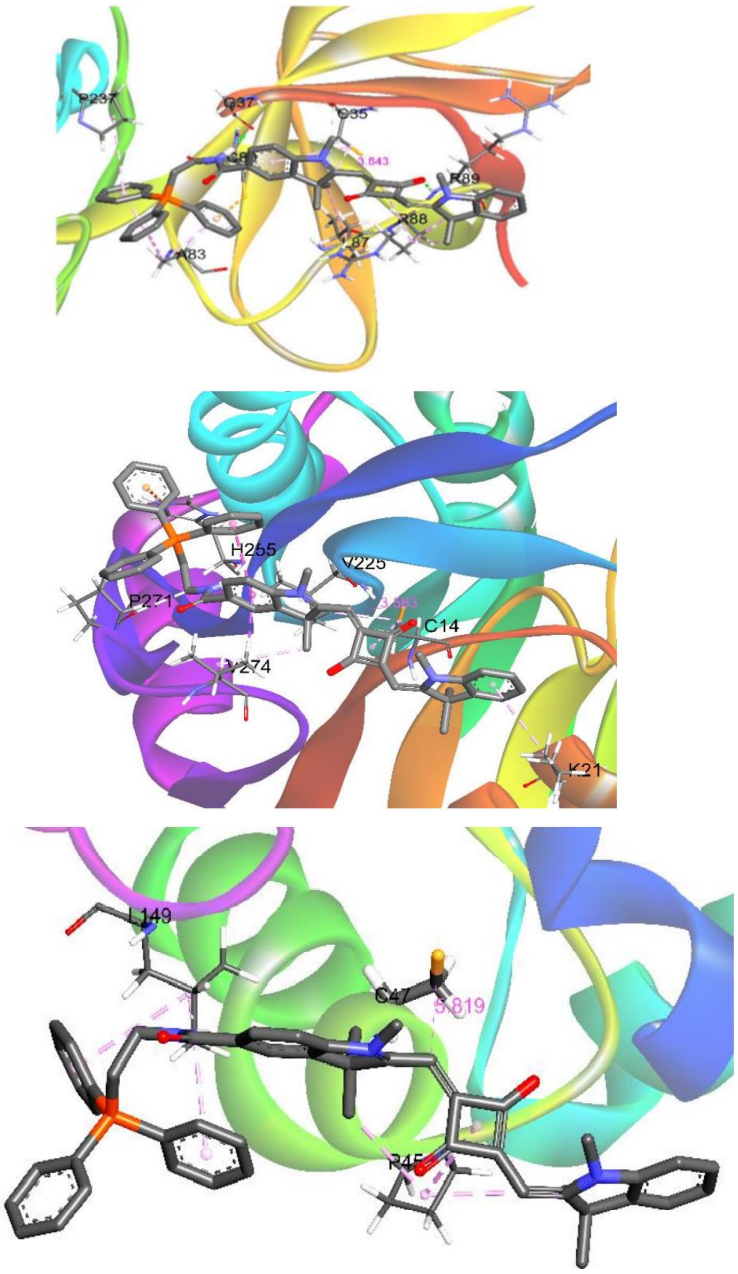

Figure 26. Docking poses of MSQ with the Cys exposed protein (a) ATP synthase subunit beta 1 (PDB: 4Q4L), (b) Nit2 (PDB: 4H5U), and (c) human peroxiredoxin 5 (PDB: 1H4O).

Synthesis of Unsymmetrical SQRot-COOH Using the MW-Assisted Solid-Phase Protocol on 2-CTC Resin and the Construction of MSQRot.

Herein the SQ-COOH molecule is loaded on a low-loading 2-chlorotrityl chloride (2-CTC) resin through −COOH.[15] Efforts to synthesize the rotaxane molecule through a direct slippage method in solution are ineffective. A template-directed clipping reaction on 2-CTC resin is used to transform SQ-COOH to SQRot-COOH under MW conditions (**Scheme 2**).[16] Most strikingly, the unwanted side products of the conventional synthesis, whose formation is the most major drawback of rotaxane construction, can be easily removed in the solid phase by following the washing steps with suitable solvents. Eventually, the desired rotaxane is obtained from the resin support. The SQRot-COOH is cleaved from the 2-CTC resin and further conjugated with TPP^+ functionality to obtain MSQRot (**Scheme 2**). Here MSQRot consists of an unsymmetrical SQ chromophore as an NIR imaging signaling unit tethered with a lipophilic cationic TPP^+ group to target mitochondria and a macrocycle to shelter and protect the chromophore from nucleophilic attack inside the mitochondria. The unsymmetrical MSQRot is acquired in satisfactory yield and is characterized by numerous spectroscopic techniques including NMR spectroscopy (**Figure 16, 17**) as well as high resolution ESI-MS. [**Figure 18a**]. MSQRot displays one ^{31}P NMR peak at 24.8 ppm for the TPP^+ group [**Figure 18b]**. A control symmetrical rotaxane (SQRot) lacking the TPP^+ moiety is also synthesized (**Scheme 3**). The changes in ^1H NMR chemical shifts caused by MSQRot formation have been compared with the free macrocycle and MSQ (**Scheme 1**). Most notable is the extreme downfield shift for macrocycle proton “C” and “NH” due to hydrogen bonding with SQ O atoms. Moreover, an upfield shift of

macrocyclic protons E and F is observed for rotaxane formation. For MSQRot, the anthracene residues of the macrocycle create anisotropic shielding zones for the 5,5′ (two well-separated singlet) protons of the MSQ, and hence an upfield shift in ^{1}H NMR is observed (**Figure 27**).

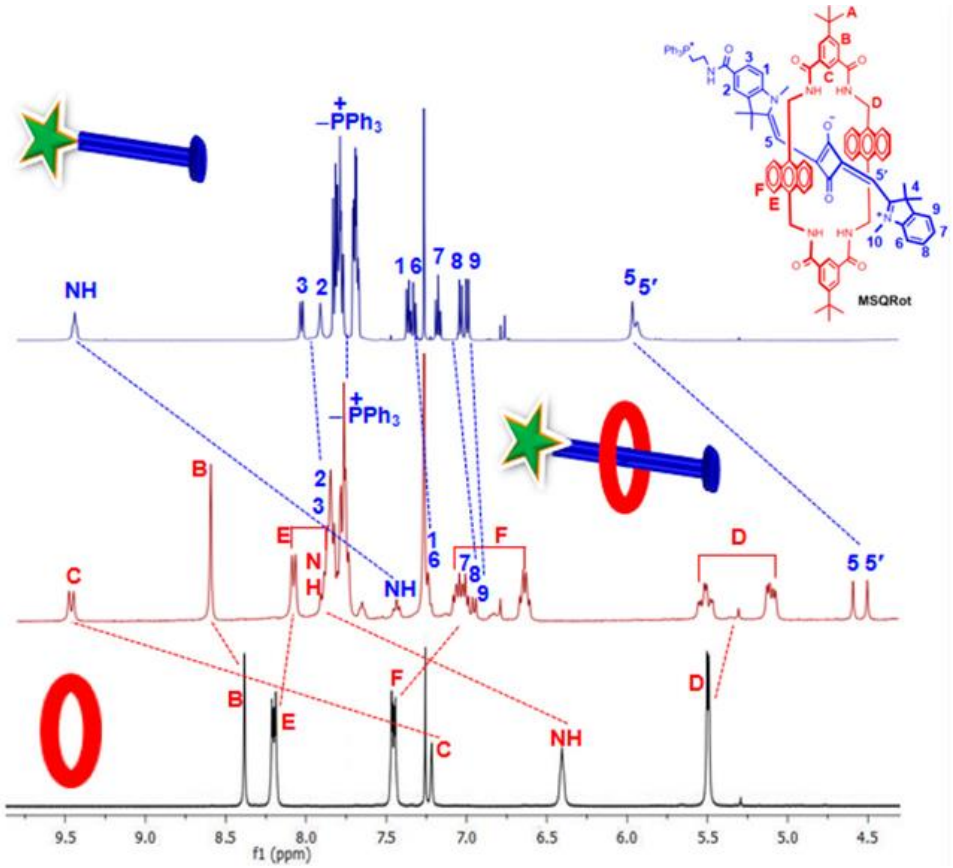

Figure 27. Partial ^{1}H NMR stacking of the free macrocycle, MSQRot, and MSQ in $CDCl_3$.

DFT Study and Single Crystal X-Ray Structure: The B3LYP/6-31+G** energy-minimized structure shows that the two 1,3,3-trimethylindolin rings of MSQ are in the *trans* configuration in the encapsulated form of MSQRot (**Figure 28**). Tetralactam N−H bonds and two C−H bonds of the phenyl ring of the macrocycle are forming hydrogen bonds with two O atoms of the C_4O_2 residue of MSQ. The central C_4O_2 core of MSQ, which is highly electron-deficient and sandwiched between the two electron-rich anthracene moieties (centroid-to-centroid, anthracene residues to C_4O_2 ring, distance is 3.9 Å), is stabilized through a D−A−D-type interaction and thus is expected to block nucleophilic attacks.

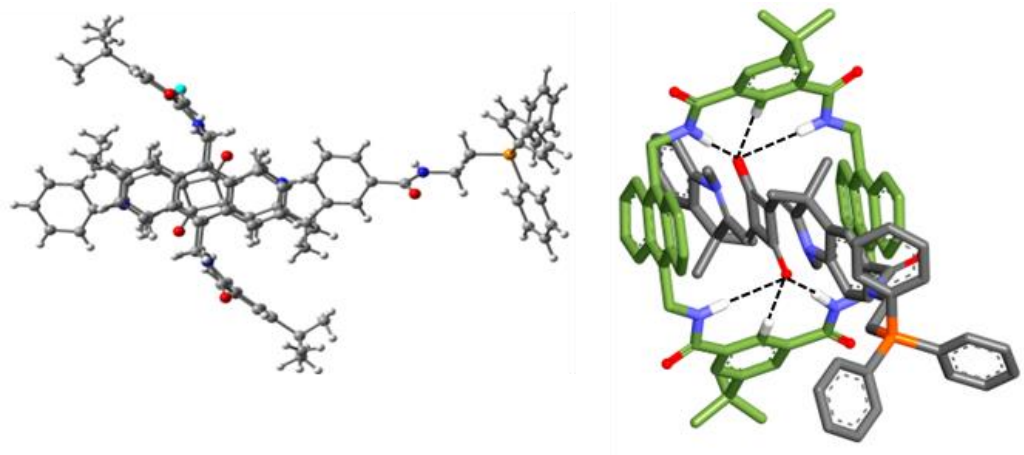

Figure 28. B3LYP/6-31+G** energy-minimized structure of MSQRot.

We are fortunate to obtain the single-crystal X-ray structure of the control symmetrical SQRot molecule lacking the TPP^+ group, which also exhibited a *trans* orientation similar to that of the N-methyl indoline residues (**Figure 29**). Four N−H bonds and two phenyl C−H bonds of the macrocycle are forming hydrogen bonds with SQ O atoms (N−H···O as well as C−H···O hydrogen-

bond distance is ca. 2.3 Å). The C_4O_2 core is also forming D−A−D-type interactions with two anthracene residues (D−A distance 3.7 Å) in SQRot. The centroid-to-centroid distance between the anthracene residues and the C_4O_2 core is 3.7 Å.

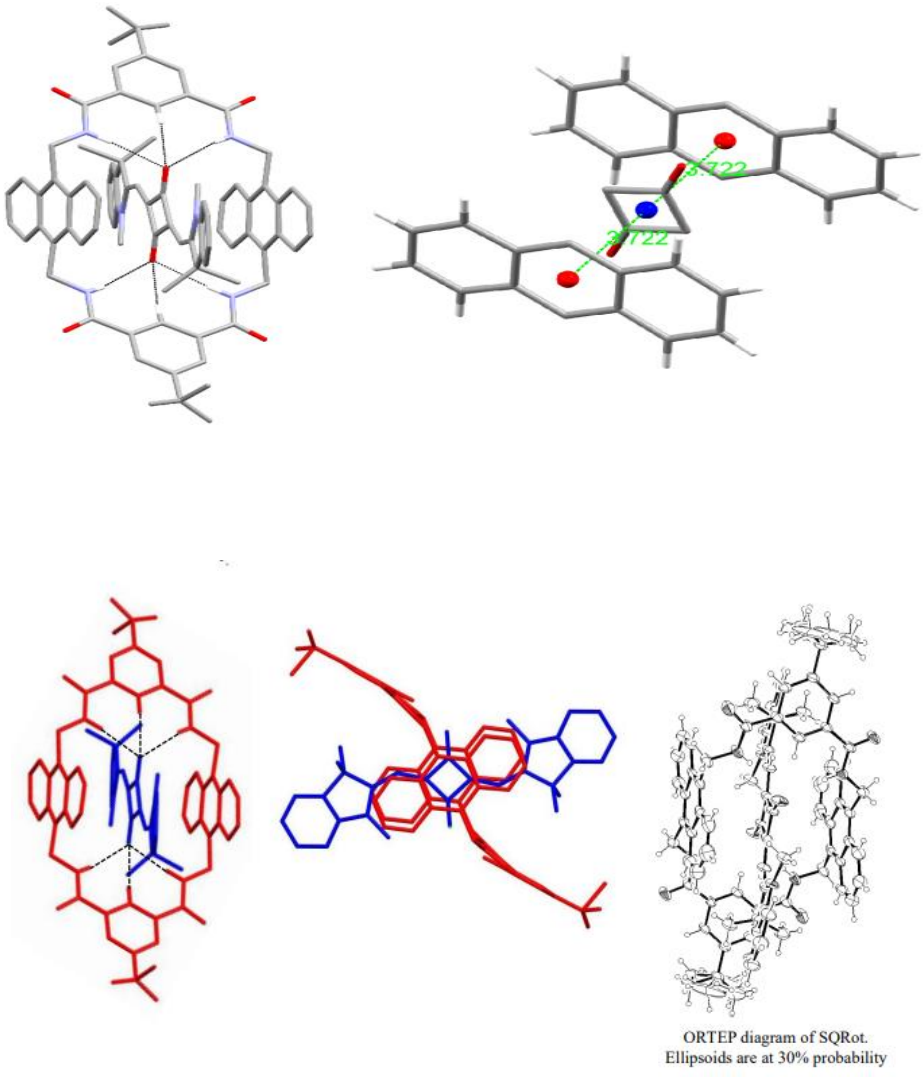

Figure 29. Single-crystal X-ray structure of control SQRot.

Photophysical Study: The λ_{abs} and λ_{em} of MSQRot show a characteristic bathochromic shift ca. 12 nm from the original spectra of MSQ in $CHCl_3$ **[Figure 30 a, b]**. The absorption spectra of unsymmetrical MSQRot revealed an intense peak (λ_{max}) at 652 nm in $CHCl_3$ with a large molarextinction coefficient of 1.5 × 105 M^{-1} cm^{-1} (**Table 5**). The λ_{em} of MSQRot is observed to be 670 nm in $CHCl_3$. There is a 3.5-fold augmentation in the MSQRot quantum yield [$(\Phi_f)_{MSQRot}$ = 0.53] in comparison with MSQ [$(\Phi_f)_{MSQ}$ =0.15] in DMSO, which is due to the reduced rotational and vibrational motions of the entrapped MSQ and because the consequent nonradiative excited-state relaxation pathways are the least feasible.[17] The anthracene fluorescence at λ_{ex} 365 nm becomes weaker for MSQRot formation in comparison with the free macrocycle due to FRET from anthracene to the trapped MSQ (**Figure 31**).

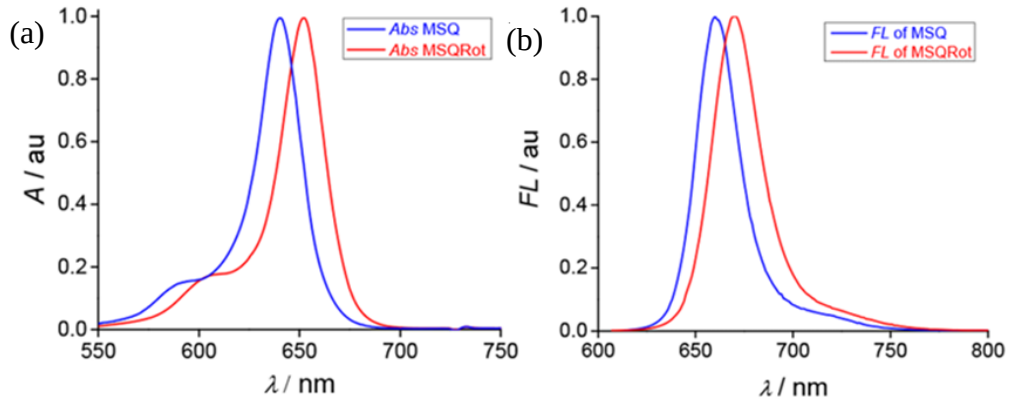

Figure 30. (a) Normalized absorption plot of MSQ (2 μM) and MSQRot (2 μM) in $CHCl_3$. (b) Normalized fluorescence plot of MSQ (2 μM) and MSQRot (2 μM) in $CHCl_3$. Absorption and emission plots showing the bathochromic shift for rotaxane formation.

Table 5. Photophysical data of MSQ and MSQRot in $CHCl_3$

Compound	Solvent	λ_{abs} (nm)	λ_{em} (nm)	Stoke shift ($\Delta\lambda$)	$\varepsilon \times 10^5$ ($M^{-1}\,cm^{-1}$)
MSQ	$CHCl_3$	640	659	19	2.26
MSQRot	$CHCl_3$	652	670	18	1.50

ε = molar extinction coefficient, λ_{abs} = absorption maximum wavelength, λ_{em} = emission maximum wavelength.

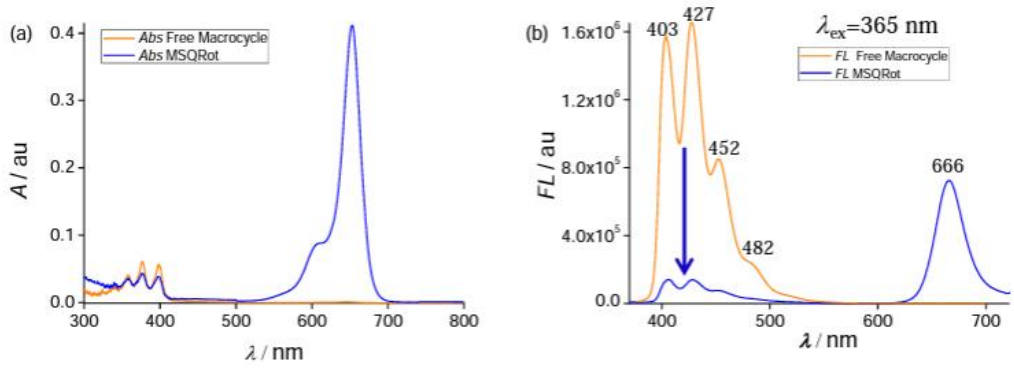

Figure 31. (a) Absorption plot of free macrocycle and MSQRot in DMSO. (b) Fluorescence plot of free macrocycle and MSQRot in DMSO (λ_{ex} 365 nm). A significant decrease in fluorescence intensity of anthracene moiety in DMSO with increase fluorescence emission of MSQ was observed within interlocked MSQRot structure which indicates efficient fluorescence energy transfer from excited macrocycle to MSQ of MSQRot in solution.

Biocompatibility and Cell Viability:

Dethreading could be a potential drawback of rotaxane located inside the subcellular organelles.[18] ^1H NMR studies in $CDCl_3$ at 37 °C for 2 days showed no dissociation of the MSQ from MSQRot. The mechanical stability of MSQRot is also investigated by absorption/emission spectroscopy in $CHCl_3$.There is no evidence of MSQRot dethreading after 48 h at 37°C.

This confirmed that the gem-dimethyl and N-methyl groups in 1,3,3-trimethylindoline residues and the TPP^+ groupare bulky enough to prevent MSQRot dethreading. The plausible biological interference from GSH at mitochondrial pH 8 at 37 °C is inspected over 48 h. No significant emission changes in MSQRot are perceived in GSH at pH 8 (**Figure 32**). Cell viability studies show that the MSQRot is less toxic to HeLa carcinoma and the noncancerous HEK293 cell line (**Figure 33**). The outstanding biocompatibility, insignificant cytotoxicity, narrow NIR absorption/emission band, and high quantum yield further make the MSQRot a smart choice for organelle staining.

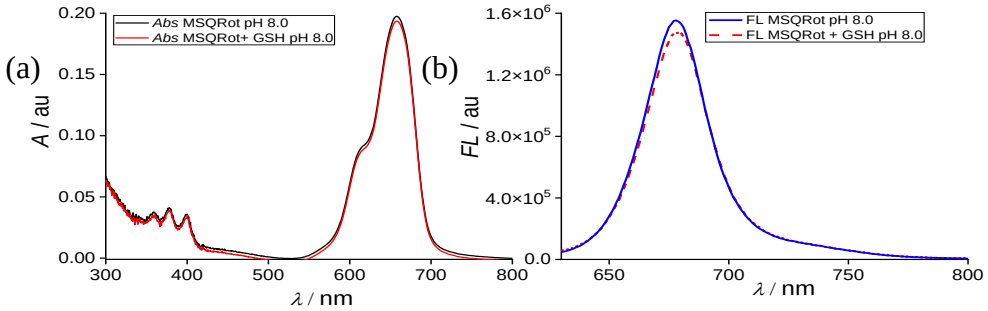

Figure 32: (a) Absorption plot of MSQRot (2 μM) and after the addition of 20 μM GSH solution in mitochondrial pH 8.0, 37°C, 48 h. (b) Fluorescence spectra of MSQRot (2 μM) and in presence of 20 μM GSH (pH 8.0, 37°C, 48 h). No significant changes in absorption and fluorescence intensities are observed when MSQRot solution is titrated with GSH in mitochondrial pH 8.0 over 48 h at 37°C.

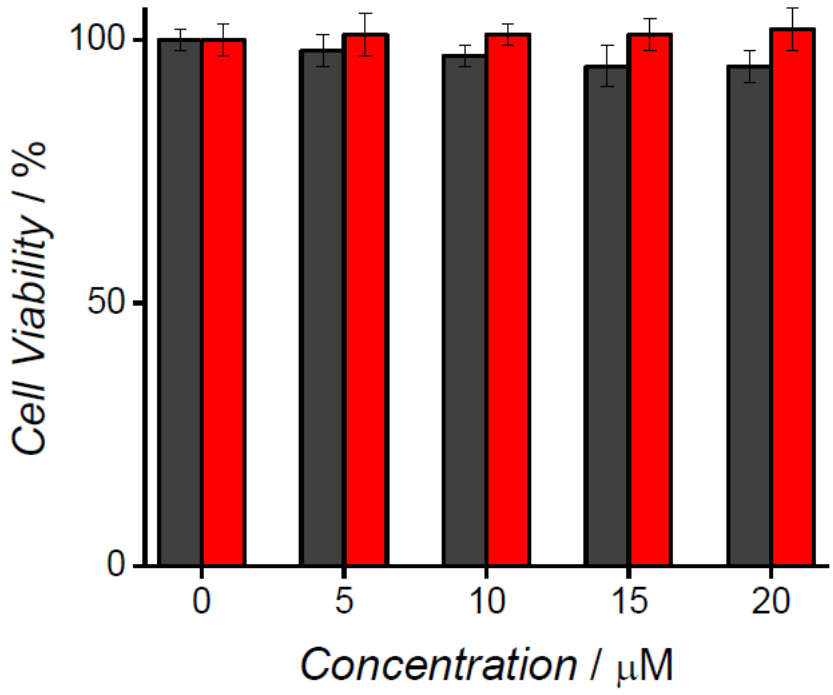

Figure 33. Cell viability of HeLa carcenoma cell line (red) and healthy human embryonic kidney (HEK293) cell line (grey) incubated with different doses (5, 10, 15, and 20 μM per well) of MSQRot for 24 hours.

Confocal Laser Scanning Microscopic Study:

To confirm the mitochondrial selectivity, a colocalization test involving MSQRot is executed in HeLa and A549 carcinoma cells with a mitochondria specific marker, MitoTracker Green (MTG). The MSQRot displayed decent colocalization with MTG in the confocal microscopy with a Pearson's correlation (PC) coefficient of 0.89 for HeLa and 0.85 for A549 (**Figures 34, 35**).

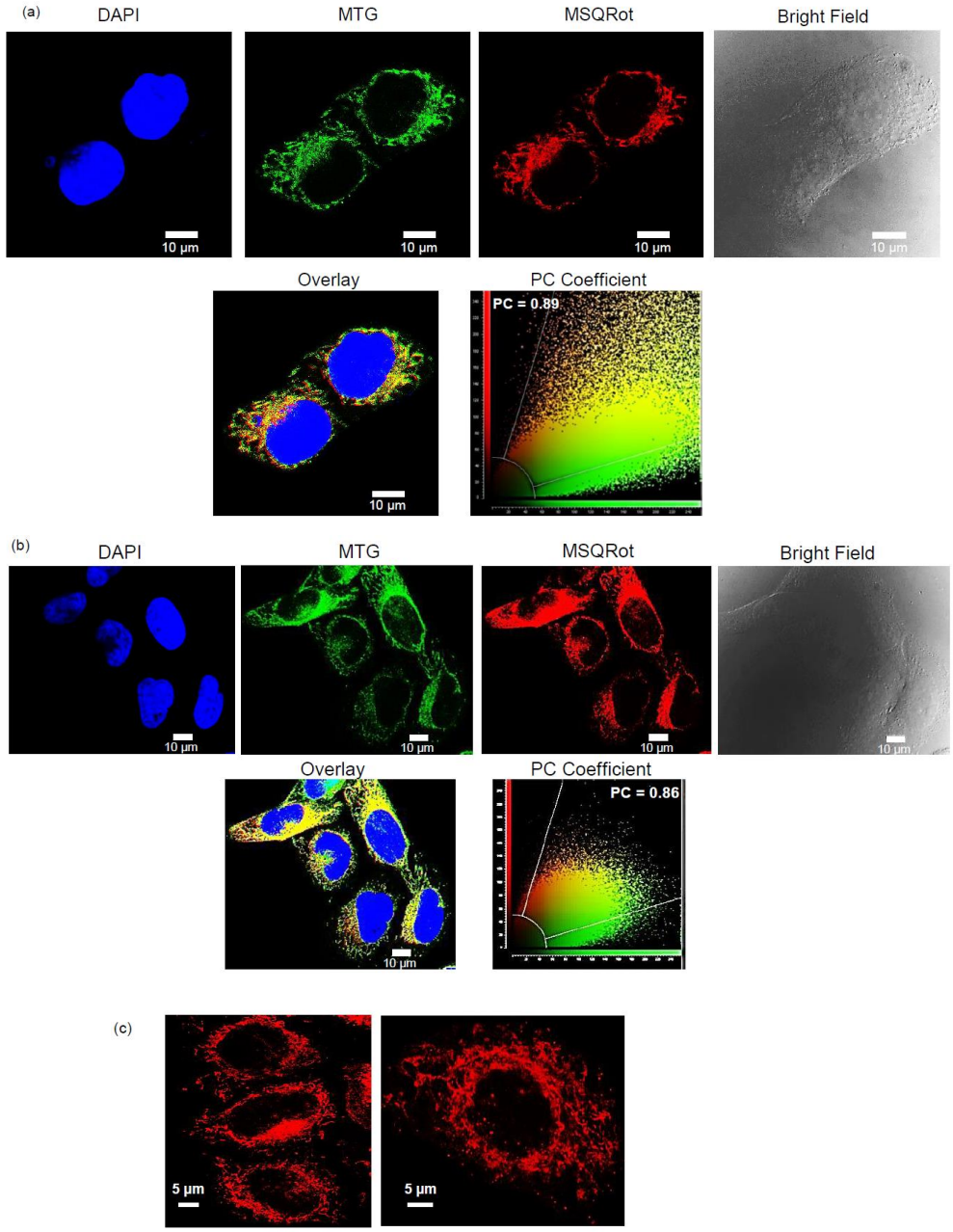

Figure 34. (a,b) Confocal microscopic images of MSQRot colocalized with MitoTracker Green (MTG) in fixed HeLa carcinoma cells. DAPI (blue channel), MTG (green channel), and MSQRot (red channel) are recorded using

laser excitation wavelengths at 359 nm, 490 nm, and 645 nm, respectively. Colocalization scatter plot displays Pearson's correlation (PC) coefficient: (a) 0.89 and (b) 0.86. (c) Confocal images at higher magnification (100× oil plan apochromatic objective) of fixed HeLa cells treated with MSQRot.

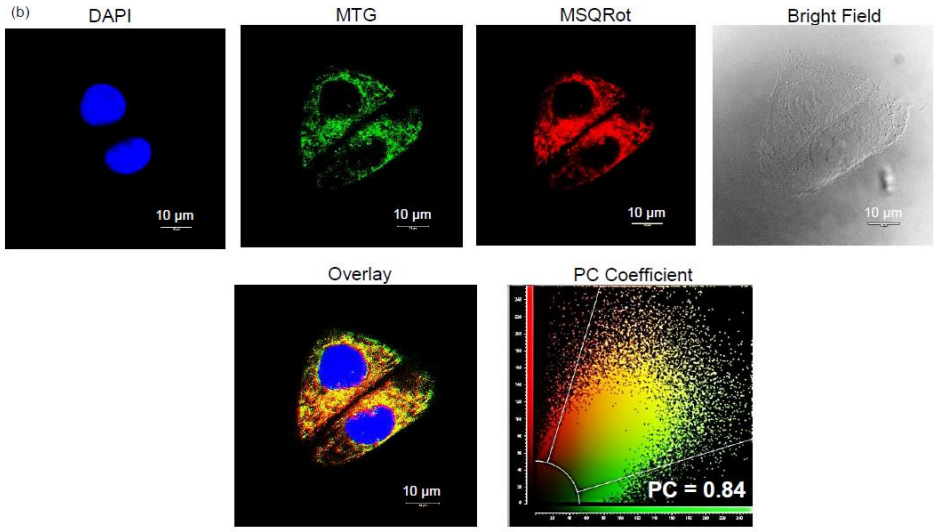

Figure 35. (a,b) Confocal images of MSQRot colocalized with MTG in lung adenocarcinoma A549 cells. Colocalization scatter plot displays PC coefficient: (a) 0.85 and (b) 0.84.

Accumulation of MSQRot inside the mitochondria:

The accumulation of MSQRot in the mitochondria is anticipated to be 500−1000 times greater than that in the extracellular region due to the potential gradient ($\Delta\Psi_m$ −150 to −180 mV vs plasma membrane potential −30 to −60 mV). The inner mitochondrial concentrations of MSQRot in HeLa cells are determined by fluorescence analysis to be 1.3 ± 0.3 mM and 4.2 ± 0.6 mM, which are greater than the original exterior concentrations of 2 and 5 µM, respectively (**Figure 36**).

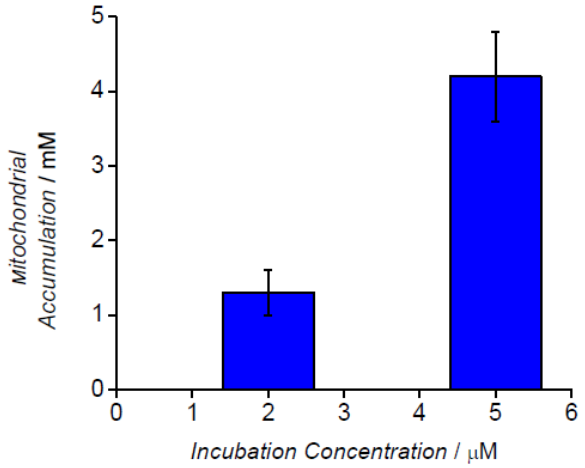

Figure 36. Concentrations of MSQRot inside the mitochondria of HeLa cells with respect to the original exterior concentrations of 2 μM and 5 μM, respectively.

Mitochondrial Target Selectivity of MSQRot vs Control Symmetrical Molecule SQRot:

The mitochondrial target selectivity of MSQRot is compared with a control symmetrical SQRot lacking the TPP^+ functionality. SQRot stains inside the A549 cells; however, confocal images show that it is poorly colocalized with mitochondria tracker MTG (Figure 37). So, TPP^+ group is required to target mitochondria.

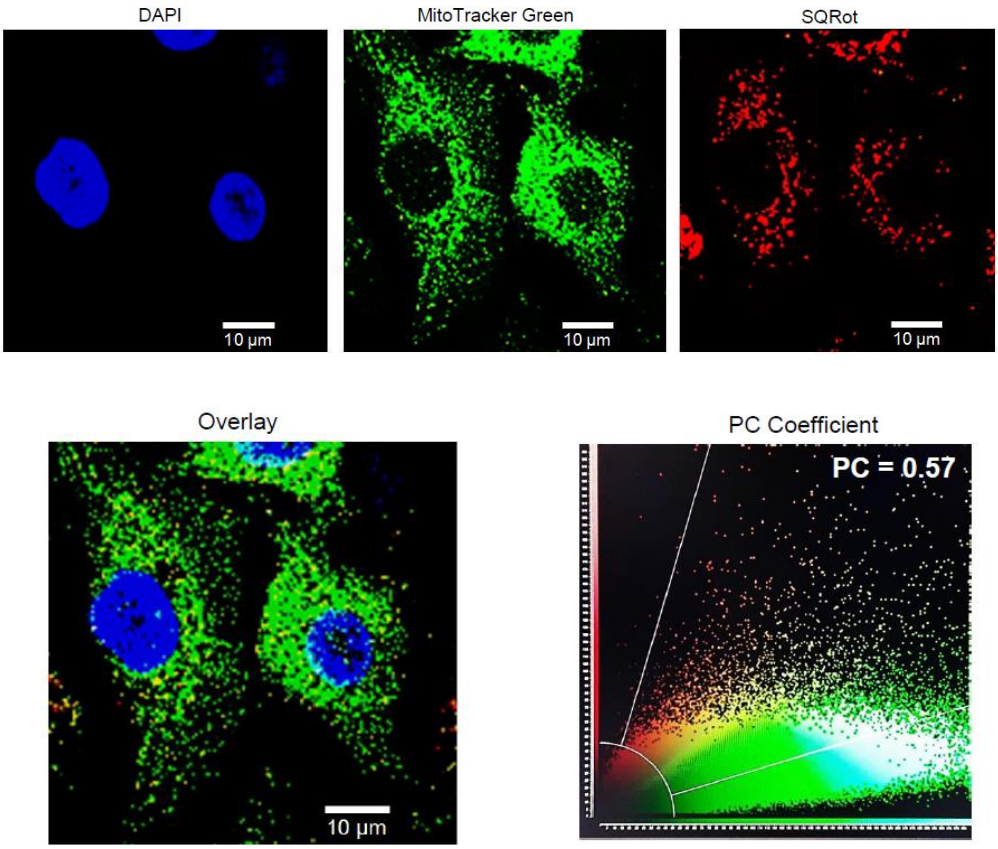

Figure 37. Confocal microscopic images of control symmetrical SQRot molecule colocalized with MitoTracker Green in A549 carcinoma cells. SQRot dye stains inside the A549 cells and is confined to small punctate compartments; however, overlay image indicates that it is poorly colocalized with mitochondria tracker MTG. Colocalization scatter plot shows PC coefficient: 0.57.

Cartesian coordinates and total energies (Hartrees) of B3LYP/6-31+G** energy minimized structure of MSQ (**Figure 38**).

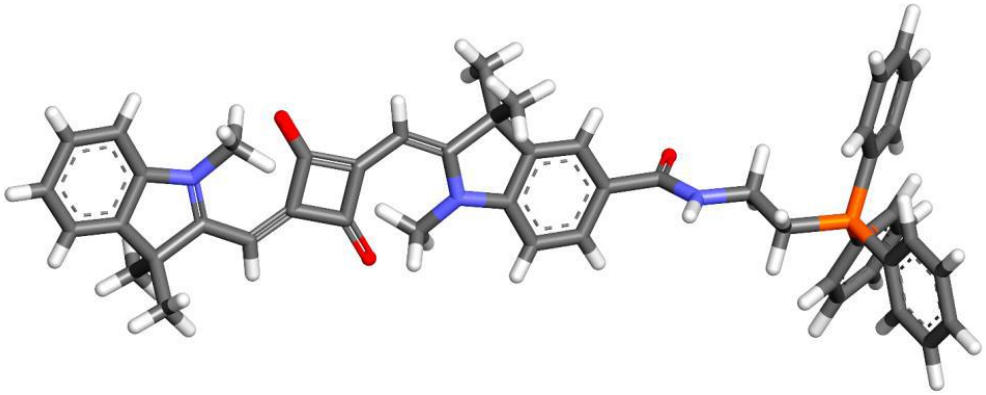

Figure 38: B3LYP/6-31+G** energy minimized structure of MSQ.

FASTA sequence of

ATP synthase subunit beta 1

MAHHHHHHMGTLEAQTQGPGSMSTAALVEGKIVQ**C**IGAVIDVEFPRES
MPKIYDALILEGSELTLEVQQQLGDGVVRTI**C**LGASDGLRRGVVVKNT
GNPISVPVGKPTLGRIMDVLGRPIDEAGPIESENKRSIHQKAPAFDELSPS
TELLETGIKVIDLI**C**PFAKGGKVGLFGGAGVGKTVNMMELINNIAKEH
GGYSVFAGVGERTREGNDFYHEMKDSNVLDKVALVYGQMNEPPGNL
RVALTGLTMAEHFRDEGLDVLFFVDNIYRFTLAGTEVSALLGRMPSAV
GYQPTLAEEMGKLQERITSTKKGSITSVQAVYVPADDLTDPSPATTFGH
LDATVVLSRDIASLGIYPAVDPLDSTSRQIDPNVIGEEHYSITRRVQQTL
QRYKELRDIIAILGMDELSPEDKLSVARARKIQRFLSQPFHVAEVFTGSP
GKYVPLKETIRGFKMI VDGE**C**DHLPEQAFYMVGTIDEAFEKAKKIQ.

ATP synthase subunit beta 1 contains Cys35, Cys80, Cys162, and Cys460 residues.

Nit2

MGSSHHHHHHSSGLVPRGSHMASMTGGQQMGRGSMTSKLKRVAVAQ
L**C**SSADLTKNLKVVKELISEAIQKKADVVFLPEASDYLSQNPLHSRYLA
QKSPKFIRQLQSSITDLVRDNSRNIDVSIGVHLPPSEQDLLEGNDRVRNV
LLYIDHEGKILQEYQKLHLFDVDVPNGPILKESKSVQPGKAIPDIIESPLG
KLGSAI**C**YDIRFPEFSLKLRSMGAEIL**C**FPSAFTIKTGEAHWELLGRARA
VDTQ**C**YVLMPGQVGMHDLSDPEWEKQSHMSAL.

human peroxiredoxin 5 proteins

APIKVGDAIPAVEVFEGEPGNKVNLAELFKGKKGVLFGVPGAFTPG**C**S
KTHLPGFVEQAEALKAKGVQVVA**C**LSVNDAFVTGEWGRAHKAEGKV
RLLADPTGAFGKETDLLLDDSLVSIFGNRRLKRFSMVVQDGIVKALNV
EPDGTGLT**C**SLAPNIISQL

Conclusions: In summary, the macrocycle gives shelter and protects the MSQ dye from nucleophilic attack inside the mitochondria. This rotaxane molecule can be functionalized to target specific cellular organelles. MSQRot with an appended targeting TPP^+ group could be an effective molecular probe for mitochondrial therapy with NIR imaging diagnostics.

REFERENCES:

[1] (a) Zhu, H.; Fan, J.; Du, J.; Peng, X. *Acc. Chem. Res*. **2016**, *49*, 2115−2126. (b) Wang, L.; Frei, M. S.; Salim, A.; Johnsson, K. *J. Am. Chem. Soc*. **2019**, *141*, 2770−2781.

[2] (a) Yan, R.; Hu, Y.; Liu, F.; Wei, S.; Fang, D.; Shuhendler, A. J.;Liu, H.; Chen, H.-Y.; Ye, D. *J. Am. Chem. Soc*. **2019**, *141*, 10331−10341.

(b) Ducharme, G. T.; LaCasse, Z.; Sheth, T.; Nesterova, I. V.; Nesterov, E. E. *Angew. Chem., Int. Ed*. **2020**, *59*, 8440−8444.

[3] Liew, S. S.; Qin, X.; Zhou, J.; Li, L.; Huang, W.; Yao, S. Q. *Angew. Chem., Int. Ed.* **2020**, DOI: 10.1002/anie.201915826.

[4] Babu, P. S. S.; Manu, P. M.; Dhanya, T. J.; Tapas, P.; Meera, R. N.; Surendran, A.; Aneesh, K. A.; Vadakkancheril, S. J.; Ramaiah, D.; Nair, S. A.; Pillai, M. R. *Sci. Rep*. **2017**, *7*, 42126.

[5] (a) Hewage, H. S.; Anslyn, E. V. *J. Am. Chem. Soc*. **2009**, *131*,13099−13106.

(b) Arunkumar, E.; Forbes, C. C.; Noll, B. C.; Smith, B. D. *J. Am. Chem. Soc.* **2005**, *127*, 3288−3289.

(c) Anees, P.; Sreejith, S.; Ajayaghosh, A. *J. Am. Chem. Soc*. **2014**, *136*, 13233−13239

[6] Chen, H.; Farahat, M. S.; Law, K.-Y.; Whitten, D. G. *J. Am. Chem. Soc*. **1996**, *118*, 2584−2594.

[7] (a) Stoddart, J. F. *Angew. Chem., Int. Ed*. **2017**, *56*, 11094−11125.

(b) Craig, M. R.; Hutchings, M. G.; Claridge, T. D. W.; Anderson, H. L. *Angew. Chem., Int. Ed.* **2001**, *40*, 1071−1074.

(c) Lee, S.; Chen, C.-H.; Flood, A. H. *Nat. Chem.* **2013**, *5*, 704−710.

[8] (a) Johnson, J. R.; Fu, N.; Arunkumar, E.; Leevy, W. M.; Gammon, S. T.; Piwnica-Worms, D.; Smith, B. D. *Angew. Chem., Int. Ed*. **2007**, *46*, 5528−5531.

(b) Jarvis, T. S.; Collins, C. G.; Dempsey, J. M.; Oliver, A. G.; Smith, B. D. *J. Org. Chem.* **2017**, *82*, 5819−5825.

(c) Gassensmith, J. J.; Arunkumar, E.; Barr, L.; Baumes, J. M.; DiVittorio, K. M.; Johnson, J. R.; Noll, B. C.; Smith, B. D. *J. Am. Chem. Soc*. **2007**, *129*, 15054−15059.

[9] Sheldrick, G. M. *Acta Cryst.*, **2015,** *A71*, 3–8.

[10] Sheldrick, G. M. *Acta Cryst.*, **2015,** *C71*, 3–8.

[11] Dolomanov, O. V.; Bourhis, L. J.; Gildea, R. J.; Howard, J. A. K.; Puschmann, H. *J. Appl. Cryst.*, **2009,** *42*, 339–341.

[12] Frisch, M. J.; Trucks, G. W.; Schlegel, H. B.; Scuseria, G. E.; Robb, M. A.; Cheeseman, J. R.; Scalmani, G.; Barone, V.; Mennucci, B.; Petersson, G. A. et al. Gaussian 09W Revision D.01, Gaussian, Inc., Wallingford CT, USA, **2009**.

[13] Zielonka, J.; Joseph, J.; Sikora, A.; Hardy, M.; Ouari, O.; Vasquez-Vivar, J.; Cheng, G.; Lopez, M.; Kalyanaraman, B. *Chem. Rev.* **2017**, *117*, 10043−10120.

[14] Barbero, N.; Magistris, C.; Park, J.; Saccone, D.; Quagliotto, P.; Buscaino, R.; Medana, C.; Barolo, C.; Viscardi, G. *Org. Lett*. **2015**, *17*, 3306−3309.

[15] López-Macià, A.; Jiménez, J. C.; Royo, M.; Giralt, E.; Albericio, F. *J. Am. Chem. Soc.* **2001**, *123*, 11398−11401.

[16] Leigh, D. A.; Murphy, A.; Smart, J. P.; Slawin, A. M. Z. *Angew.Chem., Int. Ed. Engl*. **1997**, *36*, 728−732.

[17] Collins, C. G.; Baumes, J. M.; Smith, B. D. *Chem. Commun*. **2011**, *47*, 12352−12354.

[18] Carrasco-Ruiz, A.; Tiburcio, J. *Org. Lett*. **2015**, *17*, 1858−1861.

Chapter 4

Construction of Red Fluorescent Dual Targeting Mechanically Interlocked Molecules for Live Cancer Cell Specific Lysosomal Staining and Multicolor Cellular Imaging

Introduction:

Development of red fluorescent mechanically interlocked molecules for active targeting of live cancer cells followed by selective internalization and imaging of malignant organelles are important with respect to visible and other fluorescent biomarkers.[1−5] Red and NIR lights (650−900 nm) have deep tissue permeation with low background and autofluorescence signals from endogenous biomolecules, which offers an effective method for high-performance live cell imaging.[6−9] Certain receptors are overexpressed at the tumor site such as $\alpha_v\beta_3$ integrin, and it is imperative to design suitable ligands to target those receptors through molecular recognition.[10−12] Among the various intracellular organelles, lysosomes are the key target for all malignant cells.[13−15] Lysosomes are the membrane-bound cellular organelles with low pH 4−5.They encompass a variety of degradable enzymes and are liable for the disruption of nucleic acids, lipids, proteins, etc. as well as being responsible for exocytosis.[16,17] Abnormalities in lysosomes are accountable for lysosomal storage disorders, neurodegenerative diseases, and cancer.[18−21] Explicit targeting and tracking of cancer cell lysosomes are the crucial stages for the early diagnosis and development of drugs for cancer.[22−24] Nevertheless, it is challenging to develop lysosome targeting probes for cancer cells due to the complexity in live carcinoma cell milieu. The present live cancer cell lysosome targeting probes have substantial boundaries, like less target selectivity, lower and broad excitation/emission bands, low brightness inside the acidic lysosome, and cytotoxicity.[25−27] Squaraines (SQ) are a class of organic dyes with narrow and intense red and NIR absorption/emission bands. SQ dyes have been used in photodynamic and photothermal therapies, chemosensors, low band gap polymers, optoelectronic, stimuli responsive materials, photovoltaics, and

nonlinear optics.[28,29] However, compared to other probes, SQ dyes have been less explored in live cell organelle targeted imaging. We envisage that the electron deficient central cyclobutene ring of the squarylium (SQ) chromophore could be vulnerable for nucleophilic attack inside the live carcinoma cell lysosomes; hence, fluorescence might be bleached once LysoSQ dye accumulates in the lysosome.[30,31] Furthermore, SQ dyes have a tendency to form aggregates, which lead to noteworthy broadening of their absorption/ emission bands inside the live cell organelles.[32,33] These are the probable drawbacks for the construction of SQ-based lysosomal staining agent. We hypothesize that the encapsulation of LysoSQ inside a macrocycle to form rotaxane which is stabilized by a noncovalent interaction might be a master plan to improve probe performance inside the malignant lysosomes.[34–37] Smith et al. have made pioneering contributions for the construction of squaraine rotaxane.[38,39] However, the synthesis of cancer cell specific lysosome targeting water-soluble unsymmetrical red emissive trimethylindoline squaraine rotaxane LysoSQRot-$(RGDS)_2$ is a difficult job. The synthesized alkyne-containing rotaxanes SSQRot2-$(Alkyne)_2$ and LysoSQRot2-$(Alkyne)_2$ are conjugated with cancer cell specific azide functionalized RGDS peptide (N_3-RGDS) by click chemistry using copper(I) catalyzed azide-alkyne cycloaddition (CuAAC) on the Wang resin to develop red emissive rotaxane/RGDS conjugate SSQRot-$(RGDS)_2$ and LysoSQRot-$(RGDS)_2$.[40] This solid phase method on the Wang resin allows for easy purification with high yields of rotaxane/RGDS conjugates. The rotaxane based dye molecules have fascinating topological features; however, their live cancer cell selective organelle targeted imaging properties are rarely exploited. The molecule LysoSQRot-$(RGDS)_2$ has four distinctive structural features: (a) an unsymmetrical SQ chromophore for red fluorescence imaging, (b) a macrocycle to provide shelter and shield the SQ

probe from nucleophilic attack inside the lysosomes, (c) two RGDS peptides conjugated at the macrocycle through solid phase click chemistry to enhance the water solubility and to target $\alpha_V\beta_3$ integrin which is overexpressed at the tumor site, and (d) morpholine functionality tethered at the SQ axle to target malignant lysosomes. Active targeting of live cancer cells followed by selective internalization and staining of malignant lysosomes by LysoSQRot-$(RGDS)_2$ is demonstrated using confocal laser scanning microscopy (CLSM) and compared with control rotaxane molecules. Real-time monitoring of live cancer cell lysosomes as well as 3D and multicolor cellular imaging are also achieved. To the best of our knowledge, this is the first report of a water-soluble, red fluorescent, biocompatible, dual targeting mechanically interlocked probe LysoSQRot-$(RGDS)_2$ where cancer cell specific RGDS peptide is conjugated at the macrocycle and lysosome targeting morpholine functionality is tethered at the axle for active targeting of live cancer cells followed by selective internalization and imaging of malignant lysosomes along with real-time tracking and 3D and multicolor cellular imaging applications.

Experimental Methods

General Methods and Materials

Synthesis, Purification, and Characterization of Symmetrical and Unsymmetrical Squaraine Rotaxane Molecules:

Herein, we have designed and synthesized an unsymmetrical 1,3,3-trimethylindoline SQ dye tethered with morpholine component (LysoSQ) which are characterized by innumerable spectroscopic techniques (**Figures 1−4**). 5-(prop-2-yn-1-yloxy)isophthalic acid has been synthesized starting from 5-hydroxy isophthalic acid and Characterized by NMR (**Figures 5-9**). The

USQ-COOH is conjugated with lysosome targeting morpholine functionality using the amide coupling protocol to obtain LysoSQ in good yield (**Scheme 1**). Using the clipping approach and high dilution, synthesize the Macrocycle 1 and Macrocycle 2-Alkyne (**Scheme 2**). Efforts to construct rotaxane molecule LysoSQRot2-(Alkyne)$_2$ by a direct slippage method using LysoSQ and Macrocycle 2-Alkyne were ineffective, perhaps due to the steric bulk of the dimethyl substituents in indoline residues of LysoSQ. A template-directed clipping reaction is utilized to synthesize rotaxane molecules SSQRot1 (**Scheme 3**), SSQRot2-(Alkyne)$_2$ (**Scheme 4**), and LysoSQRot2-(Alkyne)$_2$ (**Scheme 4**). which are characterized by innumerable spectroscopic techniques (**Figures 10−24**). We got the single-crystal X-ray structure of unsymmetrical SQ with a -COOH group (USQ-COOH) (**Figures 25a, Table 1**). The single-crystal X-ray structures confirm the formation of Macrocycle 2-Alkyne as well as SSQRot1 and SSQRot2-(Alkyne)$_2$ rotaxane molecules (**Figures 25b, 26a, 26b, and Table 1**).

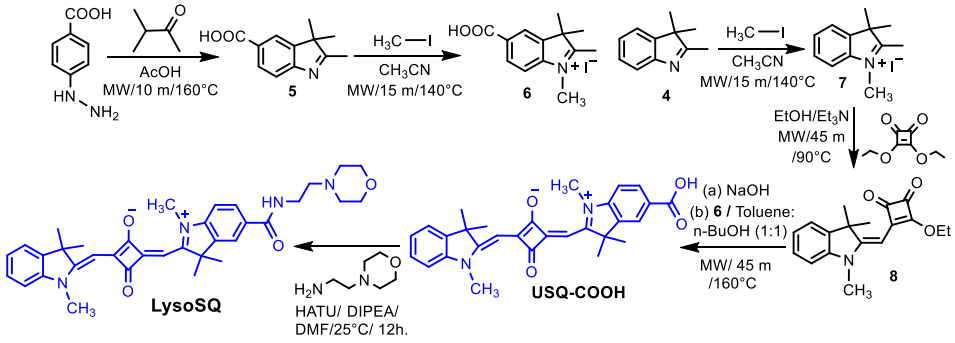

Scheme 1: Synthesis of unsymmetrical SQ dye USQ-COOH and LysoSQ.

The synthetic procedure and characterizations of compounds 5, 6, and 8 are reported in Chapter 3.

Synthesis of unsymmetrical squaraine USQ-COOH: The hydrolyzed product of **8** (0.37 mg, 1.37 mmol) and compound **6** (0.47 g, 1.37 mmol) were taken in a MW vessel containing a 1:1 *v*/*v* mixture of n-BuOH (2 mL) and toluene (2 mL), which was sealed and heated in a MW system at 160ºC for 45 min. Then the reaction mixture was cooled to room temperature. Deep blue colored solution was concentrated under reduced pressure and the crude compound was purified by 5% MeOH/DCM (R_f = 0.3) to obtain a deep blue colored pure solid USQ-COOH. Yield: 0.47 g (1.37 mmol).

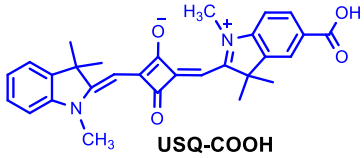

USQ-COOH

^{1}H NMR (300 MHz, DMSO-d_6, 25°C): δ = 12.79 (1H, s), 8.01 (1H, s), 7.98 (1H, d, J = 8.1 Hz), 7.60 (1H, d, J = 7.2 Hz), 7.48–7.43 (2H, m), 7.37 (1H, d, J = 8.4 Hz), 7.27 (1H, t, J = 6.3 Hz), 5.90 (1H, s), 5.80 (1H, s), 3.69 (3H, s), 3.58 (3H, s), and 1.74 (12H, s) ppm.^{13}C NMR (75 MHz, DMSO-d_6, 25°C): δ = 181.6, 180.4, 176.6, 171.4, 167.6, 166.9, 142.2, 141.4, 129.9, 127.7, 124.1, 122.6, 121.9, 110.7, 108.9, 87.2, 48.8, 47.4, 30.6, 26.3, and 25.8 ppm.

We have the single crystal X-ray structure of **USQ-COOH** molecule

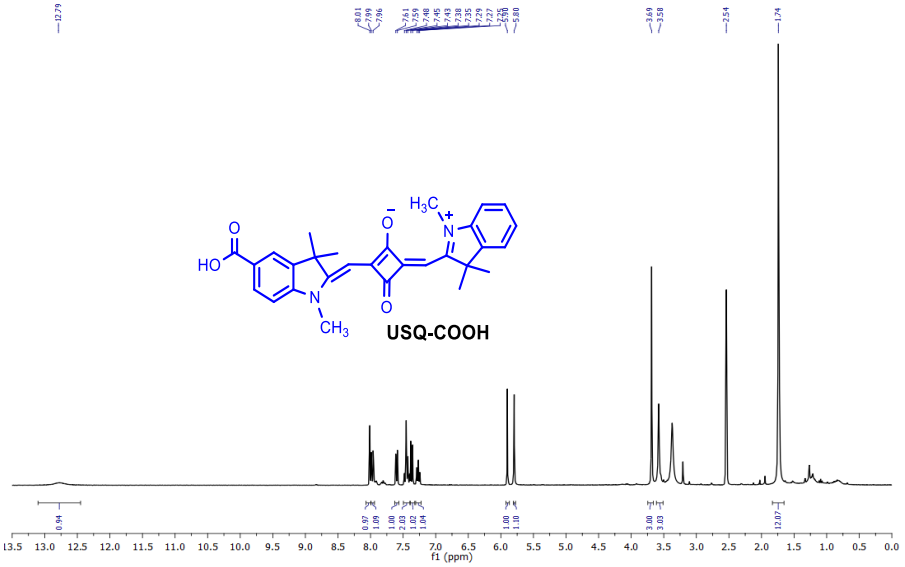

Figure 1: ^{1}H NMR (300 MHz, DMSO-d_6, 25°C) spectrum of USQ-COOH.

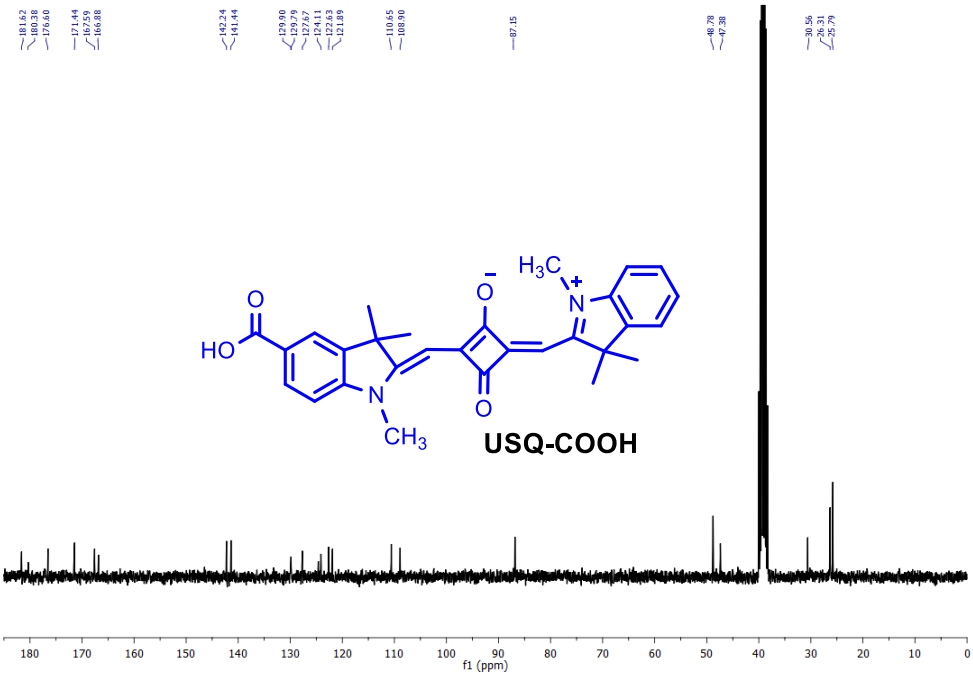

Figure 2: ^{13}C NMR (75 MHz, DMSO-d_6, 25°C) spectrum of USQ-COOH.

Synthesis of LysoSQ: The compound USQ-COOH (0.4 g, 0.85 mmol), HATU (0.35 g, 0.93 mmol) was dissolved in DMF (5 mL) followed by DIPEA (600 µL) was added to the reaction mixture and stirred for 15 min at 0°C. Then 4-(2-Aminoethyl) morpholine (122 µL, 0.93 mmol) was added and stirred for 12 hr at room temperature. The reaction mixture was extracted with DCM (3×100 mL), the combined organic layer was dried using Na_2SO_4 and concentrated under reduced pressure to acquire the crude compound. The crude material was subjected to column chromatography by 3% MeOH/DCM (R_f =0.4) to get a deep blue coloured solid product LysoSQ.

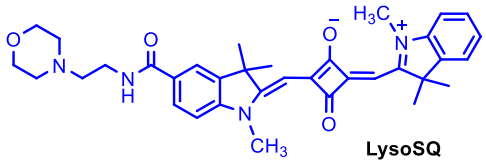

LysoSQ

Yield: 0.43 g (87%).

^{1}H NMR (300 MHz, $CDCl_3$, 25°C): δ = 7.80 (1H, s), 7.76 (1H, d, J = 9.9 Hz), 7.40-7.34 (2H, m), 7.22 (1H, t, J = 7.5 Hz), 7.08 (1H, d, J = 8.1 Hz), 6.99 (1H, d, J = 8.4 Hz), 6.87 (1H, t, J = 4.8 Hz), 6.01 (1H, s), 5.96 (1H, s), 3.78-3.75 (4H, m), 3.66 (3H, s), 3.61-3.57 (2H, m), 3.52 (3H, s), 2.66 (2H, t, J = 6.1 Hz), 2.57-2.54 (4H, m), and 1.79 (12H, s) ppm.

^{13}C NMR (75 MHz, $CDCl_3$, 25°C): δ = 182.3, 178.6, 172.6, 169.4, 167.0, 145.7, 142.8, 142.1, 139.3, 135.9, 130.9, 129.3, 128.8, 128.0, 127.3, 124.5, 122.3, 121.3, 114.1, 109.8, 108.3, 87.7, 87.4, 66.9, 65.6, 57.1, 53.4, 49.7, 48.6, 36.1, 34.3, 31.9, 30.3, 29.7, 27.2, and 26.9 ppm.

HRMS (ESI +ve) *m/z*: Observed for $C_{35}H_{40}N_4O_4$ $[M]^+$ = 580.3041, $[M]^+$ calcd = 580.3050.Photophysical properties in DMSO λ_{abs}= 633 nm, λ_{em}= 647 nm, Stokes shift ($\Delta\lambda$) = 14 nm, ε = 1.70 ×10^5 $M^{-1}cm^{-1}$, Φ_f = 0.21 in DMSO (Φ_f of Zinc phthalocyanine as reference = 0.20 in DMSO).

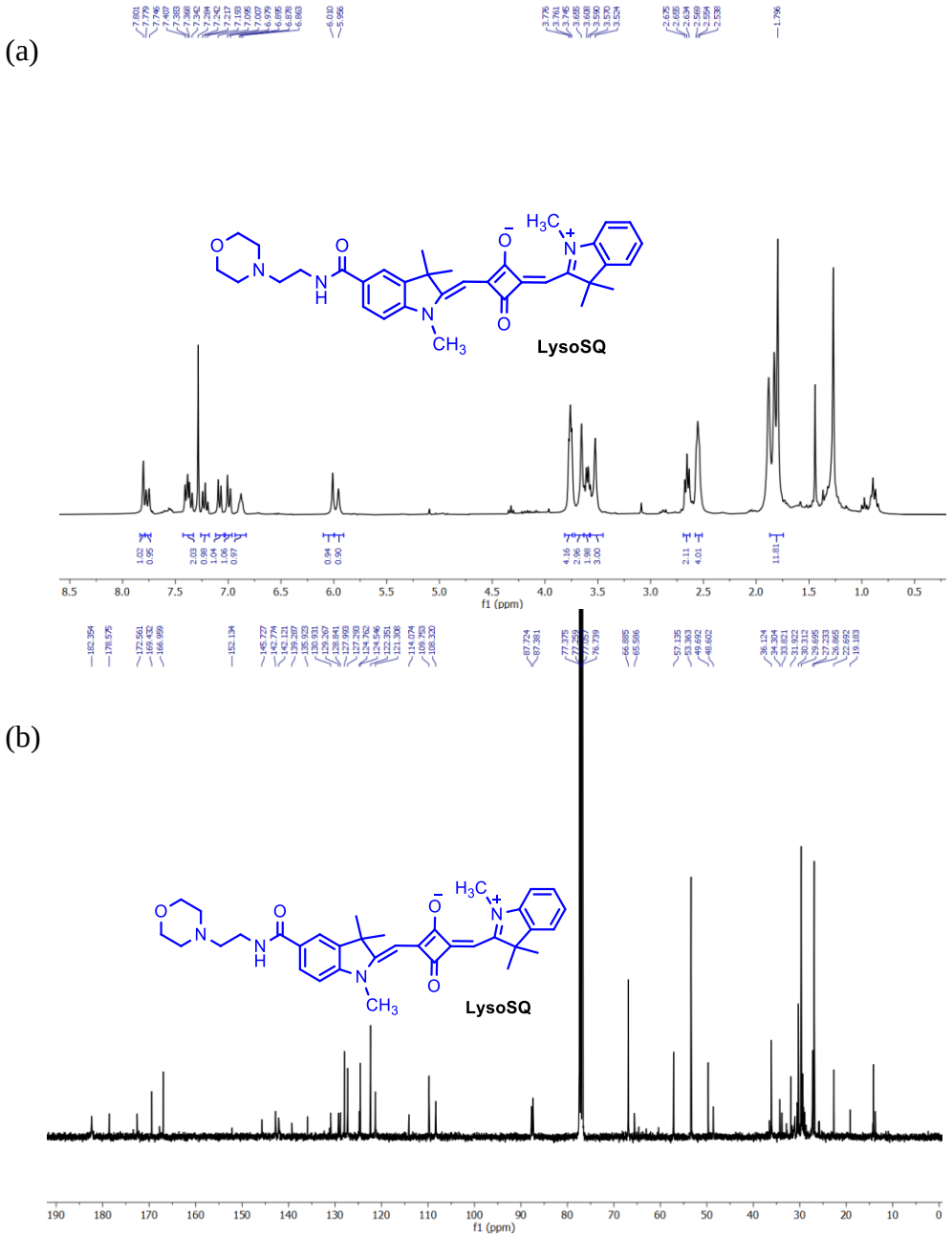

Figure 3. (a) ^{1}H NMR (300 MHz, $CDCl_3$, 25°C) spectrum of LysoSQ (b) ^{13}C NMR (75 MHz, $CDCl_3$, 25°C) spectrum of LysoSQ.

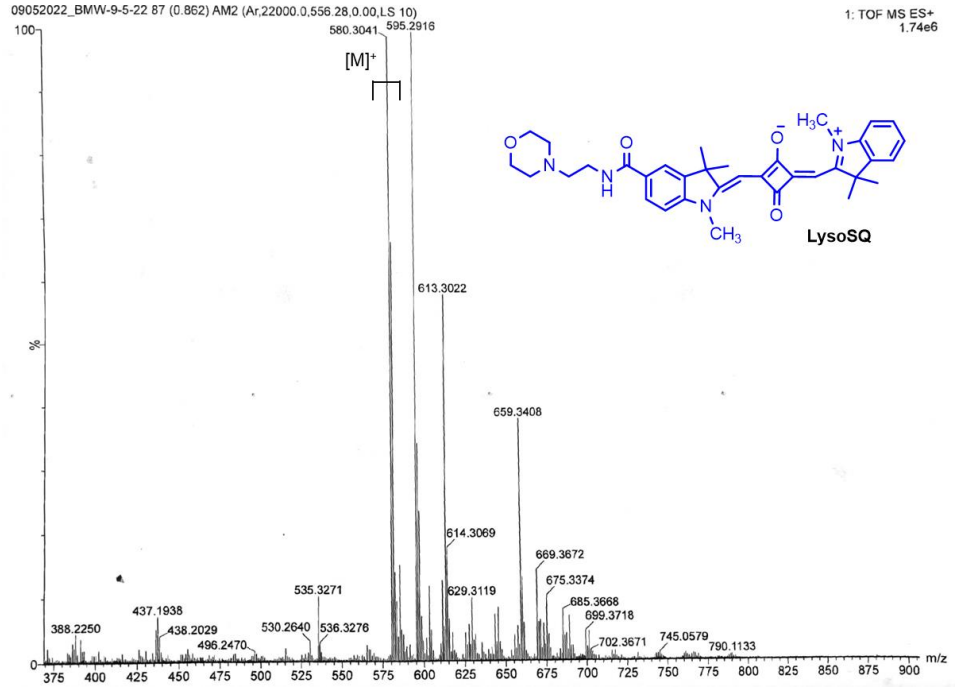

Figure 4. HRMS (ESI +ve) spectrum of **LysoSQ**.

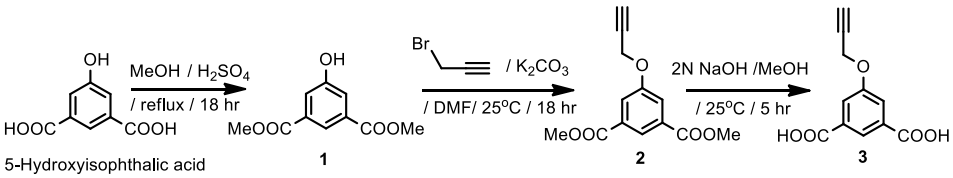

Synthesis of dimethyl 5-hydroxyisophthalate (1): 5-Hydroxyisophthalic acid (5.47 g, 30 mmol) was dissolved in MeOH (100 mL) and conc. H_2SO_4 (5 mL) was added slowly. The resulting reaction mixture was refluxed for 18 hr using an oil bath. A clear solution was obtained which was cooled to room temperature and poured in ice-cold water (300 mL). White precipitates were formed which was filtered, washed several times with H_2O and dried under vacuum to obtain the pure product **1** as a white solid.

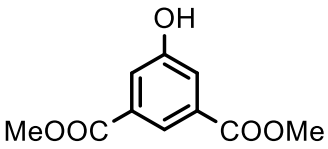

1

Yield: 5.68 g (90%)**.** ^{1}H NMR (300 MHz, DMSO-d_6, 25°C): δ =10.34 (1H, s), 7.95 (1H, s), 7.57 (2H, s), and 3.87 (6H, s) ppm.^{13}C NMR (75 MHz, DMSO-d_6, 25°C): δ = 165.8, 158.3, 131.8, 120.9, 120.6, and 52.8 ppm.

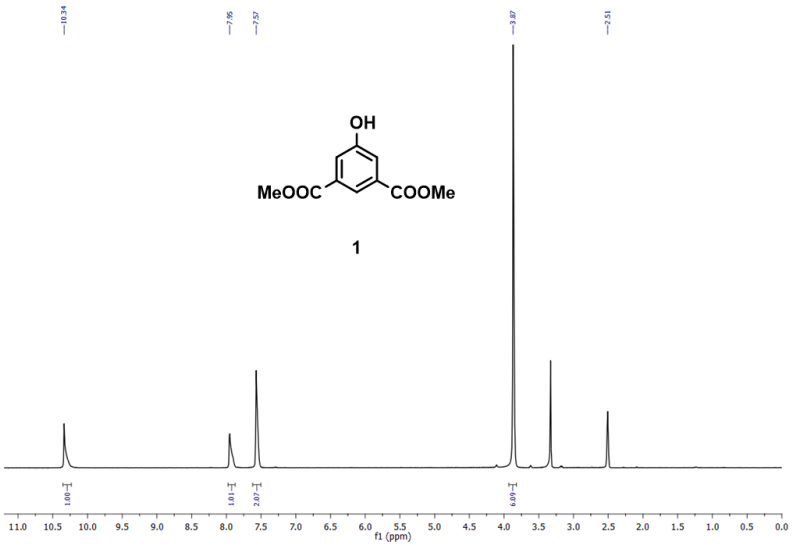

Figure 5. ^{1}H NMR (300 MHz, DMSO-d_6, 25°C) spectrum of compound 1.

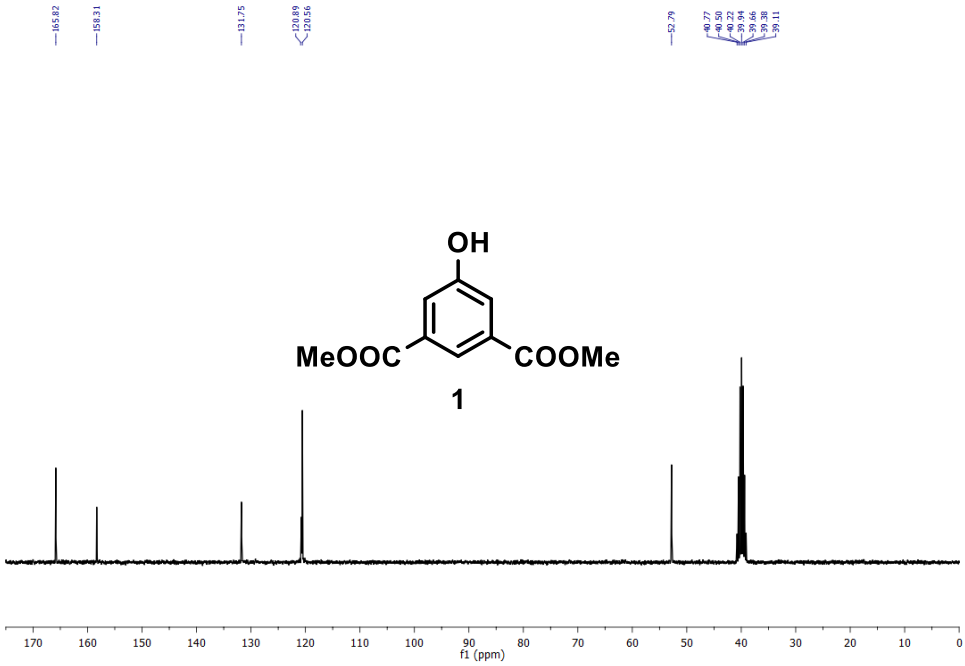

Figure 6. ^{13}C NMR (75 MHz, DMSO-d_6, 25°C) spectrum of 1.

Synthesis of dimethyl 5-(prop-2-yn-1-yloxy)isophthalate (2): Dimethyl-5-hydroxyisophthalate (4.2 g, 20 mmol) and K_2CO_3 (4.14 g, 30 mmol) were dissolved in anhydrous DMF (40 mL). Propargyl bromide (80% in toluene) (3 mL, 40 mmol) was added drop-wise to the reaction mixture over 10 min. The reaction mixture was stirred at 25°C for 18 hr under N_2 atmosphere. Then the reaction mixture was poured into ice-cold H_2O (200 mL). A white precipitate was obtained. It was filtered and washed H_2O (5×) to acquire the pure compound **2** as a white solid. Yield: 4.21 g (85%).

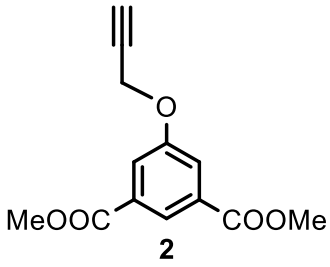

^{1}H NMR (300 MHz, $CDCl_3$, 25°C): δ = 8.32 (1H, s), 7.83 (2H, s), 4.80 (2H, s), 25°C): δ = 165.9, 157.5, 131.9, 123.8, 120.3, 77.6, 76.3, 56.2, and 52.5 ppm.

(a)

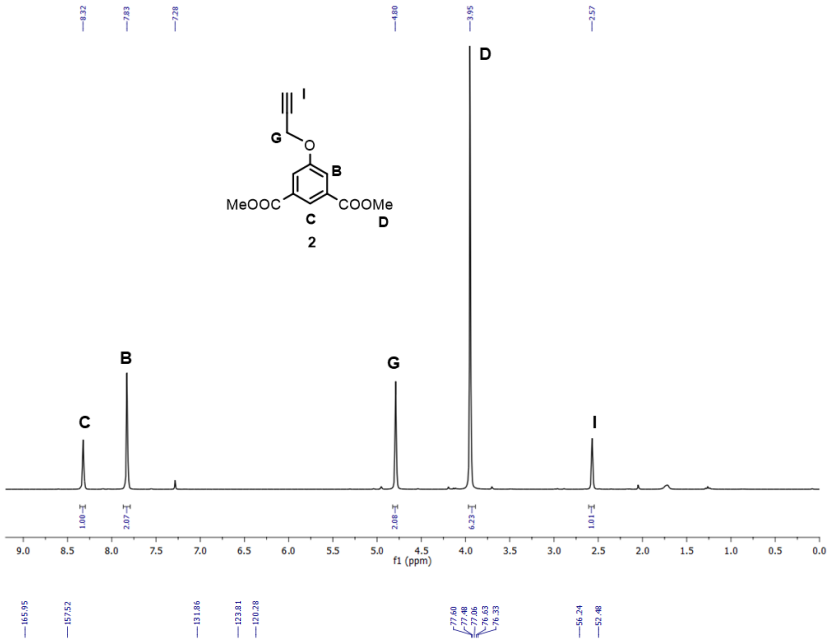

(b)

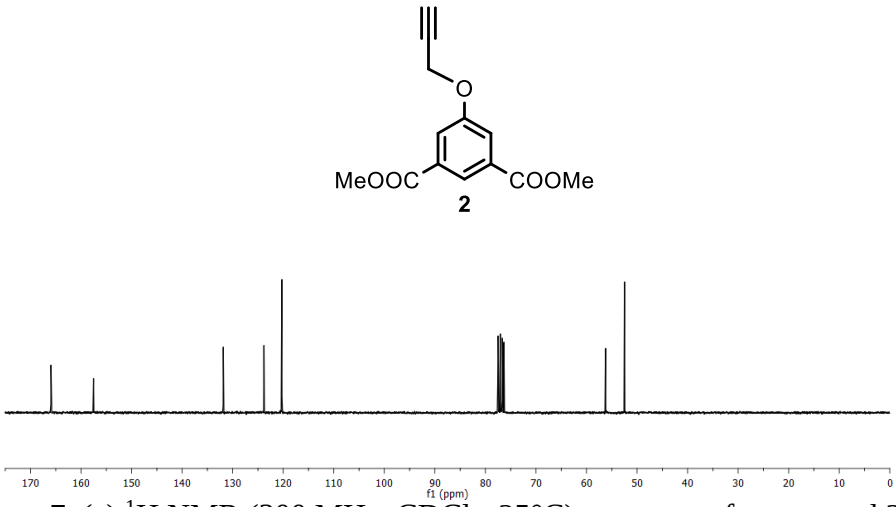

Figure 7. (a) ^{1}H NMR (300 MHz, $CDCl_3$, 25°C) spectrum of compound 2.

(b) ^{13}C NMR (75 MHz, $CDCl_3$, 25°C) spectrum of 2.

Synthesis of 5-(prop-2-yn-1-yloxy)isophthalic acid (3): Compound 2 (3.7 g, 15 mmol), MeOH (30 mL), and 2(N) NaOH (10 mL) were taken in a round bottomed flask (100 mL). The resulting mixture was stirred for 5 hr at 25°C. The volume of the reaction mixture was concentrated under reduced pressure. It was extracted with EtOAc (3×100 mL), aqueous layer was collected in a 250 mL conical flask and acidified by using 2(N) HCl (pH up to 2-3) to obtain a white precipitate. The precipitate was filtered and washed several times with cold H_2O to acquire the pure compound **3** as a white solid. Yield: 3.1 g (94%)

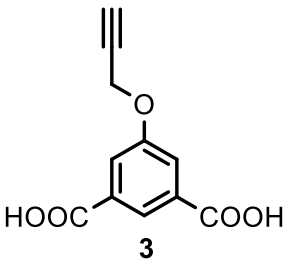

^{1}H NMR (300 MHz, DMSO-d_6, 25°C): δ =13.34 (2H, s), 8.12 (1H, s), 7.73 (2H, s), 4.95 (2H, s), and 3.63 (1H, s) ppm. ^{13}C NMR (75 MHz, DMSO-d_6, 25°C): δ = 166.8, 157.8, 133.1, 123.4, 120.1, 79.4, 79.1, and 56.4 ppm.

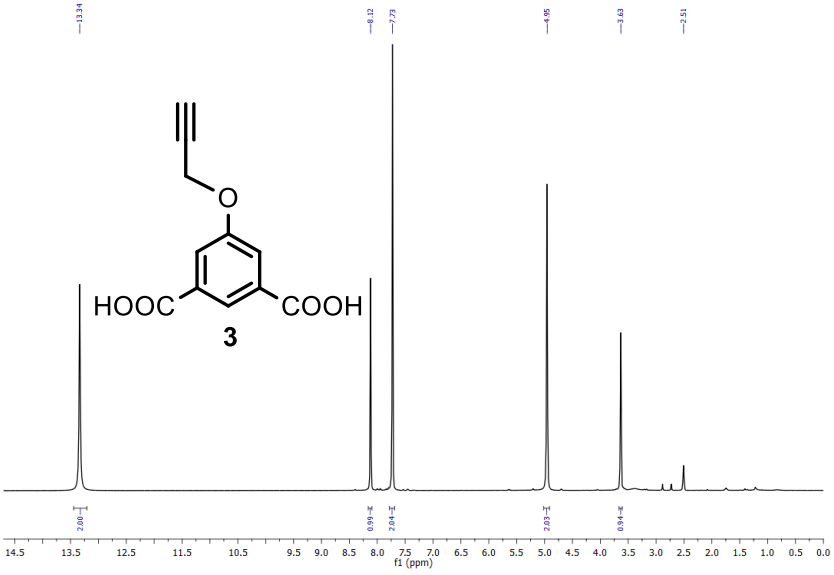

Figure 8. ^{1}H NMR (300 MHz, DMSO-d_6, 25°C) spectrum of compound 3.

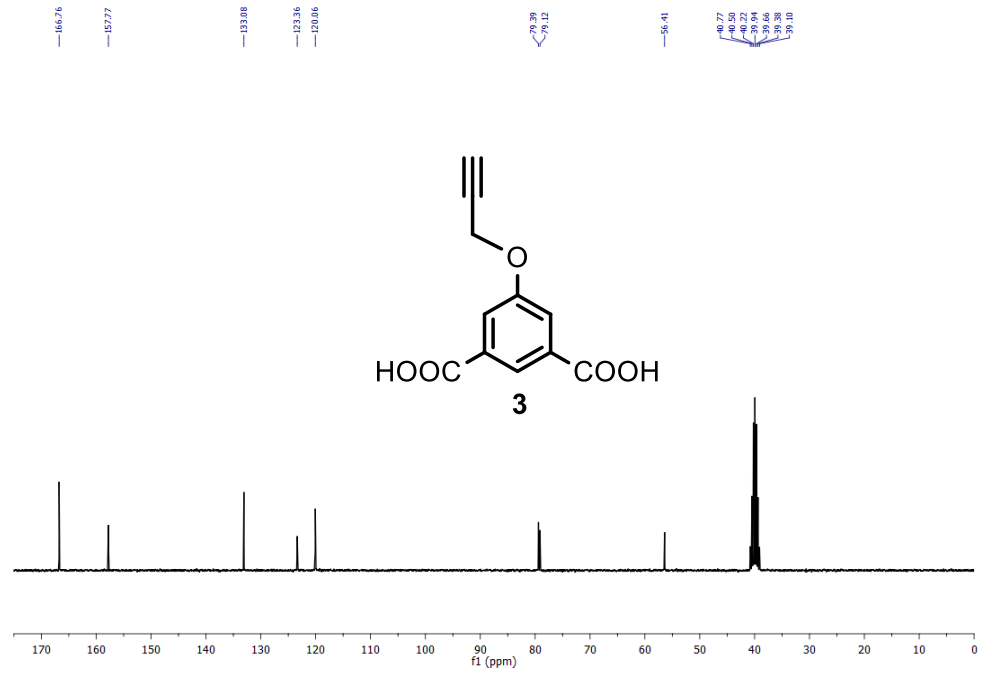

Figure 9. ^{13}C NMR (75 MHz, DMSO-d_6, 25°C) spectrum of 3.

Macrocycle 1 and Macrocycle 2-Alkyne:

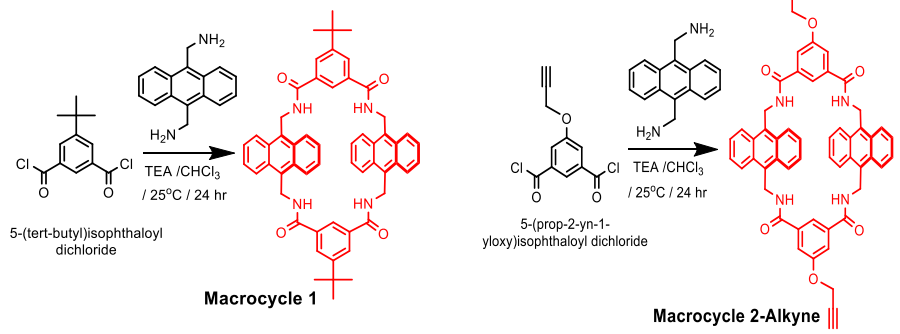

Scheme 2: Synthesize of Macrocycle 1 and Macrocycle 2-Alkyne

Synthesis of Macrocycle 1: 9,10-Bis(aminomethyl)anthracene (0.19 g, 0.81 mmol) and 5-(*tert*-butyl)isophthaloyl dichloride (0.21 g, 0.81 mmol) were separately dissolved in dry $CHCl_3$ (20 mL). Each solution was taken into separate 50 mL syringes. Et_3N (0.5 mL) was added to the syringe comprising

9,10-bis(aminomethyl)anthracene. To a stirred solution of anhydrous $CHCl_3$ (40 mL) in a two neck round bottomed flask the two solutions were added using syringes at the same time drop wise over 6 hr. After 18 hr stirring at 25°C, the solution was concentrated under reduced pressure to get the crude product. The crude product was purified by column chromatography using 2% MeOH/$CHCl_3$ to obtain a pale yellow colored pure solid Macrocycle 1.

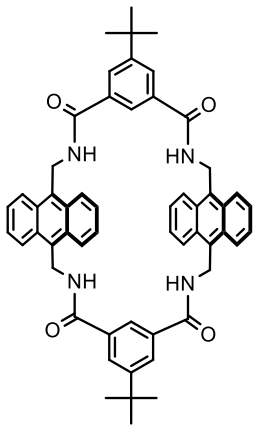

Macrocycle 1

Yield: 0.19 g (27.9%).

^{1}H NMR (300 MHz, $CDCl_3$, 25°C): δ = 8.39 (4H, s), 8.20 (8H, dd, J = 6.8 Hz, J = 3.2 Hz), 7.46 (8H, dd, J = 6.8 Hz, J = 3.2 Hz), 7.22 (2H, s), 6.41 (4H, br), 5.50 (8H, d, J = 3.0 Hz), and 1.45 (18H, s) ppm. ^{13}C NMR (75 MHz, $CDCl_3$ + CD_3OD, 25°C): δ = 171.2, 136.9, 134.1, 133.4, 133.2, 130.3, 128.4, 100.0, 40.9, 39.1, 35.0, and 33.5 ppm.

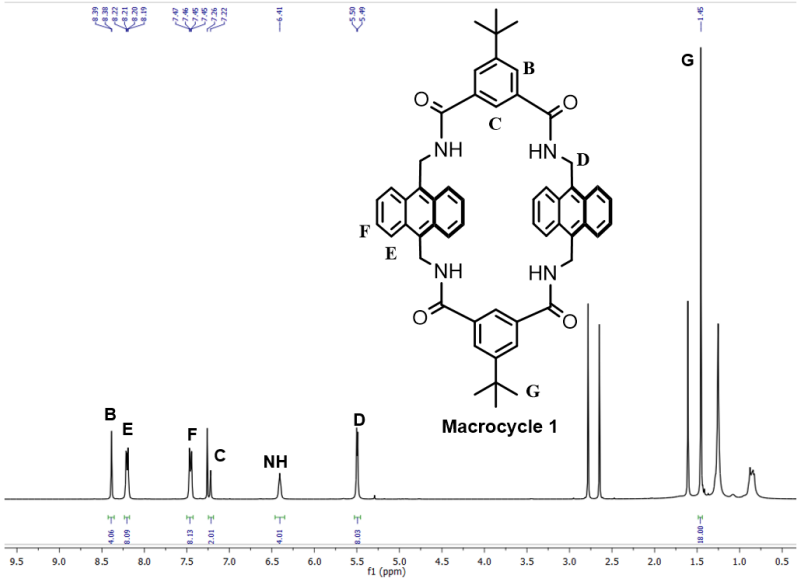

Figure 10.^{1}H NMR (300 MHz, $CDCl_3$, 25°C) spectrum of the Macrocycle 1.

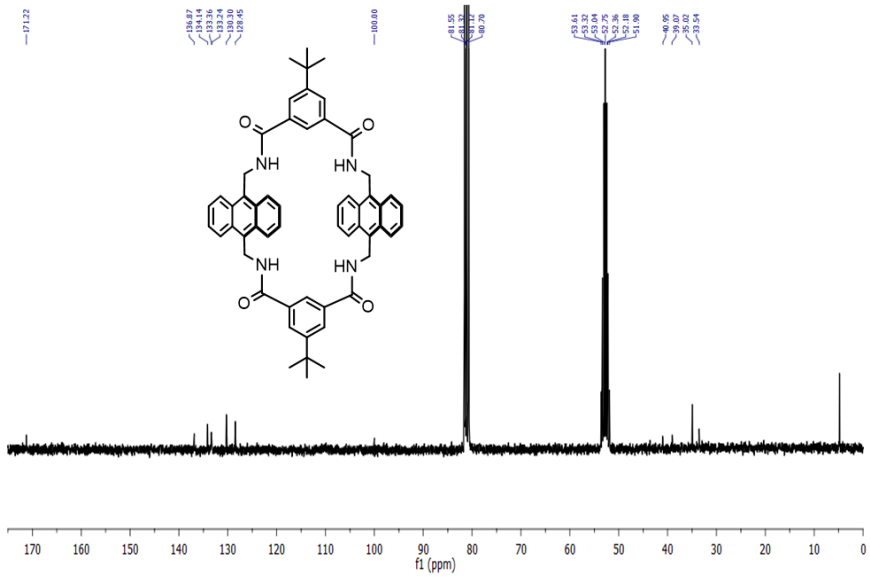

Figure 11. ^{13}C NMR (75 MHz, $CDCl_3$ + CD_3OD 25°C) spectrum of the Macrocycle 1.

Synthesis of Macrocycle 2-Alkyne: 9,10-Bis(aminomethyl)anthracene (0.19 g, 0.81 mmol) and 5-(prop-2-yn-1-yloxy)isophthaloyl dichloride (0.21 g, 0.81 mmol) were individually dissolved in anhydrous $CHCl_3$ (25 mL). The $CHCl_3$ solutions of each of the compound were taken into separate 50 mL syringes. Et_3N (0.5 mL) was added into the syringe having 9,10-bis(aminomethyl)anthracene. To a stirred solution of anhydrous $CHCl_3$ (40 mL) in a two neck round bottomed flask the two solutions were added using syringes at the same time drop wise over 6 hr. After stirring for 18 hr at 25°C, the solution was concentrated under reduced pressure to get the crude product. The crude

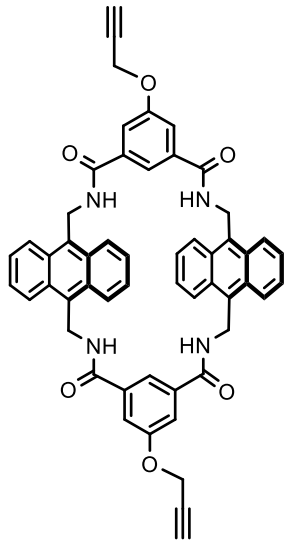

Macrocycle 2-Alkyne

product was purified by column chromatography using 10-15 % $CHCl_3$/Acetone to obtain a pale yellow colored pure solid Macrocycle 2-Alkyne.

Yield: 0.197 g (29%).

^{1}H NMR (300 MHz, $CDCl_3$, 25°C): δ = 8.20–8.18 (8H, m), 7.94 (4H, s), 7.46–7.44 (8H, m), 6.98 (2H, s), 6.34 (4H, br), 5.50 (8H, d, J = 3.0 Hz), 4.85 (4H, s), and 2.63 (2H, s) ppm. ^{13}C NMR (75 MHz, $CDCl_3$, 25°C): δ = 165.8, 138.5, 130.2, 128.1, 126.7, 124.4, 121.3, 77.5, 76.6, 65.9, 56.2, 29.7, and 15.3 ppm. HRMS (ESI +ve) m/z: Observed for $C_{54}H_{40}N_4O_6$ $[M]^+$ = 840.2938, $[M]^+$ calcd = 840.2948. We have the single crystal X-ray structure of **Macrocycle 2-Alkyne**.

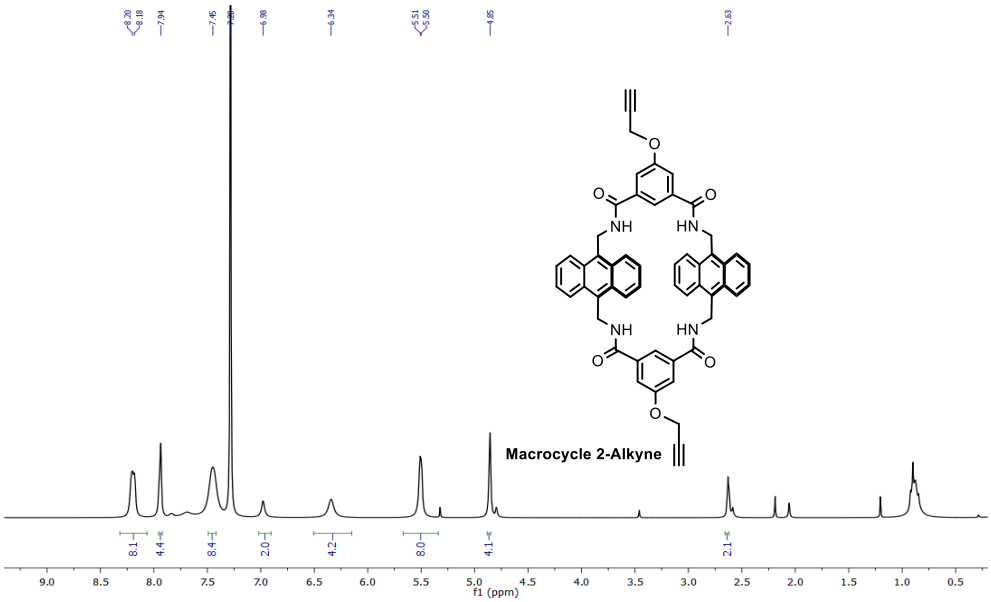

Figure 12.^{1}H NMR (300 MHz, $CDCl_3$, 25°C) spectrum of the Macrocycle 2-Alkyne.

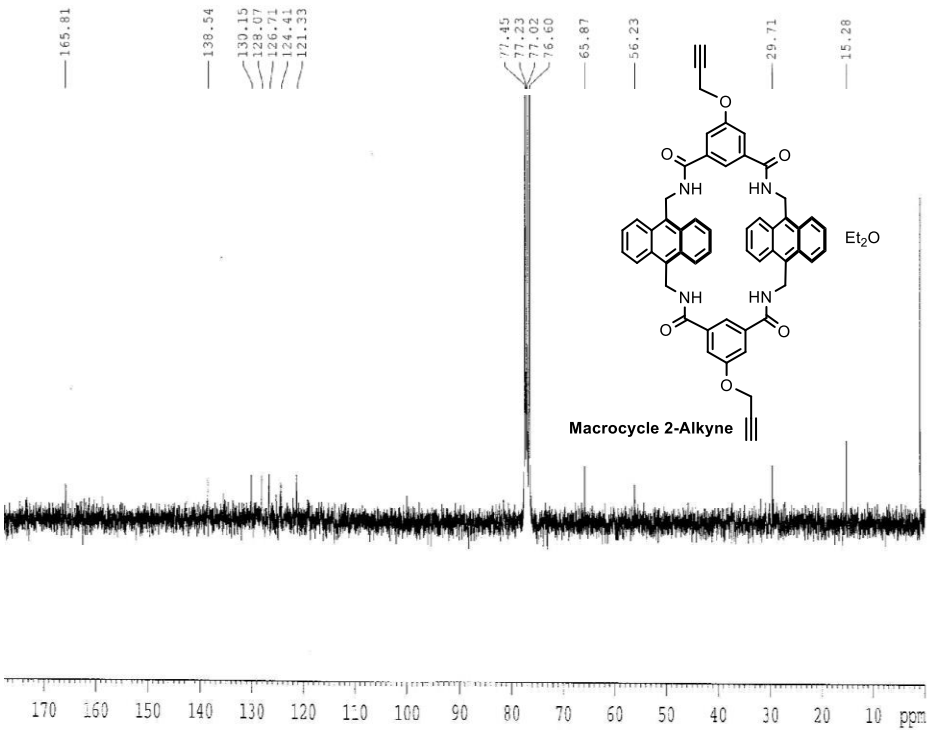

Figure 13. ^{13}C NMR (75 MHz, $CDCl_3$, 25°C) spectrum of the Macrocycle 2-Alkyne.

Symmetrical Squaraine Dye (SSQ):

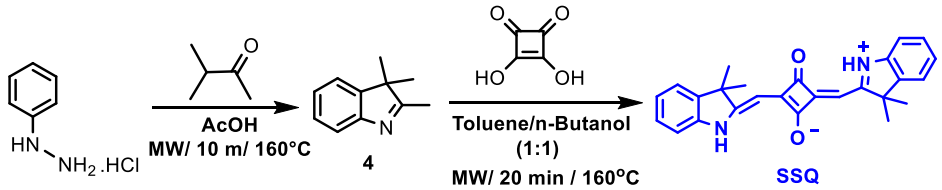

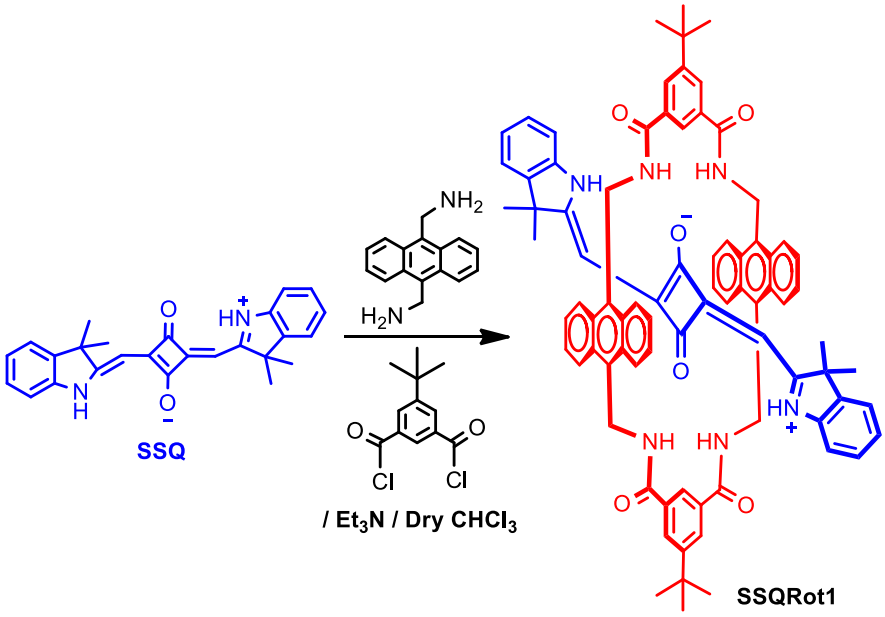

Scheme 3. Synthesis of SSQ dye and the rotaxane molecule SSQRot1.

Synthesis of 2,3,3-Trimethylindolenine (4): 3-Methyl-2-butanone (2 ml, 19 mmol), phenylhydrazine hydrochloride (1 g, 6.91 mmol), and glacial AcOH (6 mL) were taken in a MW vessel equipped with a magnetic stir bar, which was sealed and heated in a MW system at 160°C for 20 min at 20 W. The reaction mixture was cooled to room temperature. The solvent was removed under reduced pressure and the crude product was purified by column chromatography (20% EtOAc/Hexane) to get a brown orange liquid of pure compound 2,3,3-Trimethylindolenine (**4**). Yield: 0.99 g (90%)

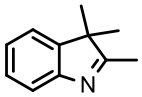

4

^{1}H NMR (300 MHz, $CDCl_3$, 25°C): δ = 7.55 (1H, d, J = 7.6 Hz), 7.34–7.28 (2H, m), 7.23–7.18 (1H, m), 2.29 (3H, s), and 1.31 (6H, s) ppm.

^{13}C NMR (75 MHz, $CDCl_3$, 25°C): δ = 188.0, 153.7, 145.7, 127.6, 125.1, 121.3, 119.9, 53.6, 23.1, and 15.4 ppm.

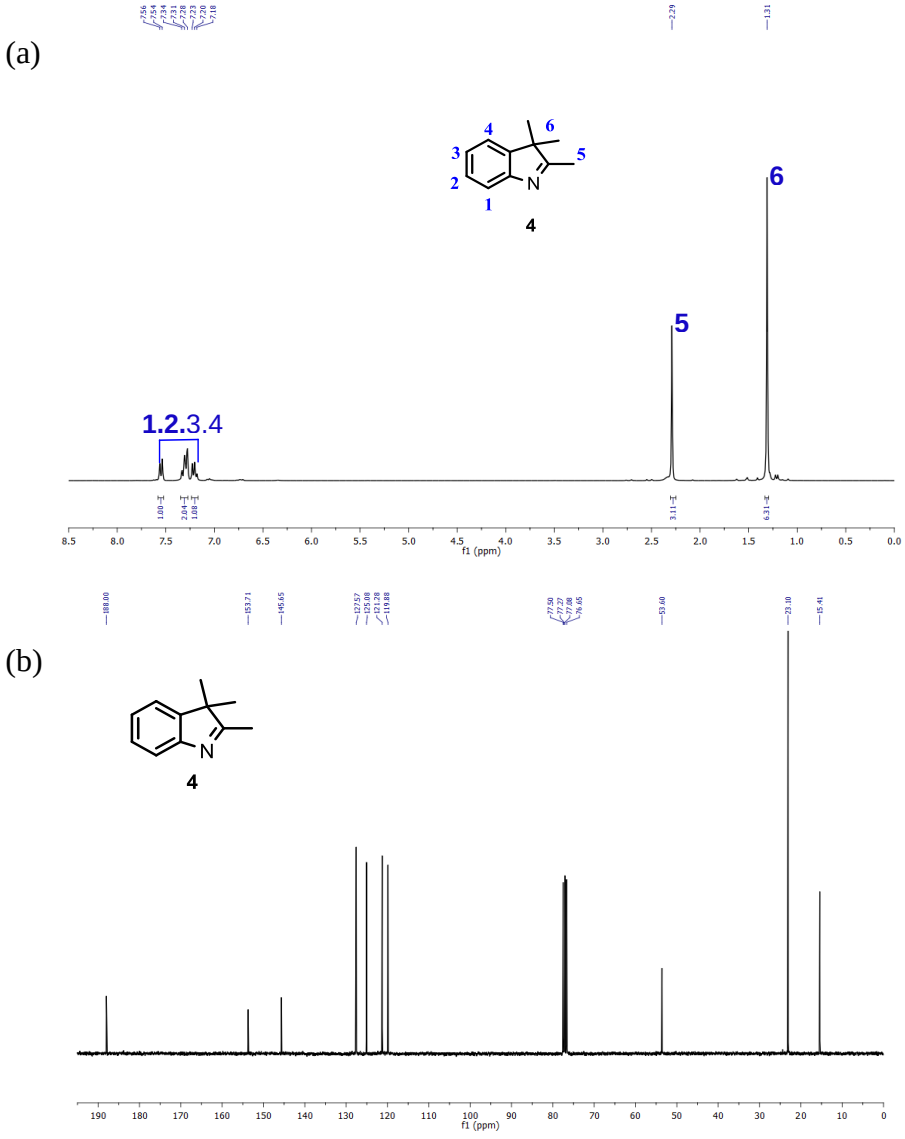

Figure 14. (a) ^{1}H NMR (300 MHz, $CDCl_3$, 25°C) spectrum of compound 2,3,3-trimethyl-indolenine (compound 4). (b) ^{13}C NMR (75 MHz, $CDCl_3$, 25°C) spectrum of compound 4.

Synthesis of SSQ: 2,3,3-Trimethylindolenine (0.5 g, 3.14 mmol) and squaric acid (0.18 g, 1.57 mmol) were taken in a MW vessel containing a 1:1 *v*/*v* mixture of n-BuOH (1 mL) and toluene (1 mL), which was sealed and heated in a MW system at 160°C for 20 min at 30 W. Then the reaction mixture was cooled to room temperature. Deep blue colored solution was concentrated under reduced pressure and the crude product was recrystallized by n-BuOH to get blue crystals, which was filtered and washed with Et_2O (R_f = 0.3, 0.5% MeOH/ DCM) to obtain deep blue colored crystals of SSQ. Yield: 0.56 g (90%).

SSQ

^{1}H NMR (300 MHz, $CDCl_3$, 25°C): δ = 12.83 (1H, s), 12.54 (1H, s), 7.30–7.18 (4H, m), 7.13–7.06 (4H, m), 5.52 (1H, s), 5.45 (1H, s), and 1.45 (12H, s) ppm.

^{13}C NMR (75 MHz, $CDCl_3$, 25°C): δ = 183.4, 175.8, 175.2, 141.9, 139.0, 128.3, 123.2, 122.3, 111.5, 86.1, 48.7, and 26.6 ppm. HRMS (ESI +ve) *m*/*z*: Observed for $C_{26}H_{25}N_2O_2$ $[M+H]^+$ = 397.1915, $[M+H]^+$ calcd = 397.1911.

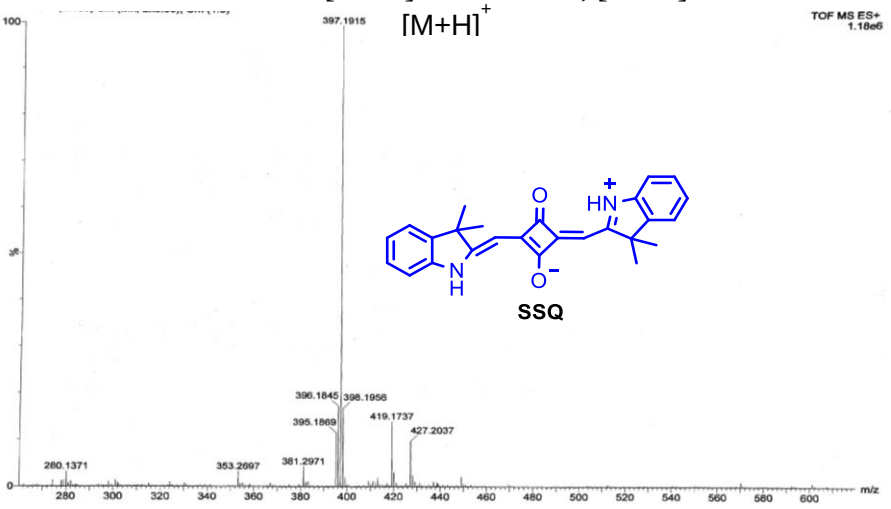

Figure 15. HRMS (ESI +ve) spectrum of SSQ.

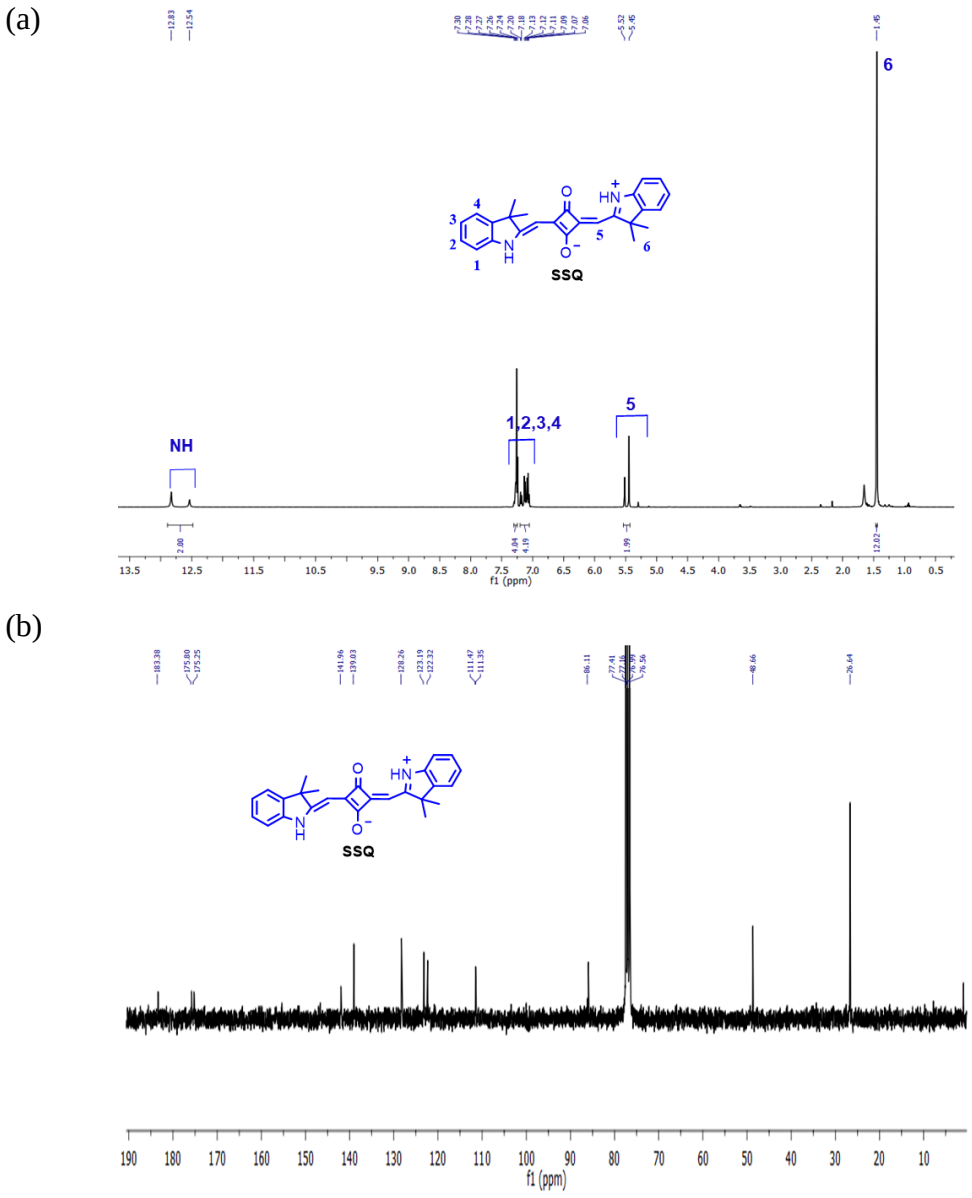

Figure 16. (a) ^{1}H NMR (300 MHz, $CDCl_3$, 25°C) spectrum of compound SSQ. (b) ^{13}C NMR (75 MHz, $CDCl_3$, 25°C) spectrum of SSQ.

Synthesis of SSQRot1: 9,10-bis(aminomethyl)anthracene (0.23 g, 0.97 mmol) and 5-(*tert*-butyl)isophthaloyl dichloride (0.25 g, 0.97 mmol) were dissolved individually in dry $CHCl_3$ (30 mL). Each solution was taken into separate 50 mL syringe. Et_3N (0.7 mL) was added into the syringe containing 9,10-bis(aminomethyl)anthracene. To a stirred solution of SSQ (0.10 g, 0.24 mmol) in anhydrous $CHCl_3$ (120 mL) in a two neck round bottomed flask the two previously prepared solutions were added simultaneously drop wise over 6 hr using syringes. After 24 hr stirring at 25°C, the resulting solution was concentrated under reduced pressure to obtain the crude product. The crude product was purified by column chromatography using 1% Acetone/$CHCl_3$ to obtain a see green colored pure solid SSQRot1.

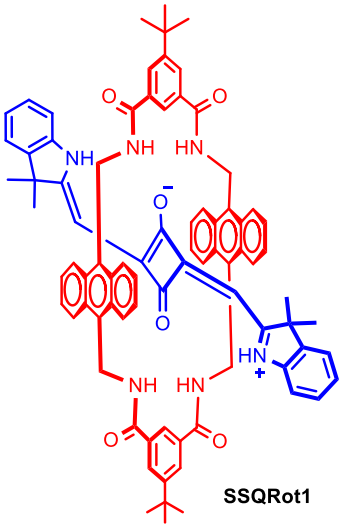

SSQRot1

Yield: 0.036 g (12%)

^{1}H NMR (300 MHz, $CDCl_3$, 25°C): δ = 10.20 (2H, s), 8.59 (4H, s), 8.46 (2H, s), 8.07 (4H, d, J = 9.0 Hz), 7.89 (4H, d, J = 9.0 Hz),7.48 (4H, br), 7.18–7.14 (4H, m), 6.96–6.85 (8H, m), 6.83–6.78 (4H, m), 5.72–5.65 (4H, m), 5.24–5.18 (4H, m), 4.05 (2H, s), 1.54 (12H, s), and 1.26 (18H, s) ppm.

^{13}C NMR (75 MHz, $CDCl_3$, 25°C): δ = 181.3, 174.3, 168.7, 166.4, 153.3, 140.9, 138.5, 133.2, 130.3, 130.0, 129.8, 129.0, 128.0, 126.3, 125.9, 124.6, 123.9, 122.1, 120.3, 112.4, 100.0, 83.8, 48.3, 37.2, 35.4, 33.6, 31.9, 31.3, 29.7, 29.5, 29.3, 29.1, 27.7, 24.8, and 22.7 ppm.

HRMS (ESI +ve) *m/z*: Observed for $C_{82}H_{77}N_6O_6$ $[M+H]^+$ = 1241.5840, $[M+H]^+$ calcd = 1241.5899.

Photophysical properties in DMF λ_{abs}= 657 nm, λ_{em}= 670 nm, Stokes shift ($\Delta\lambda$) = 13 nm, ε = 1.10 ×10^5 $M^{-1}cm^{-1}$, Φ_f = 0.14 in DMF (Φ_f of Zinc phthalocyanine as reference = 0.17 in DMF), τ = 0.187901±0.114794 ns in DMSO.

We have the single crystal X-ray structure of **SSQRot1**.

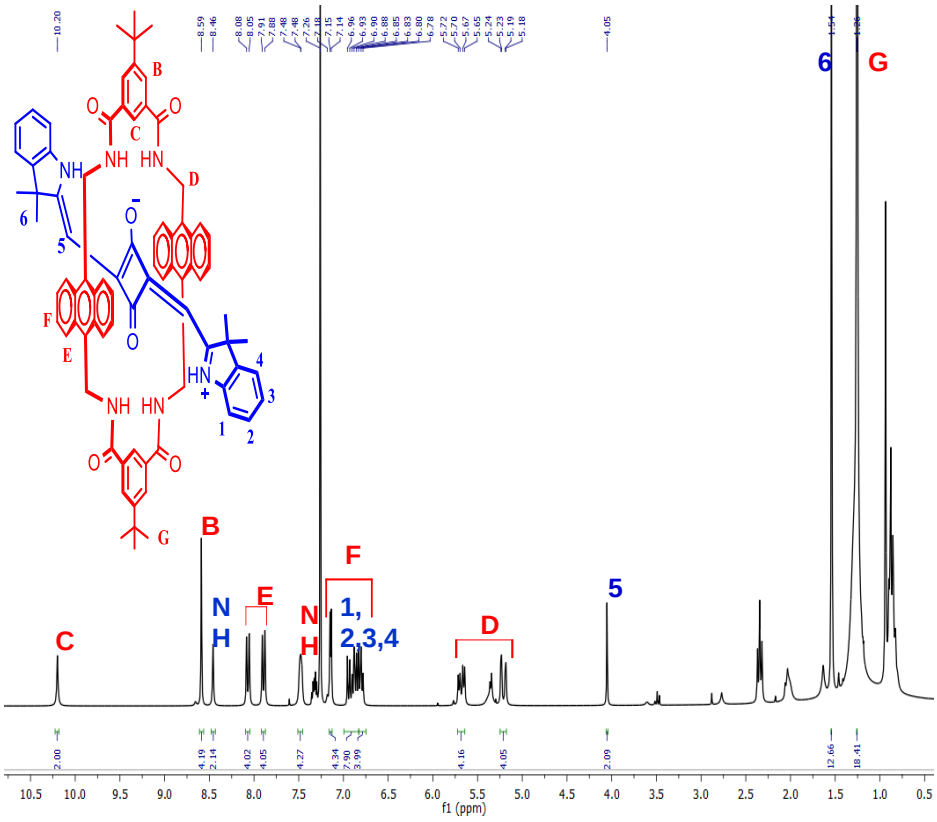

Figure 17. ^{1}H NMR (300 MHz, $CDCl_3$, 25°C) spectrum of compound SSQRot1.

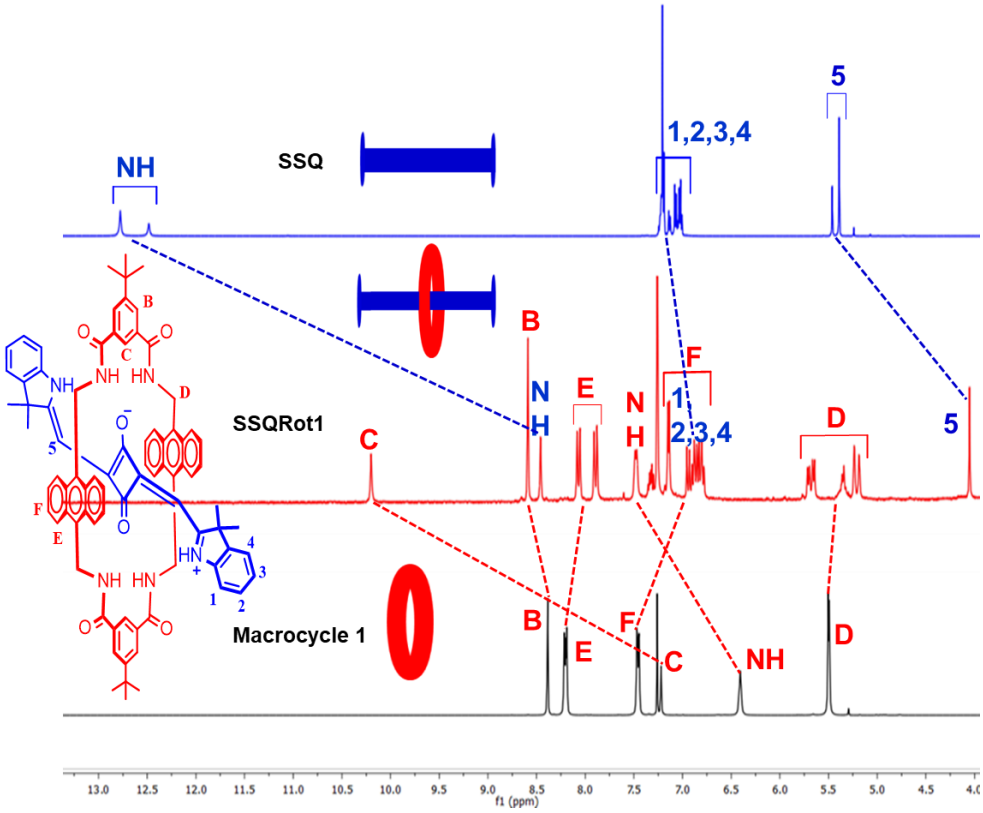

Figure 18. Partial ^{1}H NMR (300 MHz, $CDCl_3$, 25°C) stacking of **empty Macrocycle 1**, **SSQRot1**, and **SSQ** showing downfield shift of macrocycle proton C, NH and upfield shift of E, F as well as SSQ proton 5 designate rotaxane formation.

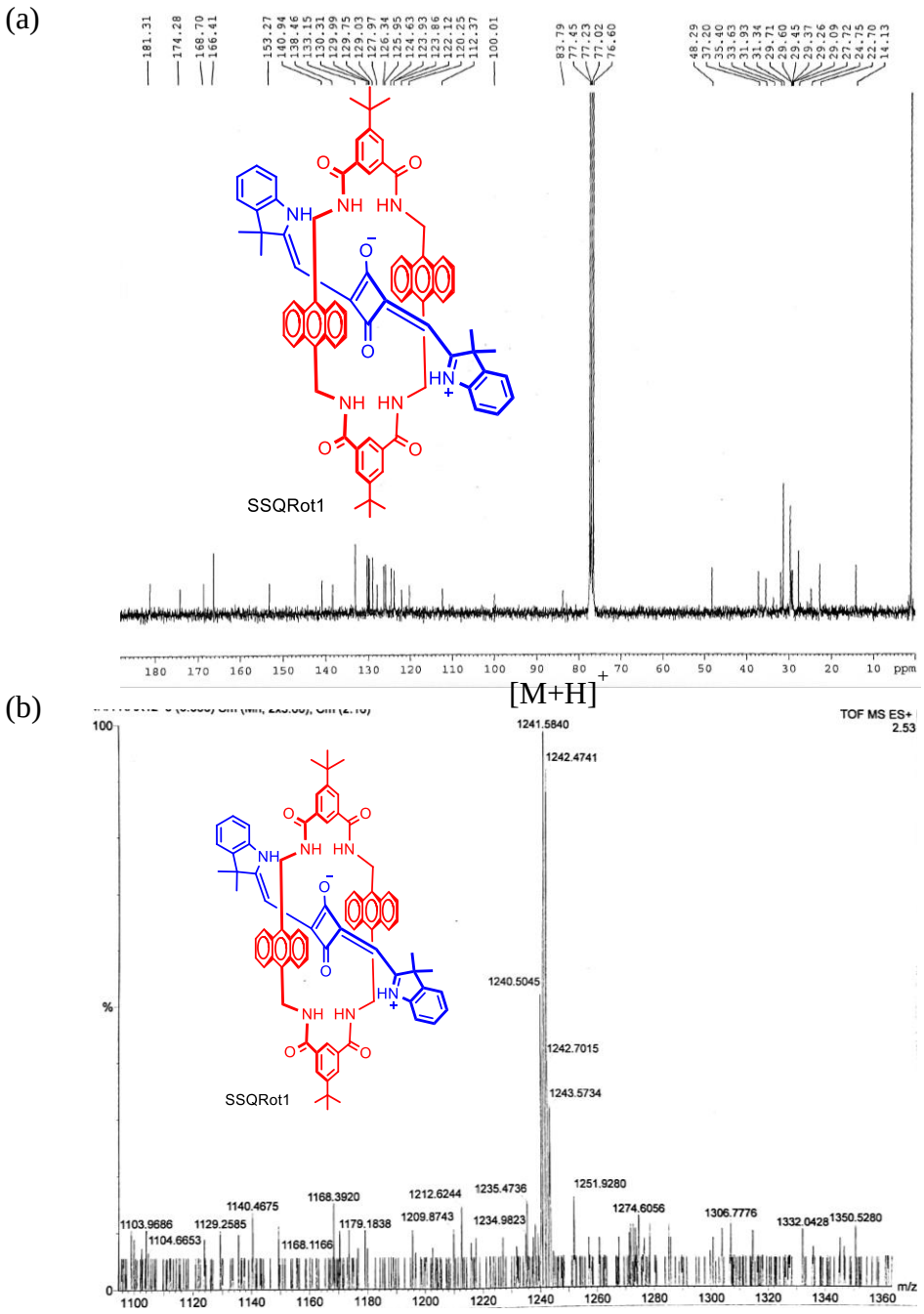

Figure 19. (a) ^{13}C NMR (75 MHz, $CDCl_3$, 25°C) spectrum of SSQRot1. (b) HRMS (ESI +ve) spectrum of SSQRot1.

Synthesis of rotaxane molecules SSQRot2-(Alkyne)$_2$ and LysoSQRot2-(Alkyne)$_2$.

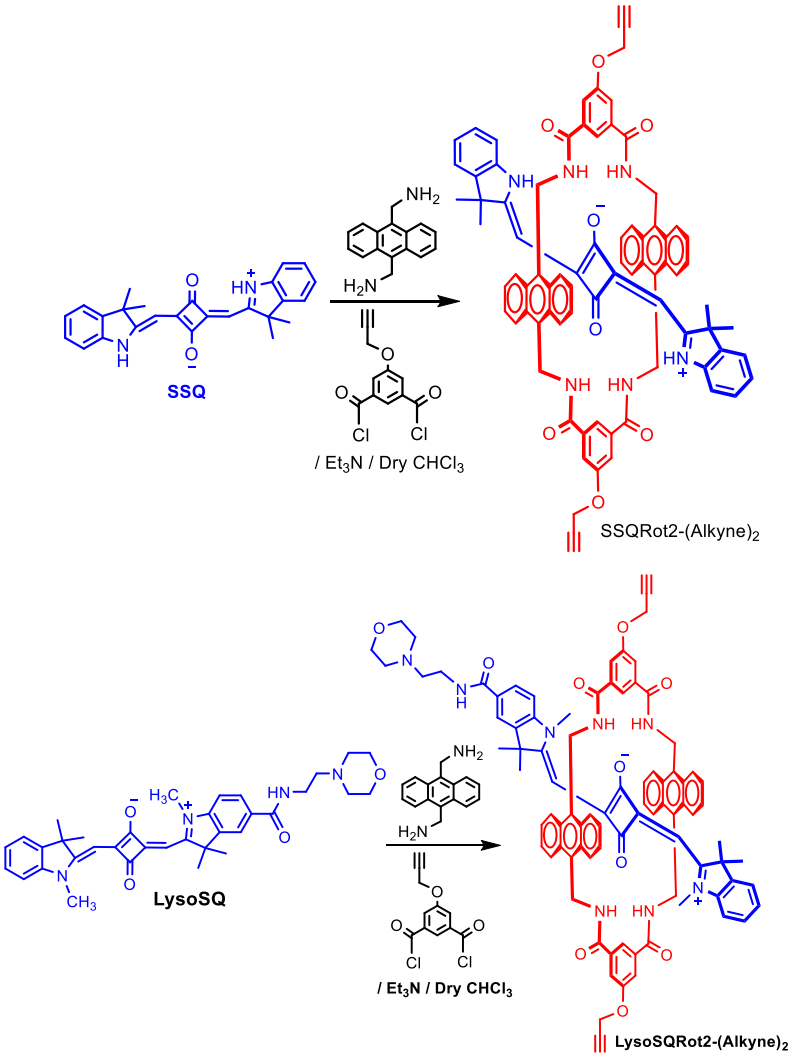

Scheme 4. Synthesis of the rotaxane molecules SSQRot2-(Alkyne)$_2$ and LysoSQRot2-(Alkyne)$_2$**.**

Synthesis of SSQRot2-(Alkyne)$_2$: 5-(prop-2-yn-1-yloxy)isophthaloyl dichloride (0.3 g, 1.17 mmol) and 9,10-bis(aminomethyl)anthracene (0.27 g, 1.17 mmol) were dissolved separately in anhydrous $CHCl_3$ (40 mL). Each solution was taken into separate 50 mL syringe. Et_3N (1 mL) was added to the syringe containing 9,10-bis(aminomethyl)anthracene. To a stirred solution of SSQ (0.12 g, 0.3 mmol) in anhydrous $CHCl_3$ (120 mL) in a two neck round bottomed flask the two previously prepared solutions were added simultaneously drop wise over 6 hr using syringes. After 24 hr stirring at 25°C, the resulting solution was concentrated under reduced pressure to get the crude product. The crude product was purified by column chromatography using 5% Acetone/$CHCl_3$ to obtain a see green colored pure solid SSQRot2-(Alkyne)$_2$.

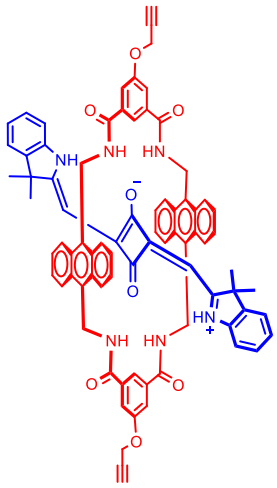

SSQRot2-(Alkyne)$_2$

Yield: 0.063 g (17%)

^{1}H NMR (300 MHz, $CDCl_3$, 25°C): δ =10.19 (2H, s), 8.33 (2H, s), 8.19 (4H, s), 8.09 (4H, d, J = 9.0 Hz), 7.91 (4H, d, J = 9.0 Hz), 7.53 (4H, br), 7.18 (4H, d, J = 6.0 Hz), 6.99–6.90 (8H, m), 6.85–6.80 (4H, m), 5.71–5.64 (4H, m), 5.26–5.20 (4H, m), 4.98 (4H, s), 4.14 (2H, s), 2.68 (2H, s), and 1.58 (12H, s) ppm.

Photophysical properties in DMF λ_{abs}= 657 nm, λ_{em}= 668 nm, Stokes shift ($\Delta\lambda$) = 11 nm, ε = 1.39 ×10^5 M^{-1}cm^{-1}, Φ_f = 0.14 in DMF (Φ_f of Zinc phthalocyanine as reference = 0.17 in DMF), τ = 0.212204±0.186021 ns in DMSO.

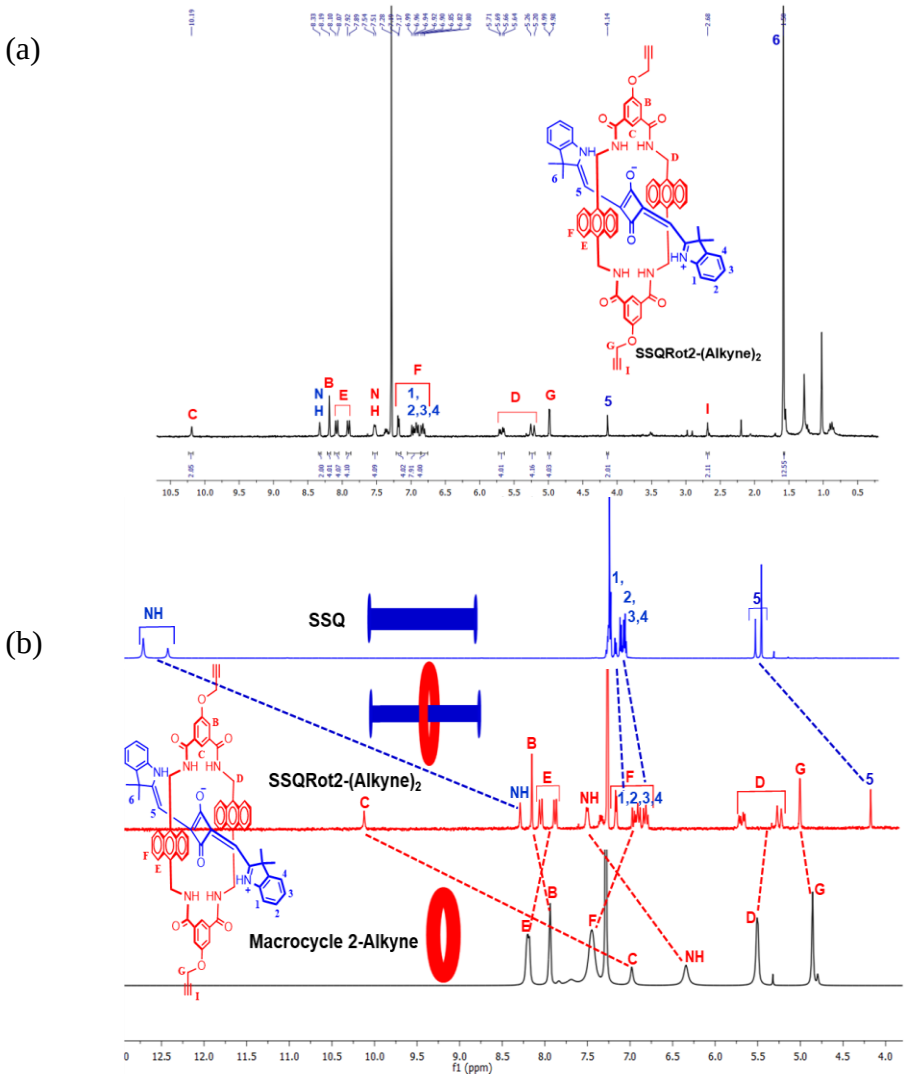

Figure 20. (a) ^{1}H NMR (300 MHz, $CDCl_3$, 25°C) spectrum of compound SSQRot2-(Alkyne)$_2$. (b) Partial ^{1}H NMR (300 MHz, $CDCl_3$, 25°C) stacking of empty Macrocycle 2-Alkyne, SSQRot2-(Alkyne)$_2$, and SSQ showing downfield shift of macrocycle proton C, NH and upfield shift of E, F as well as SSQ proton 5 designate rotaxane formation.

Synthesis of LysoSQRot2-(Alkyne)$_2$: 5-(prop-2-yn-1-yloxy)isophthaloyl dichloride (0.21 g, 0.81 mmol) and 9,10-bis(aminomethyl)anthracene (0.193 g, 0.81 mmol) were dissolved separately in anhydrous $CHCl_3$ (30 mL). Each solution was taken into separate 50 mL syringe. Et_3N (1 mL) was added to the syringe containing 9,10-bis(aminomethyl)anthracene. To a stirred solution of LysoSQ (0.116 g, 0.2 mmol) in anhydrous $CHCl_3$ (40 mL) in a two neck round bottomed flask the two previously prepared solutions were added simultaneously drop wise over 6 hr using syringes. After 24 hr stirring at 25°C, the resulting solution was concentrated under reduced pressure to get the crude product. The crude product was purified by column chromatography using 2% MeOH/$CHCl_3$ to obtain a see green colored pure solid LysoSQRot2-(Alkyne)$_2$.

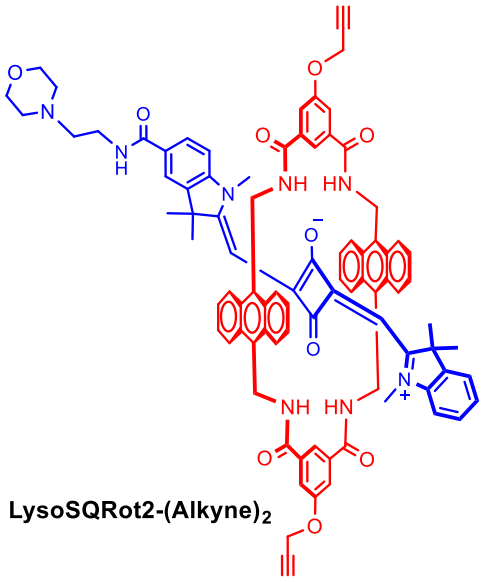

LysoSQRot2-(Alkyne)$_2$

Yield: 0.071 g (25%)

^{1}H NMR (300 MHz, $CDCl_3$, 25°C): δ = 9.38 (1H, s), 9.34 (1H, s), 8.19 (4H, s), 8.09 (4H, d, J = 9.6 Hz), 7.87–7.82 (9H, m), 7.69 (1H, s), 7.48 (1H, t, J = 6.9 Hz), 7.33–7.29 (3H, m), 7.09–7.05 (4H, m), 6.99 (1H, d, J = 8.1 Hz), 6.96 (1H, d, J = 8.0 Hz), 6.66 (4H, t, J = 8.0 Hz), 5.5 (4H, dd, J = 4.8 Hz, J = 14.7 Hz,), 5.09 (4H, d, J = 13.8 Hz), 5.0 (4H, s), 4. 61 (1H, s), 4.54 (1H, s), 3.81–3.79 (4H, m), 3.76–3.72 (2H, m), 3.64–3.65 (2H, m), 2.72 (3H, s), 2.70 (2H, s), 2.65 (3H, s), 2.61–2.57 (4H, m), and 1.17 (12H, s) ppm.

^{13}C NMR (100 MHz, $CDCl_3$, 25°C): δ = 181.6, 173.2, 170.5, 168.7, 166.5, 165.8, 158.8, 146.4, 143.4, 139.2, 135.9, 134.8, 132.3, 131.2, 130.9, 130.1,

128.9, 125.6, 124.8, 122.4, 121.5, 118.9, 117.7, 114.08, 109.8, 108.5, 83.8, 66.8, 65.6, 63.1, 60.4, 56.4, 53.4, 50.2, 49.3, 38.1, 34.3, 33.9, 32.9, 31.9, 30.8, 29.7, 28.3, 27.8, 25.9, 22.7 and 19.2 ppm.

2D NMR: ^{1}H–^{1}H gCOSY (Gradient-selected Correlation Spectroscopy) NMR analysis established coupling connectivity (**Figure 24**). ^{1}H–^{1}H ROESY (Rotating frame Overhauser Effect Spectroscopy) NMR (**Figure 23b**) displayed spatial proximity of protons C,C′ to protons 5,5′; protons F to protons 4, and protons E to protons 5, 5′ confirming rotaxane structure.

HRMS (ESI +ve) *m/z*: observed for $C_{89}H_{81}N_8O_{10}$ $[M+H]^+$ = 1421.7175, $[M+H]^+$ calcd = 1421.6070. observed for $[M+2H]^{2+}$ = 711.3383, $[M+2H]^{2+}$ calcd = 711.3071 (*m*/*z*, *z* = 2).

Photophysical properties in DMSO λ_{abs}= 653 nm, λ_{em}= 665 nm, Stokes shift ($\Delta\lambda$) = 12 nm, ε = 1.82 ×10^5 $M^{-1}cm^{-1}$, Φ_f = 0.15 in DMSO (Φ_f of Zinc phthalocyanine as reference = 0.20 in DMSO), τ = 3.47881±0.031487 ns in DMSO.

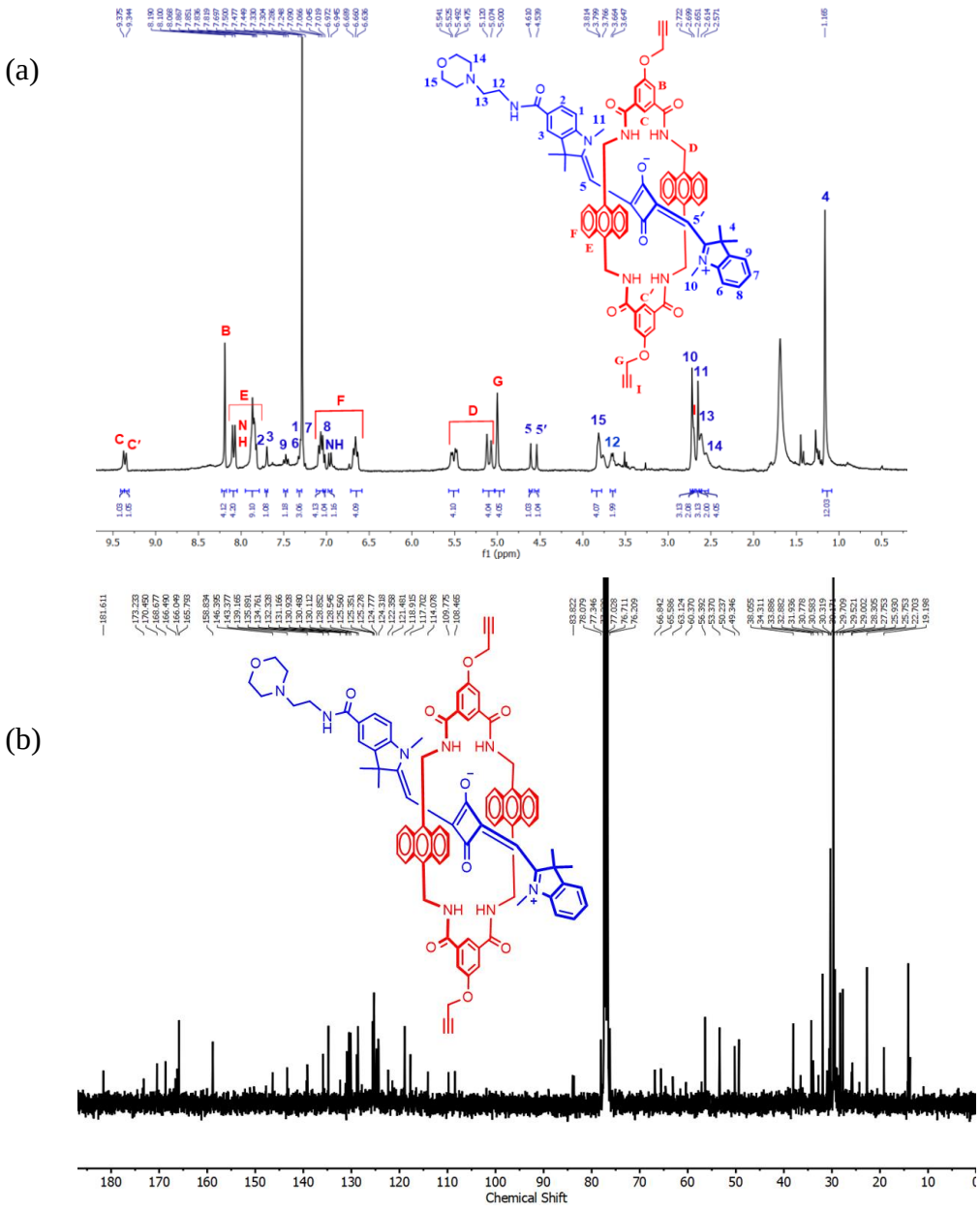

Figure 21. (a) ^{1}H NMR (300 MHz, $CDCl_3$, 25°C) spectrum of compound LysoSQRot2-(Alkyne)$_2$. (b)^{13}C NMR (100 MHz, $CDCl_3$, 25°C) spectrum of LysoSQRot2-(Alkyne)$_2$.

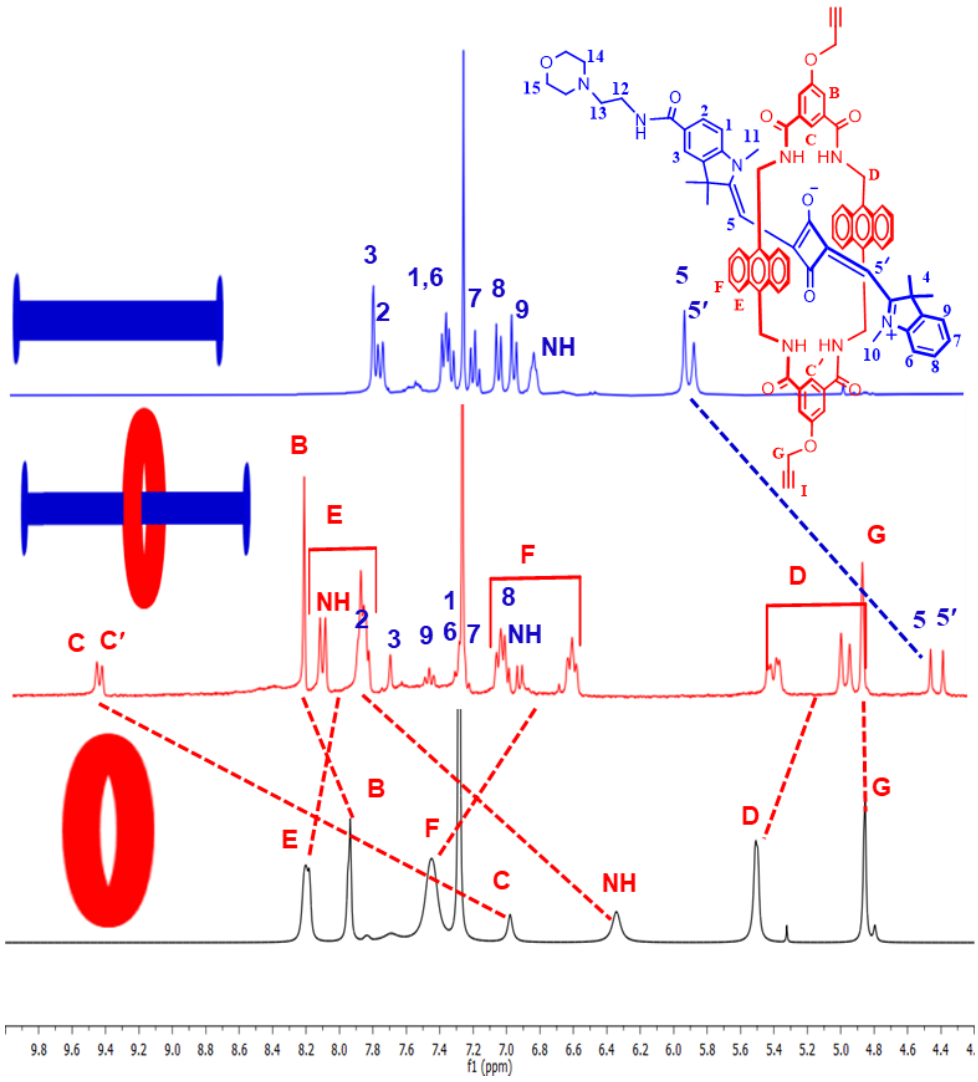

Figure 22. Partial ^{1}H NMR (300 MHz, $CDCl_3$, 25 °C) stacking of empty Macrocycle 2-Alkyne, LysoSQRot2-(Alkyne)$_2$, and LysoSQ showing a downfield shift of Macrocycle 2-Alkyne proton C, NH and upfield shift of E, F, as well as LysoSQ proton 5,5′ designate rotaxane formation.

(a)

(b)

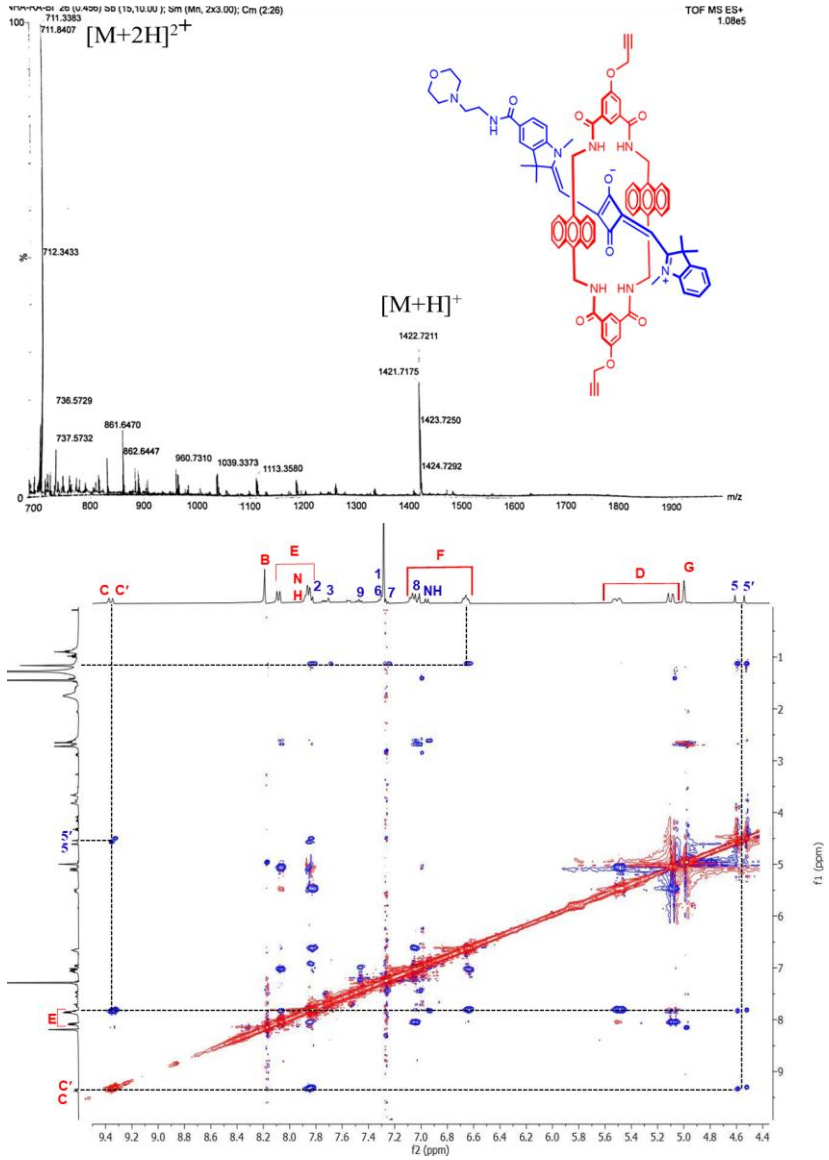

Figure 23. (a) HRMS (ESI +ve) spectrum of LysoSQRot2-(Alkyne)$_2$.(b) Partial ^{1}H-^{1}H ROESY (Rotating frame Overhauser Effect Spectroscopy) NMR (400 MHz, $CDCl_3$, 25°C) spectrum of LysoSQRot2-(Alkyne)$_2$. Protons C,C′ correlates with 5,5′; F correlates with 4, and E correlates with 5, 5′ confirming rotaxane formation.

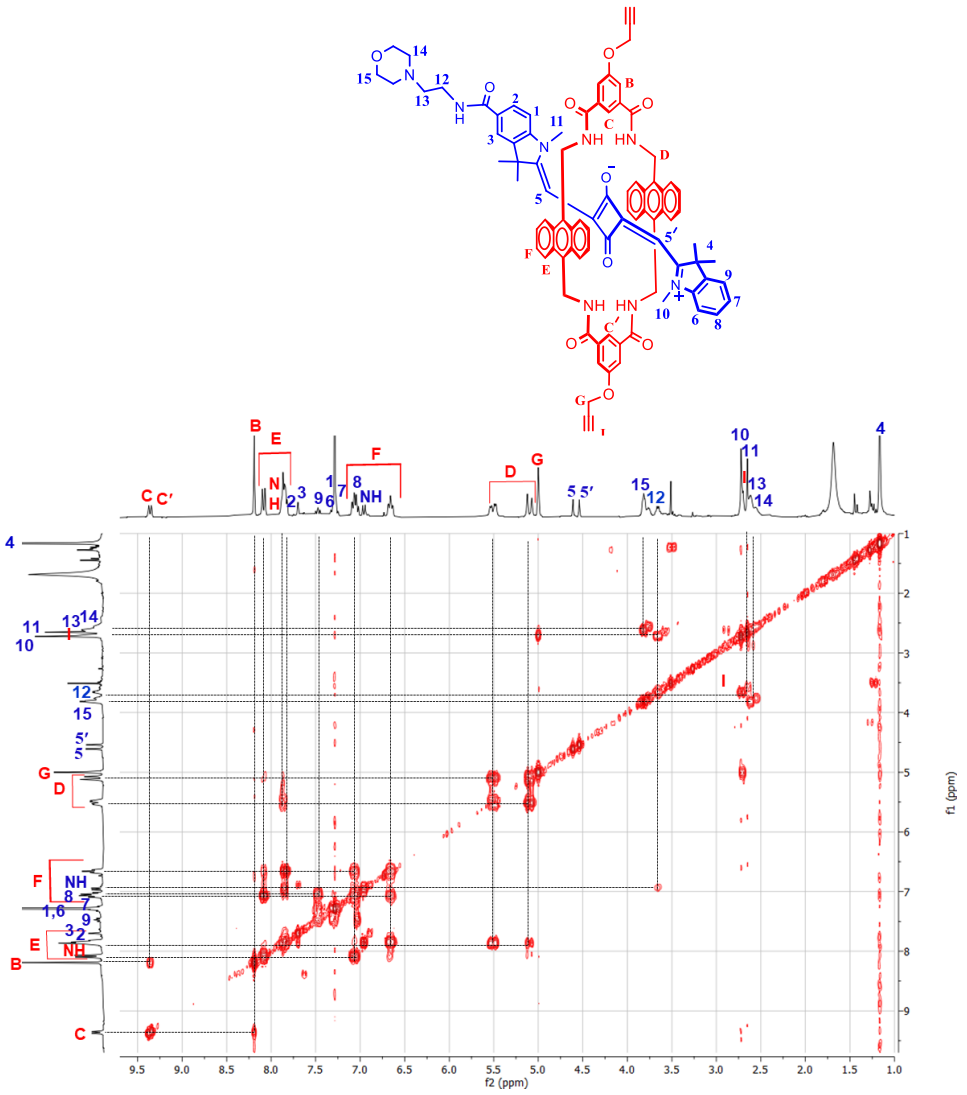

Figure 24. Partial ^{1}H-^{1}H gCOSY (Gradient-selected Correlation Spectroscopy) NMR (300 MHz, $CDCl_3$, 25°C) spectrum of LysoSQRot2-(Alkyne)$_2$.

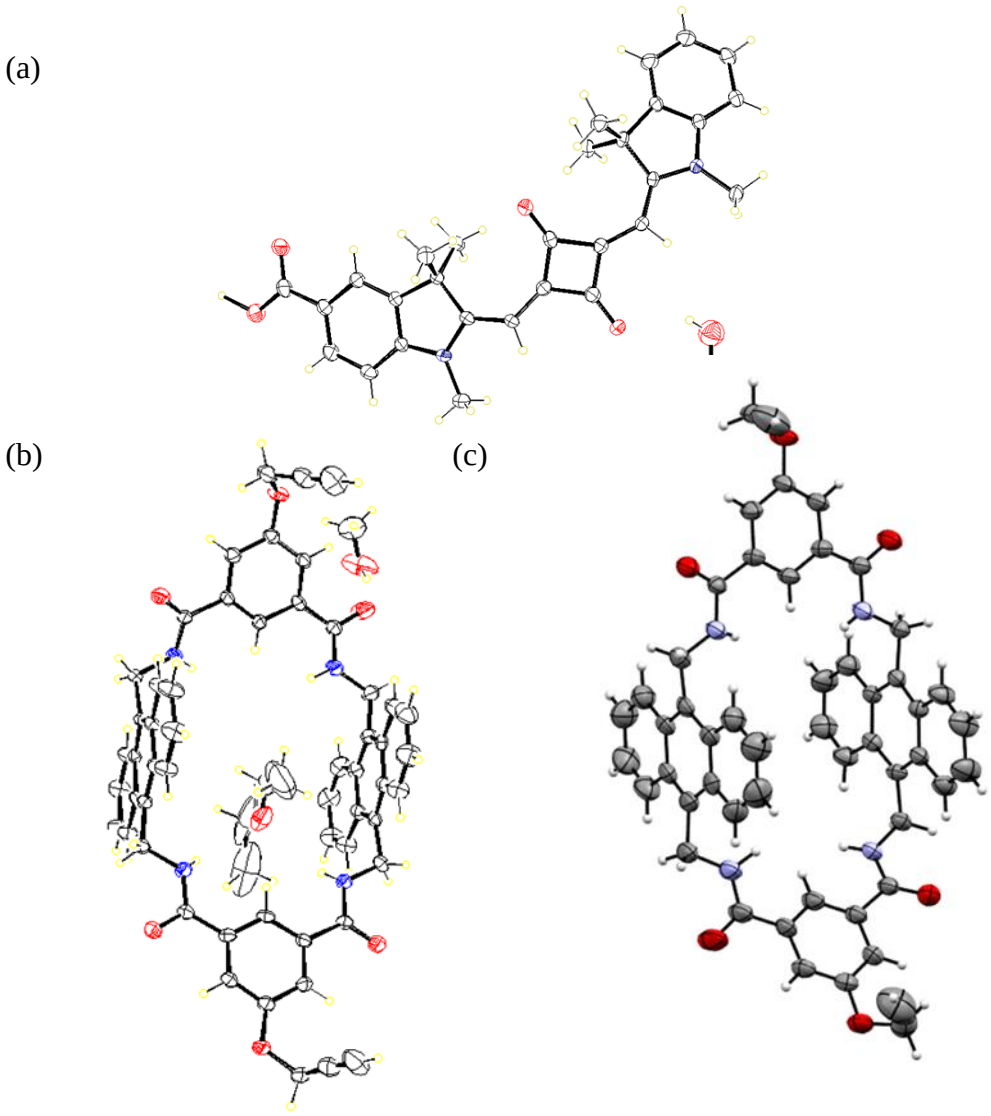

Figure 25. (a) ORTEP diagram of USQ-COOH. (b) ORTEP diagram of Macrocycle 2-Alkyne. (c) ORTEP diagram of Macrocycle 2-Alkyne without the solvent molecules for clarity. Ellipsoids are at 30% probability.

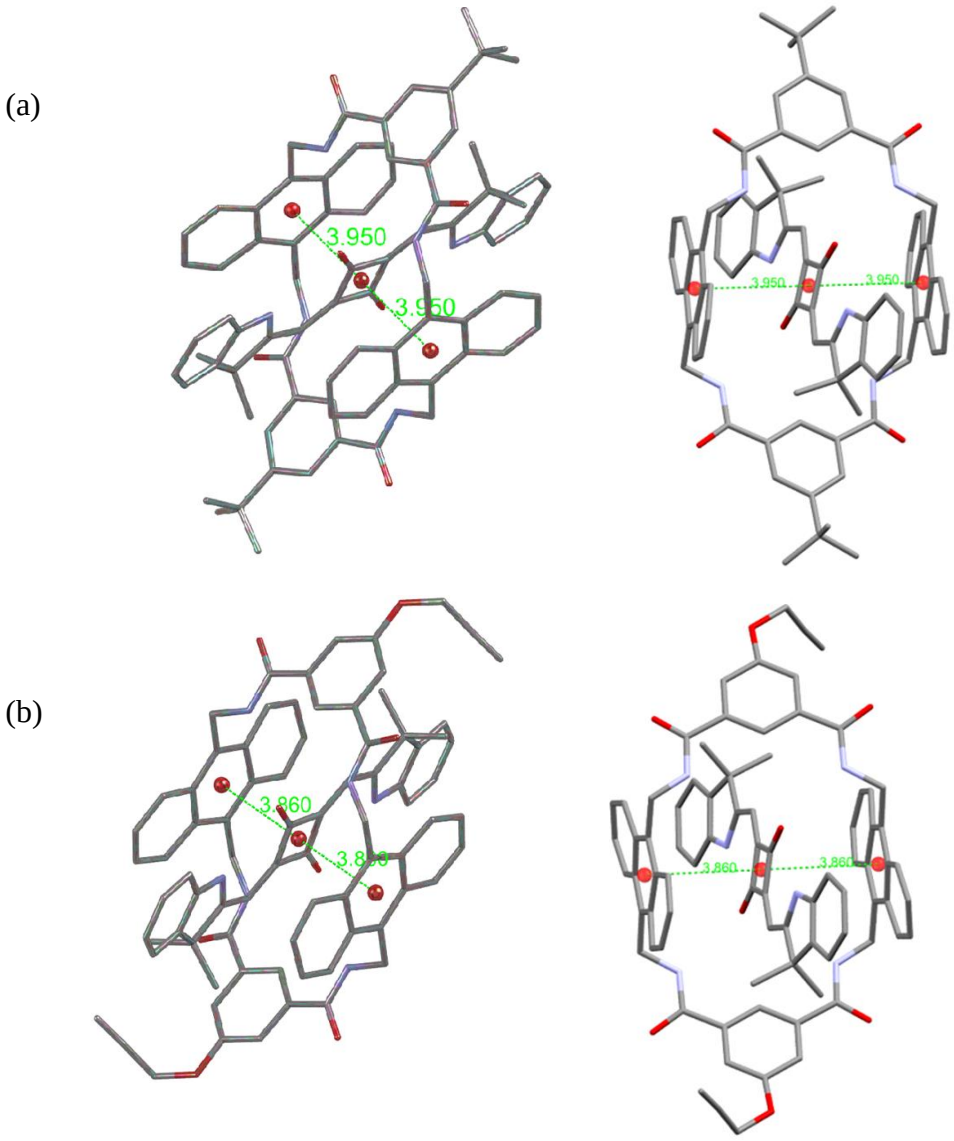

Figure 26. The centroid-to-centroid donor–acceptor distance between the donor anthracene moieties and the acceptor C_4O_2 core is (a) 3.95 Å for SSQRot1 and (b) 3.86 Å for SSQRot2-$(Alkyne)_2$.

Table 1. Crystallographic data of compounds USQ-COOH, Macrocycle 2-Alkyne, SSQRot1, and SSQRot2-(Alkyne)$_2$.

Description	USQ-COOH	Macrocycle 2-Alkyne	SSQRot1	SSQRot2-(Alkyne)$_2$
formula sum	C60 H63.70 N4 O10	C57.34 H50.92 N4 O7.71	C82 H76 N6 O6 [+ solvent]	C86 H76 N6 O10
formula weight	1000.85	919.39	1241.49	1353.53
crystal system	monoclinic	triclinic	triclinic	triclinic
space group	*P* 21/c	*P* -1	*P* -1	*P* -1
***a* (Å)**	16.535(15)	11.428(5)	10.287(5)	11.550(12)
***b* (Å)**	7.195(7)	14.231(6)	11.953(5)	12.221(14)
***c* (Å)**	22.06(2)	16.320(7)	16.778(7)	14.158(17)
***α* (°)**	90	101.784(12)	72.327(11)	88.41(4)
***β* (°)**	94.33(3)	100.343(12)	81.234(11)	67.04(4)
***γ* (°)**	90	95.861(12)	76.697(11)	78.15(4)
***V* (Å^3)**	2617(4)	2529.3(19)	1905.3(15)	1798(4)
Z	2	2	1	1
***D*$_{calcd}$ (g cm^{-3})**	1.270	1.207	1.082	1.250
***μ* (mm^{-1})**	0.087	0.081	0.068	0.082
***T* (K)**	293	293	293	293
***λ* (Å)**	0.71073	0.71073	0.71073	0.71073
***R*$_1$**	0.0991	0.0988	0.0997	0.0867
***wR*$_2$**	0.2070	0.2574	0.3395	0.2987
CCDC No.	2128042	2128044	2128045	2128046

The Macrocycle 2-Alkyne containing rotaxanes SSQRot2-(Alkyne)$_2$ and LysoSQRot2-(Alkyne)$_2$ are bioconjugated with cancer cell target specific peptide N_3-RGDS by click chemistry on the Wang resin to develop red emissive rotaxane/RGDS conjugates SSQRot-(RGDS)$_2$ and LysoSQRot-(RGDS)$_2$, respectively. Here, the rotaxane molecule LysoSQRot-(RDGS)$_2$ consists of an unsymmetrical red emissive SQ chromophore conjugated with a morpholine functionality for lysosome targeting and two RGDS peptide tethered tetralactam macrocycles to enhance water solubility and to protect the chromophore from nucleophilic attack in the cancer cell milieu as well as to target overexpressed $\alpha_V\beta_3$ integrin.

Manual Solid-Phase Peptide Synthesis (SPPS):

Arg-Gly-Asp-Ser (RGDS) tetrapeptide and azide conjugated RGDS peptides were synthesized by manual microwave (MW)-assisted Fmoc-SPPS procedure on a MW peptide synthesizer (*CEM, Discover Bio*). Wang resin (LL, 0.60 mmol/g loading density) was used to synthesize RGDS tetrapeptide, azide linked RGDS peptide, SSQRot-$(RGDS)_2$ and LysoSQRot-$(RGDS)_2$ (**Scheme 5, 6**). Fmoc-Arg(Pbf)-OH, Fmoc-Gly-OH, Fmoc-Asp(OtBu)-OH and Fmoc-Ser(tBu)-OH amino acids were used.

First Amino Acid [Fmoc-Ser(tBu)-OH] Loading on Wang Resin (LL): The first amino acid Fmoc-Ser(tBu)-OH loading on Wang resin was performed in a SPE cartridge with frit. The Wang resin (0.1 mmol) was swollen in DMF (2 mL) for 1 h, then drains the solvent off and washed with DMF (2×). Fmoc-Ser(tBu)-OH (5 eq), HBTU (4.9 eq.) and HOBt (5 eq.) were dissolved in 2 mL DCM/DMF (1:1), subsequently DIPEA (10 eq.) was added and the mixture were taken in the SPE cartridge containing the Wang resin and stirred for 3 h under N_2 bubbling. Drain the solvent and the resin was sequentially washed with DMF (2×), DCM (2×), and MeOH (2×).

After Fmoc-Ser(tBu)-OH loading on Wang resin, the loading density was determined by UV/vis spectroscopy of the Fmoc-dibenzofulvene deprotection product.

Estimation of the First Amino Acid Loading*:* The Fmoc-Ser(tBu)-Wang resin (5 mg) and 1,8-diazabicyclo[5.4.0]undec-7-en (DBU) in NMP (2 mL, 2 % in NMP) were taken in a 10 mL volumetric flask. It was shaken for 30 min in a shaker then the 10 mL volumetric flask was filled up to the mark with CH_3CN. The solution was diluted with CH_3CN (1/12.5) and transferred to an UV quartz cuvette. The cleaved dibenzofulvene was monitored at 304 nm (ε_{304} = 7624 L

$mol^{-1}cm^{-1}$) and corrected against reference. The resin loading was calculated based on Lambert-Beer's law.

ρ(mmol/g) = 163.96×($A - A_0$)/m

ρ = loading density of the resin

A = absorption of a sample

A_0 = absorption of reference

m = mass of the analyzed resin in mg.

MW-assisted SPPS Synthesis of RGDS peptide and azide conjugated RGDS peptide: The synthesis of RGDS and azide conjugated RGDS peptides were performed using MW assisted Fmoc protocol on Wang resin at a 0.1 mmol scale.

Protocols for MW-Assisted SPPS:

1. Bubbling during the MW-assisted synthesis for all Steps: on 3 sec; off 7 sec.

2. **Fmoc deprotection**: 20% piperidine/DMF; time 210 sec, power 20 W, temperature 75ºC, delta temperature 5ºC.

To prevent aspartimide formation during the Fmoc deprotection step of Asp containing RGDS sequence, 0.1 M HOBt in the Fmoc deprotection solution (20% piperidine/0.1 M HOBt/DMF) has been used to reduce aspartimide formation.

Washing after Fmoc-deprotection: DMF (4×), DCM (4×), DMF (4×) to remove dibenzofulvene by-product.

3. **Coupling**: 0.5 M HBTU/0.5 M HOBt/2 M DIPEA/DMF;

General protocol: time 300 sec, power 20 W, temperature: 75ºC, delta temperature: 5ºC.

Arg (R) is susceptible to γ-lactam formation and hence greatly reduces the coupling efficiency. Special care was taken in case of Arg coupling to minimize side reactions. A modified double coupling has been performed for Arg. 1st

coupling: 25 min at 25°C (Power 0 W), then 2 min at 75°C (Power 30 W); 2nd coupling: 5 min at 75°C (Power 30 W).

Washing after coupling: DMF (3×), DCM (3×), DMF (3×)

After the final step, the resin was transferred into a SPE cartridge with frit and washed with DMF (5×), DCM (5×), MTBE (5×), and finally with MeOH (5×). The resins were dried in vacuum and stored at −18°C.

Test Cleavage from Wang Resin: To a pinch of the resin a mixture of TFA/EDT/TIS/H_2O (92.5/2.5/2.5/2.5 *v/v/v/v*) was added and the cleavage reaction was performed by shaking the resin for 2 h at room temperature. Afterward the resin beads were filtered off and the solvent was evaporated under N_2 stream. The RGDS peptide was precipitated by using cold MTBE. The MTBE suspension was centrifuged at −5°C. The supernatant was discarded, and the residue was washed with cold MTBE (3×) and dried to obtain the desired product RGDS and N_3-RGDS.

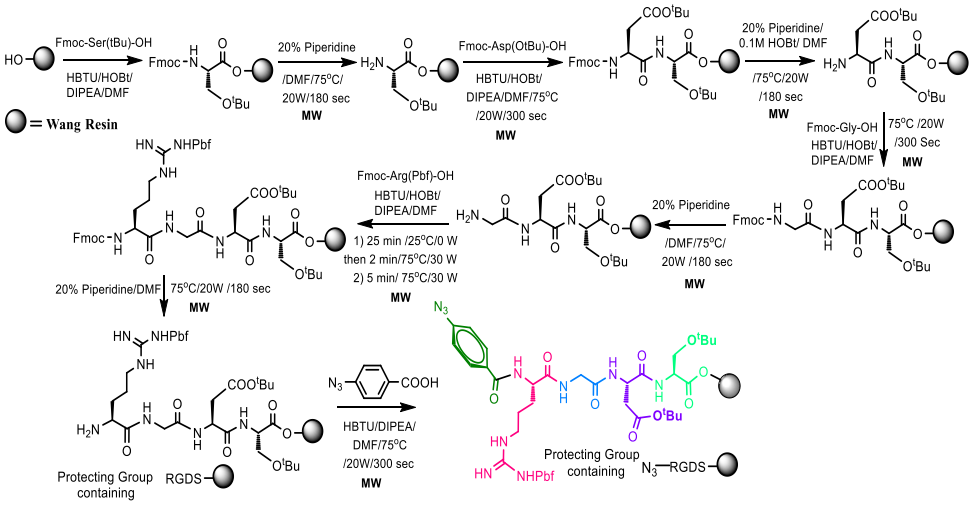

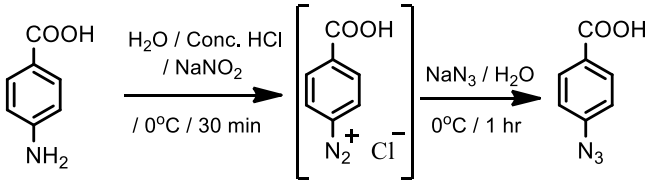

4-Aminobenzoic acid

4-Azidobenzoic acid

9

Scheme 5: Synthesis of RGDS and N_3-RGDS

Working Steps	Reagents	Reaction condition
Coupling	HBTU/HOBt/DIPEA/DMF	300 sec/75°C/20 W Special care for Arg coupling: 1) 25 min/25°C/0 W then 2 min/75°C/30 W 2) 5 min/75°C/30 W
Washing after coupling	DMF(5×), DCM(5×), DMF(5×)	
Fmoc deprotection	20% piperidine/DMF Special care for Asp Fmoc-deprotection step: 20% piperidine/DMF with 0.1 M HOBt monohydrate	210 sec/75ºC/20 W
Washing after deprotection	DMF (4×), DCM (4×), DMF (4×)	
Washing after final coupling	DMF(5×), DCM(5×), MTBE(5×), MeOH(5×)	
Test Cleavage	TFA/EDT/TIS/H_2O (92.5/2.5/2.5/2.5, *v*/*v*/*v*/*v*)	2 h/25°C

RGDS Peptide:

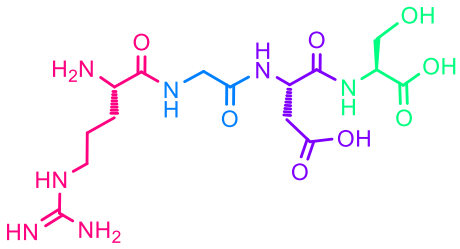

HRMS (ESI +ve) *m/z*: Observed for $C_{15}H_{28}N_7O_8^+$ $[M+H]^+$ =434.2001, $[M+H]^+$calcd = 434.1994.

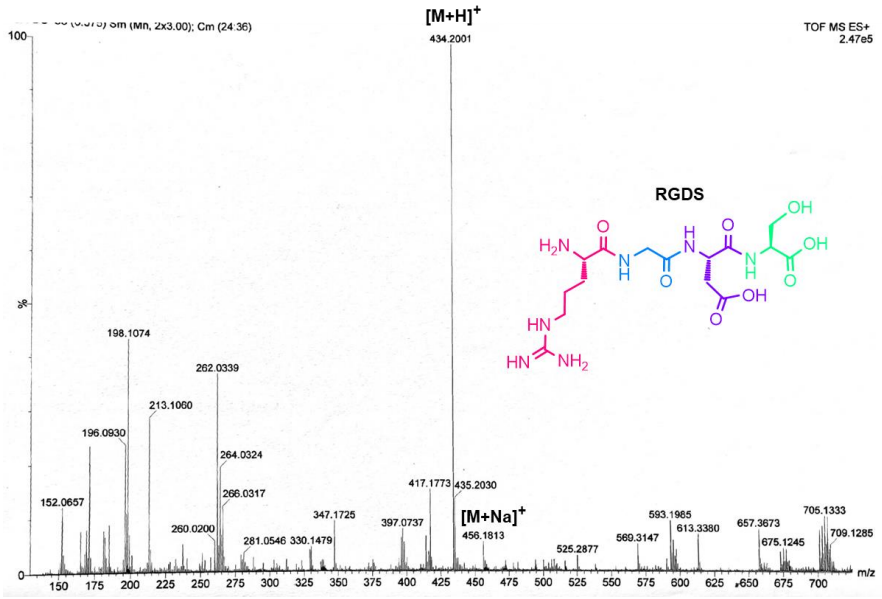

Figure 27. HRMS (ESI +ve) spectrum with isotropic distribution pattern of RGDS peptide.

Synthesis of 4-azidobenzoic acid (9): 4-Aminobenzoice acid (1.37 g, 10 mmol) was suspended in 20 mL of H_2O/conc. HCl (1:1) and cooled at 0°C.

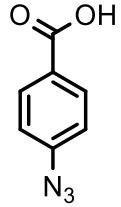

9

$NaNO_2$ (0.79 g, 11.5 mmol) was dissolved in H_2O (8 mL), cooled at 0°C and added drop wise to the suspended acidic solution of 4-aminobenzoice acid. The reaction mixture was stirred for 30 min at 0°C. NaN_3 (0.72 g, 11 mmol) was dissolved in H_2O (8 mL) and also cooled at 0°C. The cooled NaN_3 solution was added drop wise to the cooled reaction mixture and stirred for another 1 hr. The white precipitate was filtered off, washed with ice cold water and dried under vacuum to obtain a white solid of 4-azidobenzoic acid (9).

Yield: 1.1 g (67%).

^{1}H NMR (300 MHz, DMSO-d_6, 25°C): δ =12.94 (s, 1H), 7.97 (d, 2H, J = 8.1 Hz), and 7.22 (d, 2H, J = 8.1 Hz) ppm.

^{13}C NMR (75 MHz, DMSO-d_6, 25°C): δ =167.0, 144.3, 131.7, 127.7, and 119.6 ppm.

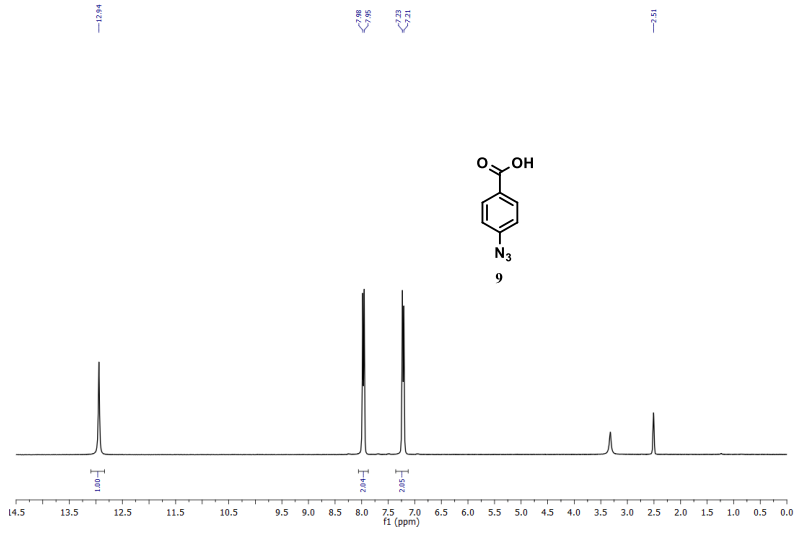

Figure 28. ^{1}H NMR (300 MHz, DMSO-d_6, 25°C) spectrum of 4-azidobenzoic acid 9.

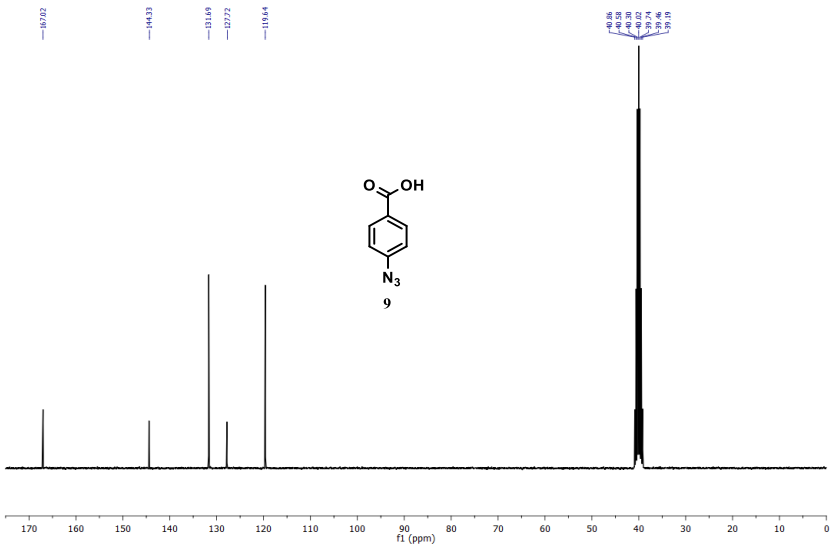

Figure 29. ^{1}H NMR (300 MHz, DMSO-d_6, 25°C) spectrum of 4-azidobenzoic acid (9).

N_3-RGDS Peptide:

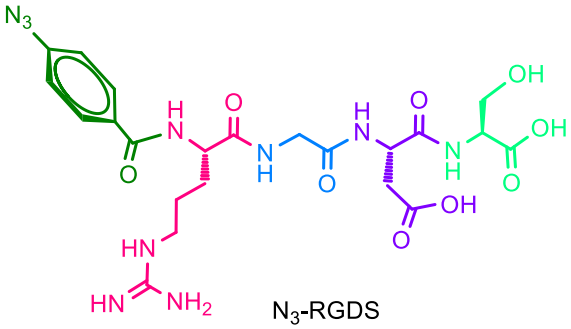

N_3-RGDS

HRMS (ESI +ve) *m/z*: Observed for $C_{22}H_{31}N_{10}O_9^+$ $[M+H]^+$ = 579.0498, $[M+H]^+$calcd = 579.2270.

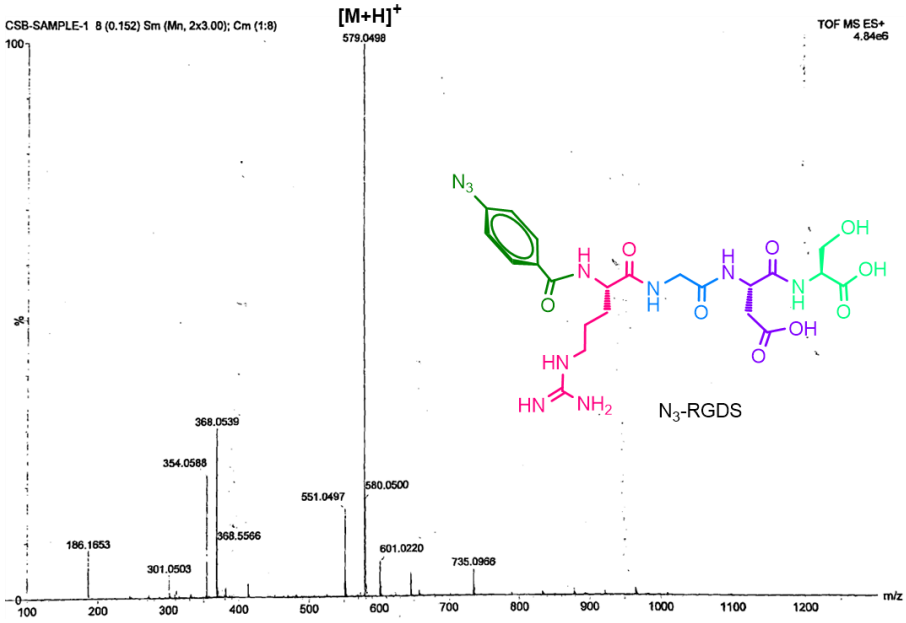

Figure 30. HRMS (ESI +ve) spectrum of N_3-RGDS.

Click Chemistry on Wang resin to Synthesize SSQRot-(RGDS)$_2$ and LysoSQRot-(RGDS)$_2$: The syntheses of SSQRot-(RGDS)$_2$ and LysoSQRot-(RGDS)$_2$ were carried out by click chemistry using copper(I)-catalyzed azide-alkyne cycloaddition (CuAAC) on the Wang resin at a 0.05 mmol scale.

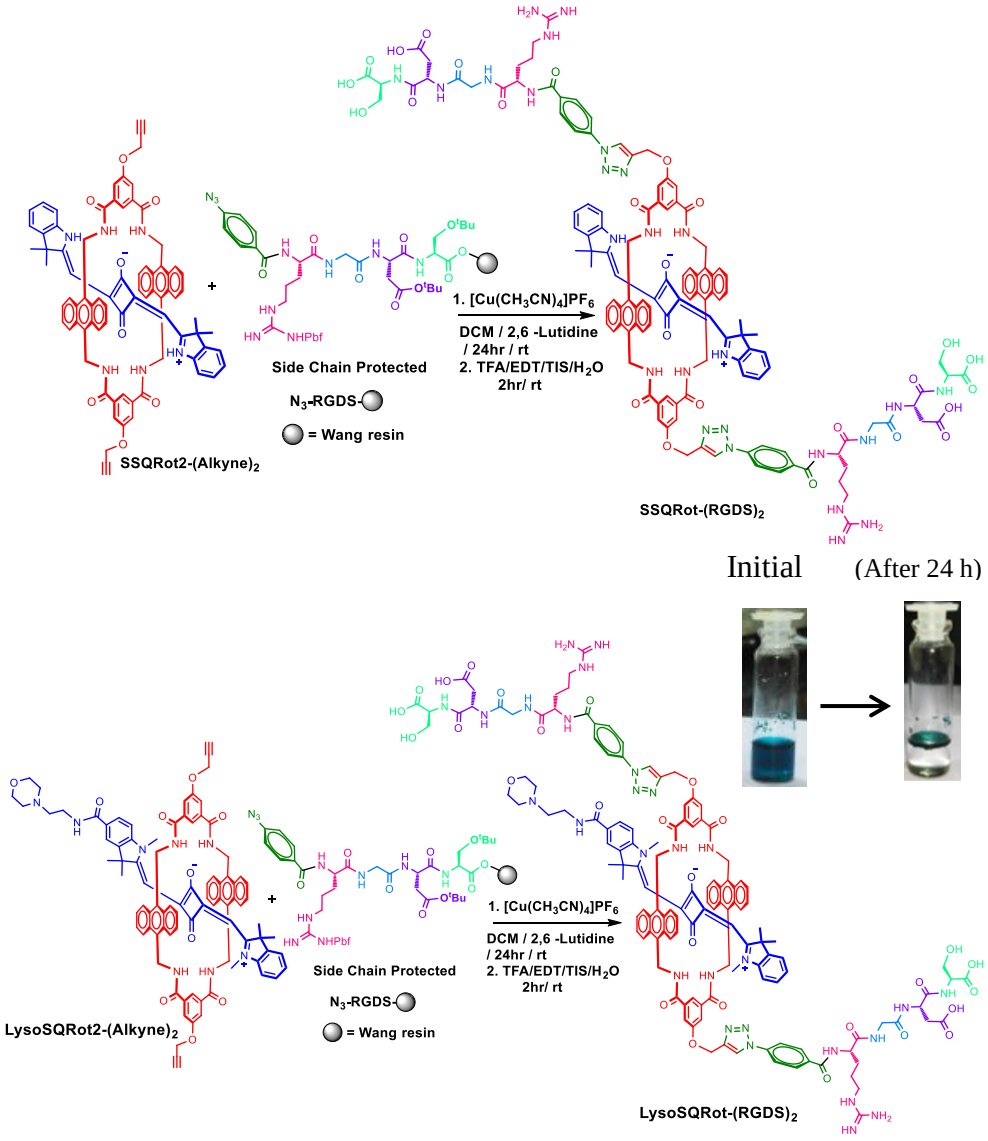

Scheme 6. Synthesis of SSQRot-(RGDS)$_2$ and LysoSQRot-(RGDS)$_2$

Synthesis of SSQRot-(RGDS)$_2$: Side chain protected N_3-RGDS-Wang resin (0.05 mmol) was swollen in 2 mL of degassed DCM for 1 hr, then SSQRot2-(Alkyne)$_2$ (0.025 mmol), 2-3 drops of 2,6-Lutidine, and $[Cu(CH_3CN)_4]PF_6$ (8.2 mg, 0.025 mmol) were added to the reaction vial. The reaction mixture was vigorously shaken at 25°C for 24 h. The resin was washed with cold Et_2O (3×) to get see green colored side chain amino acids protected SSQRot-(RGDS)$_2$-Wang resin. To a pinch of the SSQRot-(RGDS)$_2$-Wang resin a mixture of 2 mL of TFA/EDT/TIS/H_2O (92.5/2.5/2.5/2.5 *v*/*v*/*v*/*v*) was added and the resin cleavage along with the side chain amino acids deprotection reaction was performed by shaking the resin for 2 hr at 25°C. Afterward the resin beads were filtered off and the solvent was evaporated under N_2 stream. The SSQRot-(RGDS)$_2$ was precipitated by using cold Et_2O. The Et_2O suspension was centrifuged at –5°C. The supernatant was discarded, the residue was washed with cold Et_2O (3×) and dried to acquire the see green colored desired product SSQRot-(RGDS)$_2$.

HRMS (ESI +ve) *m*/*z*: Observed for $C_{124}H_{127}N_{26}O_{26}^{+3}$ $[M+3H]^{+3}$ = 798.9803, $[M+3H]^{+3}$ calcd = 798.9811 (*m*/*z*, *z* = 3).

Photophysical properties in DMSO λ_{abs}= 660 nm, λ_{em}= 675 nm, Stokes shift ($\Delta\lambda$) = 15 nm, ε = 1.49 ×10^5 $M^{-1}cm^{-1}$, Φ_f = 0.31 in DMSO (Φ_f of Zinc phthalocyanine as reference = 0.20 in DMSO), τ = 2.80816±0.033509 ns.

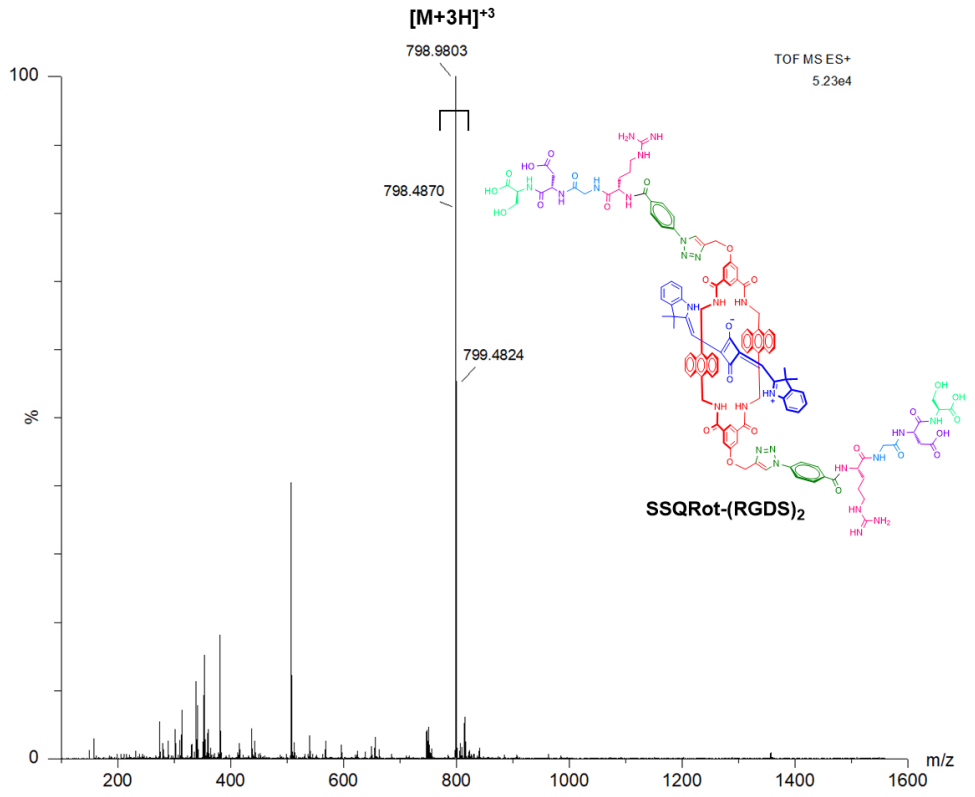

Figure 31. HRMS (ESI +ve) spectrum of SSQRot-$(RGDS)_2$.

Synthesis of LysoSQRot-$(RGDS)_2$: Side chain amino acids protected N_3-RGDS-Wang resin (0.05 mmol) was swollen in degassed DCM (2 mL) for 1 hr, then LysoSQRot2-$(Alkyne)_2$ (0.025 mmol), 2-3 drops of 2,6-Lutidine, and $[Cu(CH_3CN)_4]PF_6$ (8.2 mg, 0.025 mmol) were added to the reaction vial. The reaction mixture was vigorously shaken at 25°C for 24 hr. The resin was washed with cold Et_2O (3×) to get see green colored side chain amino acids protected LysoSQRot-$(RGDS)_2$-Wang resin. To a pinch of the LysoSQRot-$(RGDS)_2$-Wang resin a mixture of TFA/EDT/TIS/H_2O (92.5/2.5/2.5/2.5 *v*/*v*/*v*/*v*)

was added and the resin cleavage along with the side chain amino acids deprotection reaction was performed by shaking the resin for 2 h at room temperature. Afterward the resin beads were filtered off and the solvent was evaporated under N_2 stream. The LysoSQRot-$(RGDS)_2$ was precipitated by using cold Et_2O. The Et_2O suspension was centrifuged at –5°C. The supernatant was discarded, the residue was washed with cold Et_2O (3×) and dried to acquire the see green colored desired product LysoSQRot-$(RGDS)_2$.

^{1}H NMR (300 MHz, $CDCl_3$, 25°C): δ = 9.37 (1H, s), 9.32 (1H, s), 9.24 (2H, s), 8.80 (2H, br), 8.59 (2H, d, J = 7.5 Hz), 8.38 (2H, br), 8.30 (1H, br), 8.23 (2H, br), 8.19 (4H, s), 8.16-8.14 (4H, m), 8.10-8.08 (12H, m), 7.93 (1H, s), 7.81-7.77 (4H, m), 7.76-7.72 (4H, m), 7.56-7.50 (3H, m), 7.29-7.25 (8 H, m), 7.10 (4H, br), 6.66 (4H, br), 5.60 (4H, s), 5.41 (4H, br), 5.07-5.02 (4H, m), 4.70 (2H, t, J = 7.1 Hz), 4.52 (2H, m), 4.45 (2H, m), 4.43 (1H, s) 4.38 (1H, s), 4.27-4.25 (4H, m), 3.78-3.76 (4H, m), 3.74-3.71 (2H, m), 3.66 (4H, m), 3.52 (2H, m), 3.42-3.38 (4H, s), 3.17-3.16 (4H, m), 2.76-2.74 (4H, m), 2.70 (3H, s), 2.68 (3H, s), 2.52 (2H, br), 1.87-1.78 (4H, m), 1.58 (4H, m), and 1.03 (12H, s) ppm.

^{13}C NMR (100 MHz, $CDCl_3$, 25°C): δ = 181.4, 178.1, 171.3, 170.8, 170.4, 169.1, 166.8, 166.1, 157.8, 157.3, 151.4, 143.1, 142.1, 137.4, 130.9, 130.1, 129.7, 128.2, 126.1, 125.5, 122.8, 121.6, 121.1, 115.1, 113.4, 111.2, 109.7, 105.7, 87.4, 79.6, 78.9, 70.6, 66.7, 60.2, 57.9, 56.1, 53.8, 49.4, 49.0, 48.5, 45.6, 37.1, 35.9, 31.7, 29.4, 29.2, 27.1, 26.7, 22.6, and 21.24 ppm.

2D NMR: ^{1}H–^{1}H gCOSY (Gradient-selected Correlation Spectroscopy) NMR analysis established coupling connectivity (Figure S28).

HRMS (MALDI +ve) *m/z*: Observed for $C_{133}H_{140}K_5N_{28}O_{28}^{+5}$ $[M+5K]^{5+}$ = 554.5711 $[M+5K]^{5+}$ calcd = 554.5717 (*m/z*, *z* = 5).

Photophysical properties in DMSO λ_{abs}= 652 nm, λ_{em}= 665 nm, Stokes shift ($\Delta\lambda$) = 13 nm, ε = 1.52 ×10^5 $M^{-1}cm^{-1}$, Φ_f = 0.28 in DMSO (Φ_f of Zinc phthalocyanine as reference = 0.20 in DMSO), τ = 3.67633±0.031936 ns.

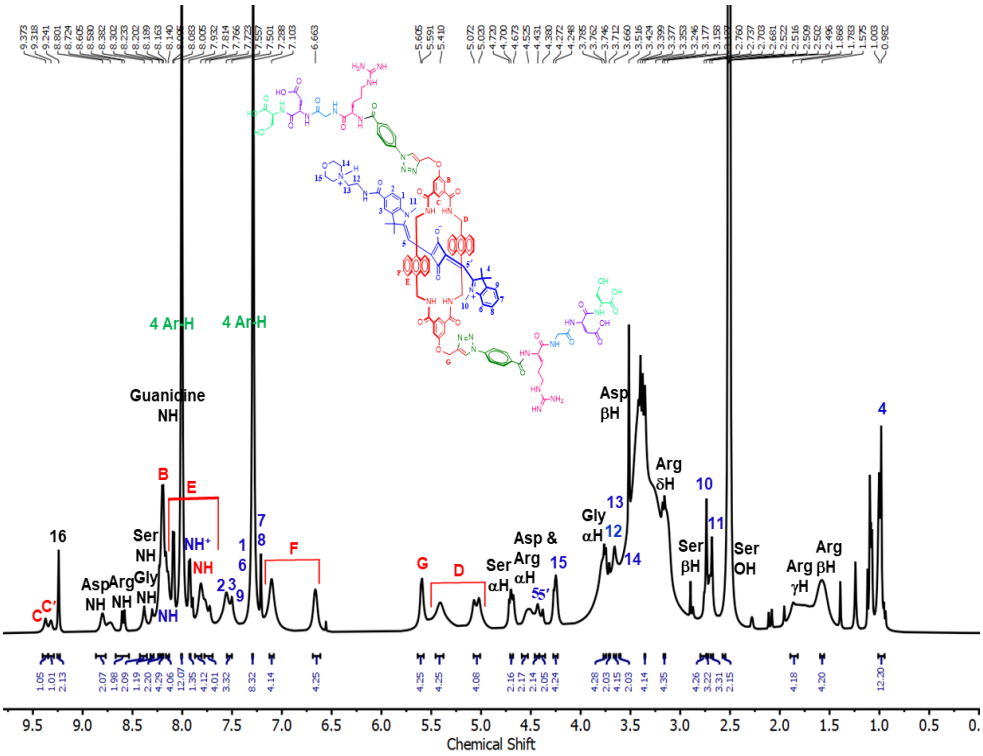

Figure 32. ^{1}H NMR (300 MHz, DMSO-d_6, 25°C) spectrum of LysoSQRot-(RGDS)$_2$

(a)

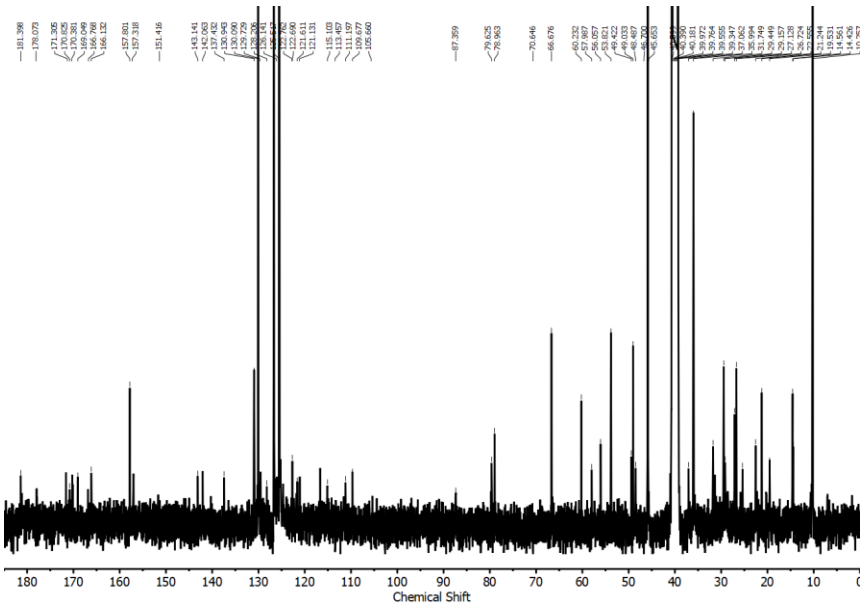

(b)

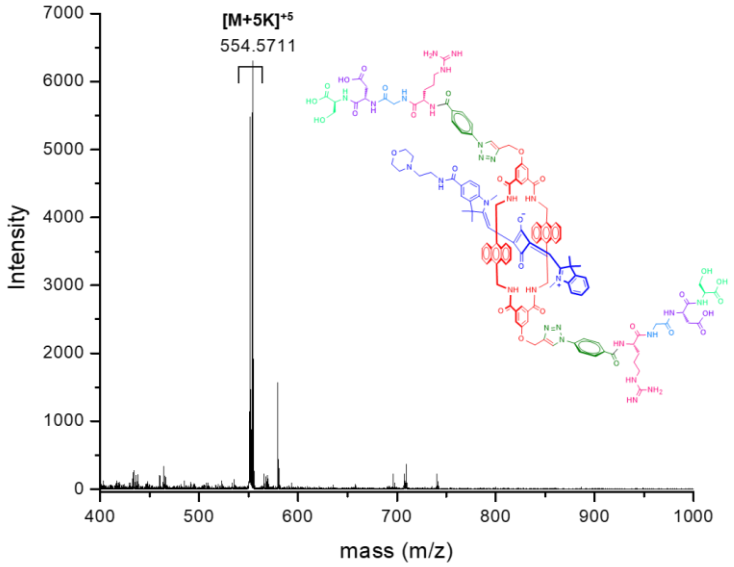

Figure 33. (a) ^{13}C NMR (100 MHz, DMSO-d_6, 25°C) spectrum of LysoSQRot-(RGDS)$_2$ (b) HRMS (MALDI) spectrum of LysoSQRot-(RGDS)$_2$.

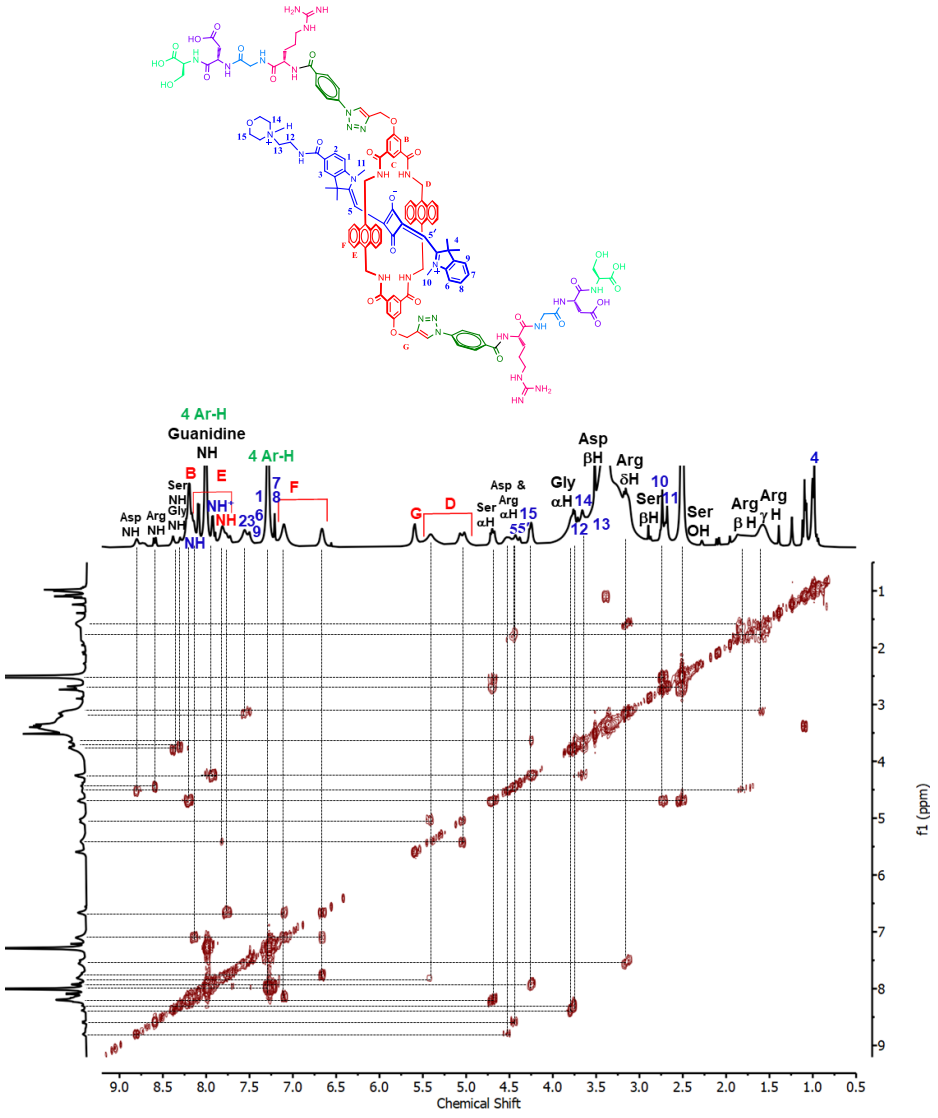

Figure 34. Partial ^{1}H-^{1}H gCOSY(Gradient-selected Correlation Spectroscopy) NMR (300 MHz, $CDCl_3$, 25°C) spectrum of LysoSQRot-$(RGDS)_2$.

METHODS:

Microwave Synthesizer: Synthesis of 2,3,3-Trimethylindolenine, symmetrical squaraine chromophore (SSQ), unsymmetrical squaraine chromophore (USQ-COOH), RGDS peptide, and azide linked RGDS peptide (N_3-RGDS) were performed using manual microwave solid phase peptide synthesizer (CEM corporation, USA make, model discover bio, precise temperature is controlled by fiber optic) with decent overall yield from easily available low cost starting materials.

NMR Spectroscopy: ^{1}H NMR, ^{13}C NMR, ^{1}H-^{1}H gCOSY, and ^{1}H-^{1}H ROESY were conducted on Bruker DPX300 MHz and DPX400 MHz spectrometers at 25°C in proper deuterated solvents. Manufacturers' provided Bruker TopSpin 3.6.2 software was used to process the data.

HRMS: High-resolution electrospray ionisation mass spectrometry (HRMS-ESI) in positive mode was achieved on a Q-TofmicroTM (Waters Corporation) mass spectrometer. Manufacturers' provided mass application software MassLynx V4.1 was used to process the data.

Single Crystal X-Ray Diffraction: Single crystals suitable for X-ray diffraction was achieved by vapour diffusion method. Diffraction data were collected on a micro focus Single Crystal X-ray Diffraction instrument (Make: Bruker, Model: D8 Quest) with MoKα radiation (a graded multilayer mirror monochromator, λ = 0.71073 Å) at 293 K. A PHOTON-100 CMOS detector was used. Structures of the molecules were solved by direct methods using the SHELXT 2014/5 program. Refinements were accomplished with a full-matrix least squares method against F^2 using SHELXL-2018/3[41-42] incorporated in Olex2[43] crystallographic collective package. The non-hydrogen atoms were refined with anisotropic thermal parameters.

Compound USQ-COOH: Blue crystals were obtained by slow evaporation from MeOH. Formula sum = C60 H63.70 N4 O10, formula weight = 1000.85, crystal system = monoclinic, space group = *P* 21/c, *a* = 16.535(15) Å, *b* = 7.195(7) Å, *c* = 22.06(2) Å, α = 90°, β= 94.33(3)°, γ = 90°, *V* = 2617(4) Å^3, Z = 2, D_{calcd} = 1.270 g cm^{-3}, μ = 0.087 mm^{-1}. The final R value was R_1 = 0.0991 and wR_2 = 0.2070 for reflections with I > 2ζ(I). CCDC number 2128042.

Compound **Macrocycle 2-Alkyne**: A solution of compound Macrocycle 2-Alkyne in MeOH was placed in a 2 mL vial and put inside a 20 mL vial filled with 10 mL Et_2O. The larger vial was capped and allow to slow diffusion. White colored block shaped crystals were obtained by vapour diffusion after 2 days. Formula sum = C57.34 H50.92 N4 O7.71, formula weight = 919.39, crystal system = triclinic, space group = *P* -1, *a* = 11.428(5) Å, *b* = 14.231(6) Å, *c* = 16.320(7) Å, α = 101.784(12)º, β = 100.343(12)°, γ = 95.861(12)°, *V* = 2529.3(19) Å^3 , *Z* = 2, D_{calcd} = 1.207 g cm^{-3}, μ = 0.081 mm^{-1}. The final R value was R_1 = 0.0988 and wR_2 = 0.2574 for reflections with I > 2ζ(I). CCDC number 2128044.

Compound SSQRot1: A solution of compound SSQRot1 in $CHCl_3$ was placed in a 2 mL vial and put inside a 20 mL vial filled with 10 mL Et_2O. The larger vial was capped and allow to slow diffusion. Blue colored block shaped crystals were obtained by vapour diffusion after 3 days. Formula sum = C82 H76 N6 O6 [+ solvent], formula weight = 1241.49, crystal system = triclinic, space group = *P* -1, *a* = 10.287(5) Å, *b* = 11.953(5) Å, *c* = 16.778(7) Å, α = 72.327(11), β = 81.234(11), γ = 76.697(11), *V* = 1905.3(15) Å^3, *Z* = 1, D_{calcd} = 1.082 g cm^{-3}, μ = 0.068 mm^{-1}. The final R value was R_1 = 0.0997 and wR_2 = 0.3395 for reflections with I > 2ζ(I). CCDC number 2128045.

Compound SSQRot2-(Alkyne)$_2$: A solution of compound SSQRot2-(Alkyne)$_2$ in a mixture of $CHCl_3$ and acetone (1:1) was placed in a 2 mL vial and put inside a 20 mL vial filled with 10 mL Et_2O. The larger vial was capped and allow to slow diffusion. Blue colored cube shaped crystals were obtained by vapour diffusion after 2 days. Formula sum = C86 H76 N6 O10, formula weight = 1353.53, crystal system = triclinic, space group = *P* -1, *a* = 11.550(12) Å, *b* = 12.221(14) Å, *c* = 14.158(17) Å, α = 88.41(4)°, β = 67.04(4)°, γ = 78.15(4)°, *V* = 1798(4) Å^3, *Z* = 1, D_{calcd} = 1.250 g cm^{-3}, μ = 0.082 mm^{-1}. The final R value was R_1 = 0. 0.0867 and wR_2 = 0. 0.2987 for reflections with I > 2ζ(I). CCDC number 2128046.

Crystallographic data were deposited at Cambridge Crystallographic Data Centre (CCDC). These data can be obtained free of charge from the Cambridge Crystallographic Data Centre, www.ccdc.cam.ac.uk/structures.

Absorption Spectroscopy: Absorption spectra were recorded by a JASCO V-730 double-beam spectrophotometer with wavelength range from 200 to 1100 nm in a quartz cuvette of 1 cm path length. Manufacturers' supplied Spectra Manager Version 2 software was used to process the data.

Fluorescence Spectroscopy: Fluorescence emissions were collected on a Horiba Jobin Yvon FluoroMax-4 spectrofluorometer operated by FluorEssence Version 3.9.0.1 software. 5 nm excitation and emission slit widths were used.

Relative Quantum Yield of the Squaraine Dye and Rotaxane Molecules: Fluorescence quantum yields (Φ_f) of the LysoSQ, SSQRot1, SSQRot2-(Alkyne)$_2$, LysoSQRot2-(Alkyne)$_2$, SSQRot-(RGDS)$_2$, and LysoSQRot-(RGDS)$_2$ molecules were calculated by relative method. The integrated fluorescence intensity of the rotaxane molecules were equated with fluorescence intensity of a reference molecule [Φ_f (st) of Zinc phthalocyanine is 0.17 in DMF and 0.20 in DMSO] by the subsequent equation.

Φ_f (u) = Φ_f (st) × [(A_{st} × F_u × η_u^2) /(A_u × F_{st} × η_{st}^2)]

Φ_f(u): fluorescence quantum yield of the synthesized rotaxane molecule

Φ_f(st): fluorescence quantum yield of the reference molecule

A_{st} and A_u: Absorbance of reference and rotaxane molecules at the excitation wavelength, respectively

F_{st} and F_u: Integrated fluorescence areas under the adjusted fluorescence spectra for the reference and rotaxane molecules, respectively

η_{st} and η_u: Refractive indices of the solvent wherein the reference and rotaxane molecules were studied, respectively

"u" refers to the unknown molecule and "st" stands for the standard molecule

The relative Quantum yields (Φ_f) of the LysoSQ and five rotaxane molecules were measured as 0.21 [LysoSQ in DMSO], 0.14 [SSQRot-1 in DMF], 0.14 [SSQRot2-$(Alkyne)_2$ in DMF], 0.15 [LysoSQRot2-$(Alkyne)_2$ in DMSO], 0.31 [SSQRot-$(RGDS)_2$ in DMSO], and 0.28 [LysoSQRot-$(RGDS)_2$ in DMSO].

Fluorescence Lifetime Measurement: Time-correlated single photon counting (TCSPC) system was exploited to record the fluorescence lifetime (τ) of rotaxane molecules [SSQRot1, SSQRot2-$(Alkyne)_2$, LysoSQRot2-$(Alkyne)_2$, SSQRot-$(RGDS)_2$, and LysoSQRot-$(RGDS)_2$] by Horiba DeltaFlex lifetime machine (Horiba Jobin Yvon IBH Ltd, Glasgow, UK). A Delta Diode laser of 650 nm (Model: DD-650L, Horiba Scientific) excitation source was used to obtain the τ of rotaxane molecules in DMSO. Fluorescence lifetime measurements and data analyses were executed by Horiba EzTime decay analysis software.

Stability of the Probes Under Photoirradiation: LysoSQ (2 μM) and LysoSQRot-$(RGDS)_2$ (2 μM) compounds were irradiated separately in PBS, pH 7.2 in exposed to air with a distance of 12 cm from a 200 W Xenon lamp (using

filter to allow wavelengths > 500 nm) over 1 h and examined the stability of the probes through absorption and fluorescence experiments.

Cell Culture: A549, MDA-MB-231, HeLa, and C2C12 cell lines were cultured in DMEM (pH 7.4) in the presence of 10% FBS and antibiotic-antimycotic solution 100×(comprising 10000 units penicillin, 10 mg streptomycin, and 25 μg amphotericin B per mL in 0.9% normal saline). The cells were preserved in a 5% CO_2 incubator at 37°C and were routinely passaged.

Cell Viability: MTT assay was used to find out the cell viability against A549 and HeLa carcinoma cell lines as well as mouse myoblast C2C12 noncancerous cell line over 24 h at different concentrations of LysoSQRot-$(RGDS)_2$. Freshly harvested A549, HeLa, and C2C12 cells were individually seeded at a density of ~10^4 cells on a 96-well plate by DMEM for 24 h incubation. Successively 24 h incubation, various doses (1, 2, 5, 10, 15, and 20 μM per well) of LysoSQRot-$(RGDS)_2$ molecule was treated at 37°C for 24 h. The A549, HeLa, and C2C12 cells were then separately incubated with MTT solution (10 μL, concentration: 5 mg mL^{-1} in PBS) at 37°C for 4 h in darkness. The consequences (performed the assay in triplicates) were measured as % of the viable cells by the succeeding formula:

Viable cells (%) = (*A* of treated cells / *A* of untreated cells) × 100.

Live Cell Confocal Laser Scanning Microscopy: Live cell confocal laser scanning microscopic (CLSM) images were taken on a Leica STELLARIS 5 with white light laser (WLL) combined with Acousto-Optical Beam Splitter (AOBS) and HyD S detectors. It was equipped with a 100× oil plan apochromatic objective. For live cell confocal microscopy A549, MDA-MB-231, and HeLa cells were separately seeded in a 35 mm glass bottomed cell culture confocal dishes (SPL Lifesciences) at a density of 10^4 cells/mL and permissible to grow in DMEM for 24 h at 37°C in a 5% CO_2 incubator.

Subsequently the cells were washed with 1x PBS for three times. After that, live A549, MDA-MB-231, and HeLa cells were separately incubated with LysoSQRot-$(RGDS)_2$ (2.0 μM) in media for 12 h in 5% CO_2 atmosphere at 37°C and then rinsed with 1x PBS for three times. As per the manufacturer's protocol the cells were incubated with LysoTracker Green DND-26 (LTG, 75 nM) at 37°C for 30 min in 5% CO_2 atmosphere. The cell lines were finally incubated with Hoechst (1.5 μg/mL) for 20 min and washed in the similar protocol. Before confocal imaging the cells were washed with 1x PBS for three times and phenol red free media was added. Confocal laser scanning microscopic images were captured by a STELLARIS 5 microscope with 100x /1.40 (Specification: HC PL APO 100x/1.40 OIL CS2) oil plan apochromatic objective. All over the live cell confocal laser scanning microscopic imaging process 37°C and 5% CO_2 atmosphere was preserved. A distinct set-up for the live cell confocal microscopy instrument maintaining 37°C and 5% CO_2 atmosphere is shown in Figure S52. Confocal microscopic images were analyzed and processed by Leica Application Suite X (LAS X 4.3.0.24308) software.

For Hoechst: laser excitation wavelength = 405 nm (blue channel, detection range of emission wavelength 415–490 nm); LysoTracker Green DND-26 (LTG): laser excitation wavelength = 498 nm (green channel, detection range of emission wavelength 500–572 nm); Rotaxane molecules: laser excitation wavelength = 638 nm, (Cy-5 channel, detection range of emission wavelength 650–710 nm).

Determination of Pearson's Correlation Coefficient (PCC): PCC is a typical statistical examination in pattern recognition for matching one CLSM image (red channel, rotaxane staining) with another (green channel, LysoTracker Green staining). PC graph can explain the magnitude of overlapping amongst two patterns in a colocalization image of A549, MDA-MB-231, and HeLa cells. PCC was obtained by the LAS X 4.3.0.24308 software.

PCC was acquired (image comprising of red and green channels) by the succeeding equation:

$$PCC = \frac{\sum_i (S1_i - S1_{avg}) * (S2_i - S2_{avg})}{[\sum_i (S1_i - S1_{avg})^2 * \sum_i (S2_i - S2_{avg})^2]^{(1/2)}}$$

S1 = signal intensity of pixels (pixel i) in the green channel

S2 = signal intensity of pixels (pixel i) in the red channel.

$\mathbf{S1_{avg}}$ = mean values of pixels in the green channel

$\mathbf{S2_{avg}}$ = mean values of pixels in the red channel.

Live Cells 3D Confocal Image using the Synthesized LysoSQRot-$(RGDS)_2$: To obtain the 3D view of lysosomal staining, Z-stack images of live A549 and HeLa cells stained with Hoechst and our synthesized LysoSQRot-$(RGDS)_2$ probe were captured by a Leica STELLARIS 5 confocal microscope. For the live cell 3D confocal image creation, the images were harvested every 0.4 μm on the Z-axis. Eighteen various frames for each channel were snapped over a time period of 6 min and ultimately regenerated with the help of LAS X software to obtain the 3D confocal image. The 3D reconstructed CLSM images evidently specify the spherical lysosomal compartment inside the live A549 and HeLa cells.

Real-Time Tracking of Lysosomes in Live Cells using the Synthesized LysoSQRot-(RGDS)$_2$ Dye: Lysosomal movement in the live A549 and HeLa cells were tracked using the synthesized lysosome targeting LysoSQRot-(RGDS)$_2$ probe over a time course of 2-3 min by a Leica STELLARIS 5 instrument. 10 frames were captured over 2 min for A549 and 3 min for HeLa cells to make separate real-time movies by LAS X software.

Multicolor Confocal Imaging of Live Carcinoma Cells: Multicolor imaging of intracellular organelles in the same live cancer cell was accomplished by a mixture of appropriate organelle staining probes with discrete excitation/emission bands. MitoTracker Green (MTG, green emitting) was used to specifically stain the mitochondria, blue-fluorescent Hoechst to label the nucleus, and the synthesized LysoSQRot-(RGDS)$_2$ to stain the lysosomes of live A549 and HeLa cells.

Multicolor confocal imaging of live A549 and HeLa cells were captured by using appropriate filters.

For MTG, laser excitation wavelength = 488 nm, green channel, detection range of emission wavelength 499–544 nm.

Hoechst, laser excitation wavelength = 405 nm, blue channel, detection range of emission wavelength 415–490 nm.

Synthesized LysoSQRot-(RGDS)$_2$ probe, laser excitation wavelength = 638 nm, Cy-5 channel, detection range of emission wavelength 650–710 nm.

Flow Cytometry: Flow cytometric assay were performed on a BD FACSVerse flow cytometer instrument (BD Biosciences) and the data were examined by BD FACSuite software.

Results and discussion:

Deviations in ^{1}H NMR Chemical Shift for Rotaxane Formation:

The deviations in ^{1}H NMR chemical shift owing to rotaxane formation for SSQRot1, SSQRot2-(Alkyne)$_2$, and LysoSQRot2-(Alkyne)$_2$ with respect to free Macrocycle 1 and Macrocycle 2-Alkyne as well as SSQ and Lyso-SQ axle, respectively, are compared (**Figures 18, Figure 20b, and 22**). Downfield shifts for macrocyclic protons "C" and "NH" owing to hydrogen bonding with squaraine oxygens are the most characteristic changes. In addition, a significant upfield shift for squaraine protons 5 and macrocyclic protons E and F are perceived for rotaxane construction. In the case of rotaxanes, the anthracene residues of the Macrocycle 1 as well as Macrocycle 2-Alkyne create anisotropic shielding zones for the 5,5′ protons of the axle; therefore, an upfield shift is detected in the ^{1}H NMR.

Single Crystal X-ray Structures of the Two Rotaxane Molecules SSQRot1 and SSQRot2-(Alkyne)$_2$:

Single crystal X-ray structures of two rotaxane molecules SSQRot1 and SSQRot2-(Alkyne)$_2$ confirm hydrogen bonding of four lactam N−H's and two aryl ring C−H's (C protons) of the macrocycle with two oxygens of the C_4O_2 residue in squaraine with average N−H・・・O and C−H・・・O distances of 2.5 Å. In the crystal structures of the rotaxanes SSQRot1 and SSQRot2-(Alkyne)2 *trans* orientations of the indoline residues inside both the macrocycles are observed (**Figure 26a, b)**. The central four-membered C_4O_2 core (A) of the squaraine axle is extremely electron deficient and packed within the electron-rich anthracene residues (D) of the Macrocycle 1 and Macrocycle 2- Alkyne with centroid-to-centroid D−A distances of 3.95 and 3.86 Å

respectively,(**Figure 26a, b)** and it is stabilized by D−A−D interactions and therefore anticipated to prevent nucleophilic attack.

Photophysical properties of SQ, LysoSQ, SSQRot-(RGDS)$_2$ and LysoSQRot-(RGDS)$_2$:

For the LysoSQRot-(RGDS)$_2$ formation, characteristic bathochromic shifts ($\Delta\lambda_{abs}$) of ca. 19 nm in DMSO and ca. 28 nm in PBS (pH 7.2) are observed with respect to the LysoSQ axle (**Figures 35, 36, and Table 2**). The λ_{abs} of LysoSQRot-(RGDS)$_2$ is observed at 653 nm in PBS (pH 7.2) with a molar extinction coefficient of 1.16 × 105M^{-1} cm^{-1} due to the $\pi\rightarrow\pi^*$ transitions with a vibronic progression at 605 nm (**Table 2**). The λ_{em} of LysoSQRot-(RGDS)$_2$ is detected at 665 nm in DMSO with a high QY of 0.28 (Figure 4a, Table S2). The molecules SSQRot-(RGDS)$_2$ and LysoSQRot-(RGDS)$_2$ are also soluble in water due to the two RGDS peptide functionalities. The λ_{em} of LysoSQRot-(RGDS)$_2$ is detected at 676 nm with a Stokes shift of 23 nm in H_2O or PBS (**Figure 36c**).

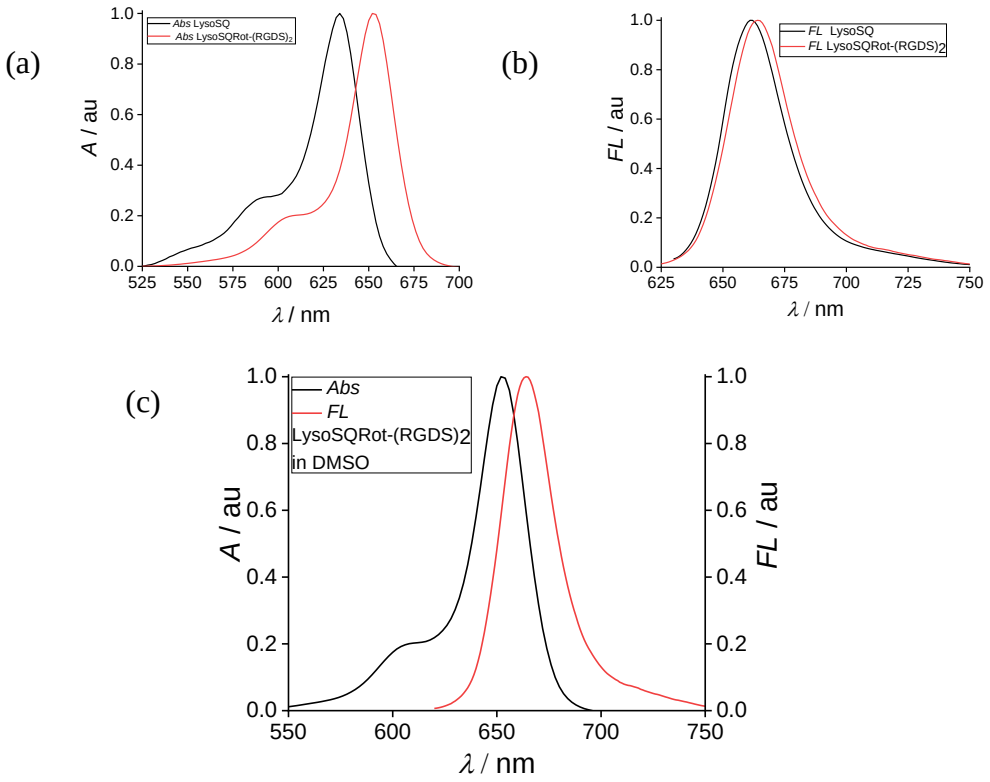

Figure 35. Normalized (a) absorption and (b) fluorescence emission plots of LysoSQ (2 μM) and LysoSQRot-$(RGDS)_2$ (2 μM) in DMSO. Absorption and emission plots display bathochromic shift in rotaxane formation. (c) Normalized absorption and emission plot of LysoSQRot-$(RGDS)_2$ in DMSO.

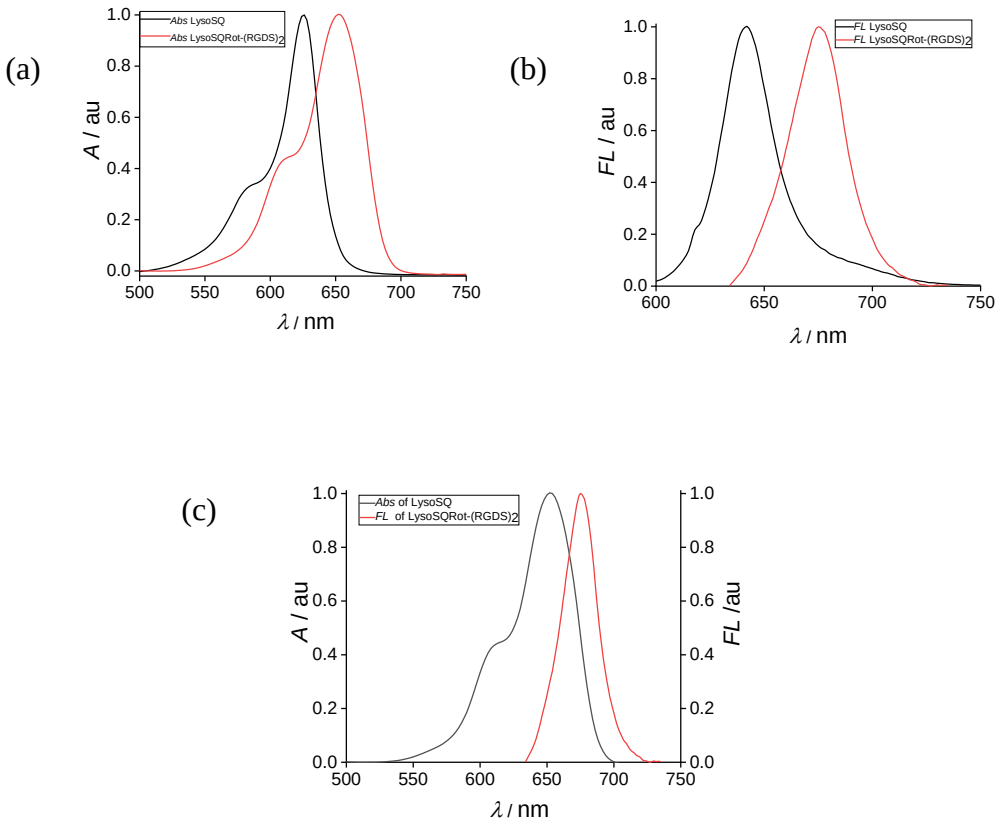

Figure 36. Normalized (a) absorption and (b) fluorescence emission plots of LysoSQ (2 μM) and LysoSQRot-$(RGDS)_2$ (2 μM) in PBS, pH=7.2. Absorption and emission plots showing bathochromic shift in rotaxane formation. (c) Normalized absorption and emission plot of LysoSQRot-$(RGDS)_2$ in PBS pH=7.2.

Table 2. Photophysical data

Compound	λ_{max} (nm)	λ_{em} (nm)	Stokes shift ($\Delta\lambda$) nm	$\varepsilon \times 10^5$ (M^{-1} cm^{-1})	QY (F)
SSQRot1	657	670	13	1.10	0.14 in DMF
SSQRot2-(Alkyne)$_2$	657	668	11	1.39	0.14 in DMF
LysoSQ	633	647	14	1.70	0.21 in DMSO
LysoSQRot2-(Alkyne)$_2$	653	665	12	1.82	0.15 in DMSO
SSQRot-(RGDS)$_2$	660	675	15	1.49	0.31 in DMSO
LysoSQRot-(RGDS)$_2$	652	665	13	1.52	0.28 in DMSO
LysoSQ	625	642	17	1.10	0.12 in PBS, pH 7.2
LysoSQRot-(RGDS)$_2$	653	676	23	1.16	0.14 in PBS, pH 7.2

The fluorescence lifetime (τ) of LysoSQRot-(RGDS)$_2$ is detected as 3.7 ns in DMSO and 2.8 ns in PBS (pH 7.2) using TCSPC which is longer in comparison with other rotaxane molecules (**Figures 37f, 38, and Table 3**). The anthracene emission (400−500 nm) at 365 nm λ_{ex} for LysoSQRot- (RGDS)$_2$ formation is diminished compared to the empty macrocycle owing to FRET from the anthracene chromophore to the stuck LysoSQ and consequently emits at a characteristic longer λ_{em} at 665 nm consistent with rotaxane formation (**Figure 39**).

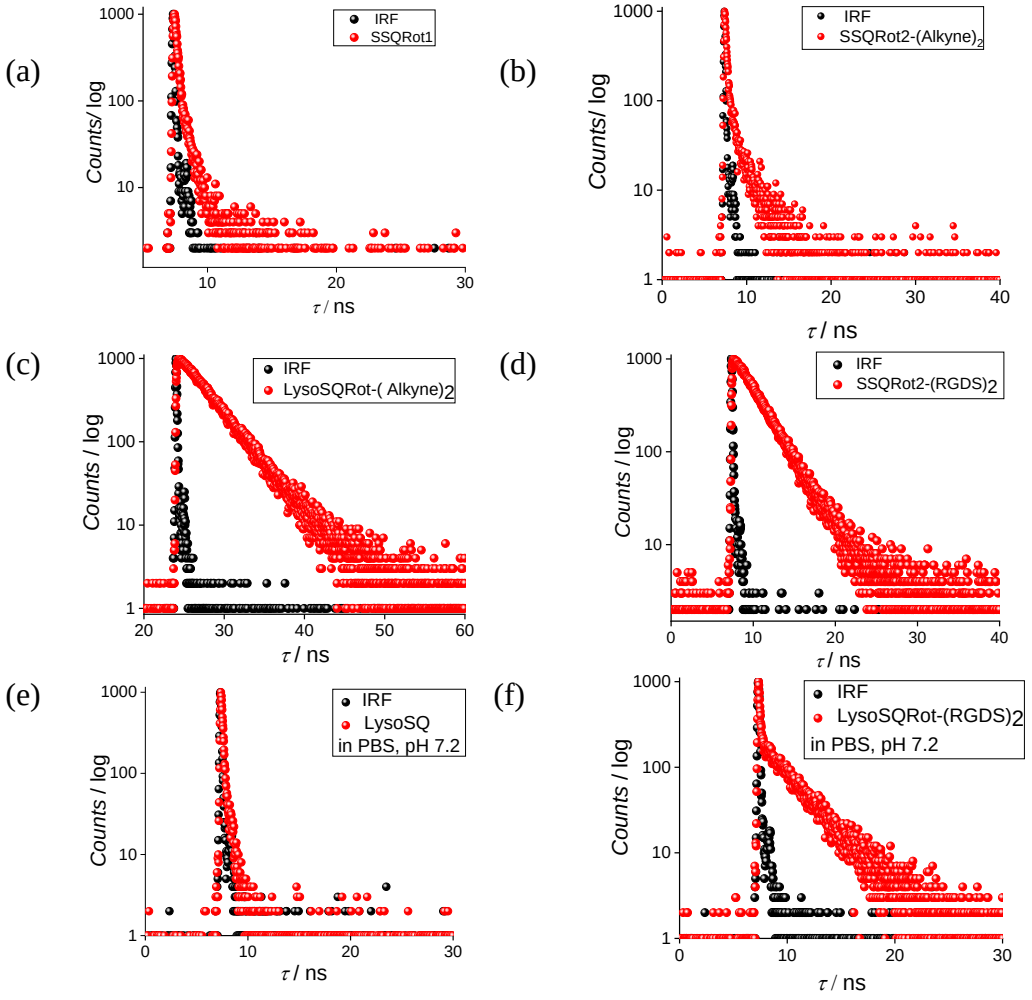

Figure 37. TCSPC plots of (a) SSQRot1, (b) SSQRot2-$(Alkyne)_2$, (c) LysoSQRot2-$(Alkyne)_2$, and (d) SSQRot-$(RGDS)_2$ in DMSO. TCSPC plots of (e) LysoSQ and (f) LysoSQRot-$(RGDS)_2$ in PBS, pH=7.2.

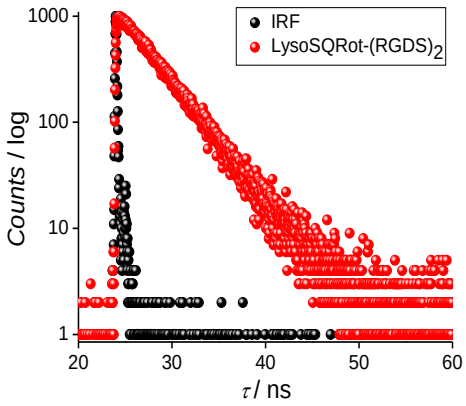

Figure 38. LysoSQRot-$(RGDS)_2$ in DMSO.

Table 3. Fluorescence lifetime (τ)

Compound	Fluorescence Lifetime (τ)
SSQRot1	0.187901±0.114794 ns in DMSO
SSQRot2-$(Alkyne)_2$	0.212204±0.186021 ns in DMSO
LysoSQRot2-$(Alkyne)_2$	3.47881±0.031487 ns in DMSO
SSQRot-$(RGDS)_2$	2.80816±0.033509 ns in DMSO
LysoSQRot-$(RGDS)_2$	3.67633±0.031936 ns in DMSO
LysoSQ	0.143283±1.38221 ns in PBS, pH 7.2
LysoSQRot-$(RGDS)_2$	2.82031±0.085037 ns in PBS, pH 7.2

(a) (b)

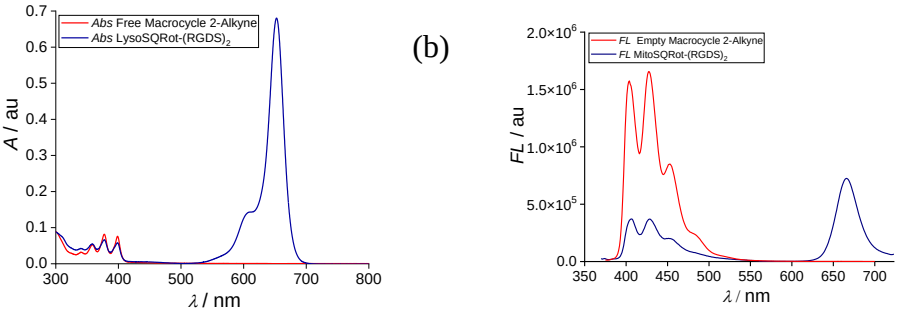

Figure 39. (a) Absorption plot of empty Macrocycle 2-Alkyne and LysoSQRot-$(RGDS)_2$ in DMSO. (b) Fluorescence emission plot at 365 nm excitation for empty Macrocycle 2-Alkyne and LysoSQRot-$(RGDS)_2$ in DMSO. A noteworthy diminution in emission intensity of anthracene functionality in DMSO was observed for LysoSQRot-$(RGDS)_2$ formation that indicates efficient FRET from excited macrocycle to LysoSQ of LysoSQRot-$(RGDS)_2$ in solution.

Biocompatibility Study of LysoSQ and LysoSQRot-(RGDS)$_2$:

Analysis of the PBS solutions of the probes at pH 7.2 after irradiation with a 200 W xenon lamp over 1 h revealed more decomposition of LysoSQ compared to mechanically interlocked LysoSQRot-(RGDS)$_2$ (**Figure 40a-d**). The macrocycle of LysoSQRot-(RGDS)$_2$ provides shelter and protects the LysoSQ chromophore from photobleaching. Unthreading might be a probable downside of rotaxanes in the live carcinoma cell organelles. UV/vis and fluorescence studies in PBS, pH 7.2 at 37 °C for 48 h showed no unthreading of the RGDS conjugated macrocycle from LysoSQRot-(RGDS)$_2$. It corroborates that the *gem*-dimethyl and *N*-methyl of indoline moieties are sufficiently bulky to block rotaxane unthreading. No noteworthy fluctuations are detected in the emission of LysoSQRot-(RGDS)$_2$ (2 μM) at 675 nm in the presence of numerous cations and anions under physiological conditions (pH 7.2, 37 °C) over 24 h (**Figure 41a-c**). Moreover, LysoSQRot-(RGDS)$_2$ is highly stable in the presence of bioactive small molecules like glutathione (GSH, 5 mM), cysteine (Cys, 5 mM), and H_2O_2 (1 mM) under physiological conditions (PBS, pH 7.2, 37 °C, 48 h) (**Figures 41d**). Furthermore, the probe LysoSQRot-(RGDS)$_2$ is more stable compared to LysoSQ in 10% fetal bovine serum (FBS) at physiological conditions (PBS, pH 7.2, 37 °C) over 24 h (**Figure 40 e,f**).

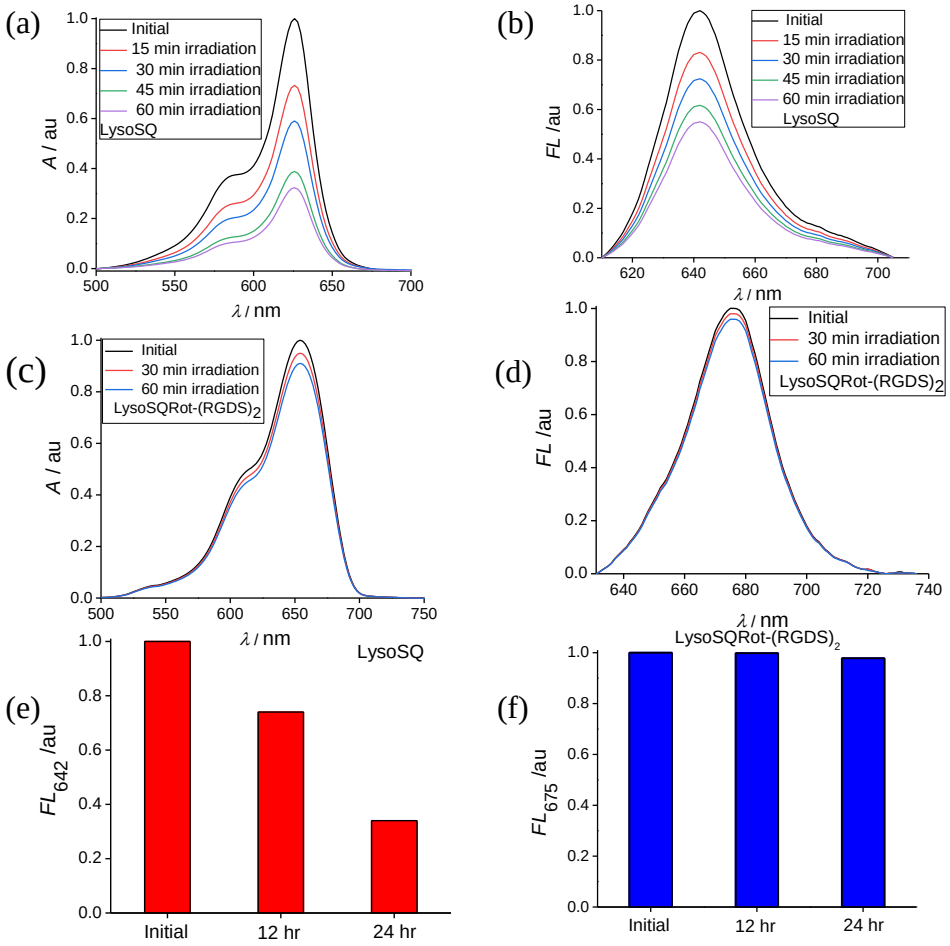

Figure 40. Irradiation of LysoSQ (2 μM) in PBS, pH 7.2 in exposed to air using a 200 W Xenon lamp (filter to allow wavelengths > 500 nm) over 1 h and examined the stability of the probes through (a) absorption and (b) emission plots. Irradiation of LysoSQRot-$(RGDS)_2$ (2 μM) in PBS, pH 7.2 in exposed to air using a 200 W Xenon lamp (filter to allow wavelengths > 500 nm) over 1 h and examined the stability of the probes through (c) absorption and (d) emission plots. Analysis of the PBS solution of the probes at pH 7.2 after irradiation with a Xenon lamp revealed more decomposition of LysoSQ compared to mechanically interlocked LysoSQRot-$(RGDS)_2$. (e) Noticeable

change in fluorescence is observed for LysoSQ (2 μM) in presence of 10% FBS (w/w) in PBS at physiological pH 7.2 over 24 h at 37°C. (f) No noticeable change in fluorescence has been detected for LysoSQRot-$(RGDS)_2$ (2 μM) in presence of 10% FBS (w/w) in PBS at physiological pH 7.2 over 24 h at 37°C.

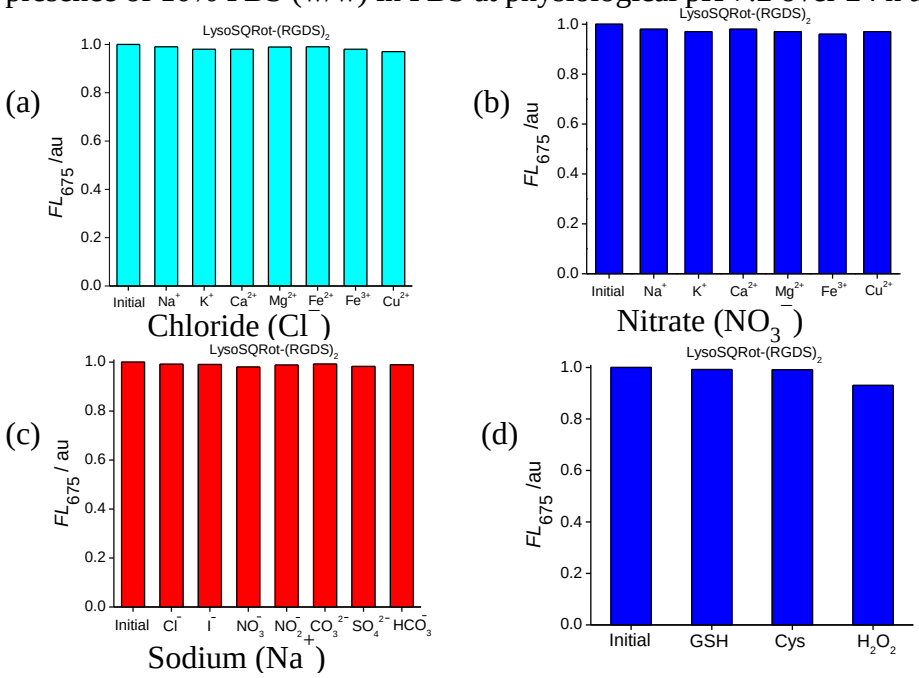

Figure 41. No noteworthy fluctuations are detected in the emission of LysoSQRot-$(RGDS)_2$ (2 μM) at 675 nm in presence of numerous cations [10 mM Na^+, 10 mM K^+ and 200 μM for Ca^{2+}, Mg^{2+}, Fe^{2+}, Fe^{3+}, and Cu^{2+}] as (a) chloride ($Cl^–$) and (b) nitrate ($NO_3^–$) salts; (c) various anions (200 μM for $Cl^–$, $I^–$, $NO_3^–$, $NO_2^–$, $CO_3^{2–}$, $SO_4^{2–}$, and $HCO_3^–$) as Na^+ salts under physiological conditions (pH 7.2, 37°C) over 24 h. (d)) Negligible fluorescence changes of LysoSQRot-$(RGDS)_2$ (2 μM) at 675 nm are detected in presence of bioactive small molecules like glutathione (GSH, 5 mM), cysteine (Cys, 5 mM), and H_2O_2 (1 mM) under physiological conditions (PBS, pH 7.4, 37°C, 48 h).

Cell viability assay (MTT):

MTT assay shows that the LysoSQRot-$(RGDS)_2$ is noncytotoxic to human lung adenocarcinoma A549 and epithelioid cervix carcinoma HeLa cell lines as well as noncancerous mouse myoblast C2C12 cell line (**Figure 42**).

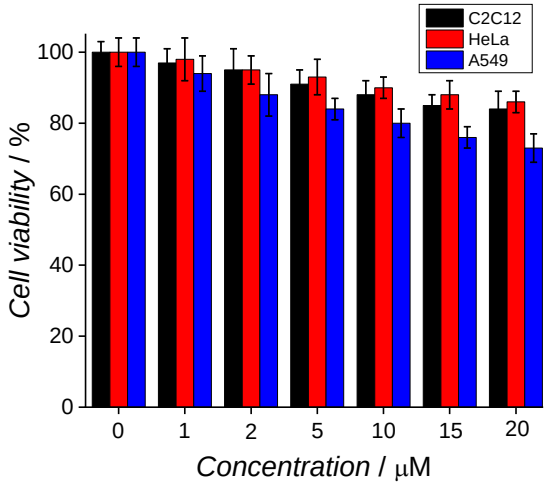

Figure 42. Cell viability assay against A549 and HeLa carcinoma cell lines as well as noncancerous mouse myoblast cell line (C2C12) over 24 h at different concentrations of LysoSQRot-$(RGDS)_2$.

Confocal laser scanning microscopy (CLSM) and Multicolor Imaging:

A LysoSQ weak signal inside the live cancer cell lysosomes is observed in confocal laser scanning microscopy (CLSM) (**Figure 43**). To enhance the lysosomal specificity, colocalization assay comprising LysoSQRot-$(RGDS)_2$ is executed in live A549, human breast adenocarcinoma MDA-MB-231, and HeLa cancer cells with LysoTracker Green DND-26 (LTG). The LysoSQRot-$(RGDS)_2$ confined to small punctate compartments and displays high levels of colocalization in the merged image of CLSM with a Pearson's correlation (PC)

coefficient of 0.82 for A549, 0.84 for MDA-MB-231, and 0.84 for HeLa cells (**Figures 45, Figure 45A, 45B, 45D**). The LysoSQRot-$(RGDS)_2$ molecule is efficiently accumulated in live cancer cells due to active targeting through RGDS and $\alpha_V\beta_3$ integrin recognition followed by selective internalization into malignant lysosomes driven by the morpholine functionality. Live cancer cells' lysosomal target selectivity of LysoSQRot-$(RGDS)_2$ is compared with the control SSQRot1 and SSQRot-$(RGDS)_2$ molecules lacking the morpholine functionality (**Figure 46)**. It is apparent that the control SSQRot-$(RGDS)_2$ also stains in the live carcinoma cells; however, the colocalization with LTG is poor (PCC 0.30) compared with LysoSQRot-$(RGDS)_2$ (**Figure 45A**). This proposes that LysoSQRot-$(RGDS)_2$ with dual targeting functionality is a proficient strategy for live cancer cell selective malignant lysosome targeting and imaging. The 3D CLSM image processing of the live cancer cells stained with the LysoSQRot-$(RGDS)_2$ probe shows the spherical lysosomal compartment (**Figure 47**). The real time lysosomal movement in the live A549 and HeLa carcinoma cells is also acquired by CLSM over a 2−3 min time span (**Figures 48 and 49**). Multicolor confocal imaging of live A549 and HeLa cells is acquired using our synthesized rotaxane in combination with other target-specific probes with distinctive $\lambda_{ex}/\lambda_{em}$ (**Figures 50A and 50B**).

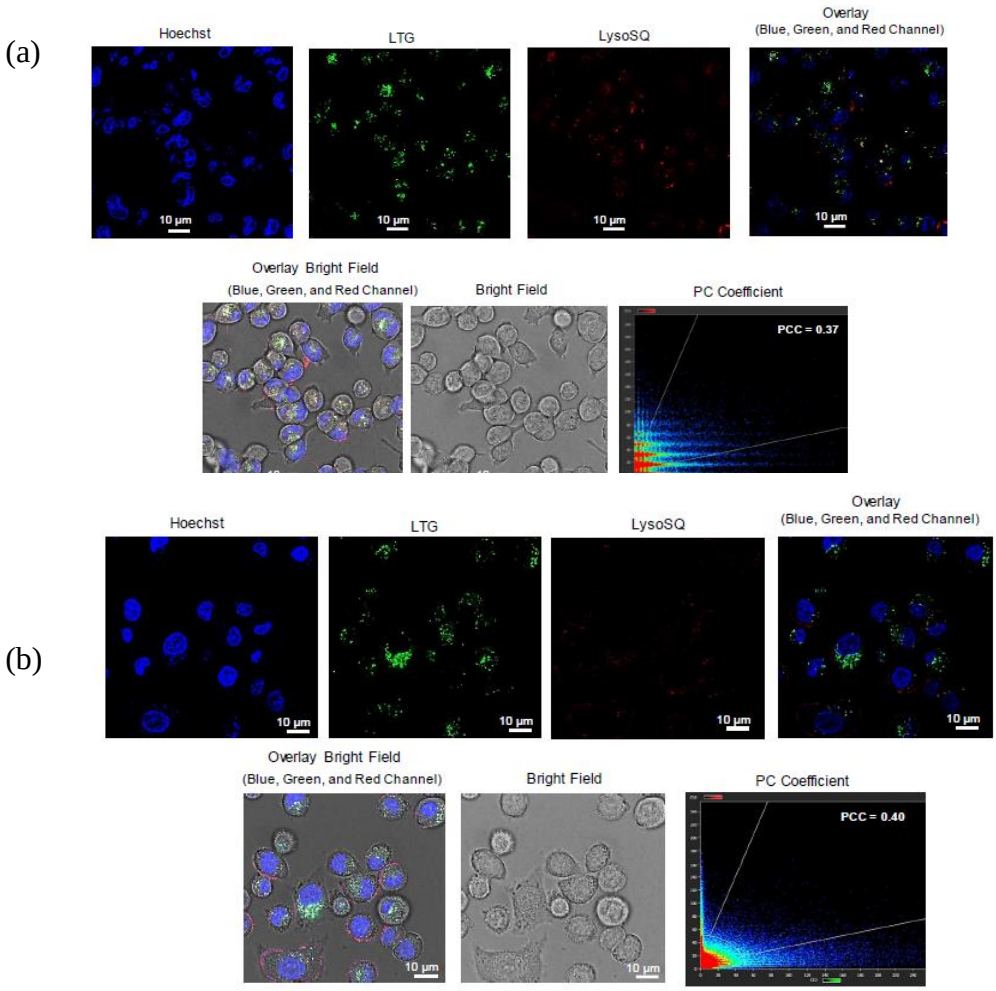

Figure 43. Confocal microscopic images of LysoSQ colocalized with LysoTracker Green (LTG) in live (a) adenocarcinoma MDA-MB-231 cells and (b) A549 carcinoma cells. Hoechst (blue channel), LTG (green channel), and LysoSQ (red channel). Red channels display weak fluorescence signal from LysoSQ.

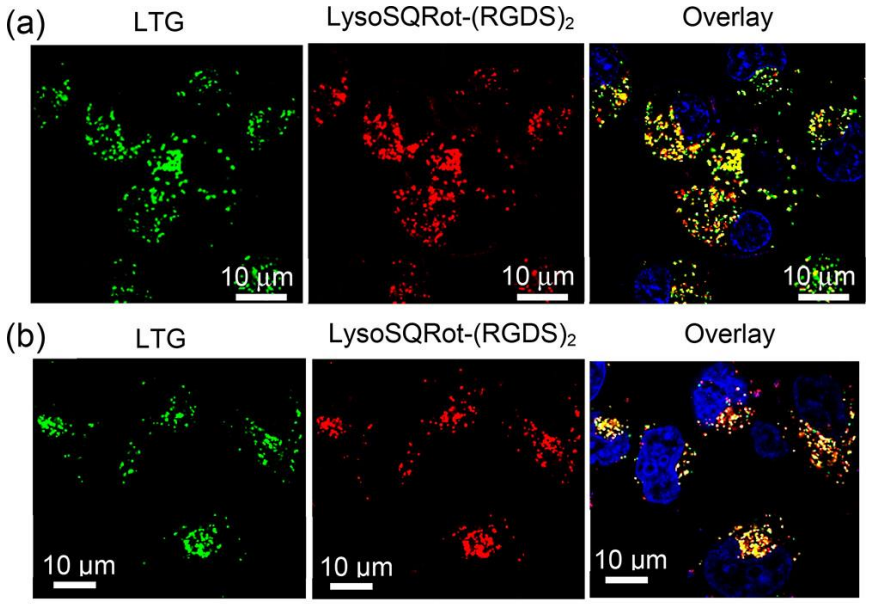

Figure 44. CLSM images of live (a) A549 and (b) HeLa cancer cells stained with LysoSQRot-(RGDS)2 and colocalized with LTG. Overlay images signify excellent colocalization in the live cancer cell lysosomes.

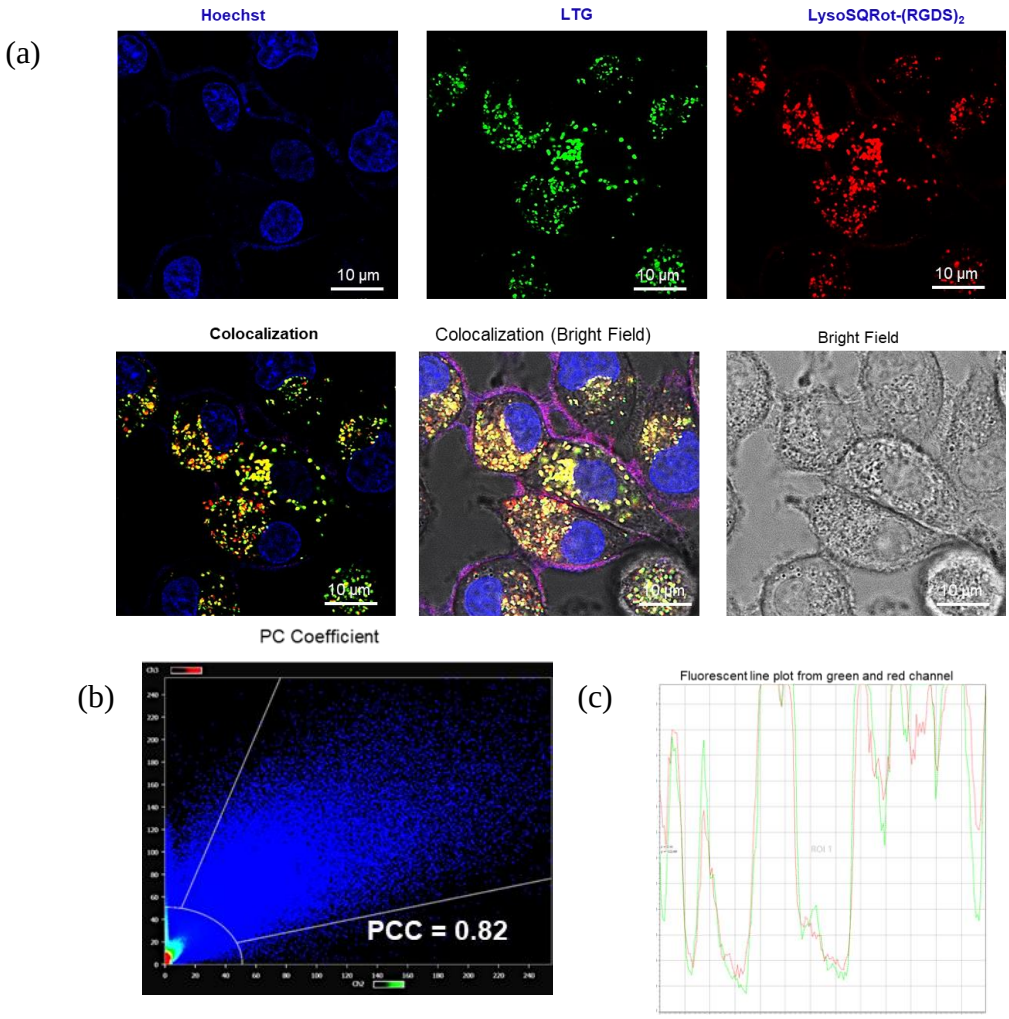

Figure 45A. (a) Confocal microscopic images of LysoSQRot-$(RGDS)_2$ colocalized with LysoTracker Green (LTG) in live A549 carcinoma cells. Hoechst (blue channel), LTG (green channel), and LysoSQRot-$(RGDS)_2$ (red channel). (b) Colocalization scatter plot displays Pearson's correlation coefficient (PCC) of 0.82. (c) Fluorescent line plot indicates excellent correlation between the fluorescent signal from green and red channel.

(a)

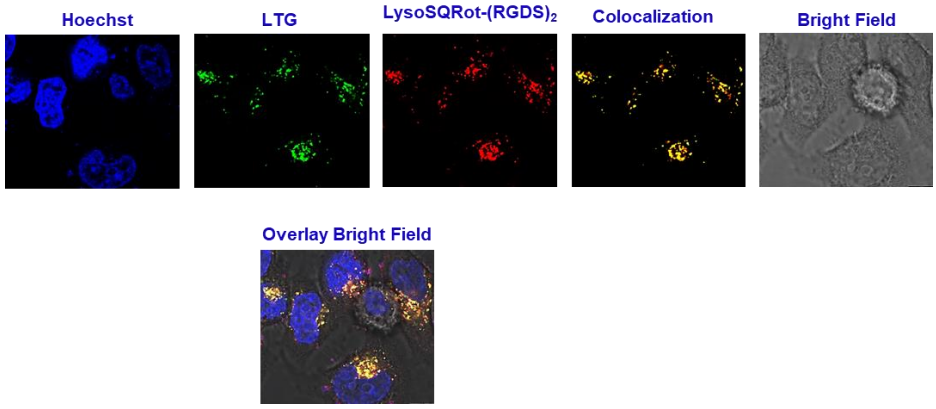

(b)

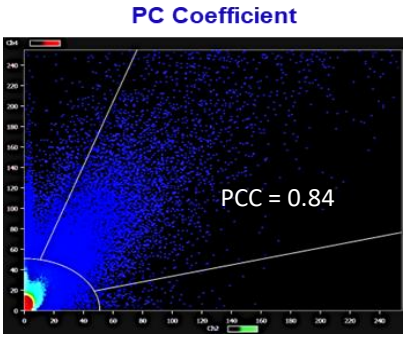

(c)

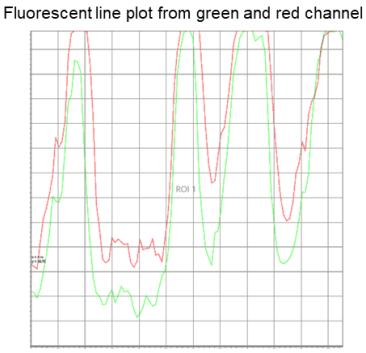

Figure 45B. (a) Confocal microscopic images of LysoSQRot-$(RGDS)_2$ colocalized with LysoTracker Green (LTG) in live HeLa carcinoma cells. Hoechst (blue channel), LTG (green channel), and LysoSQRot-$(RGDS)_2$ (red channel). (b) Colocalization scatter plot displays Pearson's correlation coefficient (PCC) of 0.84. (c) Fluorescent line plot indicates excellent correlation between the fluorescent signal from green and red channel.

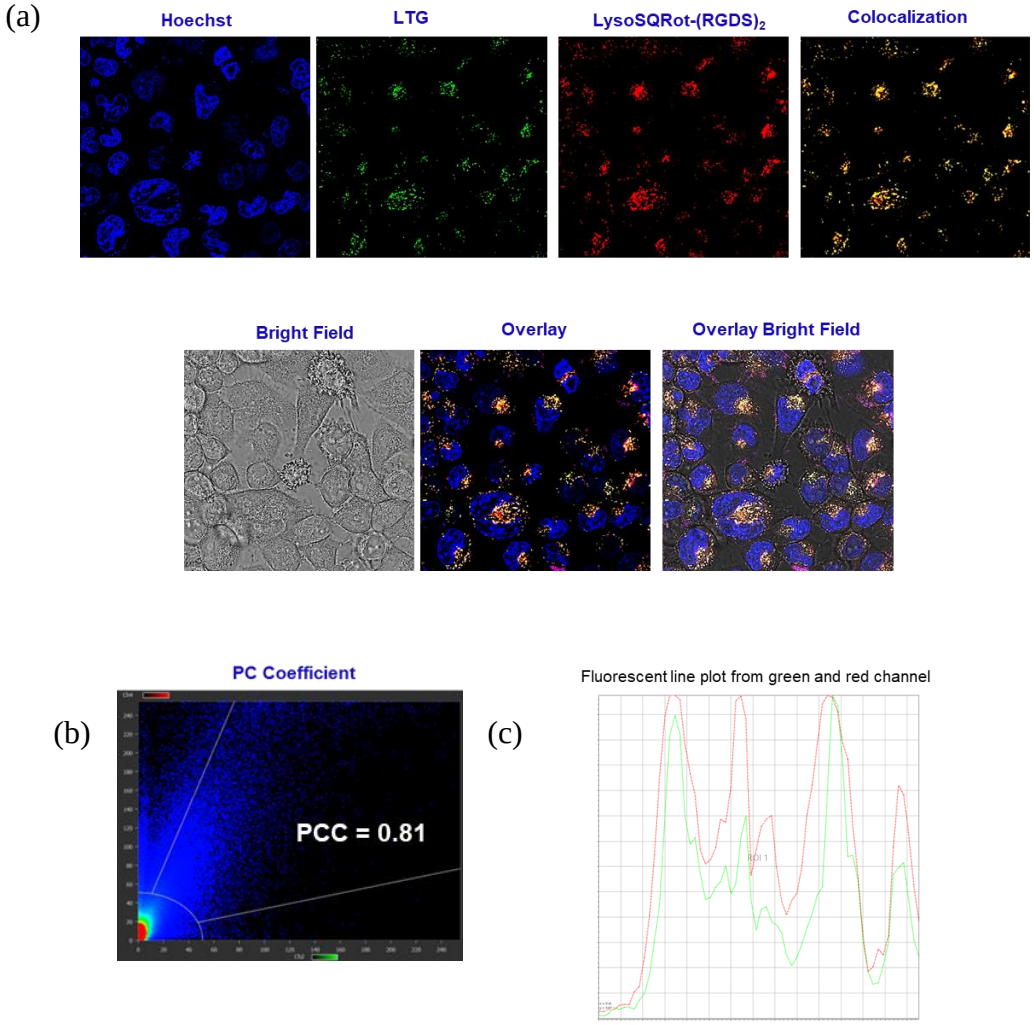

Figure 45C. (a) Confocal microscopic images of LysoSQRot-$(RGDS)_2$ colocalized with LysoTracker Green (LTG) in live HeLa carcinoma cells. Hoechst (blue channel), LTG (green channel), and LysoSQRot- $(RGDS)_2$ (red channel). (b) Colocalization scatter plot displays Pearson's correlation coefficient (PCC) of 0.81. (c) Fluorescent line plot indicates excellent correlation between the fluorescent signal from green and red channel.

(a)

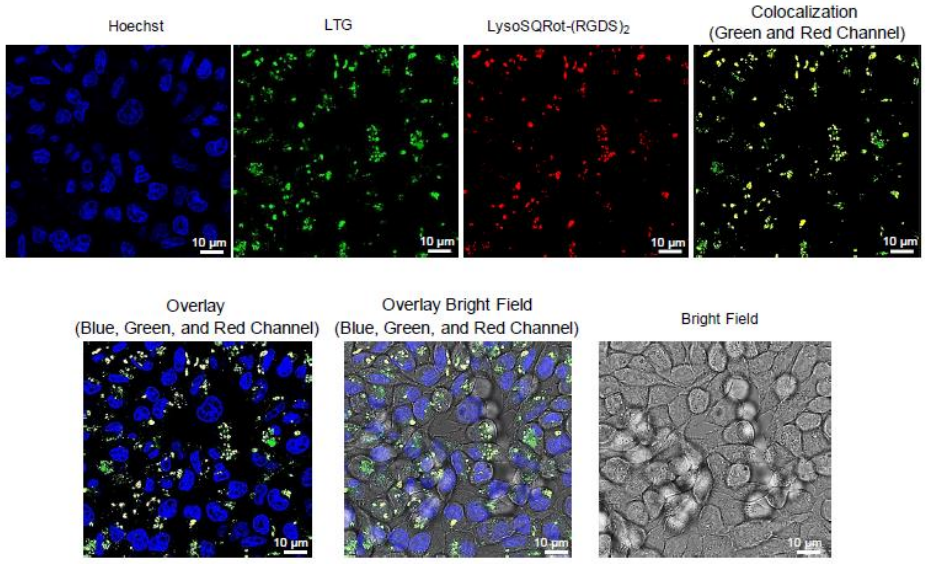

(b)

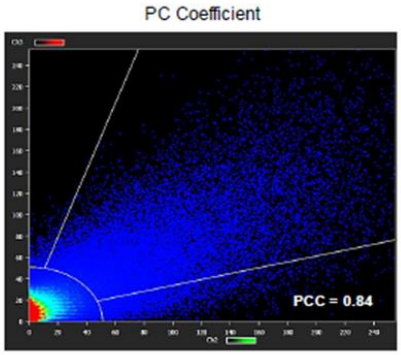

Figure 45D. (a) Confocal microscopic images of LysoSQRot-$(RGDS)_2$ colocalized with LysoTracker Green (LTG) in live human breast adenocarcinoma MDA-MB-231 cells. Hoechst (blue channel), LTG (green channel), and LysoSQRot-$(RGDS)_2$ (red channel). (b) Colocalization scatter plot displays Pearson's correlation coefficient (PCC) of 0.84.

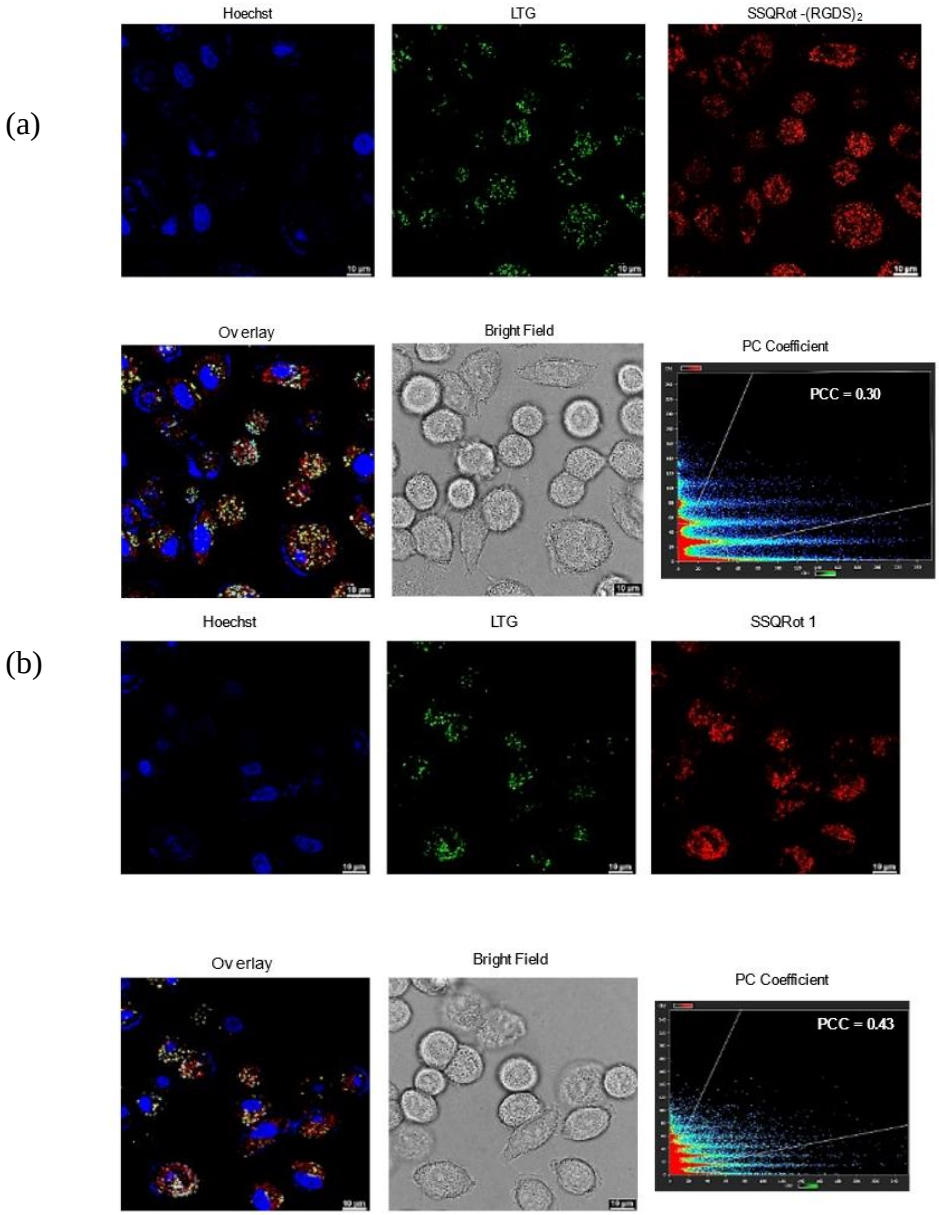

Figure 46. (a) Confocal microscopic images of control symmetrical SSQRot-$(RGDS)_2$ (lacking morpholine functionality) colocalized with LysoTracker Green (LTG) in live A549 carcinoma cells. Hoechst (blue channel), LTG (green channel), and SSQRot-$(RGDS)_2$ (red channel). Scatter plot displays Pearson's

correlation coefficient (PCC) of 0.30 indicates poor colocalization with LTG. (b) Confocal microscopic images of control symmetrical SSQRot1 colocalized with LysoTracker Green (LTG) in live A549 carcinoma cells. Hoechst (blue channel), LTG (green channel), and SSQRot1 (red channel). Scatter plot displays Pearson's correlation coefficient (PCC) of 0.43 indicates poor colocalization with LTG.

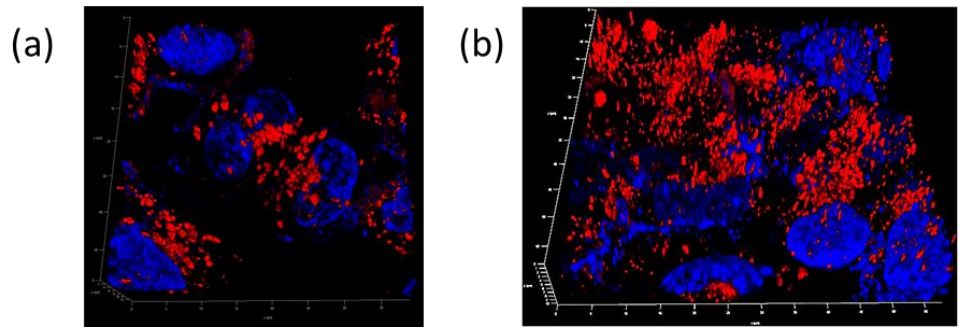

Figure 47. 3D CLSM image of the living (a) A549 and (b) HeLa carcinoma cells stained with lysosome targeting LysoSQRot-$(RGDS)_2$ dye indicate spherical lysosomal compartment (red color). Blue color specifies nuclear staining by Hoechst.

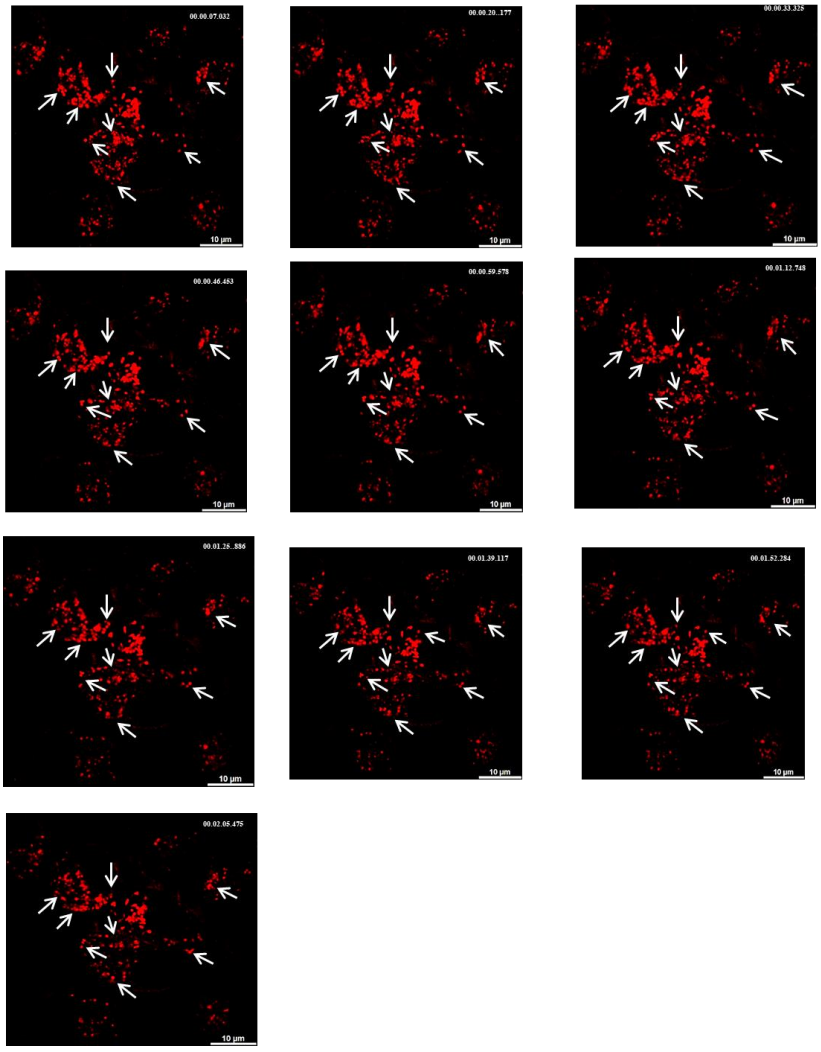

Figure 48. Real-time tracking of lysosomes inside the living A549 carcinoma cells using LysoSQRot-$(RGDS)_2$ probe by confocal laser scanning microscopy. 10 frames were collected over 2 minutes.

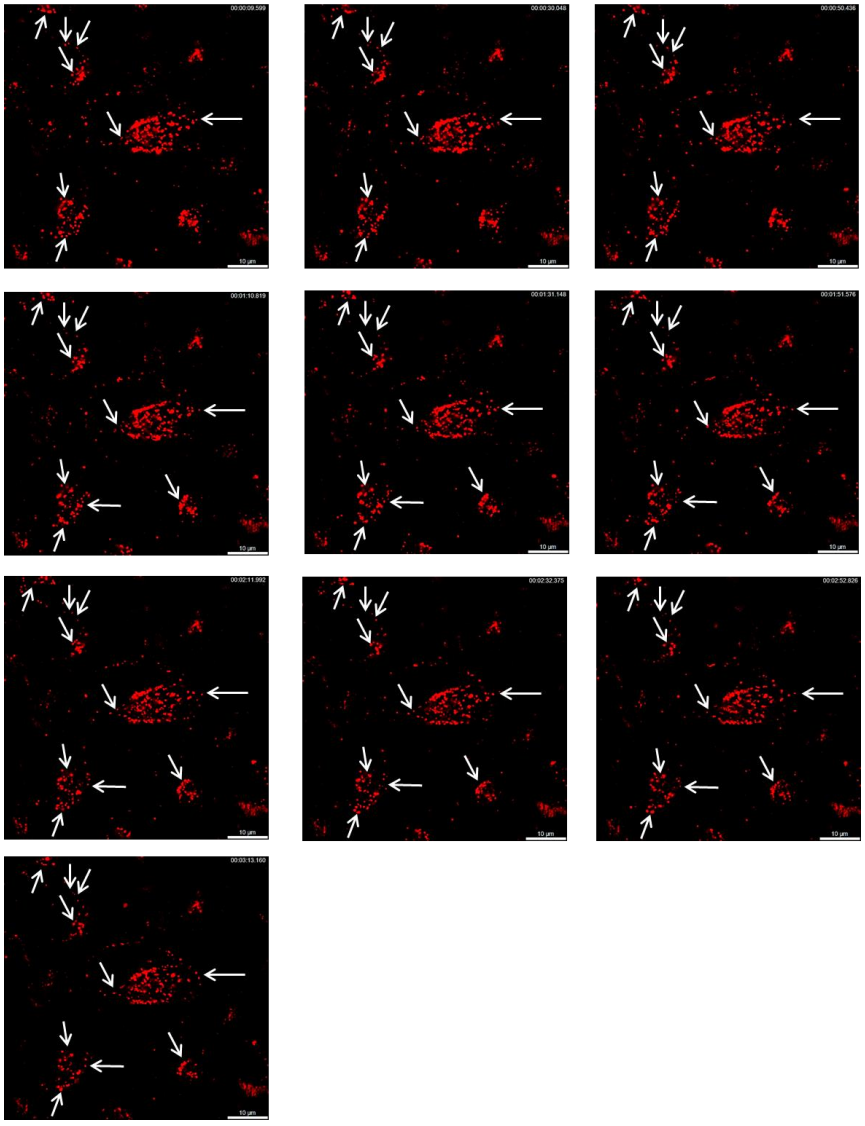

Figure 49. Real-time tracking of lysosomes inside the living HeLa carcinoma cells using LysoSQRot-$(RGDS)_2$ dye by confocal laser scanning microscopy. 10 frames were collected over 3 minutes.

.

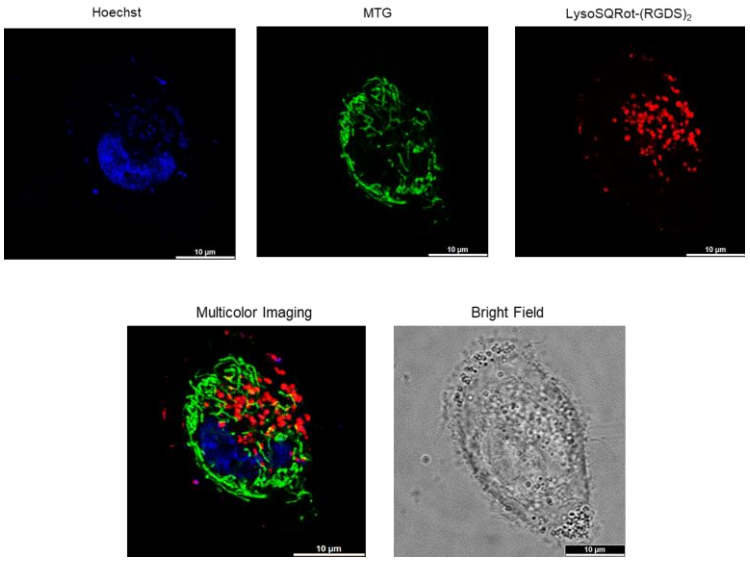

Figure 50A. Multicolor CLSM images of live A549 carcinoma cells stained with blue-fluorescent Hoechst to target nucleus (blue color), green emitting MTG to stain mitochondria (green color), and red emitting LysoSQRot-$(RGDS)_2$ to selectively track lysosome (red color). This multicolor imaging of cellular organelles in the same cell is captured by suitable filter sets in CLSM.

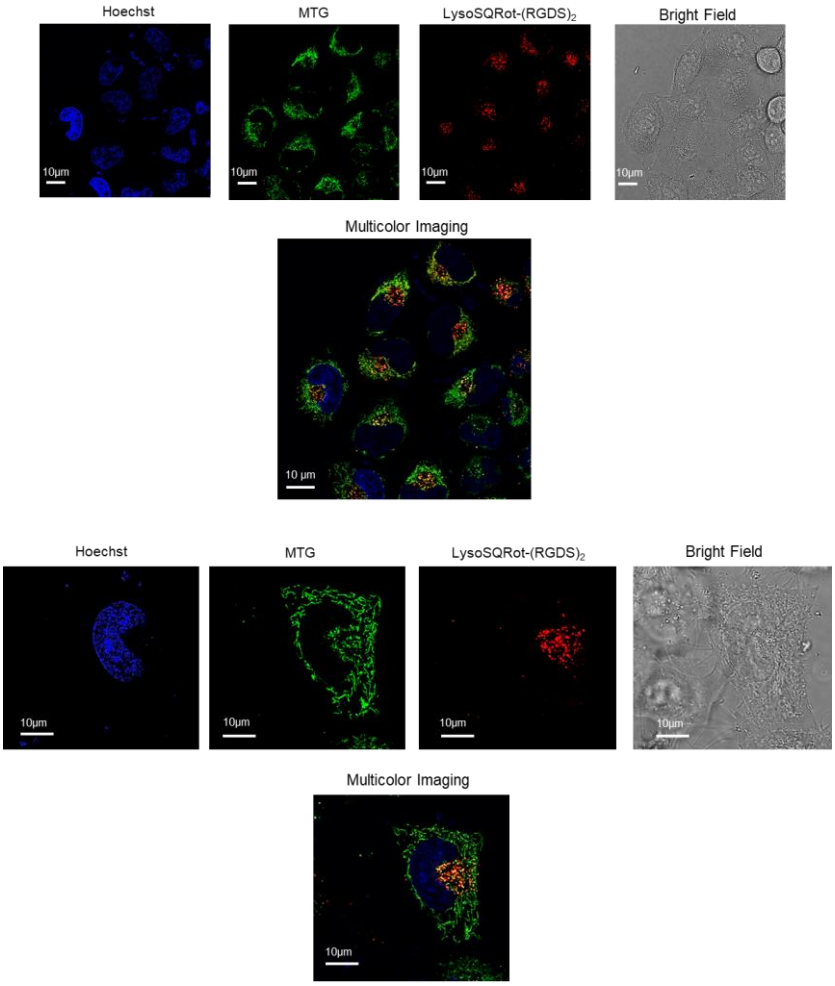

Figure 50B. Multicolor CLSM images of live HeLa cells stained with blue-fluorescent Hoechst to target nucleus (blue color), green emitting MTG to stain mitochondria (green color), and red emitting LysoSQRot-$(RGDS)_2$ to selectively track lysosome (red color). This multicolor imaging of cellular organelles in the same cell is captured by suitable filter sets in CLSM.

FACS Study: The fluorescence-activated cell sorting (FACS) displays greater internalization of the LysoSQRot-$(RGDS)_2$ probe inside the A549 carcinoma cells in comparison to C2C12 noncancerous cells. Eleven-fold and seven-fold augmentation in the fluorescence emission signal of LysoSQRot-$(RGDS)_2$ are detected in A549 cancer cells in comparison to the noncancerous C2C12 cells for 2 and 5 μM treatment, respectively, at the same incubation time (12 h) of the probe (**Figure 51).** Flow cytometric investigation validates our hypothesis that the LysoSQRot-$(RGDS)_2$ probe internalized more into the live carcinoma cells in contrast to healthy cells owing to active targeting of the overexpressed $\alpha_V\beta_3$ integrin in cancer cells through RGDS recognition.

(a)

(b)

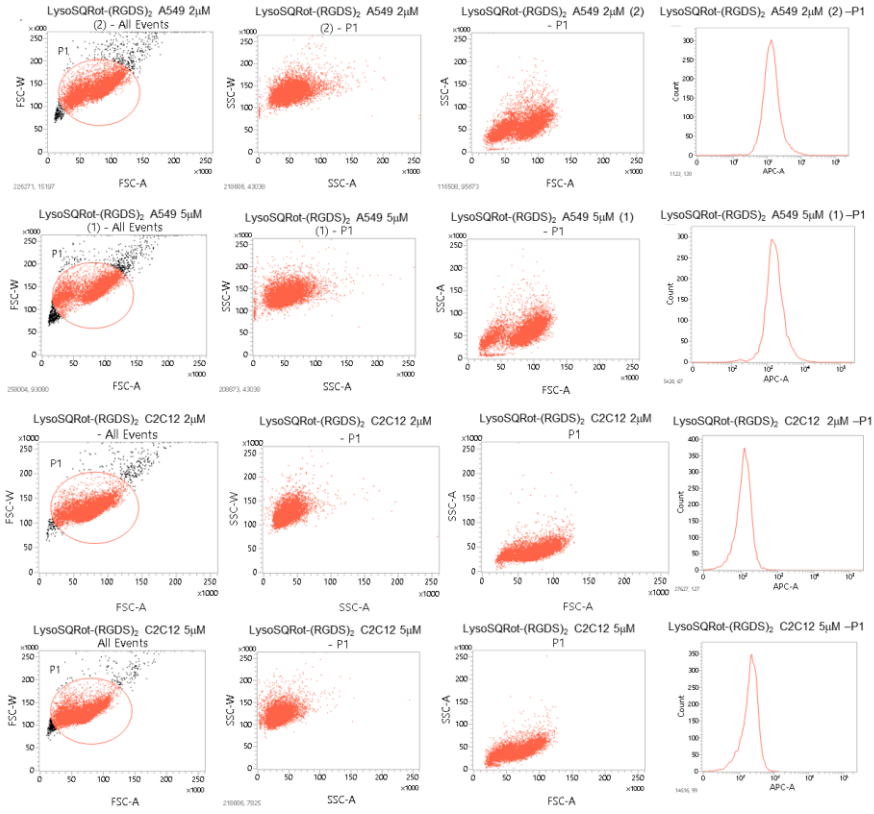

Statistics

Name	Cell line	Concentration	% Parent	APC-A Median
LysoSQRot-(RGDS)$_2$ A549 2μM	A549	2 μM	93.23	1387
LysoSQRot-(RGDS)$_2$ A549 5μM	A549	5 μM	91.60	1622
LysoSQRot-(RGDS)$_2$ C1C12 2μM	C1C12	2 μM	96.80	122
LysoSQRot-(RGDS)$_2$ C1C12 5μM	C1C12	5 μM	95.89	222

Figure 51. Fluorescence-activated cell sorting (FACS) displays greater internalization of LysoSQRot-(RGDS)$_2$ inside (a) the human lung adenocarcinoma A549 cell line than (b) the noncancerous mouse myoblast C2C12 cell line. The normal C2C12 cells and A549 cancer cells are treated with 2 μM and 5 μM, respectively, up to same incubation time (12 h) with the probes. Fluorescence intensity (median value) of LysoSQRot-(RGDS)$_2$ in the normal C2C12 cells are found 122 and 222, however, for A549 carcinoma cells the value has been detected 1387 and 1622 for 2 μM and 5 μM treatment,

respectively. 11-fold and 7-fold enhancement in the fluorescence emission intensity is noticed in A549 cancer cells compared to healthy C2C12 cells for 2 μM and 5 μM treatment, respectively.

Conclusions: In summary the interlocked unsymmetrical LysoSQ dye inside a macrocycle to construct rotaxane has been revealed to enhance probe durability in the live cancer cell lysosomes. LysoSQRot-$(RGDS)_2$ could be an effective molecular probe for live cancer cell lysosomes owing to its water solubility, intense and narrow red absorption/emission, high fluorescence quantum yield, photostability, biostability, and dual targeting functionality with live cell multicolor imaging facility. The rotaxane dye can be proficiently utilized for 3D cellular imaging and real-time monitoring of live cancer cell lysosomes. Moreover, these probes could be utilized for the imaging and study of lysosomal fusion, lysosome and mitochondrial interaction, early diagnosis of the lysosome related diseases, and targeted image guided surgery.

REFERENCES:

[1] Zhu, H.; Fan, J.; Du, J.; Peng, X. *Acc. Chem. Res.* **2016**, *49*, 2115−2126.

[2] Usama, S. M.; Marker, S. C.; Caldwell, D. R.; Patel, N. L.; Feng, Y.; Kalen, J. D.; Croix, B. S.; Schnermann, M. J. *J. Am. Chem. Soc.* **2021**, *143*, 21667−21675.

[3] Zhai, C.; Schreiber, C. L.; Coley, S. P.; Oliver, A. G.; Smith, B. D. *Angew. Chem., Int. Ed.* **2020**, *59*, 23740−23747.

[4] Zhang, H.; Liu, J.; Sun, Y.-Q.; Liu, M.; Guo, W. *J. Am. Chem. Soc.* **2020**, *142*, 17069−17078.

[5] Li, H.; Kim, D.; Yao, Q.; Ge, H.; Chung, J.; Fan, J.; Wang, J.; Peng, X.; Yoon, J. *Angew. Chem., Int. Ed.* **2021**, *60*, 17268−17289.

[6] Ma, Z.; Wang, F.; Wang, W.; Zhong, Y.; Dai, H. *Proc. Natl. Acad. Sci. U.S.A.* **2021**, *118*, e2021446118.

[7] Ji, Y.; Jones, C.; Baek, Y.; Park, G. K.; Kashiwagi, S.; Choi, H. S. *Adv. Drug Delivery Rev.* **2020**, *167*, 121−134.

[8] Wang, T.; Wang, S.; Liu, Z.; He, Z.; Yu, P.; Zhao, M.; Zhang, H.; Lu, L.; Wang, Z.; Wang, Z.; Zhang, W.; Fan, Y.; Sun, C.; Zhao, D.; Liu, W.; Bünzli, J. C. G.; Zhang, F. *Nat. Mater.* **2021**, *20*, 1571−1578.

[9] Li, H.; Kim, H.; Xu, F.; Han, J.; Yao, Q.; Wang, J.; Pu, K.; Peng, X.; Yoon, J. *Chem. Soc. Rev.* **2022**, *51*, 1795−1835.

[10] Sofias, A. M.; Toner, Y. C.; Meerwaldt, A. E.; van Leent, M. M. T.; Soultanidis, G.; Elschot, M.; Gonai, H.; Grendstad, K.; Flobak, A.; Neckmann, U.; Wolowczyk, C.; Fisher, E. L.; Reiner, T.; Davies, C. d. L.; Bjorkoy, G.; Teunissen, A. J. P.; Ochando, J.; Perez-Medina, C.; Mulder, W. J. M.; Hak, S. *ACS Nano.* **2020**, *14*, 7832−7846.

[11] Pasqualini, R.; Koivunen, E.; Ruoslahti, E. *Nat. Biotechnol.* **1997**, *15*, 542−546.

[12] de Lazaro, I.; Mooney, D. J. *Nat. Mater.* **2021**, *20*, 1469−1479.

[13] Cui, C.; Chakraborty, K.; Tang, X. A.; Schoenfelt, K. Q.; Hoffman, A.; Blank, A.; Mcbeth, B.; Pulliam, N.; Reardon, C. A.; Kulkarni, S. A.; Vaisar, T.; Ballabio, A.; Krishnan, Y.; Becker, L. **2021**, *16*, 1394−1402.

[14] Leung, K.; Chakraborty, K.; Saminathan, A.; Krishnan, Y. *Nat. Nanotechnol.* **2019**, *14*, 176−183.

(15) Mukherjee, A.; Saha, P. C.; Das, R. S.; Bera, T.; Guha, S. *ACS Sens.* **2021**, *6*, 2141−2146.

[16] Trombetta, E. S.; Ebersold, M.; Garrett, W.; Pypaert, M.; Mellman, I. *Science.* **2003**, *299*, 1400−1403.

[17] Bonam, S. R.; Wang, F.; Muller, S. *Nat. Rev. Drug Discovery*. **2019**, *18*, 923−948.

[18] De Risi, M.; Tufano, M.; Alvino, F. G.; Ferraro, M. G.; Torromino, G.; Gigante, Y.; Monfregola, J.; Marrocco, E.; Pulcrano, S.; Tunisi, L.; Lubrano, C.; Papy-Garcia, D.; Tuchman, Y.; Salleo, A.; Santoro, F.; Bellenchi, G. C.; Cristino, L.; Ballabio, A.; Fraldi, A.; De Leonibus, E. *Nat. Commun.* **2021**, *12*, 3495.

[19] Fraldi, A.; Klein, A. D.; Medina, D. L.; Settembre, C. *Annu. Rev. Neurosci.* **2016**, *39*, 277−295.

[20] Kroemer, G.; Jaattela, M. *Nat. Rev. Cancer.* **2005**, *5*, 886−897.

[21] Futerman, A. H.; van Meer, G. *Nat. Rev. Mol. Cell Biol.* **2004**, *5*, 554−565.

[22] Bonam, S. R.; Wang, F.; Muller, S. *Nat. Rev. Drug Discovery*. **2019**, *18*, 923−948.

[23] Piao, S.; Amaravadi, R. K. *Ann. N.Y. Acad. Sci.* **2016**, *1371*, 45−54.

[24] Towers, C. G.; Thorburn, A. *Cancer Discovery*. **2017**, *7*, 1218−1220.

[25] Chen, X.; Bi, Y.; Wang, T.; Li, P.; Yan, X.; Hou, S.; Bammert, C. E.; Ju, J.; Gibson, K. M.; Pavan, W. J.; Bi, L. *Sci. Rep* **2015**, *5*, 9004.

[26] Pierzyńska-Mach, A.; Janowski, P. A.; Dobrucki, J. W. *Cytometry, Part A* **2014**, *85*, 729−737.

[27] Qiu, K.; Huang, H.; Liu, B.; Liu, Y.; Huang, Z.; Chen, Y.; Ji, L.; Chao, H. *ACS Appl. Mater. Interfaces.* **2016**, *8*, 12702−12710.

[28] Ilina, K.; MacCuaig, W. M.; Laramie, M.; Jeouty, J. N.; McNally, L. R.; Henary, M. *Bioconjugate Chem.* **2020**, *31*,194−213.

[29] Ajayaghosh, A. *Acc. Chem. Res.* **2005**, *38*, 449−459.

[30] Das, R. S.; Saha, P. C.; Sepay, N.; Mukherjee, A.; Chatterjee, S.;Guha, S. *Org. Lett.* **2020**, *22*, 5839−5843.

[31] Hewage, H. S.; Anslyn, E. V. *J. Am. Chem. Soc.* **2009**, *131*, 13099−13106.

[32] Chen, H.; Farahat, M. S.; Law, K. Y.; Whitten, D. G. *J. Am. Chem. Soc.* **1996**, *118*, 2584−2594.

[33] Li, B.; Li, W.; Xu, Y.; Li, J.; Tu, J.; Sun, S. *Chem. Commun.* **2015**, *51*, 14652−14655.

[34] Stoddart, J. F. *Angew. Chem., Int. Ed.* **2017**, *56*, 11094−11125.

[35] Lee, S.; Chen, C.-H.; Flood, A. H. *Nat. Chem.* **2013**, *5*, 704−710.

[36] Movsisyan, L. D.; Franz, M.; Hampel, F.; Thompson, A. L.; Tykwinski, R. R.; Anderson, H. L. *J. Am. Chem. Soc.* **2016**, *138*, 1366−1376.

[37] Rajamalli, P.; Rizzi, F.; Li, W.; Jinks, M. A.; Gupta, A. K.; Laidlaw, B. A.; Samuel, I. D. W.; Penfold, T. J.; Goldup, S. M.; Zysman-Colman, E. *Angew. Chem., Int. Ed.* **2021**, *60*, 12066−12073.

[38] Johnson, J. R.; Fu, N.; Arunkumar, E.; Leevy, W. M.; Gammon, S. T.; Piwnica-Worms, D.; Smith, B. D. *Angew. Chem., Int. Ed.* **2007**, *46*, 5528−5531.

[39] Jarvis, T. S.; Collins, C. G.; Dempsey, J. M.; Oliver, A. G.; Smith, B. D. *J. Org. Chem.* **2017**, *82*, 5819−5825.

[40] Finn, M. G.; Kolb, H. C.; Sharpless, K. B. *Nat. Synth.* **2022**, *1*, 8−10.

[41] Sheldrick, G. M. *Acta Cryst.*, **2015,** *A71*, 3–8.

[42] Sheldrick, G. M. *Acta Cryst.*, **2015,** *C71*, 3–8.

[43] Dolomanov, O. V.; Bourhis, L. J.; Gildea, R. J.; Howard, J. A. K.; Puschmann, H. *J. Appl. Cryst.*, **2009,** *42*, 339–341.

Chapter 5

Design of Water-Soluble NIR Rotaxane Capped Superparamagnetic Fe_3O_4 Nanoparticles for Mitochondria Targeted Multimodal Imaging

Design of Water-Soluble NIR Rotaxane Capped Superparamagnetic Fe_3O_4 Nanoparticles for Mitochondria Targeted Multimodal Imaging

---

Introduction

Development of water-soluble bright near-infrared (NIR) organic fluorescent (650–900 nm) mechanically interlocked molecules (MIMs) for selective targeting and staining of specific cellular organelle is an emerging field of modern live cell imaging research.[1] In comparison to UV and visible light excitation NIR light excitation has certain benefits in the form of deep tissue penetration, little background noise, and negligible autofluorescence signal from intracellular biomolecules that proffers impressive tool for high-performance cellular imaging.[2-3] Magnetic nanoparticles (NPs) surface coated with NIR organic dyes have potential applications in hyperthermia, magnetic separation, and multimodal imaging.[4] Multimodal imaging technology based on targeted NIR fluorescence imaging in combination with magnetic resonance imaging (MRI) is the extremely important diagnostic tools for biomedical science.[5] Being the powerhouse of the cells, mitochondria often control plenty of important cellular functions and they have become one of the crucial targets within numerous cellular organelles.[6] However, it is burdensome to target mitochondria because of the double layer membrane and highly negative inner mitochondrial membrane (IMM) potential ($\Delta\Psi_m$ −220 mV for cancer cell).[7] Herein, we have designed organic lipophilic cationic squaraine (SQ) based NIR probe MitoSQ-DOPA to target mitochondria by exploiting the highly negative IMM potential.[8] We hypothesized that the electron-deficient central cyclobutene ring of MitoSQ-DOPA dye could be prone towards nucleophilic attack by biothiols, hence NIR fluorescence might be bleached once incorporation of MitoSQ-DOPA dye inside the live-cells mitochondria.[9] On top of this, SQ dyes have a propensity towards aggregate formation in aqueous solution, which may elicit notable broadening of their abs/em bands.[10] These

are the main obstacles for the organic NIR SQ probes towards targeted imaging applications. That is why in comparison to other imaging agents, SQ dyes have been less exploited in mitochondria targeted multimodal imaging applications. In order to mitigate these limitations we hypothesized that the inclusion of MitoSQ-DOPA within a macrocycle to construct MIMs that are stabilized by noncovalent interactions could be an ideal design to recover the dye function inside the live-cell mitochondria.[11] Smith and co-workers have made groundbreaking works for the design of SQ rotaxane.[12] However, the synthesis of sugar functionalized water-soluble mitochondria targeted NIR multimodal imaging agent based on dopamine conjugated unsymmetrical trimethylindoline SQ rotaxane is a challenging task. Moreover, it is also challenging to deliver magnetic NPs inside a specific cellular organelle due to less target selectivity. The surface coating of the ultrasmall superparamagnetic iron oxide NPs by the targeted rotaxanes may promote biocompatibility and diminish non-specific accumulation. Herein, the designed multifunctional MIMs MitoSQRot-(Carbo-OH)$_2$-DOPA has five unique structural characteristics: (a) unsymmetrical MitoSQ-DOPA dye for NIR fluorescence cellular imaging, (b) a macrocycle shields and defense the MitoSQ-DOPA dye from nucleophilic attack and also prevent aggregation inside the live-cells, (c) lipophilic cationic triphenylphosphonium (TPP^+) group tethered at the axle to target and stain live-cell mitochondria,[13-14] (d) catechol functionality of the dopamine residue conjugated at the axle to anchor with the superparamagnetic monodisperse small Fe_3O_4 NPs for the targeted delivery of the magnetic NPs inside the mitochondria as well as T_2-weighted MRI imaging,[15-17] and (e) two sugar residues conjugated at the macrocycle using Cu-catalyzed click chemistry to increase the water solubility of the rotaxane capped Fe_3O_4 NPs.

Selective targeting and imaging of live-cell mitochondria by rotaxane capped monodisperse magnetic Fe_3O_4 NPs [MitoSQRot-(Carbo-OH)$_2$-DOPA-Fe_3O_4] is demonstrated using confocal laser scanning microscopy (CLSM). Real-time tracking, 3D, and multicolor imaging of live-cell mitochondria are accomplished. Moreover, T_2 weighted MRI imaging has also been achieved by using water soluble MitoSQRot-(Carbo-OH)$_2$-DOPA-Fe_3O_4 NPs. Until further notice, this is the first account of a water soluble bright NIR fluorescent sugar functionalized DOPA conjugated MIMs capped superparamagnetic Fe_3O_4 NPs MitoSQRot-(Carbo-OH)$_2$-DOPA-Fe_3O_4 for mitochondrial targeted multimodal imaging.

Experimental Methods

General Methods and Materials

Synthesis, Purification, and Characterization of Unsymmetrical MitoSQ-COOH and MitoSQ-DOPA Dyes:

Herein, we have designed and synthesized unsymmetrical indolenine squaraine dye MitoSQ-COOH and MitoSQ-DOPA (**Scheme 1**). TLC was performed on TLC silica gel 60 F_{254} sheets using suitable solvent systems and identified by naked eye or UV lamp. The products were purified by column chromatographic technique using silica gel (100-200 mesh) as a stationary phase. The solvents were distilled using appropriate drying agents and used for column chromatography. Alkaline hydrolysis product of **8** is reacted with **10** under refluxing condition to afford MitoSQ-COOH. The MitoSQ-COOH dye is conjugated with TBDMS protected dopamine using amide coupling protocol to obtain MitoSQ-DOPA. Single crystal X-ray structure confirmed the formation of compound 8 (**Figures 1-17 and Table 1**).

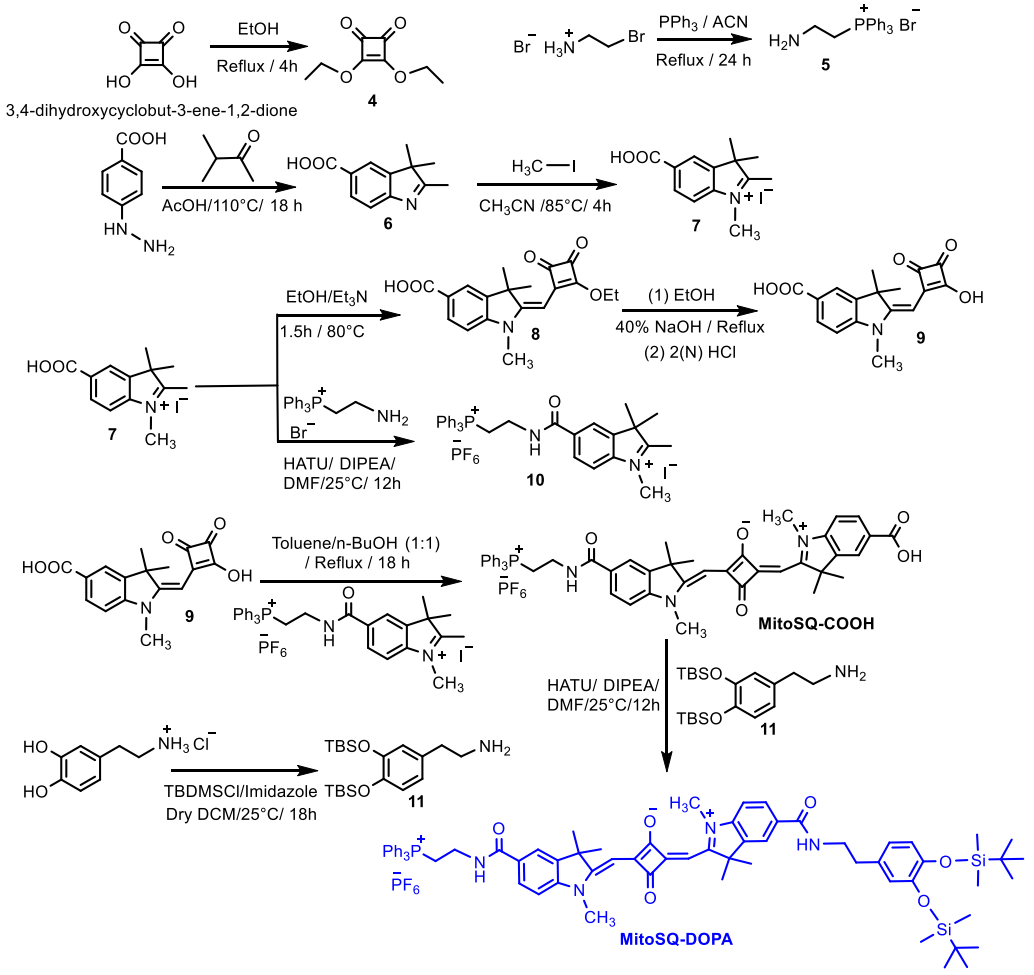

Scheme 1. Synthesis of MitoSQ-COOH, MitoSQ-DOPA and their associated precursor molecules.

3,4-Diethoxycyclobut-3-ene-1,2-dione (4): Ethanol (30 mL) solution of squaric acid (2 g, 17.54 mmol) was refluxed for 3 h. The solvent was concentrated under reduced pressure. The resultant white slurry was re-dissolved in EtOH (30 mL) and the solution was refluxed for an additional 1 h. The solvent was removed using a rotary evaporator and a similar process was

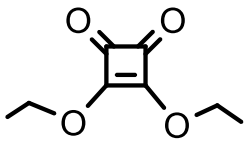

4

repeated 4 times to acquire the pure yellow oil compound 4. Yield: 2.92 g (98%).

^{1}H NMR (300 MHz, CDC_3, 25°C): δ = 4.73 (4H, q, J = 7.2 Hz), 1.47 (6H, t, J = 6.8 Hz) ppm. ^{13}C NMR (75 MHz, $CDCl_3$, 25°C): δ = 189.25, 184.21, 70.55, and 15.59 ppm. HRMS (ESI +ve) *m/z*: Observed for $C_8H_{10}NaO_4$ $[M+Na]^+$ = 193.0467, $[M+Na]^+$ calcd = 193.0471.

The spectra of ^{1}H and ^{13}C were given in Chapter 3.

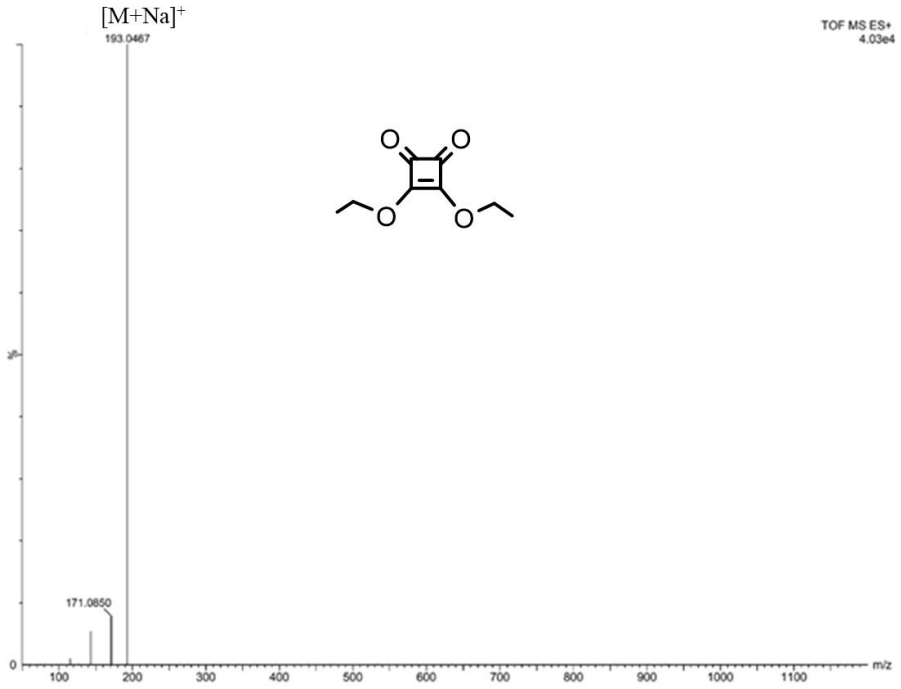

Figure 1. HRMS (ESI +ve) spectrum of Compound 4.

(2-Aminoethyl)triphenylphosphonium bromide (5): A solution of 2-bromoethylamine hydrobromide (7.81 g, 38.1 mmol) and triphenylphosphine (10 g, 38.1 mmol) in ACN (50 mL) was stirred at 80°C for 24 h in presence of N_2 environment. A white precipitate was formed, filtered, dissolved in H_2O, and

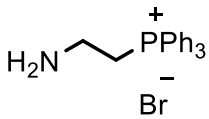

5

treated with K_2CO_3 until pH = 10-11. It was extracted with DCM and the organic layer was washed with brine (3×). The organic part was dried over anhydrous Na_2SO_4 and concentrated under reduced pressure to obtain a white residue which was washed with Et_2O (3×) to obtain the white solid pure product 5. Yield: 14.6 g (99%).

^{1}H NMR (300 MHz, $CDCl_3$, 25°C): δ = 7.83–7.64 (15H, m), 3.84–3.75 (2H, m), and 3.15–3.08 (2H, m), 2.81 (2H, br) ppm. ^{13}C NMR (75 MHz, $CDCl_3$, 25°C): δ = 134.70, 133.88, 130.49, 118.86, 118.00, 23.84, and 15.28 ppm. HRMS (ESI +ve) *m/z*: Observed for $C_{20}H_{21}NP^+$ $[M]^+$ = 306.1413, $[M]^+$ calcd = 306.1407.

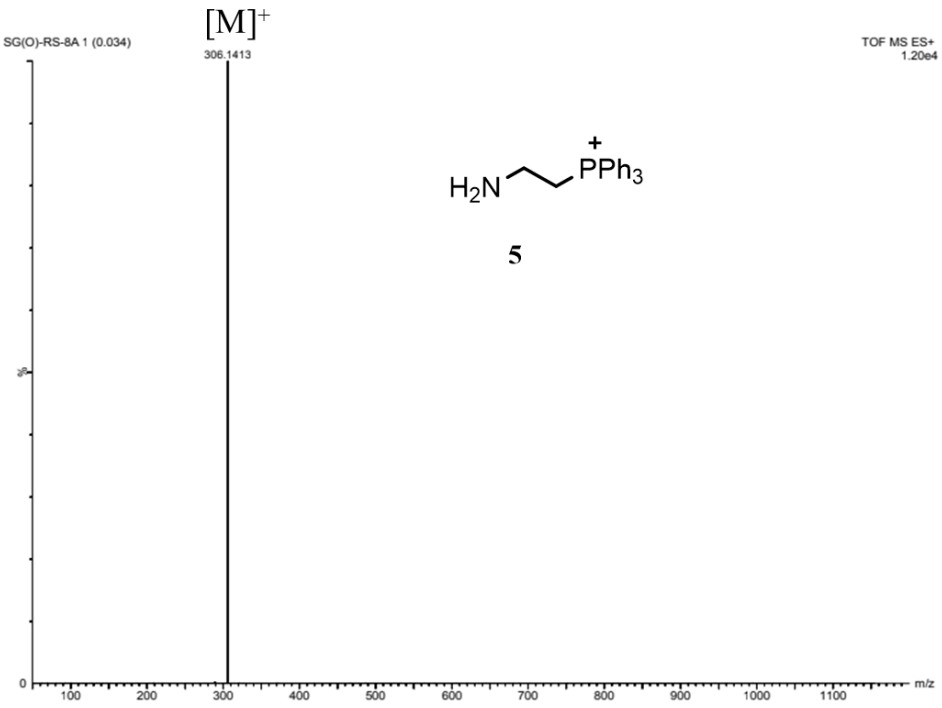

Figure 2. HRMS (ESI +ve) spectrum of Compound 5.

(a)

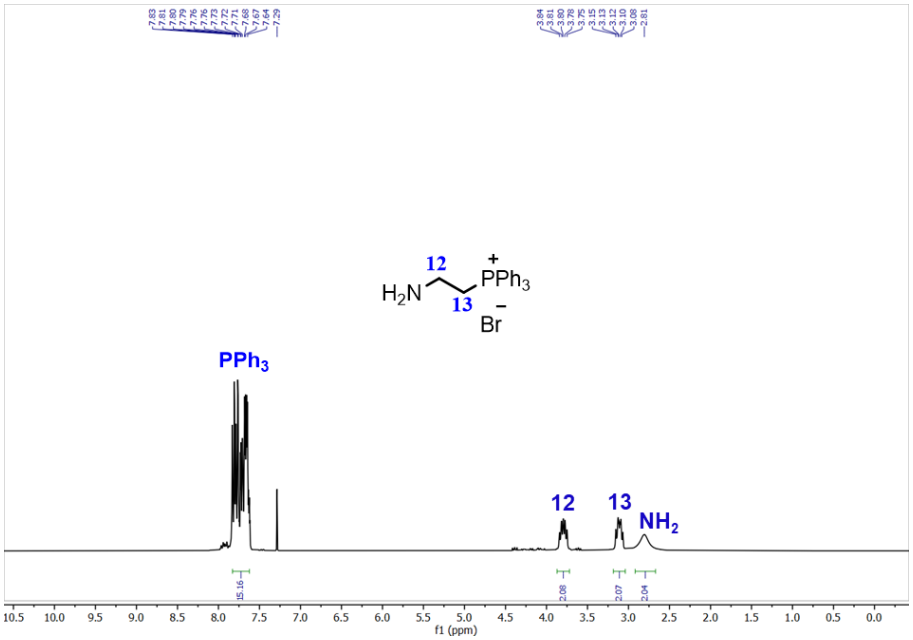

(b)

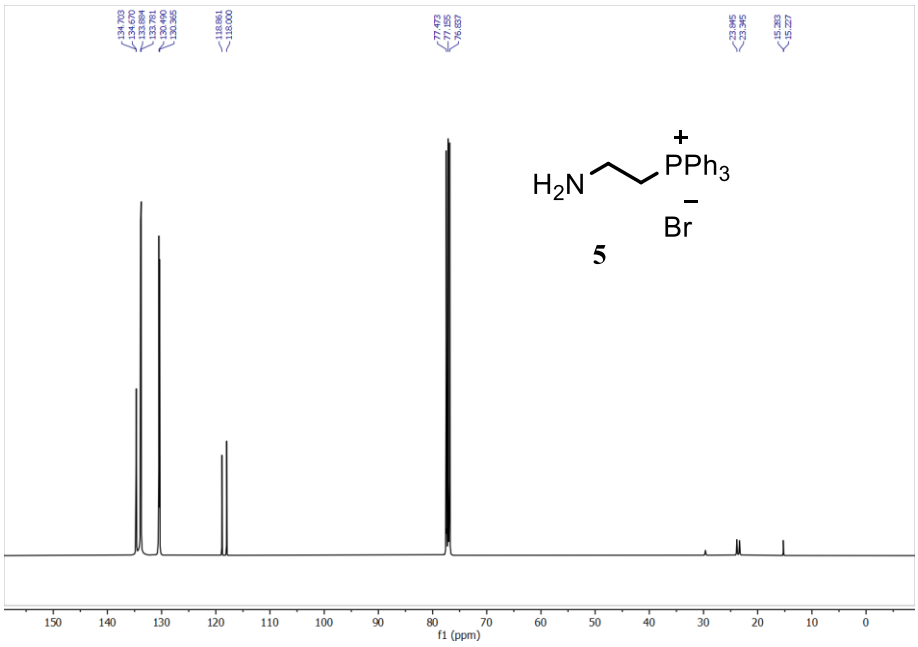

Figure 3. (a) ^{1}H NMR (300 MHz, $CDCl_3$, 25°C) spectrum of compound 5.

(b) ^{13}C NMR (75 MHz, $CDCl_3$, 25°C) spectrum of 5.

2,3,3-Trimethyl-3*H*-indole-5-carboxylic acid (6): 4-Hydrazinobenzoice acid (3.04 g, 20 mmol) and 3-methyl-2-butanone (3.64 mL, 34.5 mmol) were dissolved in 20 mL acetic acid. The reaction mixture was refluxed for 12 h, then allowed to cool to room temperature and solvent was removed under reduced pressure to obtain the crude product. The crude product was purified by column chromatography using 40% EtOAc/Hexane to acquire a light yellow colored pure compound.

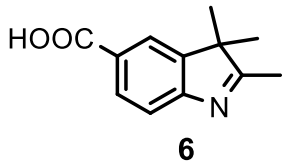

6

Yield: 2.4 g (59%)

^{1}H NMR (300 MHz, DMSO-d_6, 25°C): δ = 12.74 (1H, br), 7.97 (1H, s), 7. 89 (1H, dd, J = 8.1 Hz and 1.8 Hz), 7.48 (1H, d, J = 7.9 Hz), 2.24 (3H, s), and 1.26 (6H, s) ppm. ^{13}C NMR (75 MHz, DMSO-d_6, 25°C): δ = 192.17, 168.03, 157.93, 146.62, 130.16, 127.83, 123.24, 119.63, 53.98, 22.78, and 15.84 ppm.

HRMS (ESI +ve) *m/z*: Observed for $C_{12}H_{14}NO_2^+$ $[M+H]^+$ = 204.1028, $[M+H]^+$ calcd = 204.1019.

The spectra of ^{1}H and ^{13}C were given in Chapter 4.

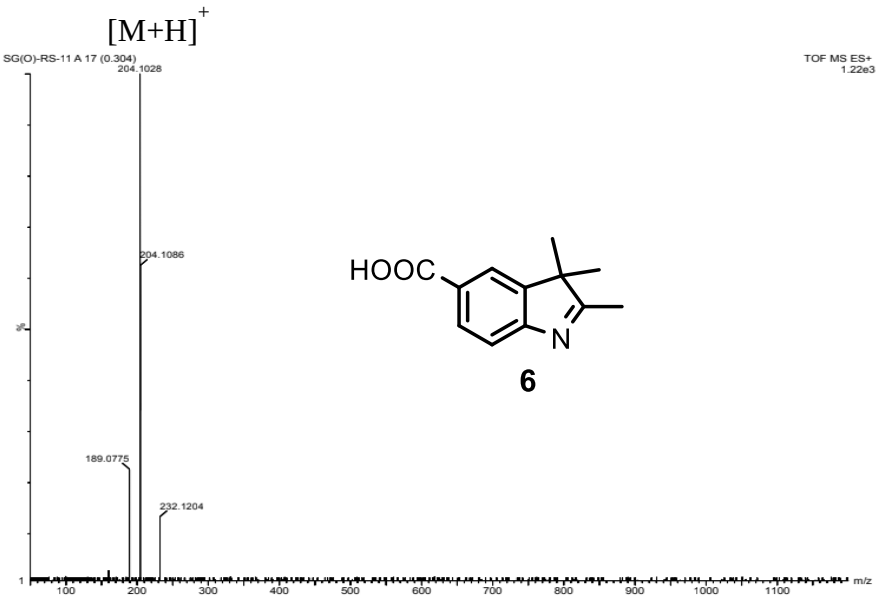

Figure 4. HRMS (ESI +ve) spectrum of Compound 6.

5-Carboxy-1,2,3,3-tetramethyl-3*H*-indol-1-ium iodide (7): Compound 6 (2 g, 9.84 mmol) and CH_3I (2 mL, 32.12 mmol) were added in a round bottomed flask containing acetonitrile (50 mL). The reaction mixture was heated at 80°C for 4 h. The solution was cooled to room temperature and diethyl ether (15 mL) was mixed to obtain a precipitate. The precipitate was filtered and the residue was washed with diethyl ether (3×) to acquire a yellow-colored pure compound 7. Yield: 3.10 g (91%)

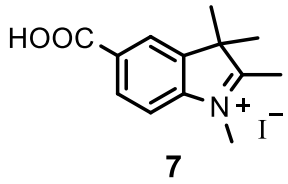

7

^{1}H NMR (300 MHz, DMSO-d_6, 25°C): δ = 8.38 (1H, s), 8.20 (1H, d, J = 8.4 Hz), 8.03 (1H, d, J = 8.2 Hz), 4.00 (3H, s), 2.82 (3H, s), and 1.57 (6H, s) ppm.

^{13}C NMR (75 MHz, DMSO-d_6, 25°C): δ = 199.55, 167.02, 145.81, 142.49, 132.09, 130.88, 124.71, 115.98, 54.81, 35.82, 22.07, and 15.50 ppm.

HRMS (ESI +ve) *m/z*: Observed for $C_{13}H_{16}NO_2^+$ $[M]^+$ = 218.1178, $[M]^+$ calcd = 218.1176.

The spectra of ^1H and ^{13}C were given in Chapter 4.

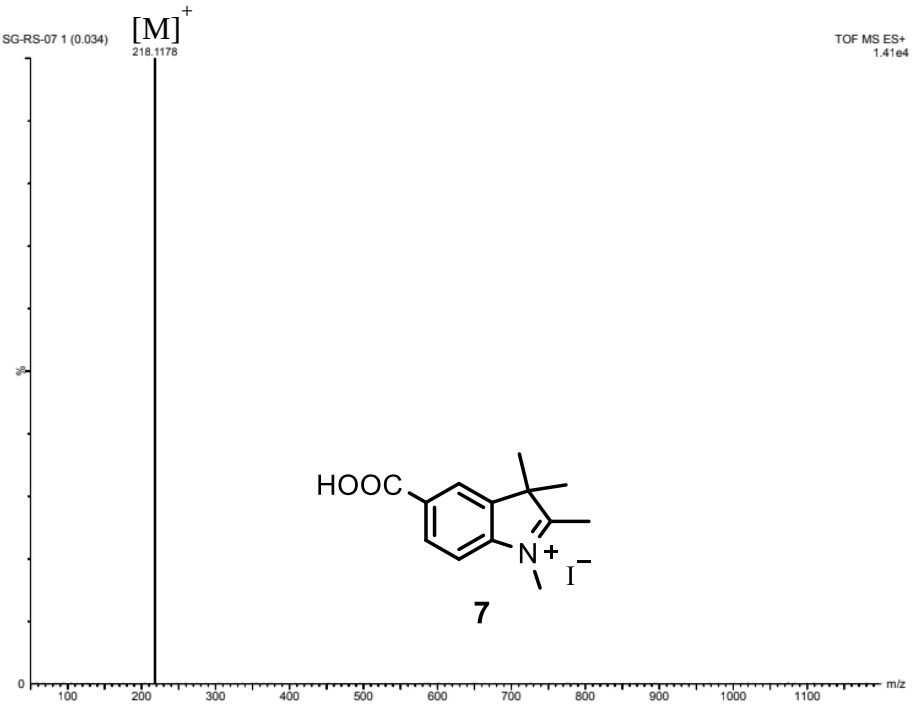

Figure 5. HRMS (ESI +ve) spectrum of Compound 7.

(*E*)-2-((2-Ethoxy-3,4-dioxocyclobut-1-en-1-yl)methylene)1,3,3trimethylindoline-5-carboxylic acid (8): Compound 7 (1.37 g, 3.98 mmol), compound 4 (0.56 g, 3.32 mmol), Et_3N (1.23 mL, 8.96 mmol), and EtOH (6 mL) were taken in a MW vessel equipped with a magnetic stir bar that was sealed and heated in a MW system at 90ºC for 45 min. The solution was cooled to room temperature. The solvent was removed using a rotary evaporator and the crude material was purified by column chromatography using 50% EtOAc / Hexane (R_f = 0.3) to acquire an orange solid.

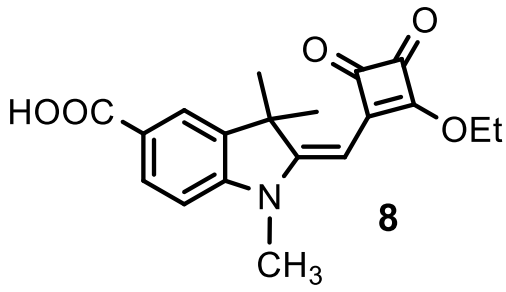

8

Yield: 0.8 g (71%).

^{1}H NMR (300 MHz, DMSO-d_6, 25°C): δ = 7.92 (1H, s), 7.89 (1H, d, J = 8.4 Hz), 7.22 (1H, d, J = 8.1 Hz), 5.37 (1H, s), 4.82 (2H, q, J = 7.2), 3.41 (3H, s), 1.57 (6H, s), and 1.44 (3H, t, J = 7.1 Hz) ppm.

^{13}C NMR (75 MHz, DMSO-d_6, 25°C): δ = 192.26, 189.51, 187.80, 173.10, 168.45, 167.4, 147.27, 140.68, 130.75, 125.04, 123.29, 108.96, 83.03, 70.51, 47.24, 30.49, 26.92, and 16.08 ppm.

HRMS (ESI +ve) *m/z*: Observed for $C_{19}H_{20}NO_5^+$ $[M+H]^+$ = 342.1343, $[M+H]^+$ calcd = 342.1336.

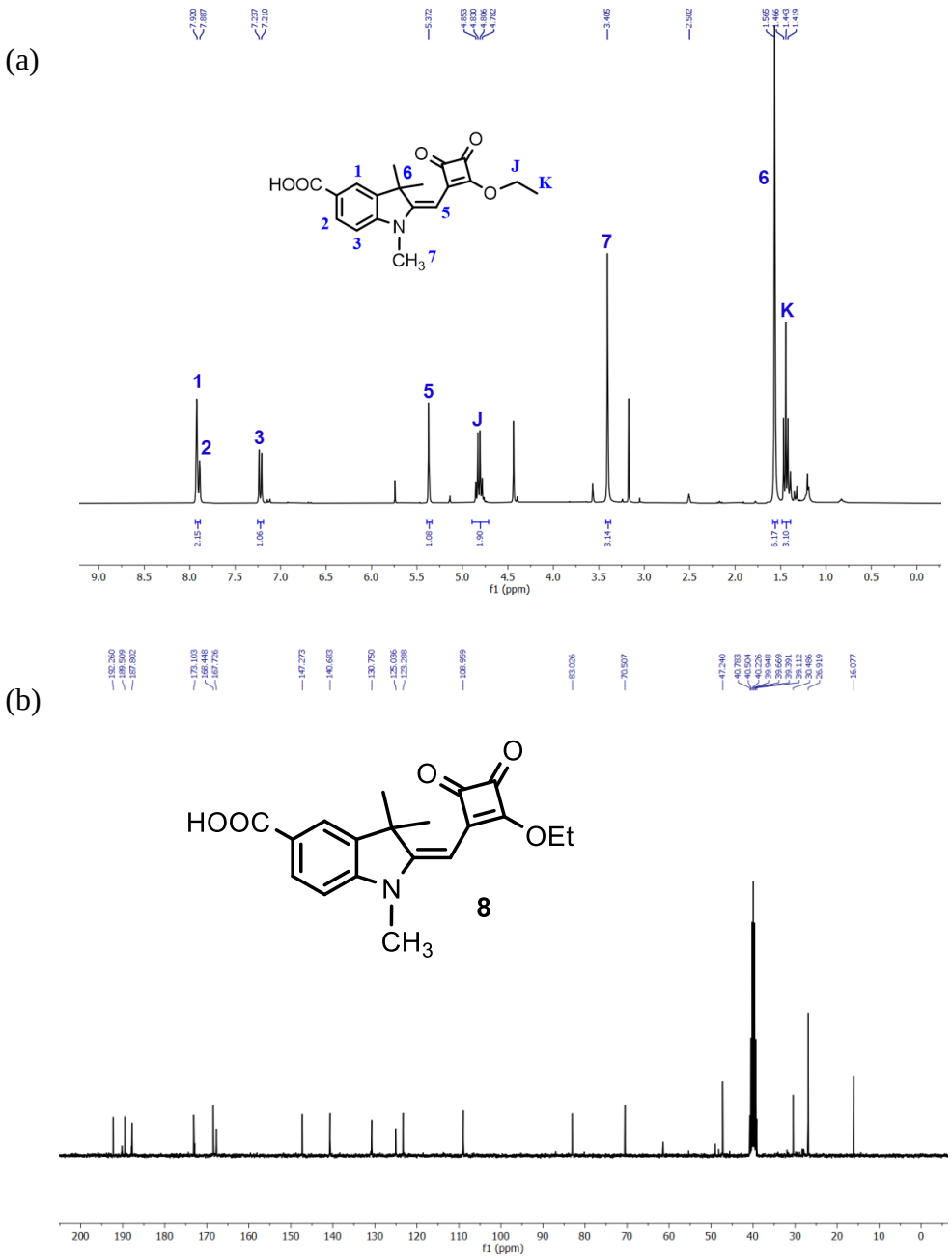

Figure 6. (a) ^{1}H NMR (300 MHz, DMSO-d_6, 25°C) spectrum of compound 8. (b) ^{13}C NMR (75 MHz, DMSO-d_6, 25°C) spectrum of 8.

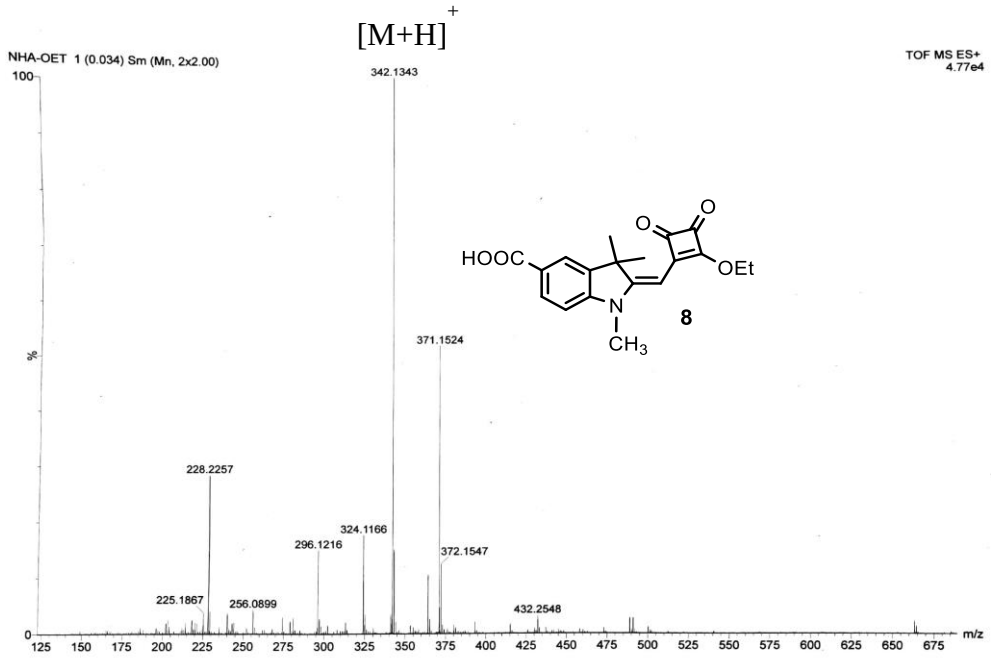

Figure 7. HRMS (ESI +ve) spectrum of Compound 8.

(*E*)-2-((2-Hydroxy-3,4-dioxocyclobut-1-en-1-yl)methylene)-1,3,3trimethylindoline-5-carboxylic acid (9): Compound 8 (0.60 g, 1.75 mmol) was dissolved in ethanol (10 mL) and refluxed. Aqueous solution of NaOH (40%, 0.4 mL) was added under the refluxing condition and the resulting mixture was stirred for 10 min. The solution was cooled to room temperature and neutralized with 2(N) HCl. The solution was concentrated under the reduced pressure and cold ethanol (5 mL) was added to obtain a precipitate. The residue was filtered and washed with cold ethanol (3×) to acquire an orange colored pure solid.

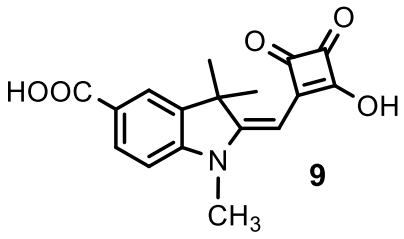

Yield: 0.32 g (58%).

^{1}H NMR (300 MHz, $CDCl_3$, 25°C): δ = 7.89 (1H, s), 7.87 (1H, d, J = 8.4 Hz), 7.16 (1H, d, J = 8.7 Hz), 5.54 (1H, s), 3.78 (1H, br), 3.37 (3H, s), and 1.58 (6H, s) ppm.

^{13}C NMR (75 MHz, $CDCl_3$, 25°C): δ = 194.38, 193.16, 174.62, 167.74, 165.53, 147.80, 140.50, 130.79, 123.94, 123.24, 108.27, 84.16, 46.68, 30.27, and 27.22 ppm. HRMS (ESI +ve) *m/z*: Observed for $C_{17}H_{15}NO_5$ $[M]^+$ = 313.0952, $[M]^+$ calcd = 313.0950.

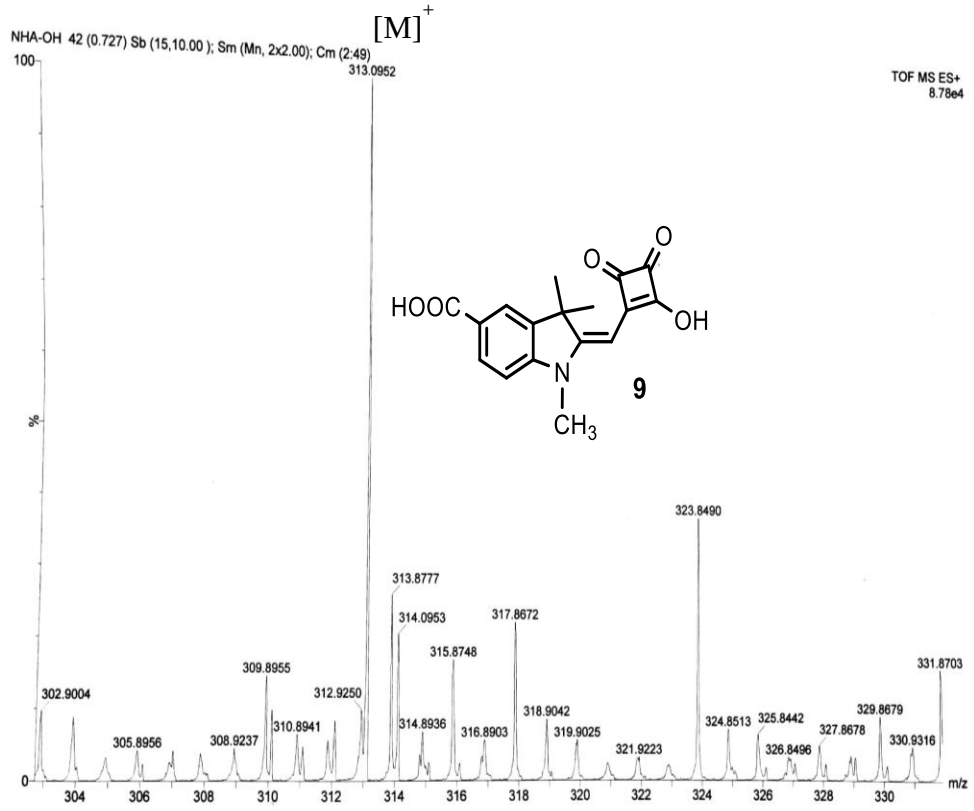

Figure 8. HRMS (ESI +ve) spectrum of compound 9.

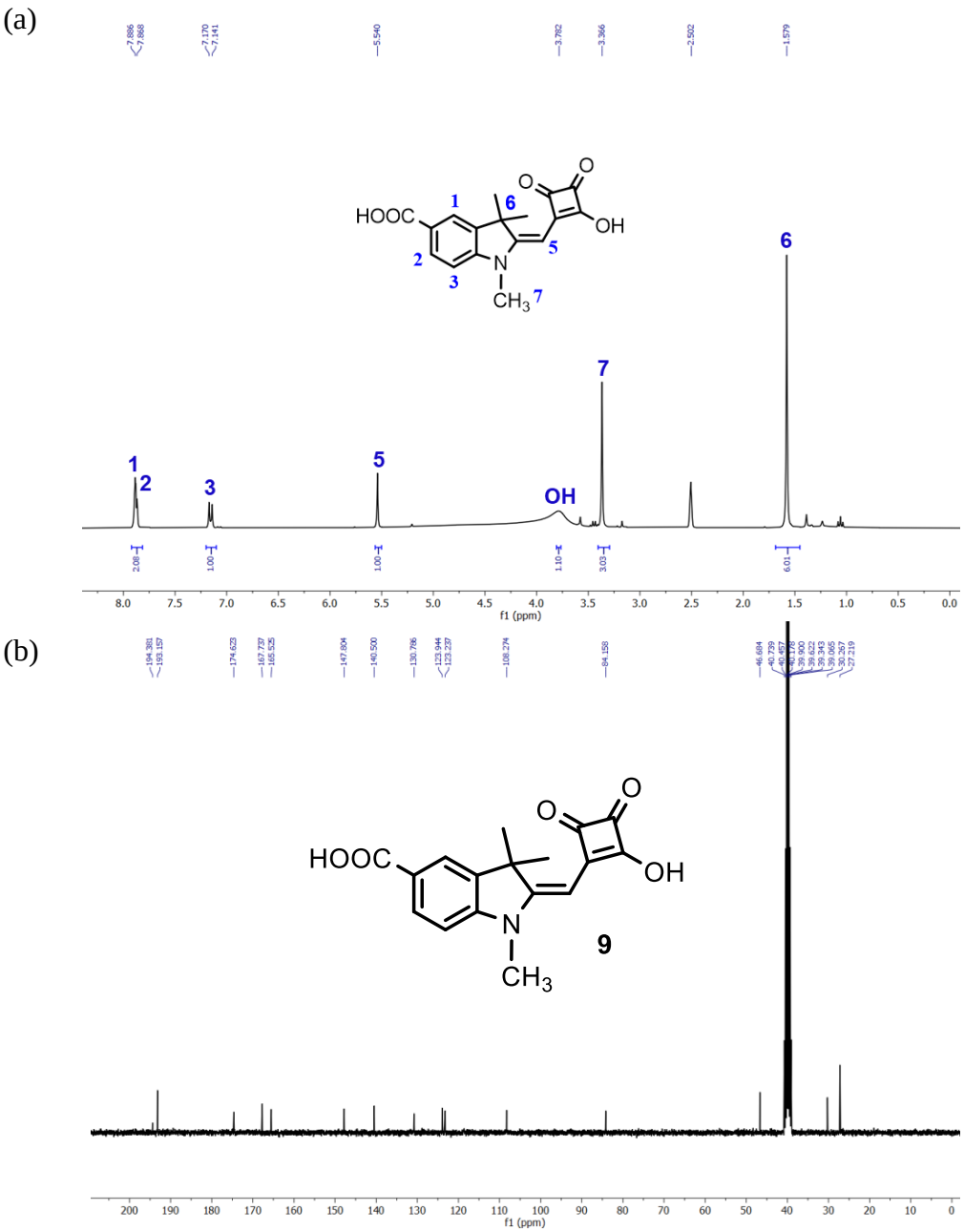

Figure 9. (a) ^{1}H NMR (300 MHz, DMSO-d_6, 25°C) spectrum of compound 9. (b) ^{13}C NMR (75 MHz, DMSO-d_6, 25°C) spectrum of 9.

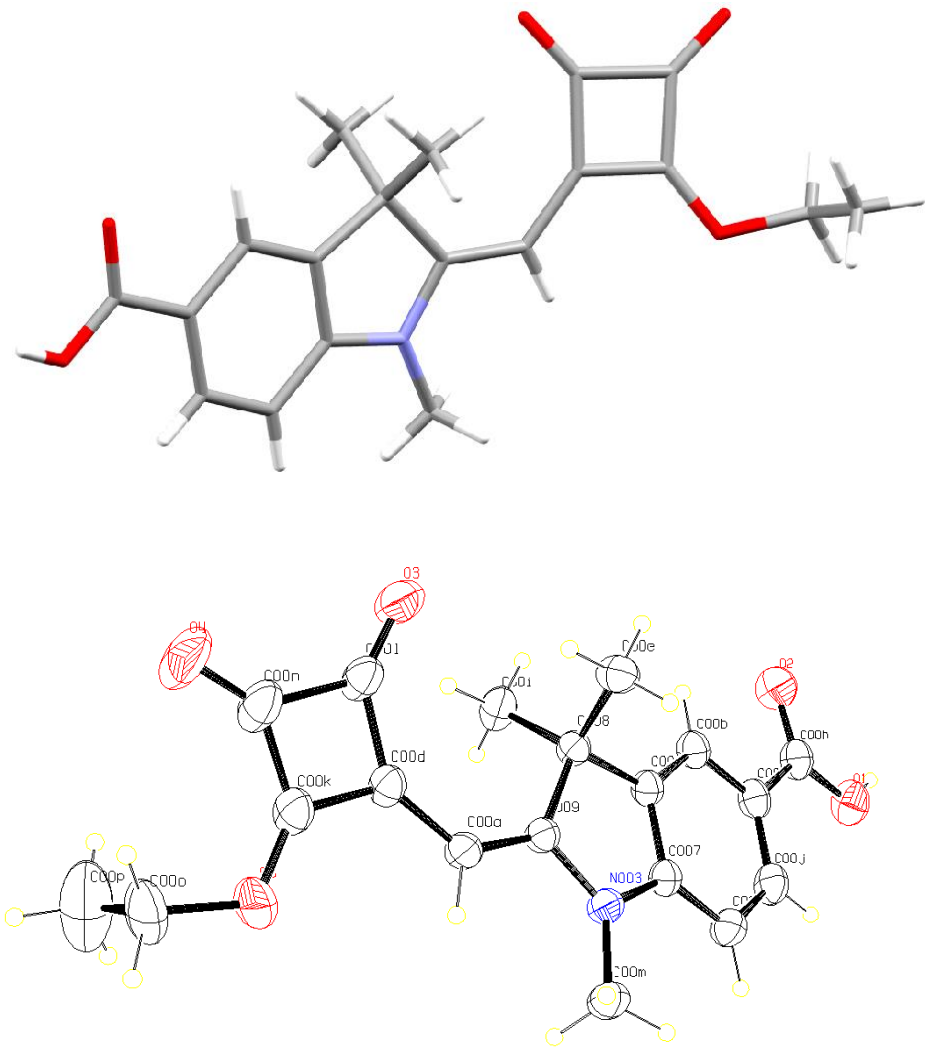

Figure 10: Single crystal X-ray structure of compound 8. Ellipsoids are drawn at the 30% probability level (ORTEP diagram).

Table 1. Crystallographic data of the compound 8.

Description	(*E*)-2-((2-Ethoxy-3,4-dioxocyclobut-1-en-1-yl)methylene)-1,3,3-trimethylindoline-5-carboxylic acid (Compound 8)
formula sum	C19 H19 N O5
formula weight	341.35
crystal system	monoclinic
space group	*P* 21/n
a (Å)	9.2413(7)
b (Å)	14.6335(12)
c (Å)	13.3411(11)
α (°)	90
β (°)	109.590(3)
γ (°)	90
V (Å^3)	1699.7(2)
Z	4
D_{calcd} (g cm^{-3})	1.334
μ (mm^{-1})	0.097
T (K)	273K
λ (Å)	0.71073
R_1	0.0516
wR_2	0.1668
CCDC No.	2260321

1,2,3,3-Tetramethyl-5-((2-(triphenylphosphonio)ethyl)carbamoyl)-3*H*-indol-1-ium hexafluorophosphate(V) iodide (10): 5-Carboxy-1,2,3,3-tetramethyl-3*H*-indol-1-ium iodide (compound 7, 0.50 g, 1.44 mmol) and HATU (0.65 g, 1.72 mmol) were dissolved in 3 mL DMF followed by 500 µL DIPEA was added into the reaction mixture and stirred for 15 min at 0°C. Then the synthesized compound (2-aminoethyl)triphenylphosphonium bromide (compound 5, 0.83 g, 2.16 mmol) was mixed into the reaction vessel and it was stirred for 12 h at room temperature in presence of N_2 atm. The solution was concentrated using a rotary evaporator to obtain the crude product. The crude material was subjected to column chromatography by 3% MeOH/DCM (R_f =0.4) to acquire a pink colored solid compound 10.

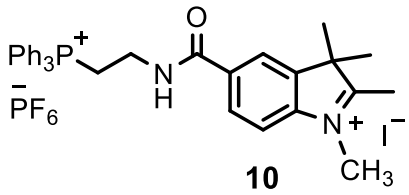

10

Yield: 0.74 g (66%).

^{1}H NMR (300 MHz, $CDCl_3$, 25°C): δ = 8.03 (1H, s), 7.81–7.71 (16H, m), 7.59 (1H, d, J = 7.2 Hz), 7.40 (1H, t, J = 5.9 Hz), 3.85–3.81 (2H, m), 3.61–3.55 (2H, m), 2.97 (3H, s), 2.89 (3H, s), and 1.36 (6H, s) ppm.

^{13}C NMR (75 MHz, $CDCl_3$, 25°C): δ = 181.79, 168.14, 167.71, 165.73, 162.63, 149.44, 145.79, 137.65, 135.30, 133.39, 130.74, 128.24, 122.68, 120.95, 118.15, 117.05, 107.76, 104.30, 44.15, 43.71, 38.57, 36.49, 34.13, 31.37, 29.65, 28.77, 26.33, 24.01, and 22.79 ppm.

(a)

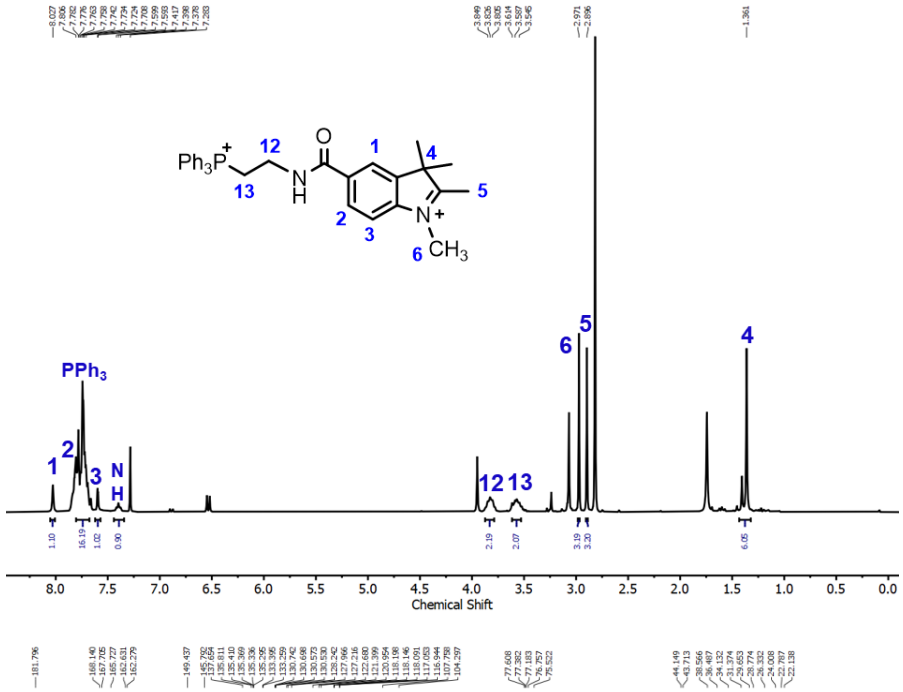

(b)

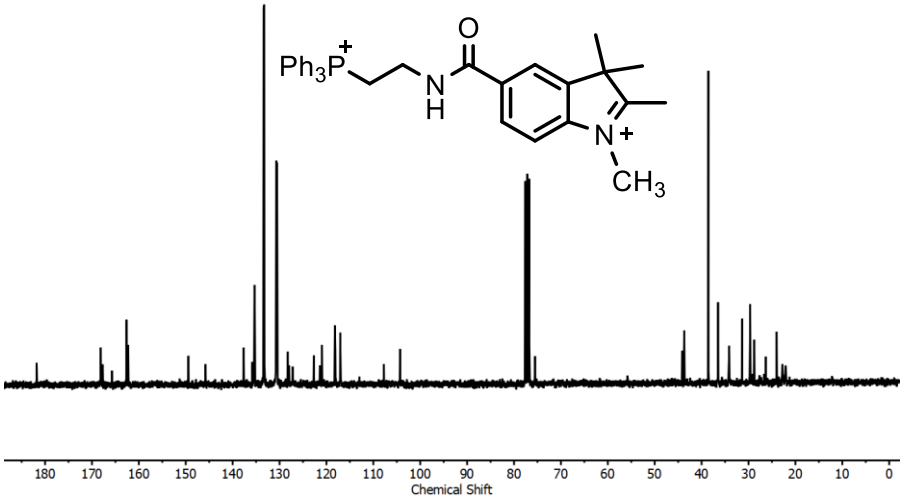

Figure 11. (a) ^{1}H NMR (300 MHz, $CDCl_3$, 25°C) spectrum of compound 10. (b) ^{13}C NMR (75 MHz, $CDCl_3$, 25°C) spectrum of 10.

(*E*)-4-((5-Carboxy-1,3,3-trimethyl-3*H*-indol-1-ium-2-yl)methylene)-3-oxo-2-(((*Z*)-1,3,3-trimethyl-5-((2(triphenylphosphonio)ethyl)carbamoyl)indolin-2-ylidene)methyl)cyclobut-1-en-1-olate hexafluorophosphate(V) (MitoSQ-COOH): The compounds 9 (0.16 mg, 0.51 mmol) and 10 (0.4 g, 0.51 mmol) were taken in a 25 mL RB flask containing a 1:1 (v/v) mixture of n-butanol (3 mL) and toluene (3 mL). The reaction mixture was stirred for 18 h at 110°C in the presence of N_2 atmosphere. A deep blue coloration was observed. The reaction mixture was cooled to room temperature. The deep blue colored solution was concentrated using a rotary evaporator and the crude product was purified by 5% MeOH/DCM (R_f = 0.3) to acquire a deep blue colored pure solid compound MitoSQ-COOH.

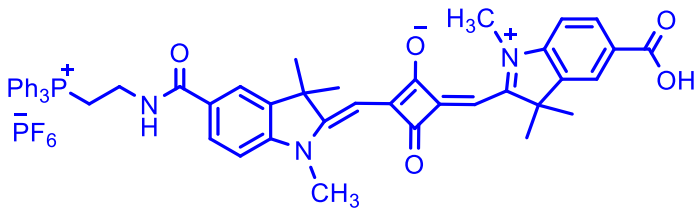

MitoSQ-COOH

Yield: 0.3 g (62%).

^{1}H NMR (300 MHz, $CDCl_3$, 25°C): δ = 9.18 (1H, t, J = 6.0 Hz), 8.02–7.94 (4H, m), 7.92–7.73 (15H, m), 7.42 (2H, d, J = 8.7 Hz), 5.86 (1H, s), 5.84 (1H, s), 3.99–3.94 (2H, m), 3.62 (6H, s), 3.39–3.37 (2H, m), and 1.72 (12H, s) ppm.

^{13}C NMR (75 MHz, $CDCl_3$, 25°C): δ = 181.26, 181.09, 180.38, 171.07, 170.45, 166.26, 146.96, 145.80, 141.68, 135.42, 134.22, 134.08, 130.76, 130.59, 129.13, 128.43, 123.51, 121.51, 119.34, 118.20, 110.38, 88.18, 60.83, 48.75, 35.15, 33.80, 31.39, 26.92, 21.69, 21.22, and 19.11 ppm.

HRMS (ESI +ve) *m/z*: Observed for $C_{50}H_{47}N_3O_5P^+[M]^+$ = 800.3252, $[M]^+$ calcd = 800.3248.

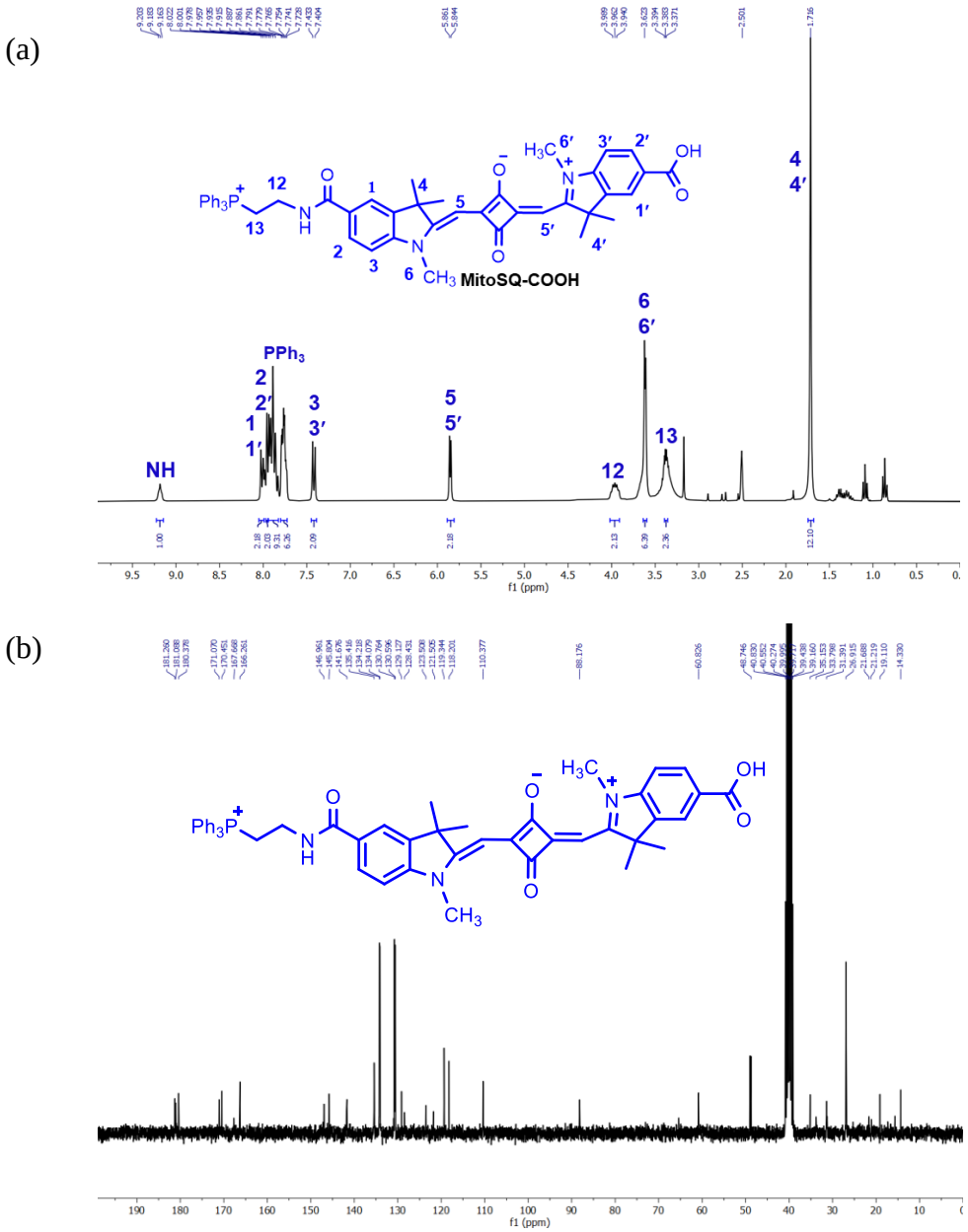

Figure 12. (a) ^{1}H NMR (300 MHz, DMSO-d_6, 25°C) spectrum of compound MitoSQ-COOH. (b) ^{13}C NMR (75 MHz, DMSO-d_6, 25°C) spectrum of MitoSQ-COOH.

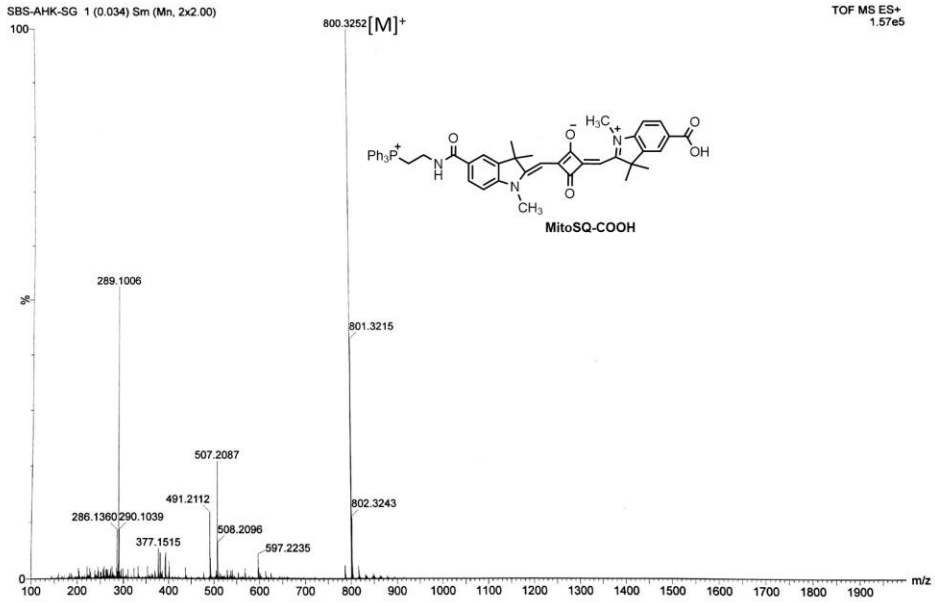

Figure 13. HRMS (ESI +ve) spectrum of MitoSQ-COOH.

2-(3,4-Bis((*tert*-butyldimethylsilyl)oxy)phenyl)ethan-1-amine (11): Dopamine hydrochloride (1.90 g, 10.0 mmol), *tert*-butyldimethylsilyl chloride (TBDMSCl, 3.77 g, 25 mmol), and imidazole (2.72 g, 39.92 mmol) were suspended in dry DCM (30 mL). The resulting suspension was stirred for 18 h under N_2 environment at 25°C. It was filtered and the filtrate was concentrated under the reduced pressure. It was extracted with Et_2O and washed with saturated $NaHCO_3$ solution (3x), water (3x) and brine (3x). The combined organic layer was dried over anh. Na_2SO_4, filtered and concentrated using a rotary evaporator to acquire the pure colorless liquid (R_f = 0.6, 10% MeOH/DCM).

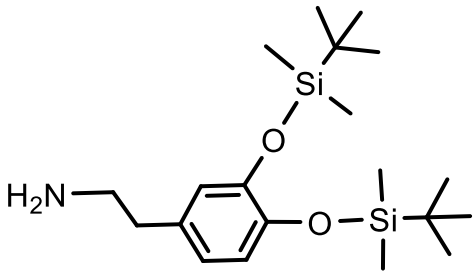

11

Yield: 2.95 g (77%).

^{1}H NMR (300 MHz, $CDCl_3$, 25°C): δ = 6.77 (1H, d, J = 7.8 Hz), 6.68–6.64 (2H, m), 3.27 (2H, br), 2.97 (2H, t, J = 7.1 Hz), 2.71 (2H, t, J = 7.2 Hz), 0.99 (18H, s), and 0.21 (12H, s) ppm.

^{13}C NMR (75 MHz, $CDCl_3$, 25°C): δ = 146.72, 145.39, 131.99, 121.67, 121.64, 121.00, 43.02, 37.92, 25.95, 25.70, 18.43, and –4.06 ppm.

HRMS (ESI +ve) *m/z*: Observed for $C_{20}H_{40}NO_2Si_2^+$ $[M+H]^+$ = 382.2571, $[M]^+$ calcd = 382.2592.

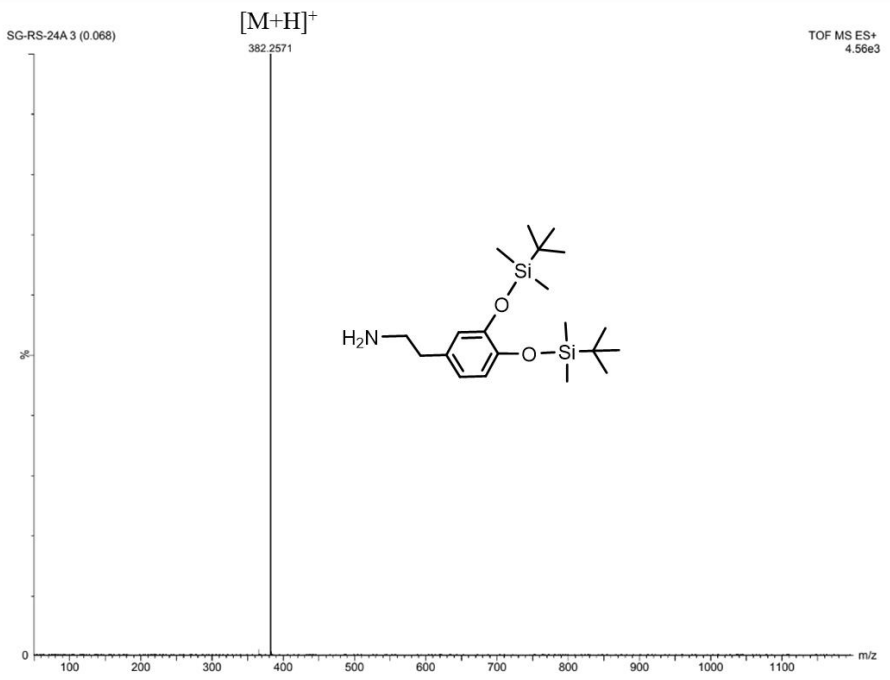

Figure 14. HRMS (ESI +ve) spectrum of compound 11.

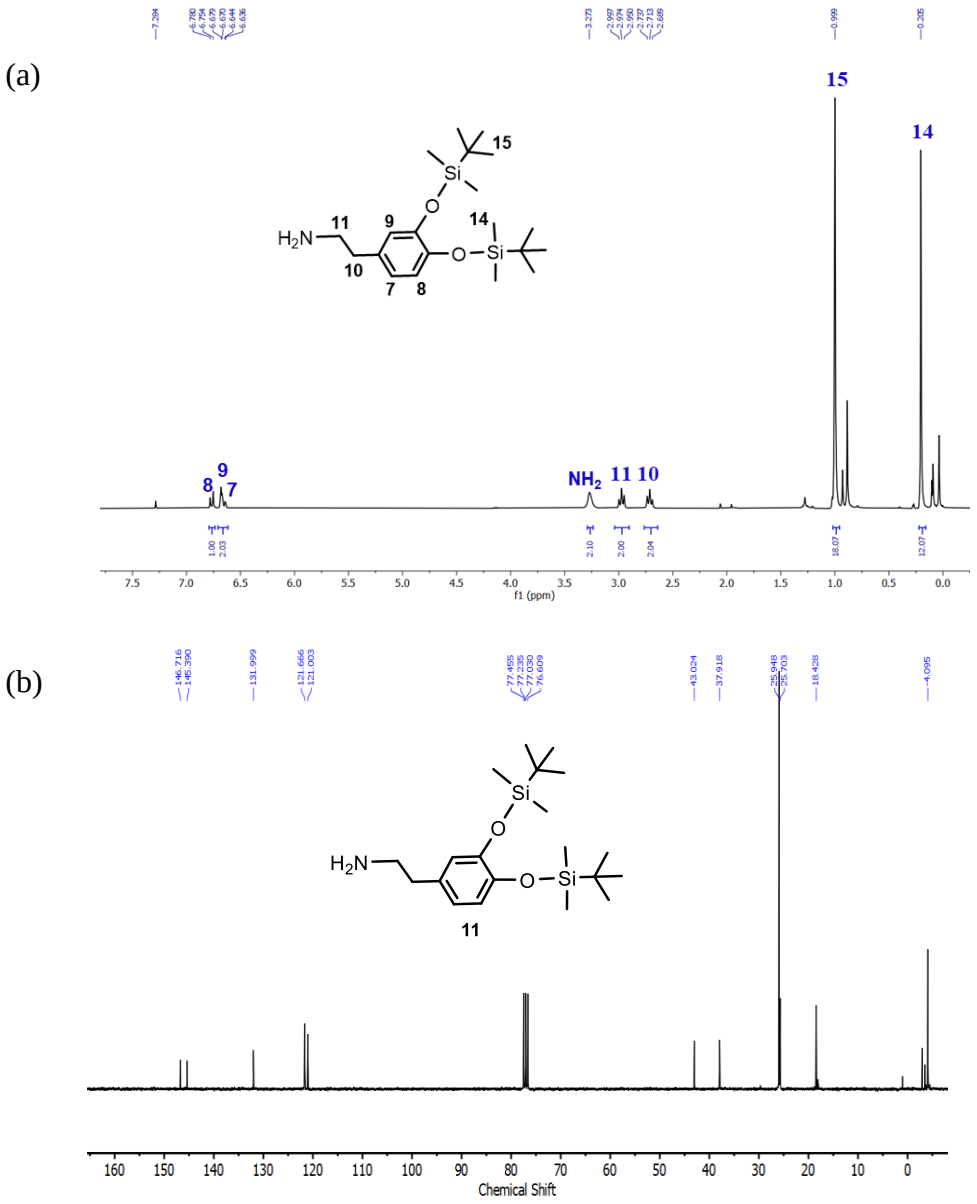

Figure 15. (a) ^{1}H NMR (300 MHz, $CDCl_3$, 25°C) spectrum of compound 11. (b) ^{13}C NMR (75 MHz, $CDCl_3$, 25°C) spectrum of 11.

(*E*)-4-((5-((3,4-Bis((*tert*-butyldimethylsilyl)oxy)phenethyl)carbamoyl)-1,3,3-trimethyl-3*H*-indol-1-ium-2-yl)methylene)-3-oxo-2-(((*Z*)-1,3,3-trimethyl-5-((2-(triphenylphosphonio)ethyl)carbamoyl)indolin-2-ylidene)methyl)cyclobut-1-en-1-olate hexafluorophosphate(V) (MitoSQ-DOPA): MitoSQ-COOH (0.2 g, 0.21 mmol) and HATU (0.087 g, 0.23 mmol) were dissolved in 3 mL DMF followed by 150 µL DIPEA was added to the reaction mixture and stirred for 15 min at 0°C. Then the synthesized compound 2-(3,4-bis((tert-butyldimethylsilyl)oxy)phenyl)ethan-1-amine (compound 11, 0.118 g, 0.31 mmol) was added and stirred for 12 h at 25°C in the presence of N_2 atmosphere. The reaction mixture was concentrated using a rotary evaporator to acquire the crude material. The crude material was subjected to column chromatography by 3% MeOH/DCM (R_f = 0.4) to obtain a deep blue colored pure solid compound MitoSQ-DOPA.

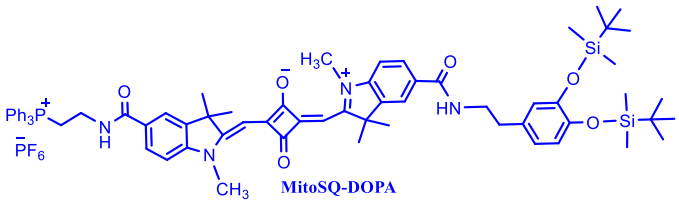

MitoSQ-DOPA

Yield: 0.2 g (73%).

^{1}H NMR (300 MHz, $CDCl_3$, 25°C): δ = 7.84 (2H, d, J = 2.4 Hz), 7.80 (2H, d, J = 7.2 Hz), 7.77–7.65 (15H, m), 7.56 (1H, t, J = 5.7 Hz), 7.06 (1H, d, J = 8.4 Hz), 6.99 (1H, d, J = 8.4 Hz), 6.80 (1H, d, J = 7.8 Hz), 6.72–6.68 (2H, m), 6.21 (1H, br), 5.98 (2H, s), 3.88–3.84 (2H, m), 3.70–3.66 (2H, m), 3.59 (6H, s), 2.97–2.82 (4H, m), 1.78 (12H, s), 0.99 (18H, s), 0.21 (6H, s), and 0.18 (6H, s) ppm.

^{13}C NMR (75 MHz, $CDCl_3$, 25°C): δ = 191.24, 182.18, 171.66, 171.08, 167.59, 166.77, 154.98, 146.91, 145.57, 135.48, 133.44, 131.93, 130.64, 130.12, 128.46, 127.31, 127.22, 121.79, 121.61, 121.11, 118.21, 117.06, 109.24,

108.85, 87.98, 49.26, 49.13, 41.42, 34.99, 34.38, 29.69, 27.11, 26.95, 25.96, 22.72, 22.08, 18.45, and –4.06 ppm.

HRMS (ESI +ve) *m/z*: observed for $C_{70}H_{84}N_4O_6PSi_2^+$ $[M]^+$ = 1163.5795, $[M]^+$ calcd = 1163.5662.

Photophysical properties in DMSO λ_{abs}= 653 nm, λ_{em}= 663 nm, Stokes shift ($\Delta\lambda$) = 10 nm, ε = 1.49 ×10^5 $M^{-1}cm^{-1}$, Φ_f = 0.23 in DMSO (Φ_f of Zinc phthalocyanine as reference = 0.20 in DMSO).

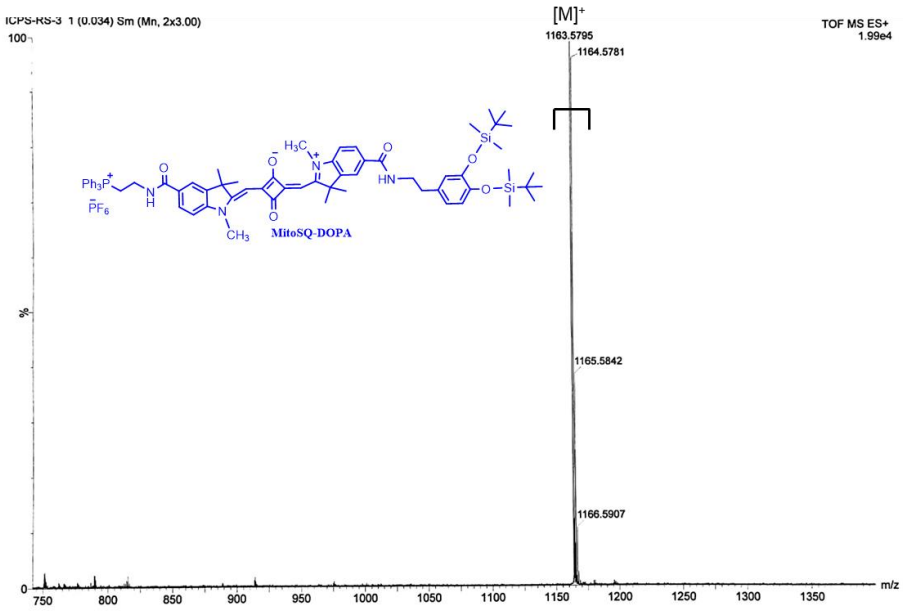

Figure 16. HRMS (ESI +ve) spectrum of MitoSQ-DOPA.

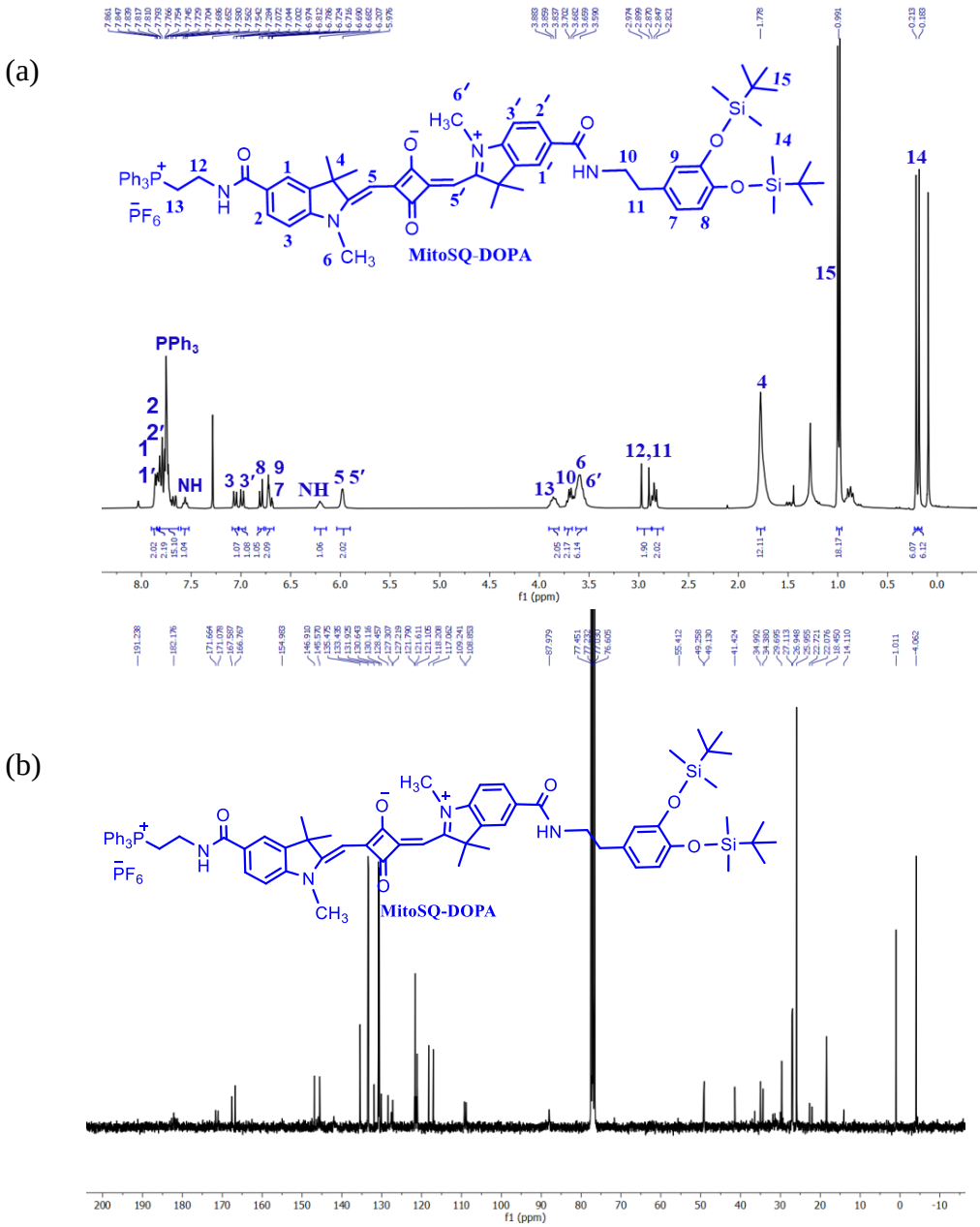

Figure 17. (a) ^{1}H NMR (300 MHz, $CDCl_3$, 25°C) spectrum of compound MitoSQ-DOPA. (b) ^{13}C NMR (75 MHz, $CDCl_3$, 25°C) spectrum of MitoSQ-DOPA.

A confocal laser scanning microscope was used to perform a cellular uptake and imaging experiment on an epithelioid cervical cancer HeLa cell line using MitoSQ-DOPA. We observed a faint NIR fluorescence signal inside the mitochondria which suggests bleaching of the dye inside the live-cell mitochondria (**Figure 18**). Moreover, aggregation has been observed in the addition of H_2O into the DMSO solution of MitoSQ-DOPA which leads to the broadening of its absorption/emission bands (**Figure 19**).[19]

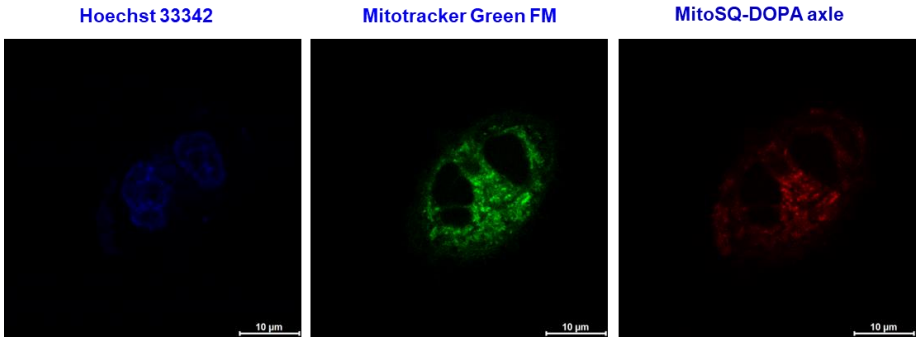

Figure 18. Confocal images of NIR MitoSQ-DOPA colocalized with MTG in epithelioid cervix carcinoma HeLa cell line.

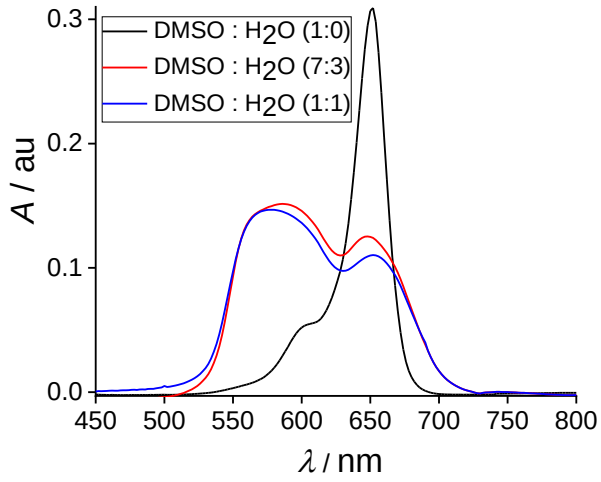

Figure 19. Absorption spectra for a molecule MitoSQ-DOPA (5 μM) in DMSO and DMSO-H_2O mixed solvent. The aggregation has been observed in the addition of H_2O into the DMSO solution of the axle.

Attempts to synthesize rotaxane molecule MitoSQRot-$(Alkyne)_2$-DOPA by a direct slippage process [MitoSQ-DOPA and Macrocycle-$(Alkyne)_2$] are unsuccessful and it is probably owing to the steric bulk of the trimethyl substituents in indolin moieties of MitoSQ-DOPA. A template directed clipping method is used to construct the rotaxane molecule MitoSQRot-$(Alkyne)_2$-DOPA (**Scheme 2**) and characterized using various spectroscopic methods (**Figure 20-26**). The Macrocycle-$(Alkyne)_2$ containing rotaxane MitoSQRot-$(Alkyne)_2$-DOPA are bioconjugated with N_3-Carbohydrate by click chemistry using CuAAC (**Scheme 3**) to form MitoSQRot-$(Carb\text{-}OAc)_2$-DOPA followed by deprotection of OAc group using 1(M) NaOMe (**Scheme 4**). Herein, the MIMs MitoSQRot-$(Carb\text{-}OH)_2$-DOPA, comprising of an unsymmetrical NIR SQ core conjugated with a lipophilic cationic TPP^+ residue and TBDMS protected DOPA moiety. In addition, carbohydrate moiety is tethered with the tetralactam macrocycle to improve water solubility and to shield the dye from nucleophilic attack in the cellular environment.

Synthetic scheme of the rotaxane MitoSQRot-$(Alkyne)_2$-DOPA:

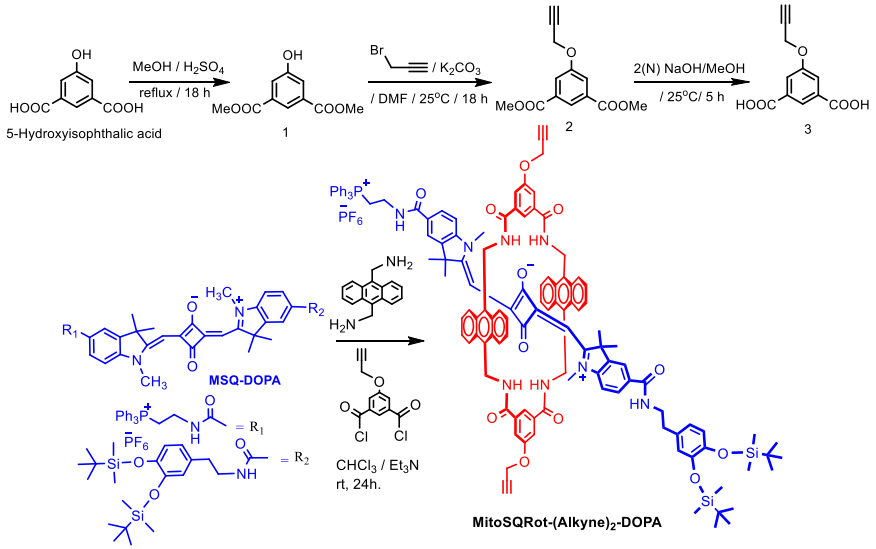

Scheme 2. Synthesis of MitoSQRot-(Alkyne)$_2$-DOPA using template directed clipping method.

Dimethyl 5-hydroxyisophthalate (1): Into CH_3OH (50 mL) solution of 5-hydroxyisophthalic acid (2.73 g, 15 mmol); conc. H_2SO_4 (2.5 mL) was mixed slowly and the resulting solution was refluxed for 18 h. A clear solution was acquired, that was cooled to room temperature then poured into ice-cold water (150 mL). White precipitates were obtained, that was filtered, washed with H_2O (5×), and dried under vacuum to achieve a white colored pure solid compound **1**.

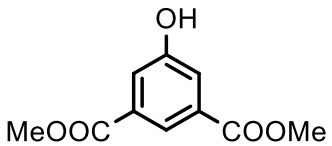

1

Yield: 2.84 g (90%).

^{1}H NMR (300 MHz, DMSO-d_6, 25°C): δ = 10.34 (1H, s), 7.95 (1H, s), 7.57 (2H, s), and 3.87 (6H, s) ppm.

^{13}C NMR (75 MHz, DMSO-d_6, 25°C): δ = 165.82, 158.31, 131.74, 120.73, 120.56, and 52.78 ppm.

The spectra of ^{1}H and ^{13}C were given in Chapter 4.

Dimethyl 5-(prop-2-yn-1-yloxy)isophthalate (2): Into anhydrous DMF (25 mL) solution of dimethyl-5-hydroxyisophthalate (2.1 g, 10 mmol) and K_2CO_3 (2.07 g, 15 mmol); propargyl bromide (80% in toluene) (1.51 mL, 20 mmol) was added dropwise over 10 min. The solution was stirred at 25°C for 18 h in a nitrogen environment then poured in ice-cold water (100 mL). A white precipitate was formed, filtered and the residue was washed several times with H_2O to obtain a white pure solid product **2**.

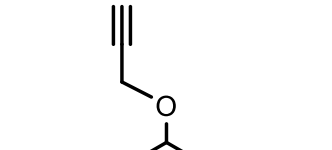

2

Yield: 2.20 g (89%).

^{1}H NMR (300 MHz, $CDCl_3$, 25°C): δ = 8.32 (1H, s), 7.82 (2H, s), 4.79 (2H, s), 3.95 (6H, s), and 2.56 (1H, s) ppm.

^{13}C NMR (75 MHz, $CDCl_3$, 25°C): δ = 165.95, 157.53, 131.86, 123.81, 119.14, 77.60, 76.34, 56.24, and 52.04 ppm.

The spectra of ^{1}H and ^{13}C were given in Chapter 4.

5-(Prop-2-yn-1-yloxy)isophthalic acid (3): CH_3OH (20 mL), 2(N) NaOH (10 mL), and compound 2 (1.85 g, 7.5 mmol) were taken in a 100 mL round bottomed flask. The solution was stirred at 25°C for 5 h. The solution was concentrated using a rotary evaporator. Water (50 mL) was added into the concentrated solution and it was extracted with EtOAc (3×100 mL). Aqueous layer was collected in a conical flask (250 mL) and acidified by using 2(N) HCl (pH 2-3) to acquire a white residue. The residue was filtered and washed with cold H_2O (5×) to obtain a white solid pure compound **3**.

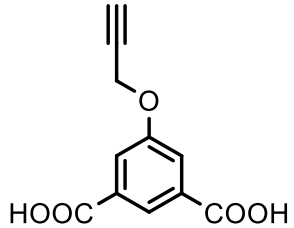

3

Yield: 1.4 g (85%)

^{1}H NMR (300 MHz, DMSO-d_6, 25°C): δ = 13.34 (2H, s), 8.11 (1H, s), 7.72 (2H, s), 4.95 (2H, s), and 3.63 (1H, s) ppm.^{13}C NMR (75 MHz, DMSO-d_6, 25°C): δ = 166.76, 157.77, 133.09, 123.36, 120.06, 79.39, 79.12, and 56.41 ppm.

The spectra of ^{1}H and ^{13}C were given in Chapter 4.

Synthesis of Macrocycle-(Alkyne)$_2$:

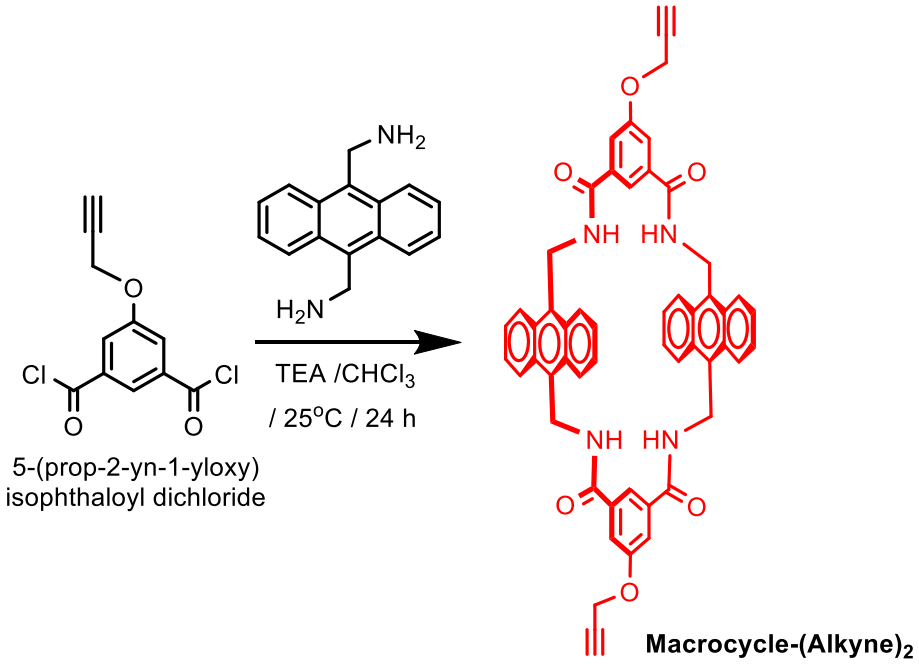

Scheme 3. Synthesis of Macrocycle-(Alkyne)$_2$.

Macrocycle-(Alkyne)$_2$: 5-(Prop-2-yn-1-yloxy)isophthaloyl dichloride (0.22 g, 0.85 mmol) and 9,10-bis(aminomethyl)anthracene (0.21 g, 0.88 mmol) were separately dissolved in anhydrous $CHCl_3$ (25 mL). The $CHCl_3$ solutions of the individual compounds were taken into two separate 50 mL syringes. Et_3N (0.5 mL) was incorporated into the syringe comprising 9,10-bis(aminomethyl)anthracene. These two solutions were added drop wise by syringes simultaneously over 6 h into a stirred solution of anhydrous $CHCl_3$ (40 mL) in a two neck round bottomed flask. After stirring at 25°C for 18 h, the

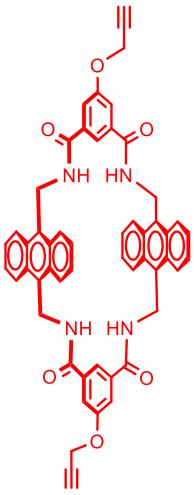

solution was concentrated using rotary evaporator to obtain the crude product and it was purified through column chromatography by $CHCl_3$/Acetone (10-15 %) to acquire pure compound Macrocycle-$(Alkyne)_2$ as a pale yellow colored solid.

Yield: 0.198 g (28%).

^1H NMR (300 MHz, $CDCl_3$, 25°C): δ = 8.16 (8H, d, J = 7.2 Hz), 7.88 (4H, s), 7.44–7.41 (8H, m), 7.08 (2H, s), 6.47 (4H, br), 5.46 (8H, d, J = 4.8 Hz), 4.75 (4H, s), and 2.62 (2H, s) ppm.

^{13}C NMR (75 MHz, $CDCl_3$, 25°C): δ = 165.81, 138.44, 135.60, 130.16, 128.08, 126.52, 124.41, 121.33, 77.45, 76.61, 56.23, and 29.71 ppm.

HRMS (ESI +ve) *m/z*: Observed for $C_{54}H_{40}N_4O_6$ $[M]^+$ = 840.2938, $[M]^+$ calcd = 840.2948.

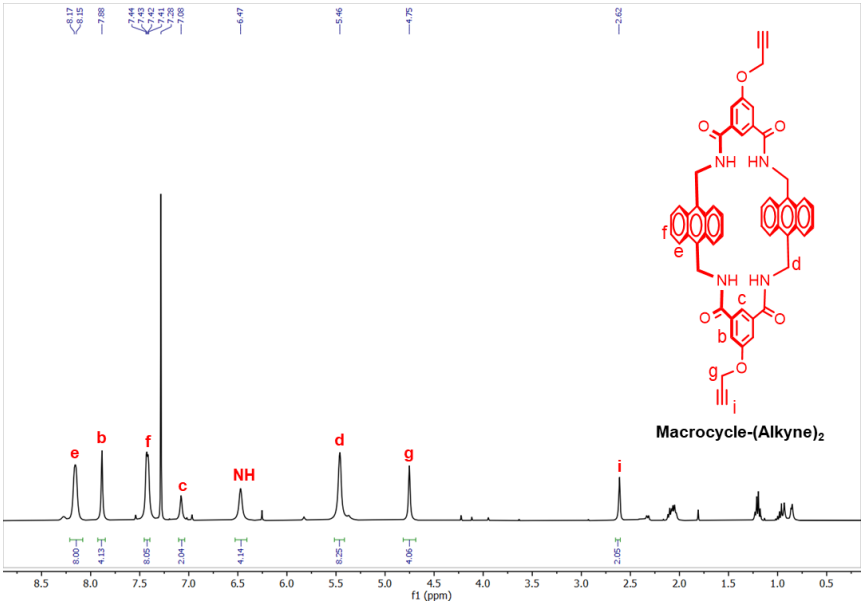

Figure 20. ^1H NMR (300 MHz, $CDCl_3$, 25°C) spectrum of the Macrocycle-$(Alkyne)_2$.

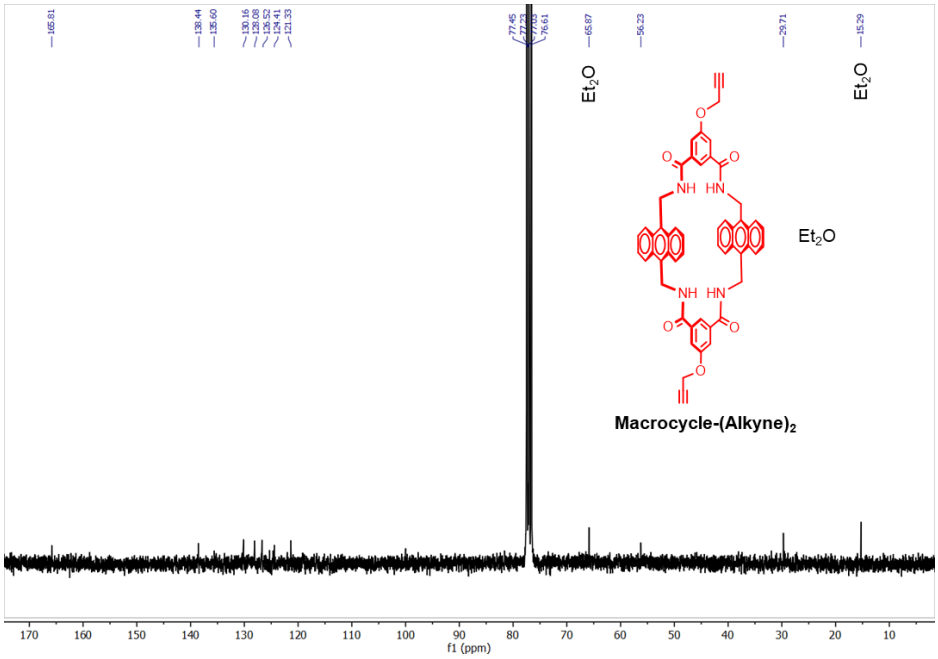

Figure 21. ^{13}C NMR (75 MHz, $CDCl_3$, 25°C) spectrum of the Macrocycle-(Alkyne)$_2$.

MitoSQRot-(Alkyne)$_2$-DOPA: 5-(Prop-2-yn-1-yloxy)isophthaloyl dichloride (0.3 g, 1.17 mmol) and 9,10-bis(aminomethyl)anthracene (0.28 g, 1.17 mmol) were dissolved separately in anhydrous $CHCl_3$ (30 mL). Each solution was taken into a separate 50 mL syringe. Et_3N (1 mL) was added to the syringe containing 9,10-bis(aminomethyl)anthracene. To a stirred solution of MitoSQ-DOPA (0.39 g, 0.3 mmol) in anhydrous $CHCl_3$ (60 mL) in a two neck round bottomed flask the two previously prepared solutions were added simultaneously drop wise over 6 h using syringes. After 24 h stirring at 25°C, the resulting solution was

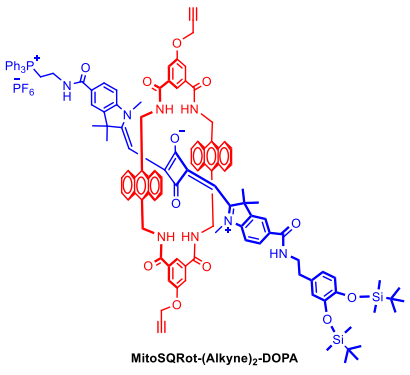

concentrated using a rotary evaporator to obtain the crude product. The crude product was purified by column chromatography using 3% MeOH/$CHCl_3$ to achieve a sea green colored pure solid MitoSQRot-(Alkyne)$_2$-DOPA.

Yield: 0.11 g (17%)

^{1}H NMR (300 MHz, $CDCl_3$, 25°C): δ = 9.33 (2H, s), 8.19 (4H, s), 8.09 (4H, d, J = 8.2 Hz), 7.95 (2H, s), 7.88–7.86 (2H, m), 7.85–7.76 (23H, m), 7.64 (1H, t, J = 5.7 Hz), 7.11–7.06 (4H, m), 7.04–7.02 (1H, m), 6.92 (1H, d, J = 7.8 Hz), 6.84 (1H, t, J = 8.1 Hz), 6.76 (2H, s), 6.69–6.62 (4H, m), 6.14 (1H, t, J = 5.8 Hz), 5.50–5.48 (4H, m), 5.13–5.08 (4H, m), 5.01 (4H, d, J = 4.2 Hz), 4.62 (1H, s), 4.59 (1H, s), 3.97–3.91 (2H, m), 3.75–3.73 (2H, m), 3.51–3.47 (2H, m), 2.88–2.86 (2H, m), 2.79 (2H, s), 2.66 (6H, s), 1.27 (12H, s), 1.02 (18H, s), and 0.23 (12H, s) ppm.

^{13}C NMR (75 MHz, $CDCl_3$, 25°C): δ = 198.23, 181.56, 173.03, 171.96, 168.34, 167.07, 166.59, 165.83, 162.02, 159.93, 158.80, 146.61, 145.74, 139.20, 135.34, 134.71, 133.49, 132.04, 130.77, 130.60, 130.46, 130.14, 128.65, 128.53, 125.41, 124.39, 121.64, 118.93, 117.28, 108.46, 100.01, 78.06, 76.61, 66.16, 56.37, 50.01, 41.39, 38.05, 34.95, 34.19, 31.94, 31.64, 29.71, 29.38, 28.13, 27.85, 27.09, 25.94, 22.71, 18.47, and –4.02 ppm.

2D NMR: ^{1}H–^{1}H gCOSY (Gradient-selected Correlation Spectroscopy) NMR (300 MHz, $CDCl_3$, 25°C) spectrum of the rotaxane MitoSQRot-(Alkyne)$_2$-DOPA confirmed the coupling connectivity (**Figure 25**). ^{1}H-^{1}H ROESY (Rotating frame Overhauser Effect Spectroscopy) NMR (300 MHz, $CDCl_3$, 25°C) spectrum of the rotaxane MitoSQRot-(Alkyne)$_2$-DOPA demonstrated proximity of the protons e with 5,5′, e with 4,4′, e with 6,6′, f with 4,4′, and f with 6,6′; confirming rotaxane formation (**Figure 26**).

HRMS (ESI +ve) *m/z*: observed for $C_{124}H_{125}N_8O_{12}PSi_2^{+2}$ $[M+H]^{+2}$ = 1002.9447, $[M+H]^{+2}$ calcd = 1002.9358.

Photophysical properties in DMSO λ_{abs}= 660 nm, λ_{em}= 671 nm, Stokes shift ($\Delta\lambda$) = 11 nm, ε = 1.38 ×10^5 $M^{-1}cm^{-1}$, Φ_f = 0.58 in DMSO (Φ_f of Zinc phthalocyanine as reference = 0.20 in DMSO).

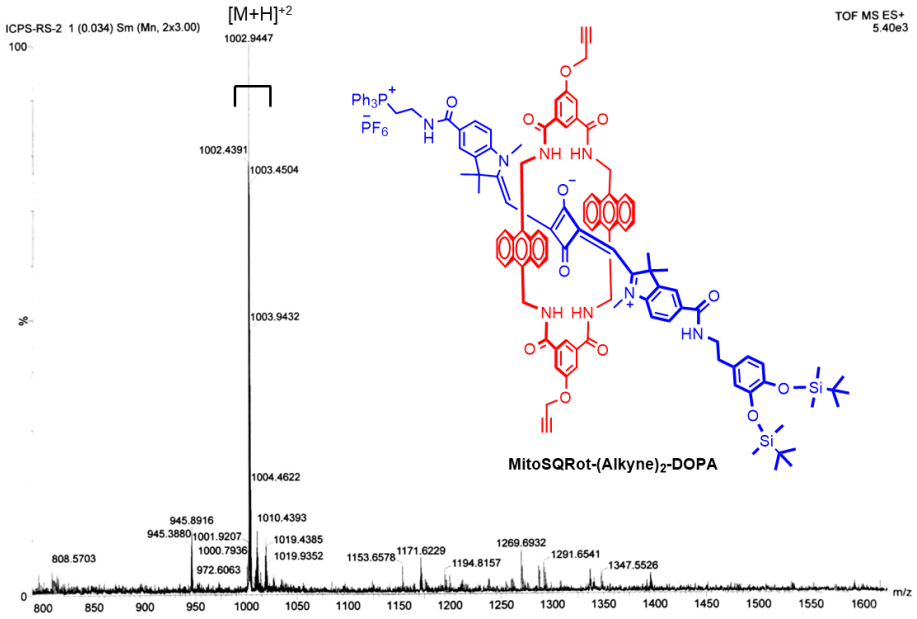

Figure 22. HRMS (ESI +ve) spectrum of the rotaxane MitoSQRot-(Alkyne)$_2$-DOPA.

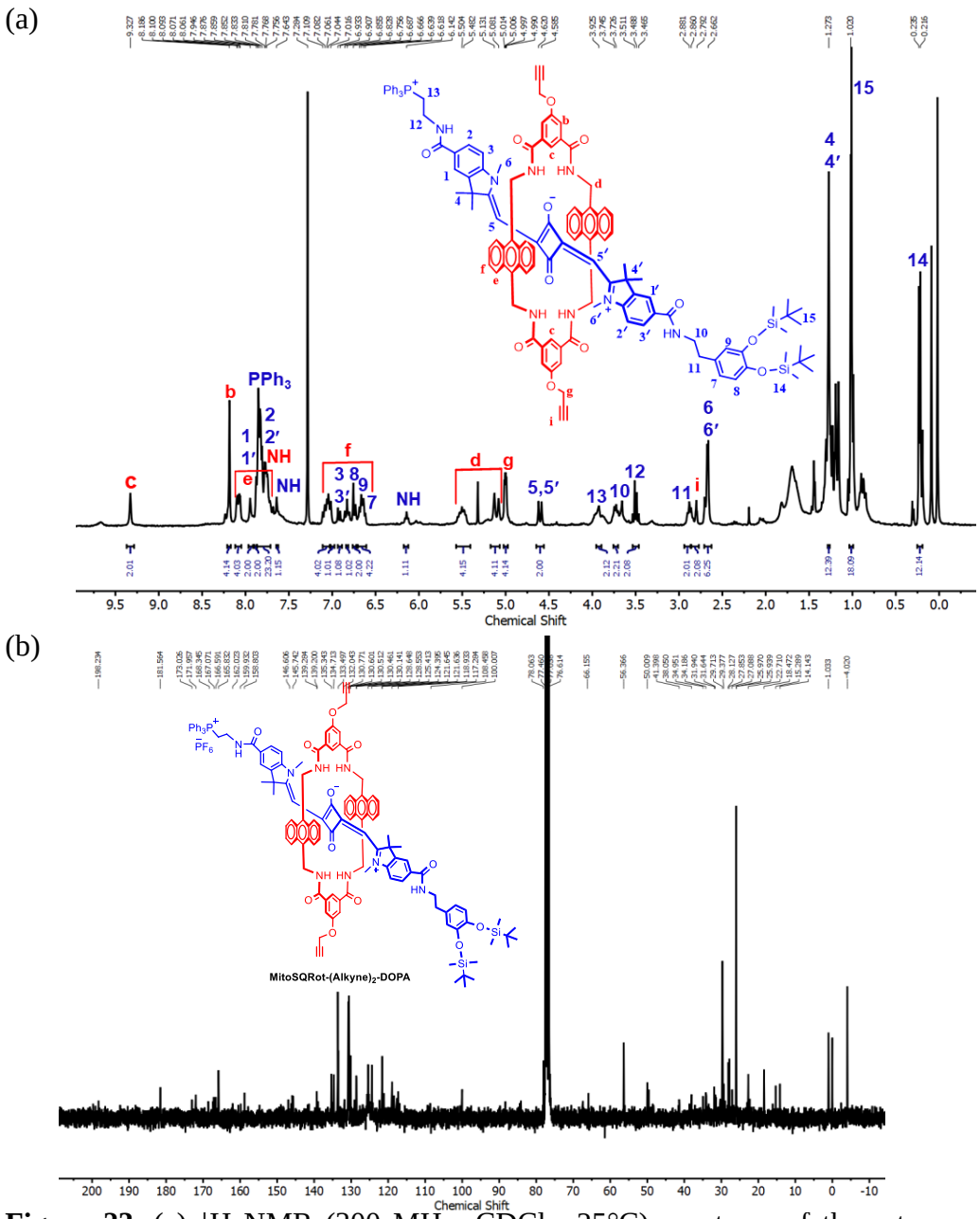

Figure 23. (a) ^{1}H NMR (300 MHz, $CDCl_3$, 25°C) spectrum of the rotaxane MitoSQRot-(Alkyne)$_2$-DOPA. (b) ^{13}C NMR (75 MHz, $CDCl_3$, 25°C) spectrum of the rotaxane MitoSQRot-(Alkyne)$_2$-DOPA.

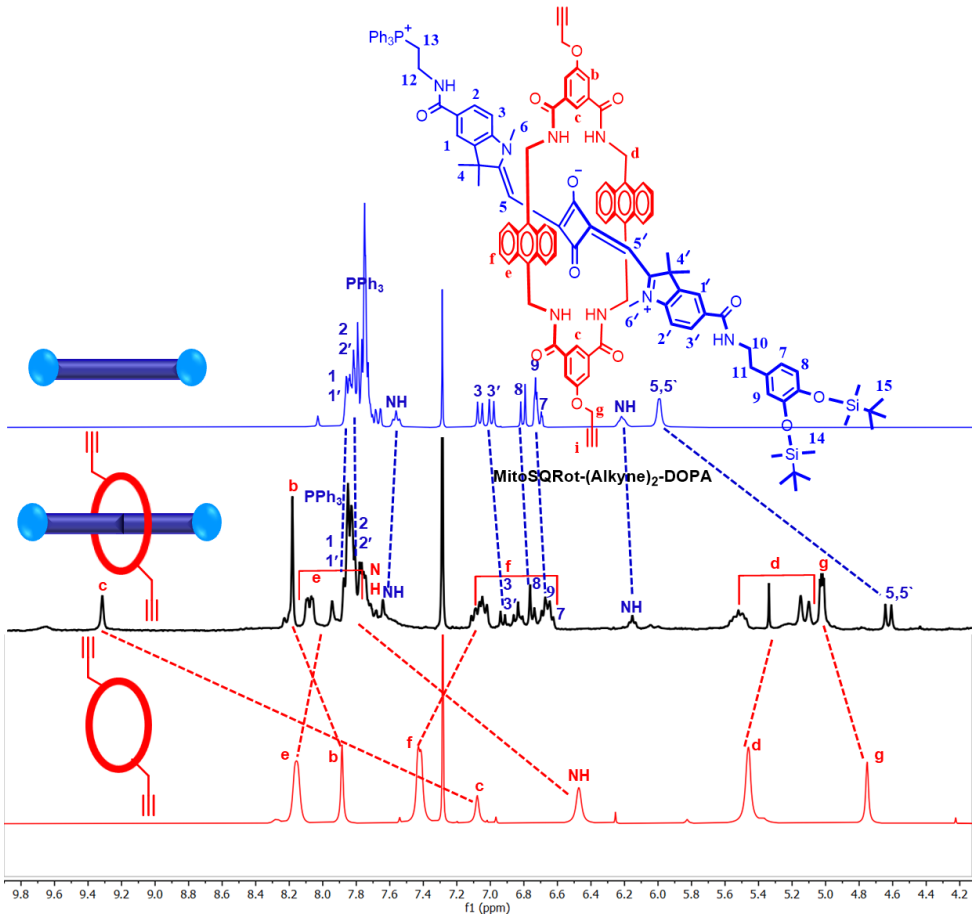

Figure 24. Partial ^{1}H NMR (300 MHz, $CDCl_3$, 25°C) stacking of the empty macrocycle, rotaxane MitoSQRot-(Alkyne)$_2$-DOPA, and axle MitoSQ-DOPA showing downfield shift of macrocycle proton c, NH and upfield shift of e, f as well as MitoSQ-DOPA axle proton 5, 5′ confirm rotaxane synthesis.

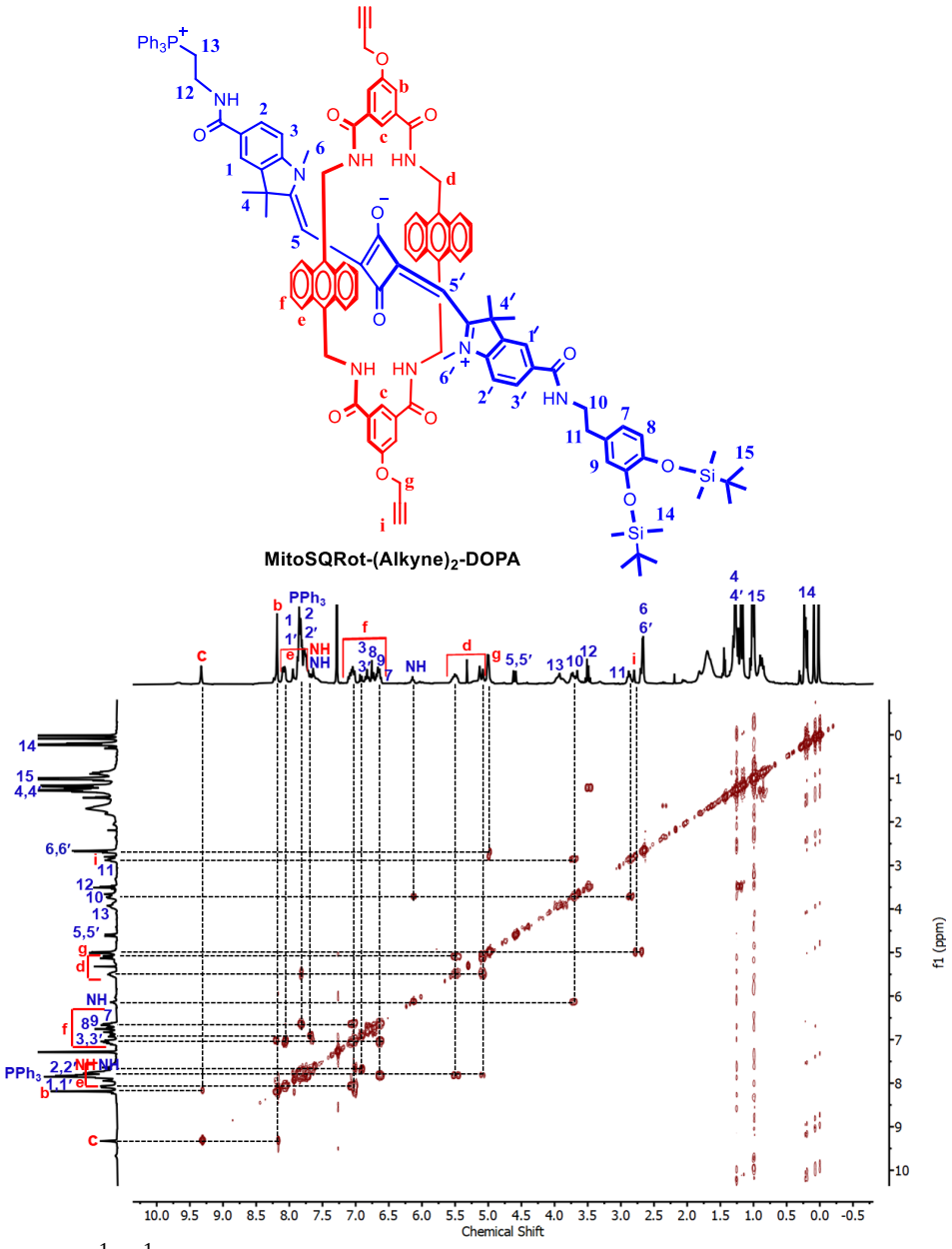

Figure 25. ^{1}H-^{1}H gCOSY (Gradient-selected Correlation Spectroscopy) NMR (300 MHz, $CDCl_3$, 25°C) spectrum of the rotaxane MitoSQRot- (Alkyne)$_2$-DOPA.

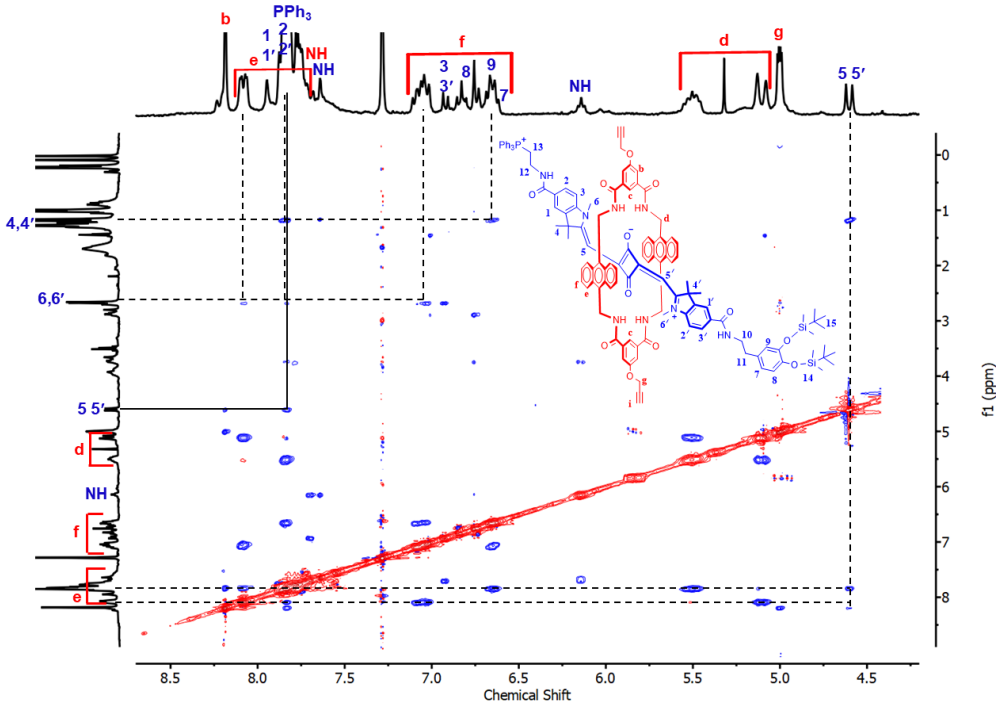

Figure 26. Partial ^{1}H-^{1}H ROESY (Rotating frame Overhauser Effect Spectroscopy) NMR (300 MHz, $CDCl_3$, 25°C) spectrum of the rotaxane MitoSQRot-(Alkyne)$_2$ -DOPA. Protons e correlates with 5,5′; e correlates with 4,4′; e correlates with 6,6′; f correlates with 4,4′; and f correlates with 6,6′; confirming rotaxane formation.

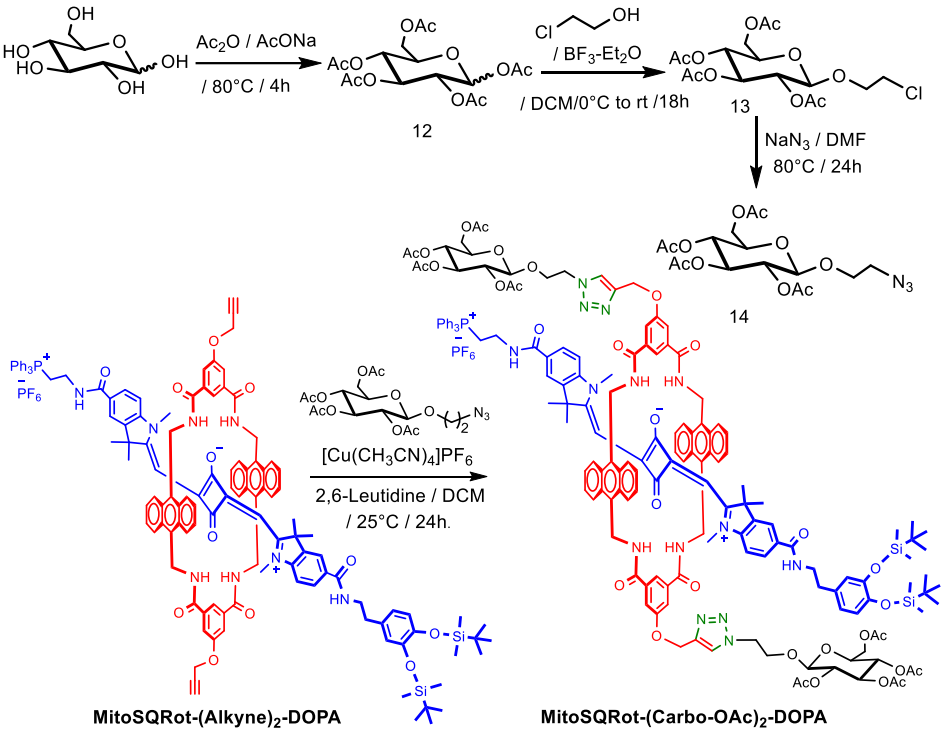

Scheme 3. Synthesis of MitoSQRot-(Carb-OAc)$_2$-DOPA.

D-Glucose pentaacetate (12): D-glucose (1 g, 5.55 mmol) Ac_2O (5.6 mL, 55.5 mmol), and AcONa (0.90 g, 11 mmol) were taken in a 50 mL round bottomed flask and the reaction mixture was stirred for 4 h at 80°C. Then CH_2Cl_2 was added into the reaction mixture and extracted with water. The organic layer was washed with saturated $NaHCO_3$ solution (2×40 mL) and brine (2×40 mL). The organic part was dried over anhydrous Na_2SO_4, filtered, and concentrated using a rotary evaporator to acquire a white solid product 12.

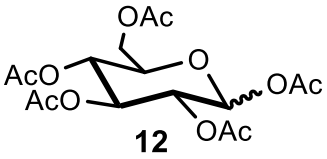

^{1}H NMR (300 MHz, $CDCl_3$, 25°C): δ = 6.30 (1H, d, J = 3.6 Hz,), 5.70 (0.31H, d, J = 8.4 Hz), 5.45 (1H, t, J = 9.9 Hz), 5.24 (0.4H, t, J = 9.3 Hz), 5.16–5.05 (2.6H, m), 4.30–4.22 (1.4H, m), 4.13–4.04 (2.5H, m), 3.85–3.80 (0.35H, m), 2.16 (2.92H, s), 2.09 (0.89H, s), 2.07 (2.7H, s), and 2.01 (12H, m) ppm.

^{13}C NMR (75 MHz, $CDCl_3$, 25°C): δ = 170.57, 170.17, 170.05, 169.62, 169.36, 169.21, 168.91, 168.72, 91.65, 89.02, 72.74, 70.20, 69.79, 69.16, 67.85, 61.42, 20.83, 20.66, 20.62, and 20.41 ppm

HRMS (ESI +ve) *m/z*: Observed for $C_{16}H_{22}O_{11}$ $[M+Na]^+$ = 413.1057, $[M+Na]^+$ calcd = 413.1054.

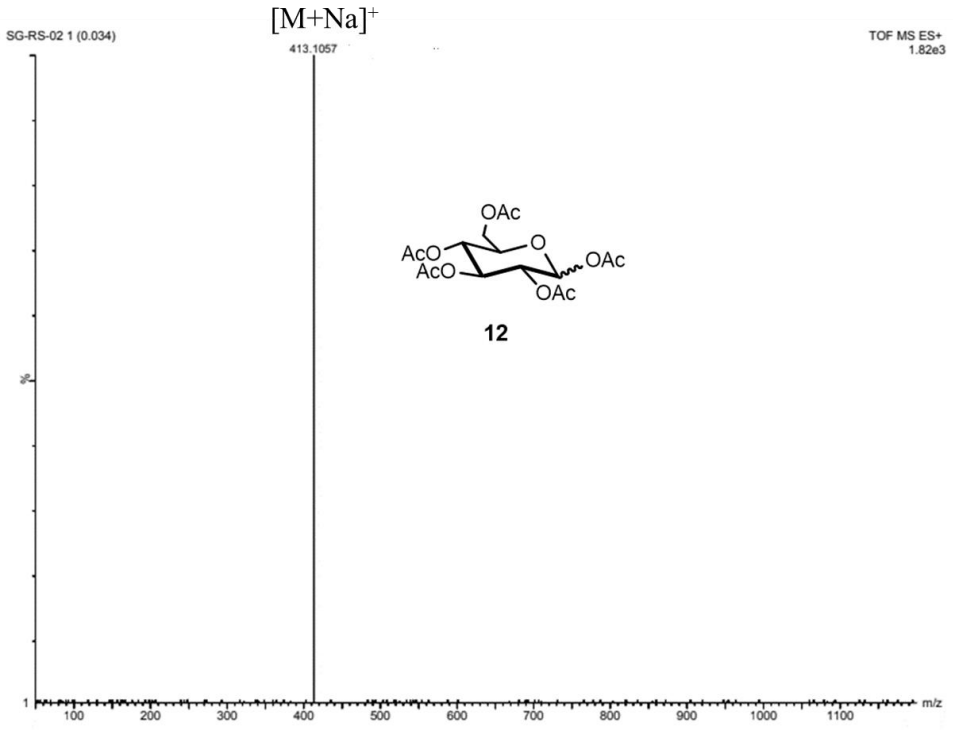

Figure 27. HRMS (ESI +ve) spectrum of Compound 12.

(a)

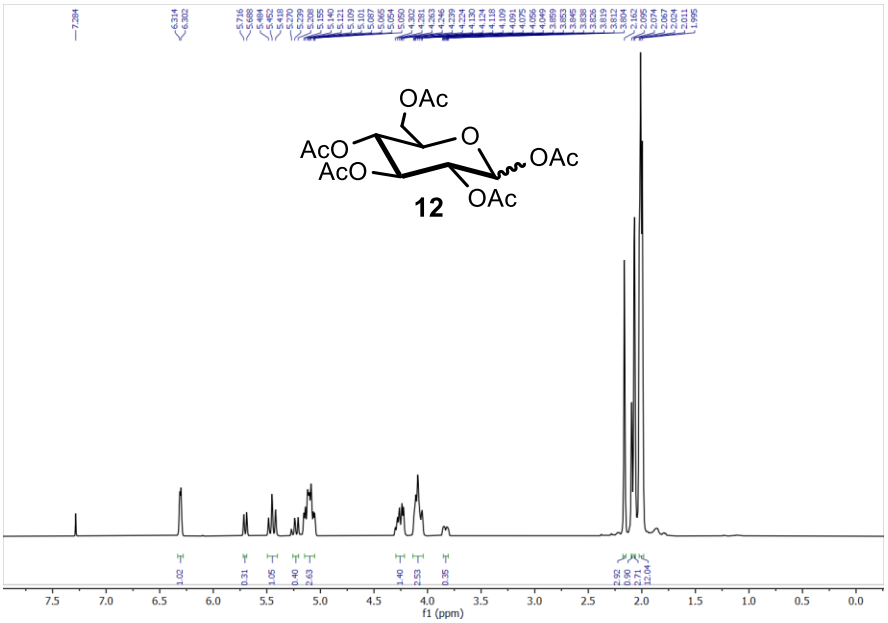

(b)

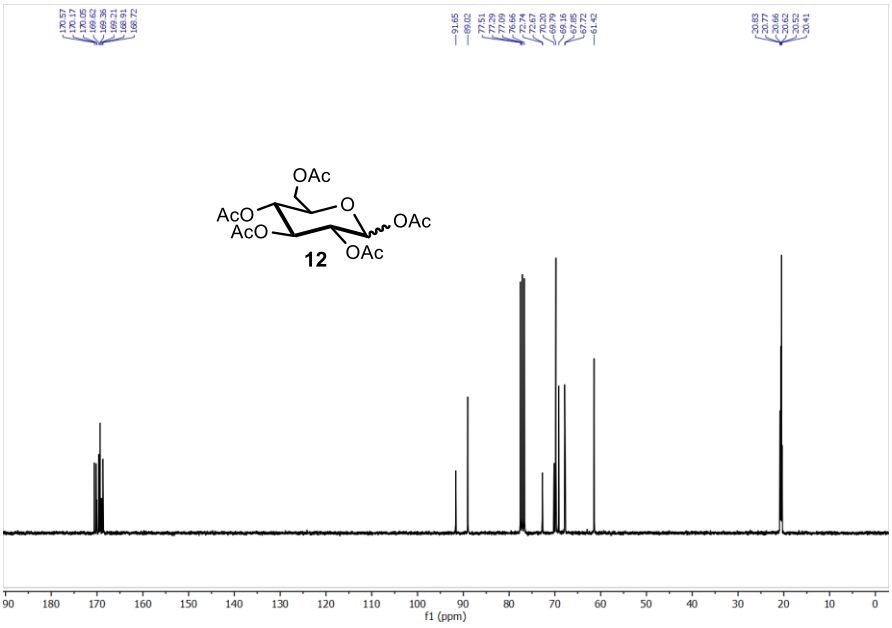

Figure 28. (a) ^{1}H NMR (300 MHz, $CDCl_3$, 25°C) spectrum of compound 12.

(b) ^{13}C NMR (75 MHz, $CDCl_3$, 25°C) spectrum of 12.

(2-Chloroethyl)-2,3,4,6-tetra-O-acetyl-*β*-D-glucopyranoside (13). D-glucose pentaacetate (1 g, 2.56 mmol) and 2-chloroethanol (0.35 mL, 5.12 mmol) were dissolved in 30 mL dry CH_2Cl_2 and degassed by bubbling with nitrogen. Boron trifluoride diethyl etherate (5 mL) was added drop wise at 0°C and the solution was stirred for 18 h at 25°C. The organic layer was washed with saturated $NaHCO_3$ solution (×3), water (×2), dried over anhydrous Na_2SO_4, filtered and concentrated using a rotary evaporator. The crude residue was purified by flash chromatography using 50% EtOAc /hexane (R_f = 0.4) to acquire a pure white solid product 13.

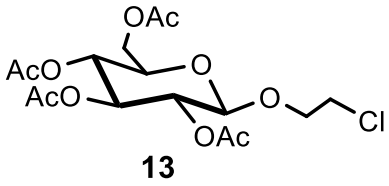

13

Yield = 0.7 g (67%).

^{1}H NMR (300 MHz, $CDCl_3$, 25°C): δ = 5.22 (1H, t, J = 9.4 Hz), 5.12 (1H, t, J = 9.3 Hz), 5.08 (1H, dd, J = 9.5 Hz, J = 8.1 Hz), 4.61 (1H, t, J = 6.2 Hz), 4.30–4.25 (1H, m), 4.20–4.13 (1H, m), 4.10–4.02 (1H, m), 3.76–3.71 (1H, m), 3.69–3.64 (1H, m), 3.54–3.47 (1H, m), 3.32–3.28 (1H, m), 2.13 (3H, s), 2.11 (3H, s), 2.04 (3H, s), and 2.02 (3H, s) ppm.

^{13}C NMR (75 MHz, $CDCl_3$, 25°C): δ = 170.67, 170.29, 169.67, 169.45, 168.77, 100.67, 72.79, 71.96, 71.05, 69.83, 68.58, 67.88, 61.83, 50.52, 20.91, 20.71, and 20.46 ppm.

HRMS (ESI +ve) m/z: Observed for $C_{16}H_{23}ClO_{10}$ $[M]^+$ = 410.0972, $[M]^+$ calcd = 410.0980.

(a)

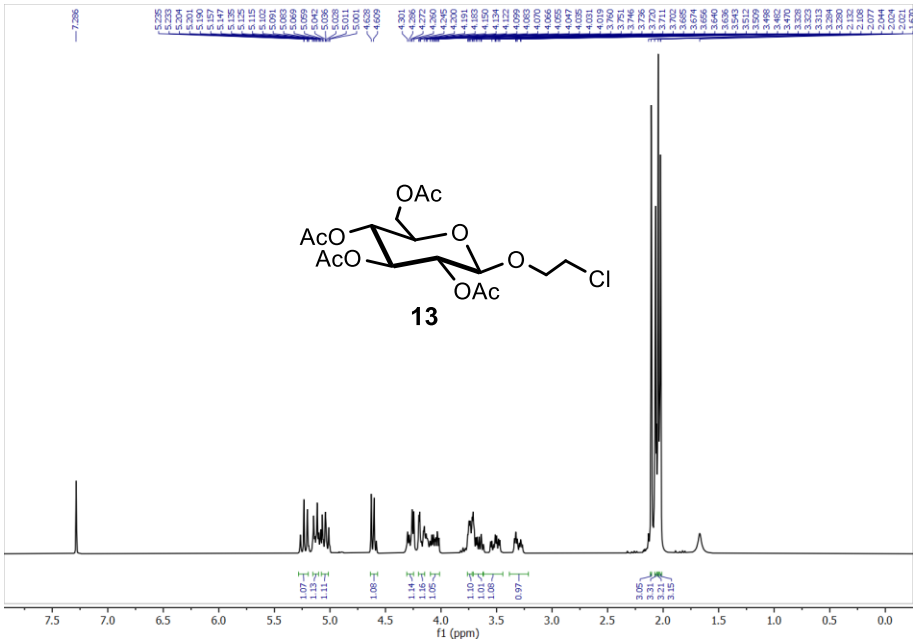

(b)

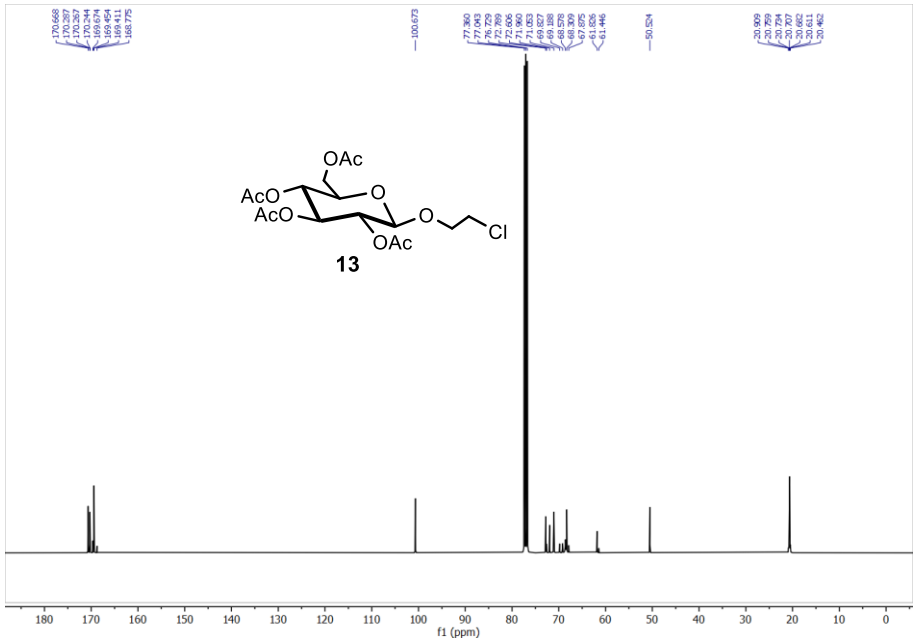

Figure 29. (a) ^{1}H NMR (300 MHz, $CDCl_3$, 25°C) spectrum of compound 13. (b) ^{13}C NMR (75 MHz, $CDCl_3$, 25°C) spectrum of 13.

(2-Azidoethyl)-2,3,4,6-tetra-O-acetyl-*β*-D-glucopyranoside (14). To a DMF (50 mL) solution of 13 (0.5 g, 1.26 mmol) NaN_3 (0.24 g, 3.78 mmol) was added and the reaction mixture was stirred at 60°C for 24 h. Then diluted with $CHCl_3$ and the organic layer was washed with saturated $NaHCO_3$ solution (2×) and brine. The organic part was dried over anh. Na_2SO_4 and concentrated using a rotary evaporator to get an off-white solid that was purified by flash chromatography by 50% EtOAc / hexane (R_f = 0.35) to get the pure white solid compound 14.

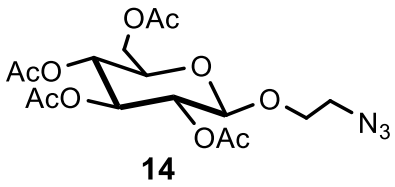

14

Yield 0.45 g (85%).

^{1}H NMR (300 MHz, $CDCl_3$, 25°C): δ = 5.23 (1H, t, J = 9.5 Hz), 5.13 (1H, t, J = 9.4 Hz), 5.06 (1H, t, J = 9.6 Hz), 4.61 (1H, d, J = 7.8 Hz), 4.29–4.24 (1H, m), 4.19–4.13 (1H, m), 4.09–4.02 (1H, m), 3.75–3.71 (1H, m), 3.68–3.60 (1H, m), 3.55–3.47 (1H, m), 3.34–3.27 (1H, m), 2.10 (3H, s), 2.07 (3H, s), 2.04 (3H, s), and 2.02 (3H, s) ppm.

^{13}C NMR (75 MHz, $CDCl_3$, 25°C): δ = 170.67, 170.29, 169.42, 168.78, 101.13, 100.67, 89.07, 72.79, 71.94, 71.04, 69.83, 69.19, 68.55, 68.32, 68.32, 67,89, 61.83, 61.46, 50.52, 42.47, 20.88, 20.68, and 20.45 ppm.

HRMS (ESI +ve) *m/z*: Observed for $C_{16}H_{23}N_3NaO_{10}^+$ $[M+Na]^+$ = 440.1309, $[M+Na]^+$ calcd = 440.1276.

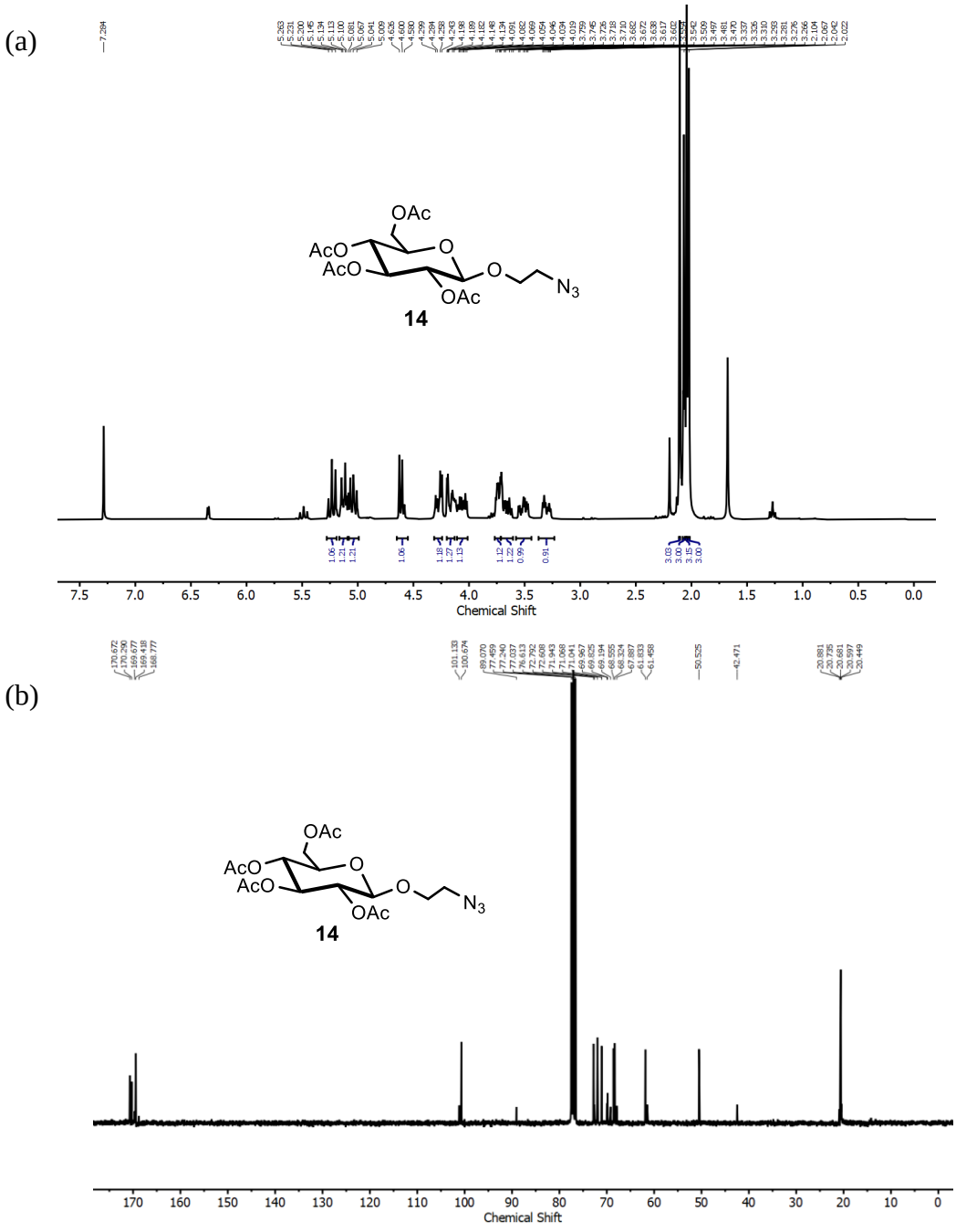

Figure 30. (a) ^{1}H NMR (300 MHz, $CDCl_3$, 25°C) spectrum of compound 14. (b) ^{13}C NMR (75 MHz, $CDCl_3$, 25°C) spectrum of 14.

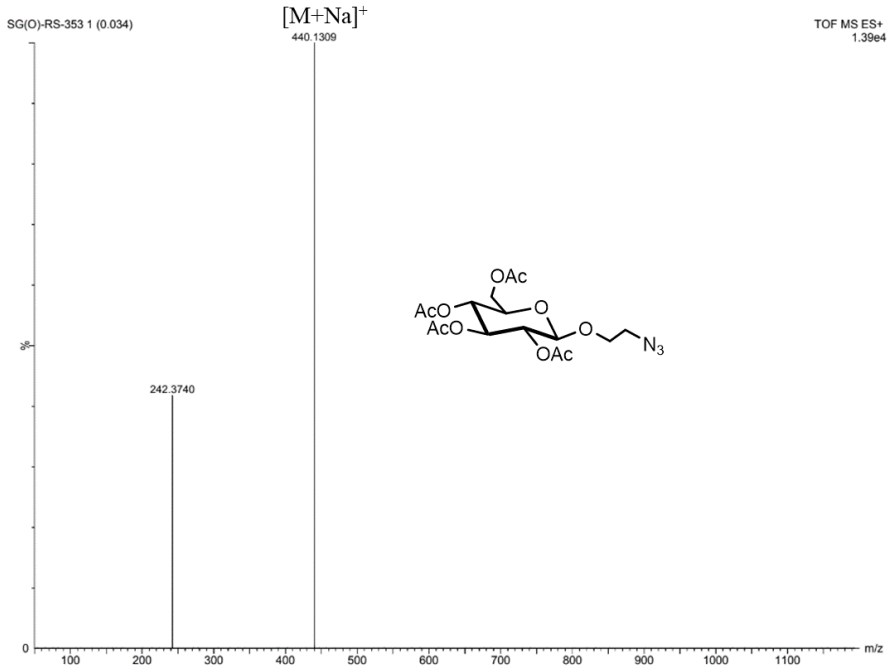

Figure 31. HRMS (ESI +ve) spectrum of 14

MitoSQRot-(Carb-OAc)$_2$-DOPA: The compound MitoSQRot-(Alkyne)$_2$-DOPA (0.1 g, 0.046 mmol) and (2-azidoethyl)-2,3,4,6-tetra-O-acetyl-*β*-D-glucopyranoside (0.058 g, 0.138 mmol) were dissolved in 10 mL of dry DCM. 2-3 drops of 2,6-lutidine was added into the solution and stirred for 5 min in presence of N_2 atmosphere. $[Cu(CH_3CN)_4]PF_6$ (0.016 g, 0.05 mmol) was added to the reaction mixture and it was stirred at 25°C for 24 h. The solvent was removed using a rotary evaporator and the crude residue was purified by column chromatography through 5% MeOH / DCM to get a sea green colored solid pure product MitoSQRot-(Carb-OAc)$_2$-DOPA.

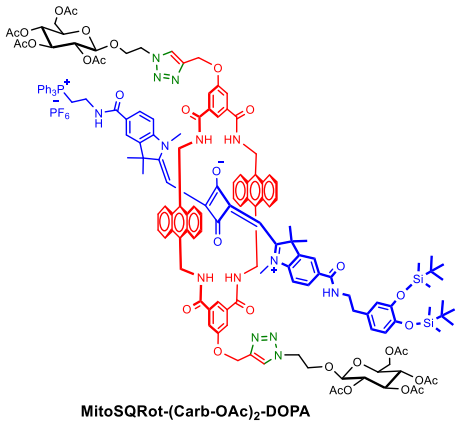

Yield: 0.1 g (15%)

^{1}H NMR (300 MHz, $CDCl_3$, 25°C): δ = 9.32 (1H, s), 9.29 (1H, s), 8.19 (4H, s), 8.09 (4H, d, J = 8.2 Hz), 7.98 (2H, s), 7.91 (2H, s), 7.88–7.75 (25H, m), 7.68 (1H, s), 7.07–7.05 (4H, m), 7.02 (1H, s), 6.94 (1H, d, J = 7.9 Hz), 6.84 (1H, d, J = 8.2 Hz), 6.76 (2H, s), 6.69–6.64 (4H, m), 6.22 (1H, br), 5.54–5.50 (4H, m), 5.29–5.21 (4H, m), 5.13–5.11 (4H, m), 5.07–5.03 (2H, m), 4.78–4.74 (2H, m), 4.63 (1H, s), 4.61 (1H, s), 4.35–4.32 (2H, m), 4.31–4.27 (4H, m), 4.25–4.20 (4H, m), 4.08–4.04 (2H, m), 3.97–3.95 (2H, m), 3.78–3.74 (4H, m), 3.72–3.70 (2H, m), 3.52–3.49 (2H, m), 3.32–3.29 (2H, m), 2.89 (2H, t, J = 5.1 Hz), 2.70 (6H, s), 2.15 (6H, s), 2.10 (6H, s), 2.06 (6H, s), 2.05 (6H, s), 1.27 (12H, s), 1.01 (18H, s), and 0.23 (12H, s) ppm.

^{13}C NMR (75 MHz, $CDCl_3$, 25°C): δ = 181.60, 172.93, 170.68, 170.19, 169.48, 167.52, 165.85, 159.61, 146.93, 145.31, 143.35, 141.17, 139.32, 135.01, 134.84, 133.66, 133.64, 131.83, 130.70, 130.57, 130.14, 128.64, 125.44, 124.64, 124.58, 121.66, 121.17, 118.80, 100.68, 91.92, 85.85, 72.80, 72.52, 72.09, 71.95, 71.08, 70.98, 69.83, 68.57, 68.33, 67.71, 62.16, 61.84, 59.19, 50.54, 50.25, 49.83, 42.16, 41.48, 37.98, 31.94, 29.71, 29.67, 29.37, 28.28, 25.98, 24.12, 22.70, 20.82, 20.75, 20.62, 18.47, 14.13, and –4.01 ppm.

HRMS (ESI +ve) *m/z*: observed for $C_{156}H_{170}N_{14}O_{32}PSi_2^+$ $[M]^+$ = 2839.3367, $[M]^+$ calcd = 2839.1410.

Photophysical properties in DMSO λ_{abs}= 659 nm, λ_{em}= 671 nm, Stokes shift ($\Delta\lambda$) = 12 nm, ε = 1.56 ×10^5 $M^{-1}cm^{-1}$, Φ_f = 0.42 in DMSO (Φ_f of Zinc phthalocyanine as reference = 0.20 in DMSO).

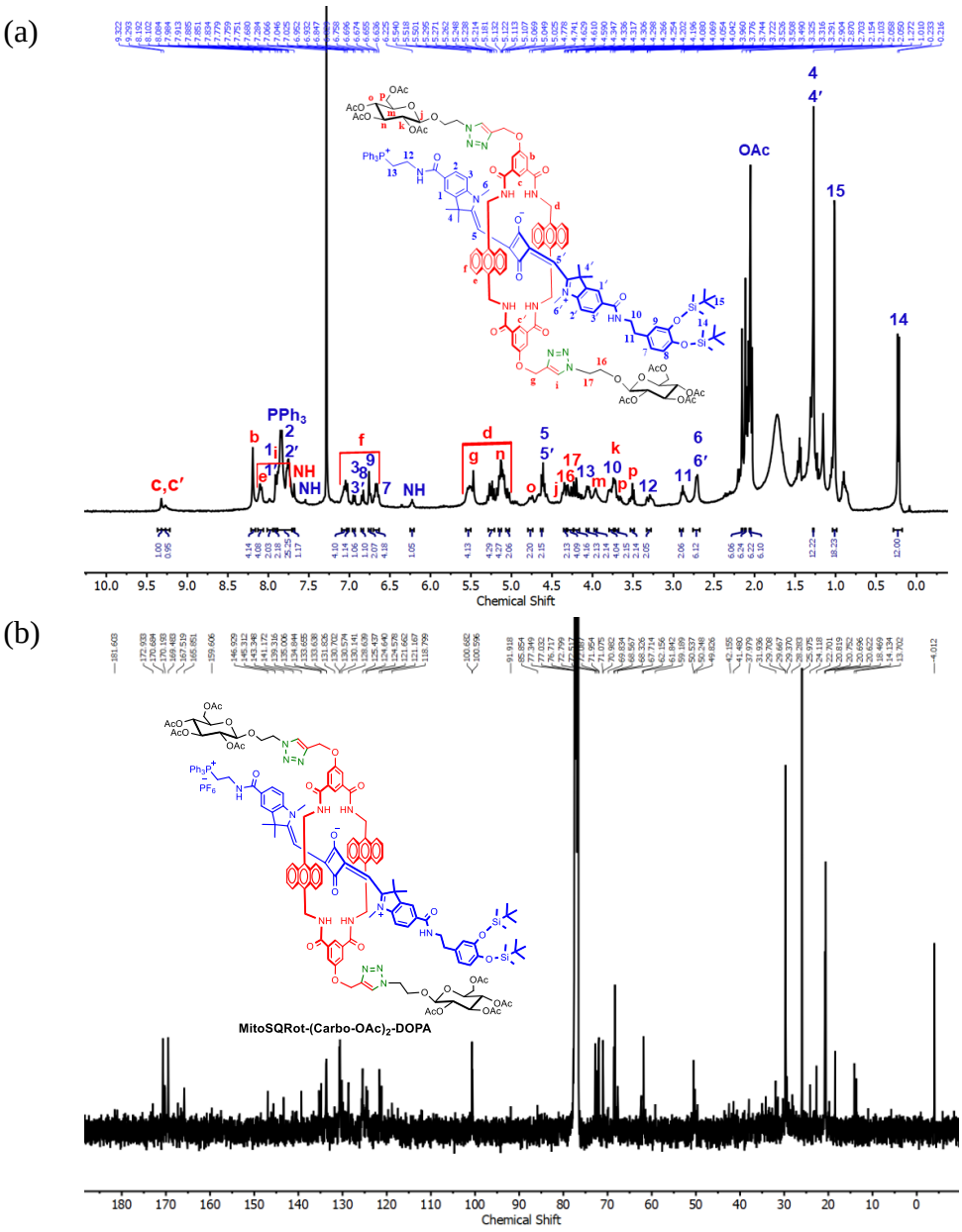

Figure 32. (a) ^{1}H NMR (300 MHz, $CDCl_3$, 25°C) spectrum of the rotaxane MitoSQRot-(Carb-OAc)$_2$-DOPA. (b) ^{13}C NMR (75 MHz, $CDCl_3$, 25°C) spectrum of the rotaxane MitoSQRot-(Carb-OAc)$_2$ -DOPA.

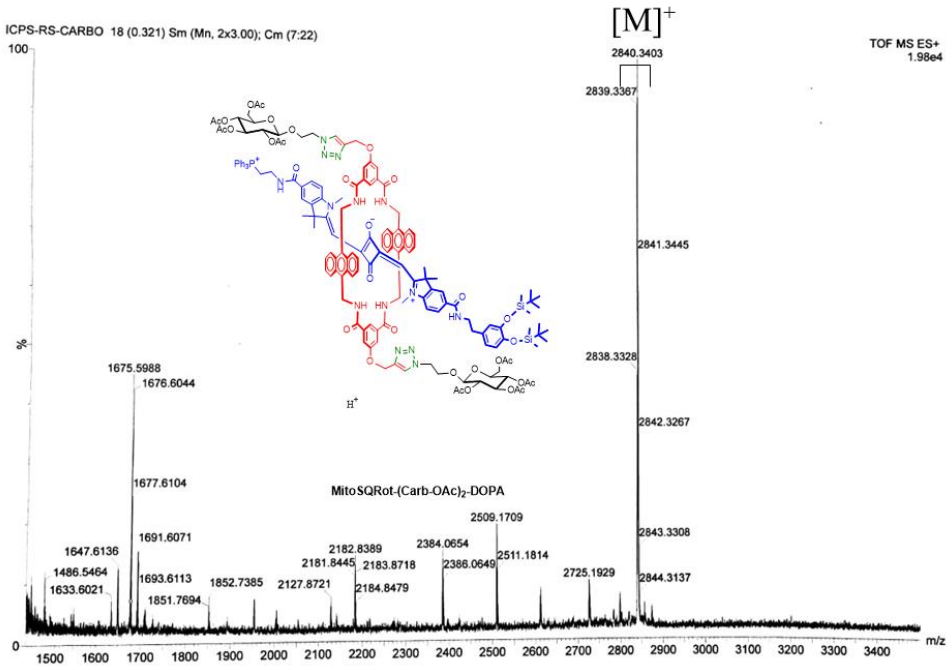

Figure 33. HRMS (ESI +ve) spectrum of MitoSQRot-(Carb-OAc)$_2$-DOPA.

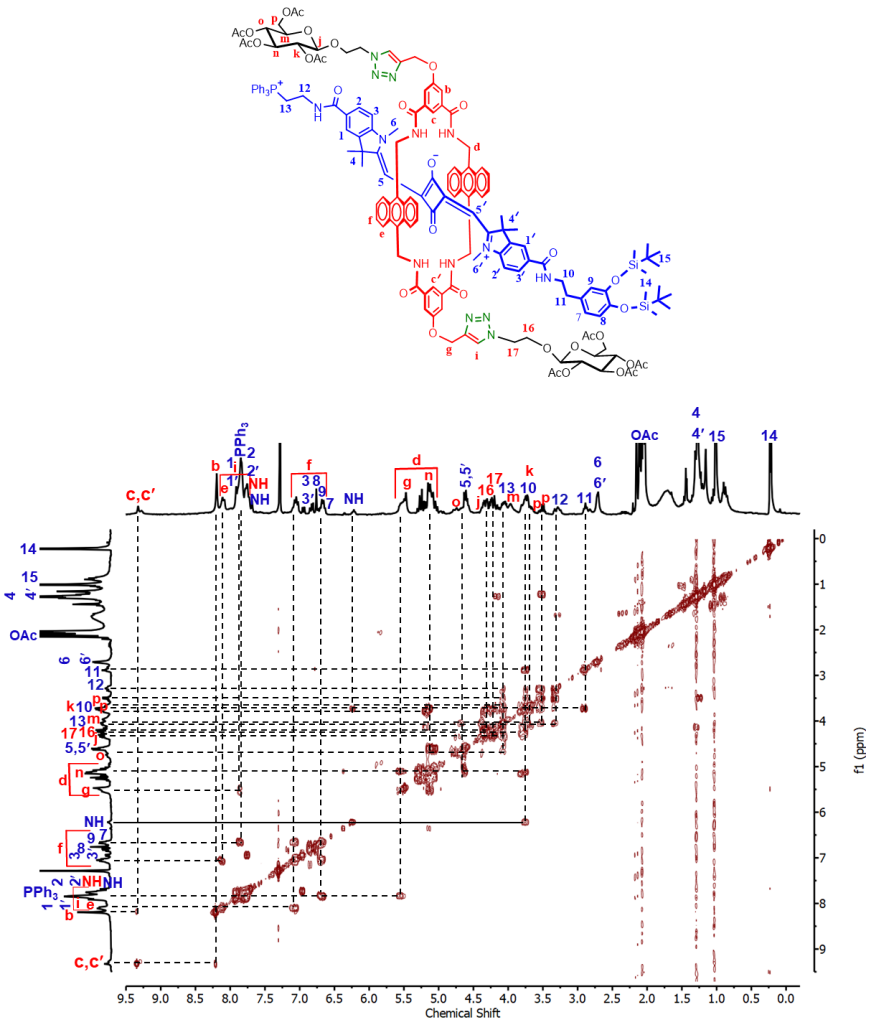

Figure 34. ^{1}H-^{1}H gCOSY (Gradient-selected Correlation Spectroscopy) NMR (300 MHz, $CDCl_3$, 25°C) spectrum of the rotaxane MitoSQRot-(Carb-OAc)$_2$-DOPA

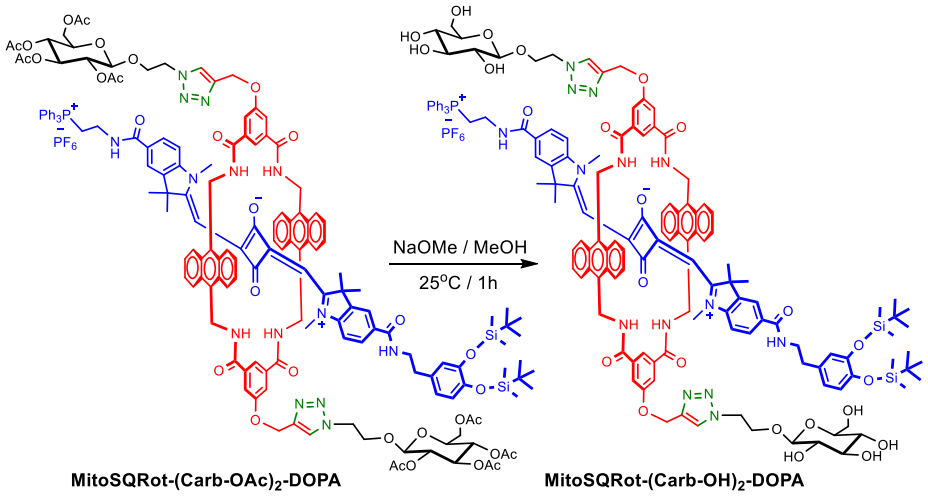

Scheme 4: Synthetic scheme for the formation of MitoSQRot-(Carb-OH)$_2$-DOPA

MitoSQRot-(Carb-OH)$_2$-DOPA: The compound MitoSQRot-(Carb-OAc)$_2$-DOPA (0.09 g, 0.03 mmol) was dissolved in 0.1(M) CH_3ONa in 10 mL CH_3OH and the solution was stirred at 25°C for 1 h. The mixture was neutralized with Amberlite IR-120 (H^+) exchange resin. It was filtered and the filtrate was concentrated using a rotary evaporator to acquire a blue colored pure solid product MitoSQRot-(Carb-OH)$_2$-DOPA.

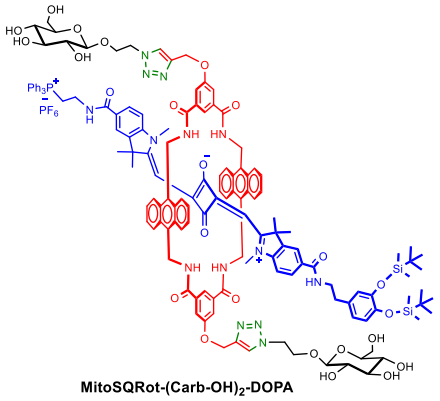

Yield: 0.05 g (63%).

^{1}H NMR (300 MHz, $CDCl_3$, 25°C): δ = 9.30 (2H, s), 8.46 (4H, s), 8.14 (4H, d, J = 8.2 Hz), 8.04 (4H, s), 7.84–7.81 (19H, m), 7.59–7.56 (6H, m), 7.33 (1H, br), 7.13–7.09 (7H, m), 6.72–6.98 (7H, m), 5.45 (12H, br), 5.20 (2H, t, J = 3.1 Hz), 5.06–5.01 (8H, m), 4.73–4.72 (2H, m), 4.71 (2H, s), 4.61–4.58 (2H, s),

4.41–4.36 (4H, m), 4.34–4.32 (4H, m), 4.17–4.14 (2H, m), 4.05–4.01 (4H, m), 3.73–3.70 (4H, m), 3.19–3.10 (4H, m), 3.09–3.06 (2H, m), 2.72 (6H, s), 1.24 (12H, s), 1.17 (18H, s), and 0.77 (12H, s) ppm.

^{13}C NMR (75 MHz, $CDCl_3$, 25°C): δ = 181.13, 180.97, 179.99, 171.06, 170.14, 166.54, 166.01, 146.27, 146.03, 145.48, 144.87, 141.62, 135.48, 134.25, 134.11, 133.38, 130.78, 130.65, 130.34, 128.84, 128.25, 121.98, 121.72, 121.50, 119.19, 118.34, 100.30, 92.73, 88.04, 87.94, 73.55, 72.82, 72.44, 71.05, 62.44, 61.69, 48.99, 48.72, 41.64, 34.86, 33.97, 31.35, 27.07, 26.94, 26.81, 26.16, 18.57, and –3.80 ppm.

HRMS (MALDI +ve) *m/z*: observed for $C_{140}H_{155}N_{14}O_{24}PSi_2^{2+}$ $[M+H]^{2+}$ = 1252.0326, $[M+H]^{2+}$ calcd = 1252.0319.

Photophysical properties in DMSO λ_{abs}= 659 nm, λ_{em}= 670 nm, Stokes shift ($\Delta\lambda$) = 11 nm, ε = 1.82 ×10^5 M^{-1}cm^{-1}, Φ_f = 0.37 in DMSO (Φ_f of Zinc phthalocyanine as reference = 0.20 in DMSO).

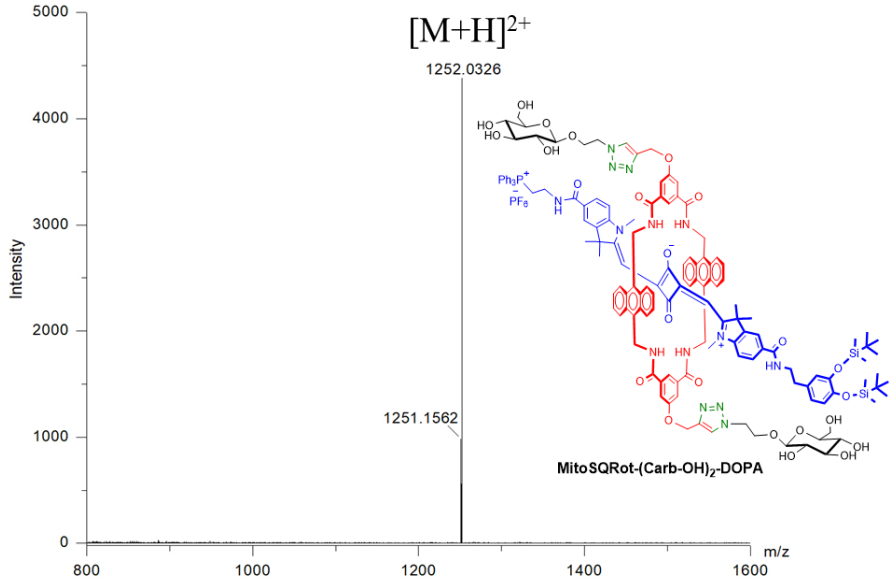

Figure 35. HRMS (MALDI) spectrum of MitoSQRot-(Carb-OH)$_2$-DOPA.

(a)

(b)

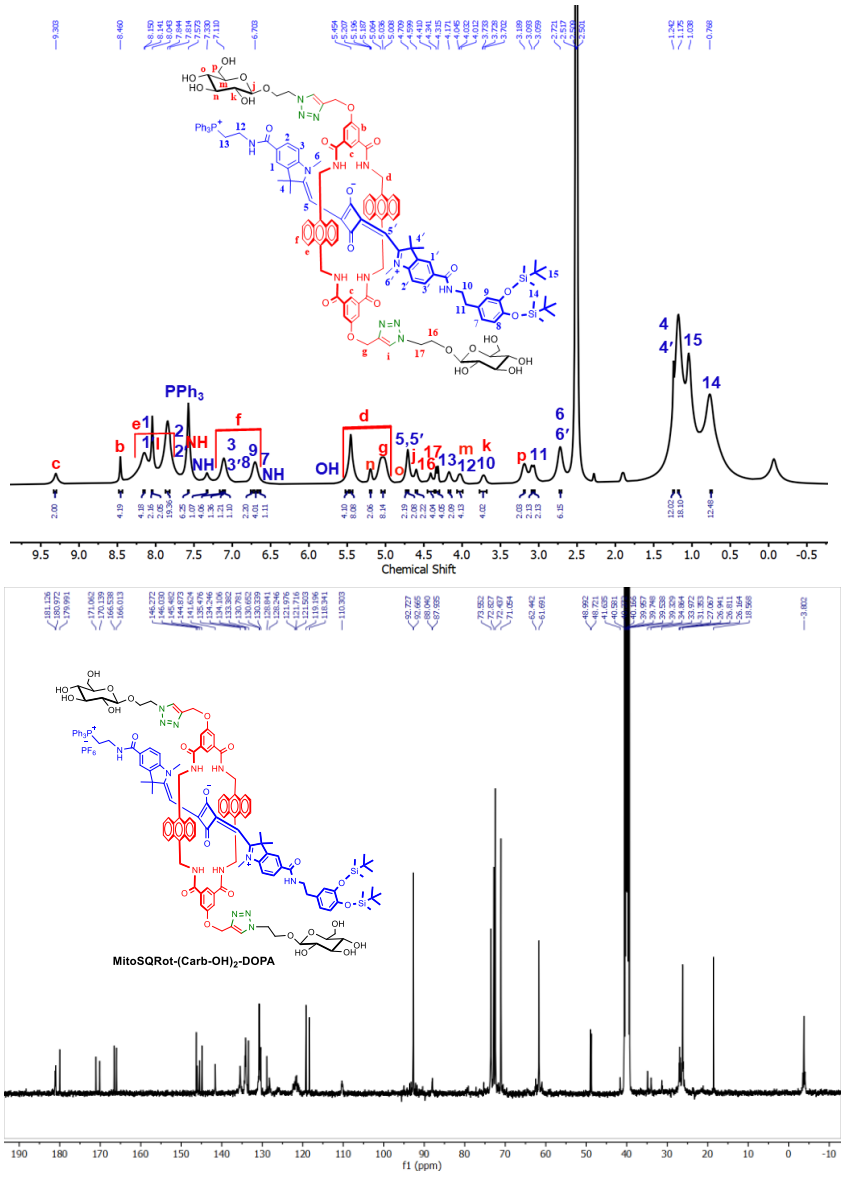

Figure 36. (a) ^{1}H NMR (300 MHz, $CDCl_3$, 25°C) spectrum of the rotaxane MitoSQRot-(Carb-OH)$_2$-DOPA. (b) ^{13}C NMR (75 MHz, $CDCl_3$, 25°C) spectrum of the rotaxane MitoSQRot-(Carbo-OH)$_2$-DOPA.

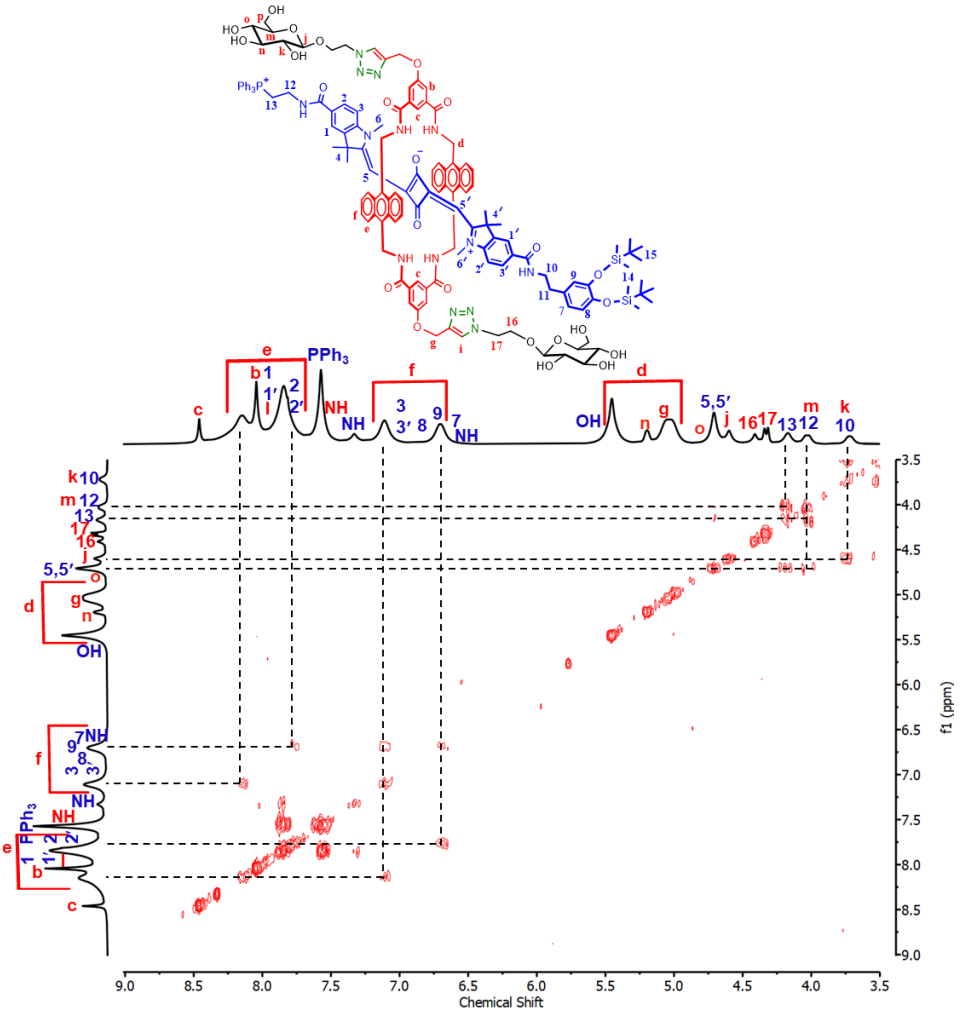

Figure 37. Partial ^{1}H-^{1}H gCOSY (Gradient-selected Correlation Spectroscopy) NMR (300 MHz, DMSO-d_6, 25°C) spectrum of MitoSQRot-(Carb-OH)$_2$-DOPA.

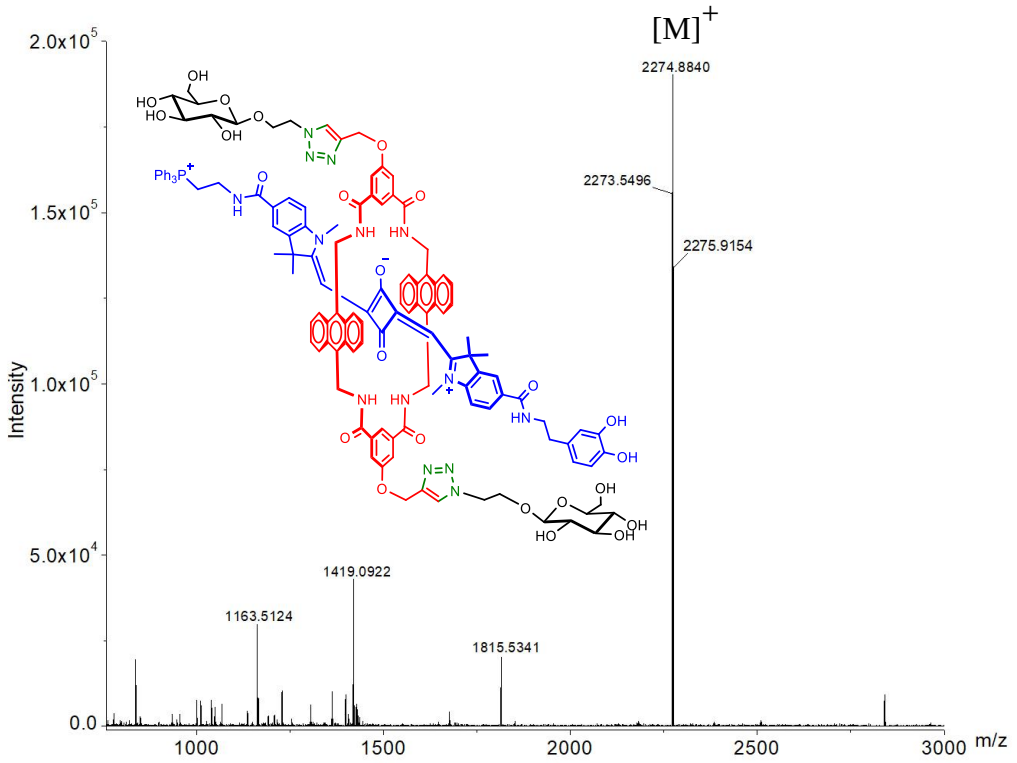

Figure 38. HRMS (MALDI) spectrum of TBDMS deprotected rotaxane MitoSQRot-(Carb-OH)$_2$-DOPA-OH.

METHODS

NMR Spectroscopy: ^{1}H, ^{13}C, and 2D NMR were conducted using Bruker DPX300 MHz and DPX400 MHz spectrometers at 298 K in appropriate deuterated solvents. Manufacturers' provided Bruker TopSpin 3.6.2 software was used to process the data.

ESI-MS (HRMS): High-resolution electrospray ionisation mass spectrometry (HRMS-ESI) in positive mode was acquired on a Q-TofmicroTM (Waters Corporation) mass spectrometer. Manufacturers' provided mass application software MassLynx V4.1 was used to process the data.

Single Crystal X-Ray Diffraction: Single crystals suitable for X-ray diffraction were obtained by vapor diffusion method. Diffraction data were collected on a micro focus Single Crystal X-ray Diffraction instrument (Make: Bruker, Model: D8 Quest) with MoKα radiation (a graded multilayer mirror monochromator, λ = 0.71073 Å) at 273 K. A PHOTON-100 CMOS detector was used. Structures were solved by direct methods using the SHELXT 2014/5 program.[20,21] Refinements were carried out with a full-matrix least squares method against F^2 using SHELXL-2018/3 incorporated in Olex2[22] crystallographic collective package. The non-hydrogen atoms were refined with anisotropic thermal parameters.

Compound 8: A solution of compound 8 in $CHCl_3$ was placed in a 2 mL vial and put inside a 20 mL vial filled with 10 mL Et_2O. The larger vial was capped and allowed to slow diffusion. Yellow colored block shaped crystals were obtained by vapor diffusion after 3 days. Formula sum = C19 H19 N O5, formula weight = 341.35, crystal system = monoclinic, space group = *P* 21/n, a = 9.2413(7) Å, b = 14.6335(12) Å, c = 13.3411(11) Å, α = 90, β = 109.590(3), γ = 90, V = 1699.7(2) Å^3, Z = 4, D_{calcd} = 1.334 g cm^{-3}, μ = 0.068 mm^{-1}. The

final R value was R_1 = 0.0516 and wR_2 = 0.1668 for reflections with I > 2ζ(I). CCDC number 2260321.

Crystallographic data were deposited at Cambridge Crystallographic Data Centre (CCDC). These data can be obtained free of charge from the Cambridge Crystallographic Data Centre, www.ccdc.cam.ac.uk/structures.

Absorption Spectroscopy: UV/vis absorption spectra were recorded by a JASCO V-730 double-beam spectrophotometer with wavelength ranges from 200 to 1100 nm in a quartz cuvette of 1 cm path length. Manufacturers' supplied Spectra Manager Version 2 software was used to process the data.

Fluorescence Spectroscopy: Fluorescence emissions were measured on a Horiba Jobin Yvon FluoroMax-4 spectrofluorometer operated by Fluor Essence Version 3.9.0.1 software. 5 nm excitation and emission slit widths were used.

Calculation of Relative Quantum Yield of the Rotaxane Molecules: Fluorescence quantum yields (Φ_f) of the rotaxane molecules were determined by relative method. The integrated fluorescence intensity of the rotaxane molecules were related with fluorescence intensity of a standard compound [Φ_f (st) of Zinc phthalocyanine in DMSO = 0.20] by the subsequent equation:

$$\Phi_f(x) = \Phi_f(st) \times [(A_{st} \times F_x \times \eta_x^2) / (A_x \times F_{st} \times \eta_{st}^2)]$$

Φ_f(x): fluorescence quantum yield of the synthesized rotaxane molecule

Φ_f(st): fluorescence quantum yield of the reference molecule

A_{st} and A_x: Absorbance of standard and rotaxane molecule at the excitation wavelength, respectively

F_{st} and F_x: Integrated fluorescence areas under the corrected fluorescence spectra for the reference and rotaxane molecule, respectively.

η_{st} and η_x: Refractive indices of the solvent in which the reference and rotaxane molecule were determined, respectively [herein, both the rotaxane and

reference molecules were dissolved in DMSO; so (η_x^2 / η_{st}^2) = 1]. "x" refers to the rotaxane molecule and "st" stands for the standard.

The relative Quantum yields (Φ_f) of the dumbbell and rotaxane molecules were determined as 0.23 for MitoSQ-DOPA, 0.58 for MitoSQRot-(Alkyne)$_2$-DOPA, 0.42 for MitoSQRot-(Carb-OAc)$_2$-DOPA, 0.37 for MitoSQRot-(Carb-OH)$_2$-DOPA, 0.38 for MitoSQRot-(Carb-OH)$_2$-DOPA-Fe_3O_4 NPs in DMSO, and 0.11 for MitoSQRot-(Carb-OH)$_2$-DOPA-Fe_3O_4 NPs in PBS pH =7.2.

Fluorescence Lifetime Measurement: Time-correlated single photon counting (TCSPC) technique was used to measure the fluorescence lifetime (τ) of rotaxane molecules by Horiba DeltaFlex lifetime machine (Horiba Jobin Yvon IBH Ltd, UK). A Delta Diode laser of 650 nm (Model: DD-650L, Horiba Scientific) excitation source was used to measure the τ for rotaxane and rotaxane capped Fe_3O_4 NPs in DMSO and PBS respectively. Fluorescence lifetime measurements and data analyses were executed by Horiba EzTime decay analysis software.

Transmission Electron Microscopy (TEM): 1 mg of Fe_3O_4 NPs surface coated with rotaxanes was dissolved in 1 mL H_2O. 10 μL of the solution was drop casted on a 300-mesh carbon coated copper grid and awaited for 2 m after that blotting with filter paper to take out the excess solution. The grid was permitted to dry in air subsequently vacuum drying for 1 day. TEM images of MitoSQRot-(Carbo-OH)$_2$-DOPA-Fe_3O_4 NPs was captured using a JEL-2100F Field Emission Electron microscope (JEOL) machine with acceleration voltage of 200 kV.

Magnetic Measurement: The magnetic measurements were carried out using a vibrating sample magnetometer (VSM) of quantum design. In the presence of a zero magnetic field, the sample was placed in the sample holder in powder

form, and the magnetic hysteresis curves were recorded by sweeping the external field between 2kOe at room temperature.

Magnetic Resonance Imaging (MRI): MRI measurements were performed at 25°C in a 9.4 T MR system (BioSpec 94/20USR, Bruker cryo platform, TX, USA). The MitoSQRot-(Carbo-OH)$_2$-DOPA-Fe_3O_4 NPs was dispersed in 600 µL of D-PBS (-) in microtubes with different concentrations of Fe (0.33, 0.165, 0.083, 0.041, 0.021, and 0 mM; Fe concentrations were determined from the ICP-OES experiment on a PerkinElmer instrument, Optical Emission Spectrometer Avio 200). The tubes were placed on a sample holder followed by putting into the MR scanner. Image acquisition was performed in the spin echo mode to determine T_2 of each sample with parameters, echo time (TE=24 ms), repetition time (TR=500 ms), resolution 192 × 192, field of view (FOV) = 4.80 cm, thickness =2.0 mm. Signal intensities were measured from region of interest (ROI) and the T_2 relaxation time was calculated by linear fitting as function of TE. The r_2 relaxivity value was obtained from the slope of linear fitting curve of $1/T_2$ values (y-axis) with Fe concentrations (x-axis).

Cell Culture: HeLa and A549 cell lines were maintained in growth media containing DMEM (pH 7.4) supplemented with 10% FBS and antibiotic-antimycotic solution 100×(containing 10000 units penicillin, 10 mg mL^{-1} streptomycin, and 25 µg mL^{-1} amphotericin B in 0.9% normal saline). The cells were preserved in a 5% CO_2 incubator at 37°C and were routinely passaged.

Cell Viability Assay: MTT assay was used to determine the cell viability of cancerous HeLa and A549 as well as non-cancerous C2C12 cell lines against MitoSQRot-(Carbo-OH)$_2$-DOPA-Fe_3O_4 NPs. Freshly harvested HeLa, A549 and C2C12 cells were discretely seeded at a population of ~10^4 cells in a 96-well plate by DMEM for 24 h incubation. Afterwards 24 h incubation, various

doses of Fe concentration (1, 2, 5, 10 and 15 ppm per well) of MitoSQRot-(Carbo-OH)$_2$-DOPA-Fe_3O_4 NPs was treated at 37°C for 24 h. The HeLa, A549 and C2C12 cells were then separately incubated with 10 µL of MTT substance (5 mg/mL in PBS) at 37°C for 4 h in darkness. After 4 h incubation, DMSO was mixed to each well and the absorption (*A*) at 570 nm was recorded (verified in triplicate) by an ELISA plate reader. The consequences (performed the assay in triplicates) were measured as the percentages of the viable cells through the succeeding equation:

Viable cells (%) = (*A* of treated cells / *A* of untreated cells) × 100.

Confocal Laser Scanning Microscopy:

Confocal laser scanning microscopic (CLSM) images were captured on a Leica STELLARIS 5 platform using HC PL APO 100×/ 1.40 OIL CS2 objective combined with white light laser (WLL) as well as Acousto-Optical Beam Splitter (AOBS) and HyD S detectors. For live cell CLSM imaging HeLa and A549 cancer cells at a density of ~10^4 cells/mL were separately seeded in 35 mm glass bottom confocal dish and allowed to get 70-80% confluency in DMEM for 24 h at 37°C in a 5% CO_2 incubator. Afterward washing with 1× PBS live cells were incubated with 2 µM solution of MitoSQRot-(Carbo-OH)$_2$-DOPA-Fe_3O_4 NPs in media for 12 hours at 37°C in 5% CO_2 environment and then the media was removed carefully and washed gently with 1× PBS. Subsequently cells were incubated first using 200 nM MitoTracker Green FM and then with Hoechst 33342 (0.1 µg mL^{-1}) for 30 and 15 min, respectively at 37°C in 5% CO_2 environment. Later the treatment process HeLa and A549 cells were finally washed two times using media before imaging. Throughout the CLSM imaging procedure 37°C and 5% CO_2 atmosphere was maintained.

For Hoechst 33342: laser excitation wavelength = 405 nm (blue channel, detection range of emission wavelength 415-480 nm); MTG: laser excitation wavelength = 488 nm (green channel, detection range of emission wavelength 499-544 nm); MitoSQRot-(Carbo-OH)$_2$-DOPA-Fe_3O_4 NPs: laser excitation wavelength = 638 nm, (Cy-5 channel, detection range of emission wavelength 650-710 nm).

Determination of Pearson's Correlation Coefficient: Pearson's correlation (PC) coefficient values were obtained by comparing the confocal images of MitoSQRot-(Carb-OH)$_2$-DOPA-Fe_3O_4 NPs with MitoTracker Green (MTG). PC coefficients were determined by the inspection of confocal micrographs with the LAS X software using Quantify tool. PC coefficient is one of the classic procedures (standard statistical analysis) in pattern recognition for matching one confocal image (green channel designates MTG staining) with another (red channel designates MitoSQRot-(Carb-OH)$_2$-DOPA-Fe_3O_4 NPs staining) and can be used to depict the extent of overlapping between two patterns in a dual-color image. To calculate PC for confocal images, all of the pixels having the same image coordinates were paired.

PC coefficient (PCC) was calculated (image consisting of red and green channels) according to the equation:

$$PCC = \frac{\sum_i (S1_i - S1_{avg}) * (S2_i - S2_{avg})}{[\sum_i (S1_i - S1_{avg})^2 * \sum_i (S2_i - S2_{avg})^2]^{(1/2)}}$$

S1 = signal intensity of pixels (pixel i) in the first (green) channel.

S2 = signal intensity of pixels (pixel i) in the second (red) channel.

$S1_{avg}$ = mean values of pixels in the first (green) channel.

$S2_{avg}$ = mean values of pixels in the second (red) channel.

The average pixel intensity ($S1_{avg}$) of an image was subtracted from the intensity of each pixel within the image (S1), and the value obtained for each pixel was multiplied by the value from the pixel's partner in the complement image ($S2-S2_{avg}$) to generate the product of the difference from the average. It was summed for the entire dataset and divided by the utmost probable sum of the product of the difference from the mean. PC is independent of signal levels and background because it subtracts the average intensity from each pixel's intensity value. PC coefficient was measured for colocalization area within the area foreground by LAS X software.

Results and Discussion:

The changes in ^{1}H NMR chemical shift due to rotaxane formation for MitoSQRot-$(Alkyne)_2$-DOPA with respect to free Macrocycle-$(Alkyne)_2$ and MitoSQ-DOPA axle, respectively, are compared (**Figure 24**). Utmost downfield shift for Macrocycle-$(Alkyne)_2$ protons 'c' and 'NH' due to hydrogen bonding with squaraine C_4O_2 core oxygens is the most characteristic change. Besides, a significant upfield shift for MitoSQ-DOPA axle protons 5, 5′ and macrocyclic protons e and f are detected for rotaxane formation. The anthracene moieties of the Macrocycle-$(Alkyne)_2$ produce anisotropic shielding regions for the 5,5′ protons of the dumbbell thus upfield shift is observed in ^{1}H NMR.

Synthesis of Rotaxane Capped Fe_3O_4 Nanoparticles:

Synthesis of Iron–Oleate Complex: The iron–oleate complex was synthesized by the subsequent protocol: $FeCl_3 \cdot 6H_2O$ (2.7 g, 10 mmol) and sodium oleate (9.13 g, 30 mmol) were dissolved in a solvent mixture containing EtOH (20 mL), DI H_2O (15 mL), and hexane (35 mL). The resulting reaction mixture was

heated for 4 h at 70°C. Then the upper organic layer comprising the iron–oleate complex was washed with DI H_2O (30 mL × 3) using a separating funnel. Subsequently the organic hexane part was evaporated using a rotary evaporator to acquire iron–oleate complex as a yellowish brown waxy solid. Yield: 95%.

Synthesis of Iron Oxide Nanocrystals: Iron-oleate complex (2.25 g, 2.5 mmol) was dissolve in 1-octadecene (12.5 g) and oleic acid (0.36 g, 1.25 mmol) at 25°C. The solution was heated to 320°C (reflux condenser was set up with cold water circulation) in an inert N_2 atmosphere with a continuous heating rate of 3.3°C min^{-1} and held at that temperature for 30 min. A severe reaction took place when the temperature approached 320°C, and the initially transparent solution became murky and brownish black. The resultant solution comprising the nanocrystals was then cooled to 25°C, and EtOH (75 mL) was added to facilitate nanocrystal precipitation. The nanocrystals were separated by centrifugation to acquire a brownish black colored solid of iron oxide (Fe_3O_4) nanoparticles.[23,24] Centrifugation and washing steps were repeated several times to completely remove the unreacted precursors. Formation of these Fe_3O_4 NPs was confirmed by Transmission electron microscopy (TEM) (**Figure 39**).

Fe_3O_4 Nanoparticles Surface Coatedted with NIR Rotaxane [MitoSQRot-(Carb-OH)$_2$-DOPA-Fe_3O_4]: TBDMS protected DOPA of the MitoSQRot-(Carb-OH)$_2$-DOPA was deprotected using TBAF/THF and characterized by HRMS (**Figure 38**) The synthesized Fe_3O_4 NPs (5 mg) were dispersed in a minimum volume of THF (0.5 mL), and the rotaxane MitoSQRot-(Carb-OH)$_2$-DOPA (20 mg) initially dissolved in ethanol (1 mL) was added to it. The resultant mixture was stirred for 18 h at 25°C. The product was precipitated by hexane and centrifuged to afford a bluish-dark pellet of the Fe_3O_4 nanoparticles capped through the catechol functionality of the rotaxane

MitoSQRot-(Carb-OH)$_2$-DOPA. The dark pellet was dispersed in H_2O which furnished a blue colored solution. The aqueous dispersion was filtered using a 0.2 μm disposable syringe filter (Millipore), and the excess free rotaxanes as well as solubilized oleic acid were removed by filtrations through a centrifugal filtration device (Millipore, Mw cutoff = 100 kDa) using DI water (3 times). The nanoparticles were dissolved in DI H_2O and finally lyophilization was performed to obtain the dark blue powdered MitoSQRot-(Carb-OH)$_2$-DOPA-Fe_3O_4 nanoparticles. The Fe_3O_4 NPs surface coated with sugar functionalized rotaxane to obtain MitoSQRot-(Carb-OH)$_2$-DOPA-Fe_3O_4 was readily dispersed in water with sea green colored solution. The synthesized MitoSQRot-(Carb-OH)$_2$-DOPA-Fe_3O_4 NPs were characterized by TEM, UV-vis, fluorescence (**Figures 40a**). The average diameter of MitoSQRot-(Carb-OH)$_2$-DOPA-Fe_3O_4 NPs are obtained to 15 nm using statistical analysis from the TEM image (**Figure 40c**). High-resolution TEM (HRTEM) images of these rotaxane capped Fe_3O_4 NPs exhibited characteristic lattice fringe patterns, demonstrating the highly crystalline nature of the nanocrystals. SAED pattern confirms the formation of rotaxane capped Fe_3O_4 nanocrystals with characteristic hkl planes (**Figure 40d**). EDX analysis of MitoSQRot-(Carb-OH)$_2$-DOPA-Fe_3O_4 NPs indicates the presence of C, N, O, F, P and Fe. C, N, O, F and P come from the NIR rotaxane molecule (**Figure 41**). Field dependent magnetization (M-H) at room temperature was performed (**Figure 42**). The room temperature magnetic hysteresis curve was determined by a vibrating sample magnetometer (VSM) with magnetic field of 2 kOe confirming its superparamagnetic nature with a typical ferromagnetic behavior with saturation magnetization of 45 emu g^{-1} **(Figure 42)**.

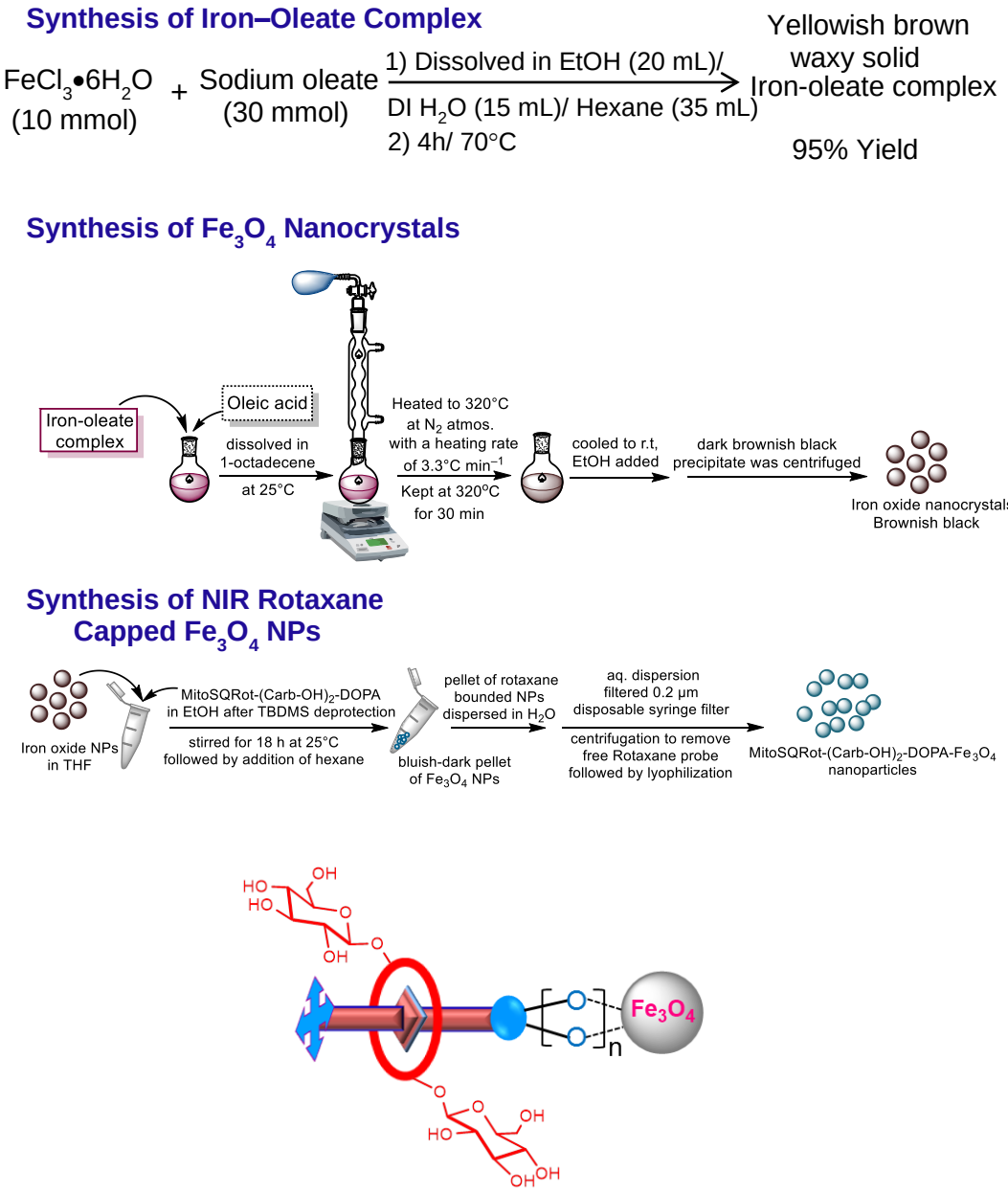

Scheme 5: Synthesis of water soluble NIR rotaxane caped superparamagnetic monodisperse Fe_3O_4 NPs.

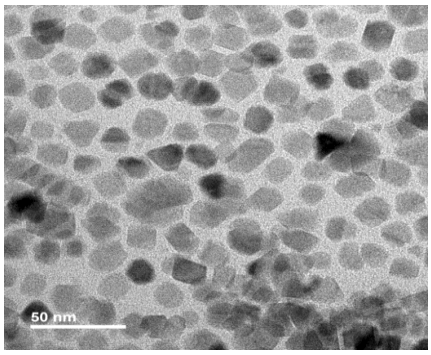

Figure 39. TEM image of Fe_3O_4 NPs.

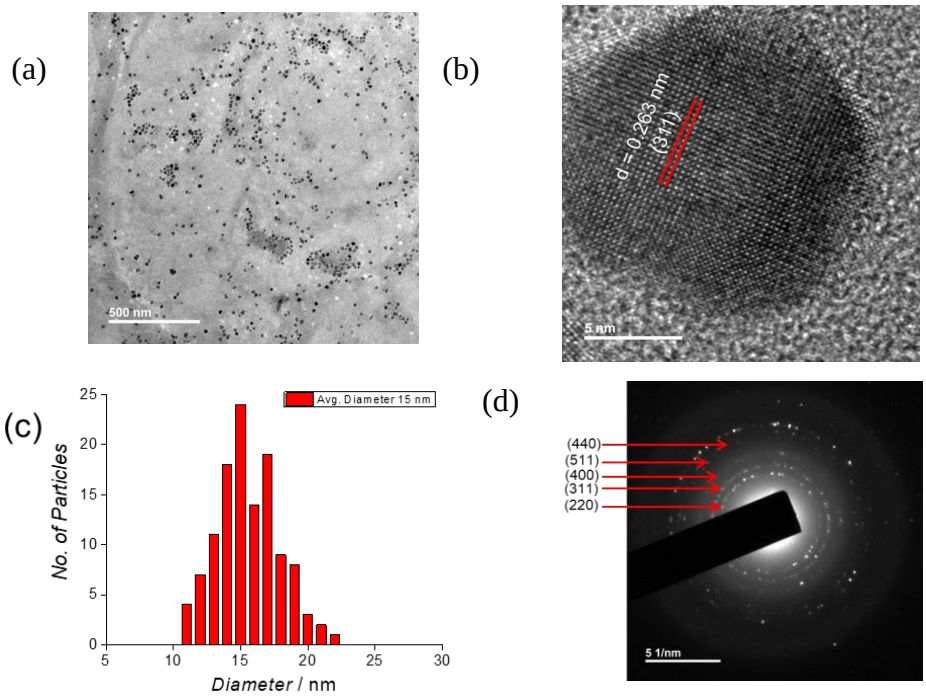

Figure 40. (a) TEM image of MitoSQRot-(Carb-OH)$_2$-DOPA-Fe_3O_4 NPs. (b) HR-TEM image exhibits lattice fringes of Fe_3O_4 NPs surface coated with NIR rotaxane. (c) Statistical analysis of the diameter of MitoSQRot-(Carb-OH)$_2$-DOPA-Fe_3O_4 NPs. (d) SAED pattern with hkl plane of MitoSQRot-(Carb-OH)$_2$-DOPA-Fe_3O_4 NPs.

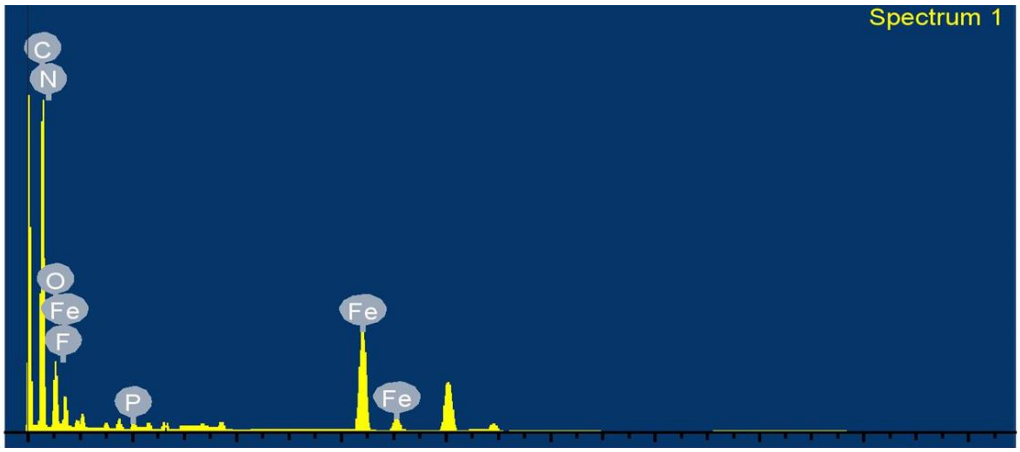

Elem...	Weight%	Atomic%
C K	58.88	77.61
N K	2.38	2.32
O K	11.27	10.95
F K	1.69	1.75
P K	0.95	0.48
Fe K	24.82	6.90
Totals	100.00	

Figure 41: EDX analysis of MitoSQRot-$(Carb\text{-}OH)_2$-DOPA-Fe_3O_4 NPs indicates the presence of C, N, O, F, P and Fe. C, N, O, F and P come from the NIR rotaxane molecule.

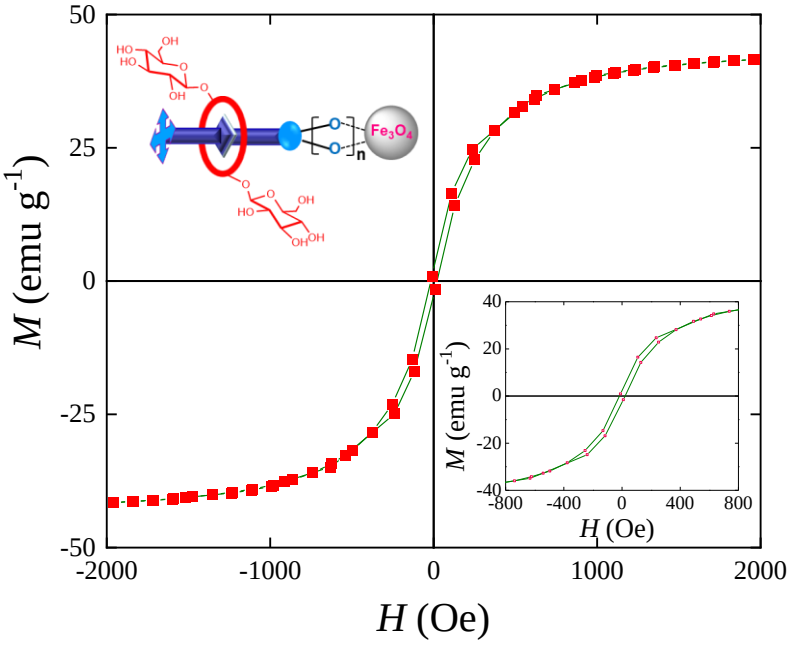

Figure 42. Field-dependent magnetization (M-H) curve at room temperature for MitoSQRot-(Carb-OH)$_2$-DOPA-Fe_3O_4 NPs at applied magnetic fields of up to 2T confirming its superparamagnetic state.

Study of photophysical properties of MitoSQ-DOPA, MitoSQRot-(Alkyne)$_2$-DOPA, MitoSQRot-(Carb-OAc)$_2$-DOPA, MitoSQRot-(Carb-OH)$_2$-DOPA, and MitoSQRot-(Carb-OH)$_2$-DOPA-Fe_3O_4 NPs:

The photophysical properties of all the four rotaxane molecules MitoSQRot-(Alkyne)$_2$-DOPA, MitoSQRot-(Carb-OAc)$_2$-DOPA, MitoSQRot-(Carb-OH)$_2$-DOPA, and MitoSQRot-(Carb-OH)$_2$-DOPA-Fe_3O_4 NPs are compared in **Table 2**. For the MitoSQRot-(Carb-OH)$_2$-DOPA formation a characteristic bathochromic-shift of ca. 6 nm in the λ_{abs} as well as λ_{em} is observed with respect to MitoSQ-DOPA axle in DMSO (**Figure 47 and Table**

2). The λ_{abs} of MitoSQRot-(Carb-OH)$_2$-DOPA is observed at 659 nm in DMSO and it is due to $\pi \rightarrow \pi^*$ transitions with a vibronic progression at 610 nm and huge molar extinction coefficient of 1.42×10^5 M^{-1} cm^{-1} (**Table 2**). The λ_{em} of MitoSQRot-(Carb-OH)$_2$-DOPA is detected at 670 nm in DMSO. MitoSQRot-(Carb-OH)$_2$-DOPA is 1.96 times brighter than the non-encapsulated MitoSQ-DOPA in DMSO.

The λ_{abs} and λ_{em} of MitoSQRot-(Carb-OH)$_2$-DOPA-Fe_3O_4 is detected at 656 nm and 670 nm, respectively in PBS (pH =7.2). There is a 1.65-fold enrichment in the MitoSQRot-(Carb-OH)$_2$-DOPA-Fe_3O_4 QY [$(\Phi_f)_{\text{MitoSQRot-(Carb-OH)2-DOPA-Fe3O4}}$ = 0.38] in contrast to MitoSQ-DOPA [$(\Phi_f)_{\text{MitoSQ-DOPA}}$ = 0.23] in DMSO that is owing to the diminished rotational and vibrational motions of the encapsulated MitoSQ-DOPA dye inside the macrocycle and hence nonradiative excited state relaxation pathways less favorable. The fluorescence lifetime (τ) of MitoSQRot-(Carb-OH)$_2$-DOPA-Fe_3O_4 NPs is detected as 3.98 ns in PBS (pH 7.2) using TCSPS (**Figure 50b and Table 3**).

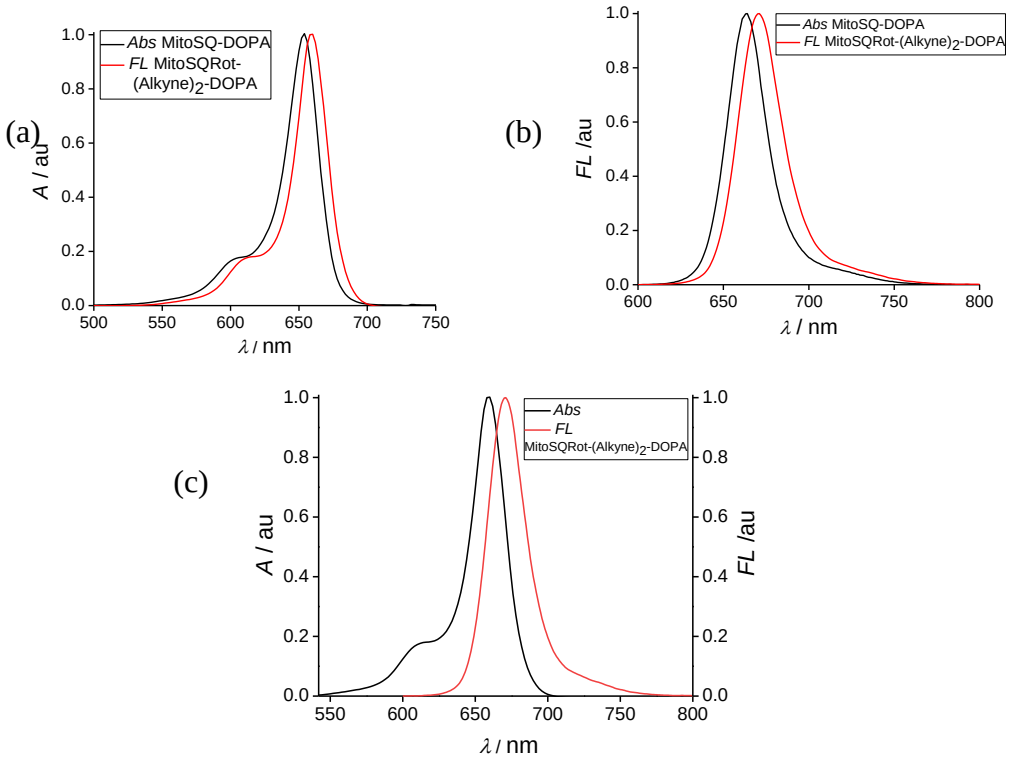

Figure 43. (a) Normalized absorption plot of MitoSQ-DOPA (2 μM) and MitoSQRot- (Alkyne)$_2$-DOPA (2 μM) in $CHCl_3$. (b) Normalized fluorescence plot of MitoSQ-DOPA (2 μM) and MitoSQRot-(Alkyne)$_2$-DOPA (2 μM) in $CHCl_3$. Absorption and emission plots display bathochromic shifts in rotaxane formation. (c) Normalized absorption and emission plot of MitoSQRot-(Alkyne)$_2$-DOPA in $CHCl_3$.

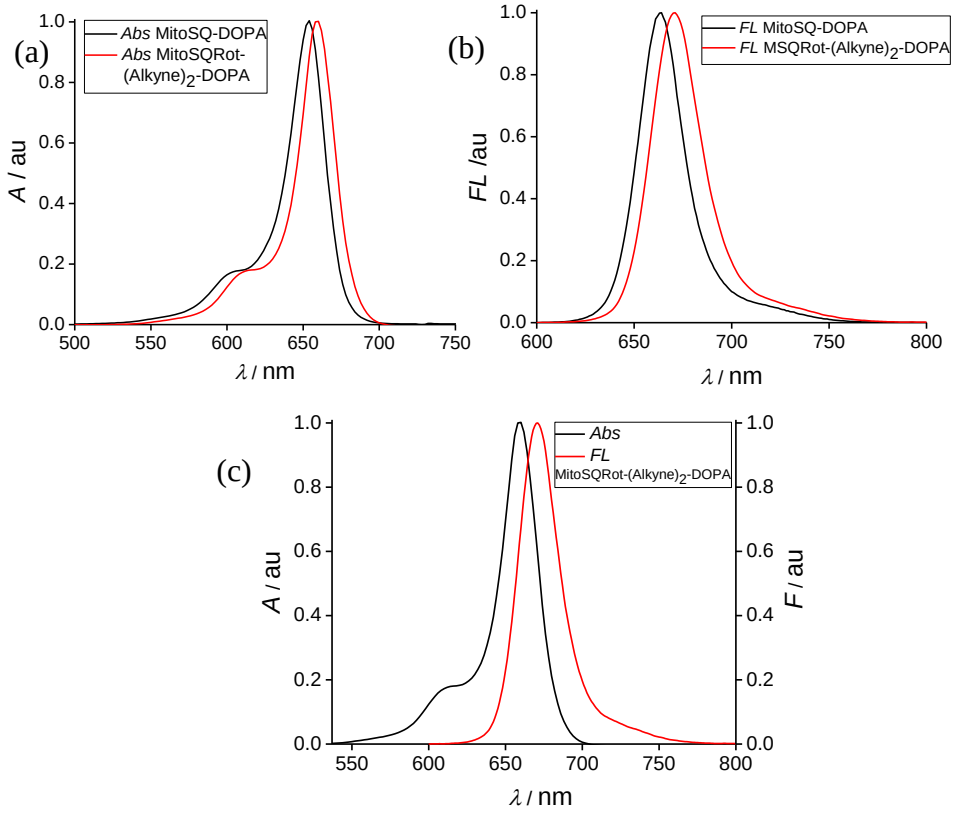

Figure 44. Normalized (a) absorption and (b) emission plots of MitoSQ-DOPA (2 μM) and MitoSQRot-(Alkyne)$_2$-DOPA (2 μM) in DMSO. Absorption and emission plots display bathochromic shifts in rotaxane formation. (c) Normalized absorption and emission plot of MitoSQRot-(Alkyne)$_2$-DOPA in DMSO.

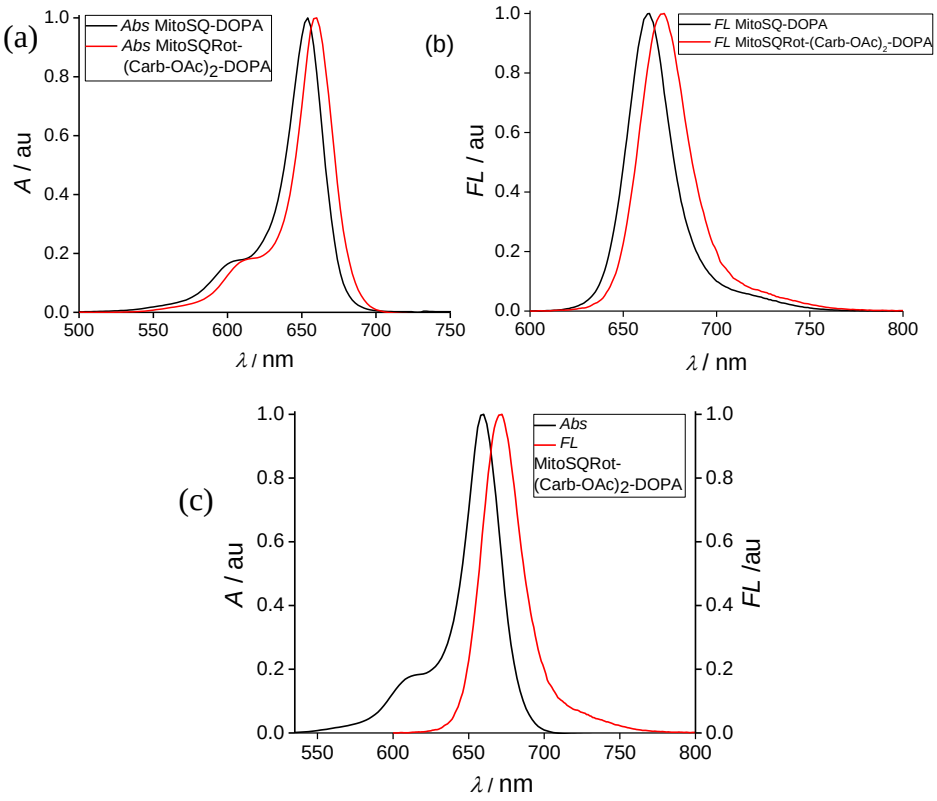

Figure 45. Normalized (a) absorption and (b) emission plots of MitoSQ-DOPA (2 μM) and MitoSQRot- (Carb-OAc)$_2$-DOPA (2 μM) in DMSO. Absorption and emission plots display bathochromic shifts in rotaxane formation. (c) Normalized absorption and emission plot of MitoSQRot-(Carb-OAc)$_2$-DOPA in DMSO.

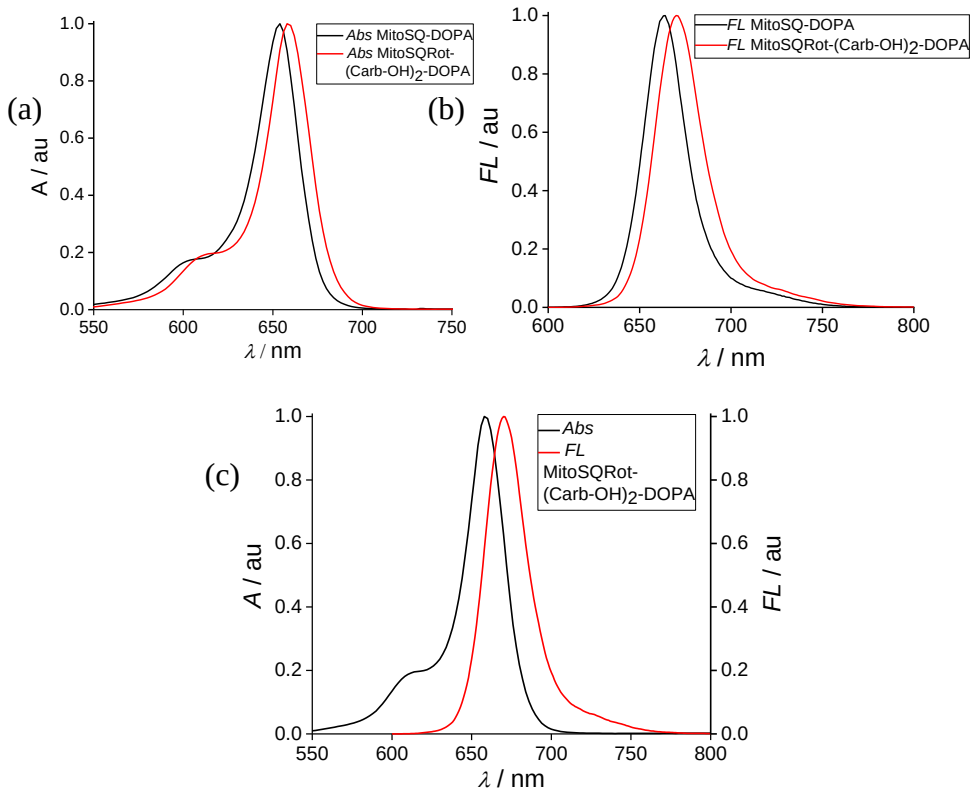

Figure 46. Normalized (a) absorption and (b) emission plots of MitoSQ-DOPA (2 μM) and MitoSQRot-(Carb-OH)$_2$-DOPA (2 μM) in DMSO. Absorption and emission plots display bathochromic shift in rotaxane formation. (c) Normalized absorption and emission plot of MitoSQRot-(Carb-OH)$_2$-DOPA in DMSO.

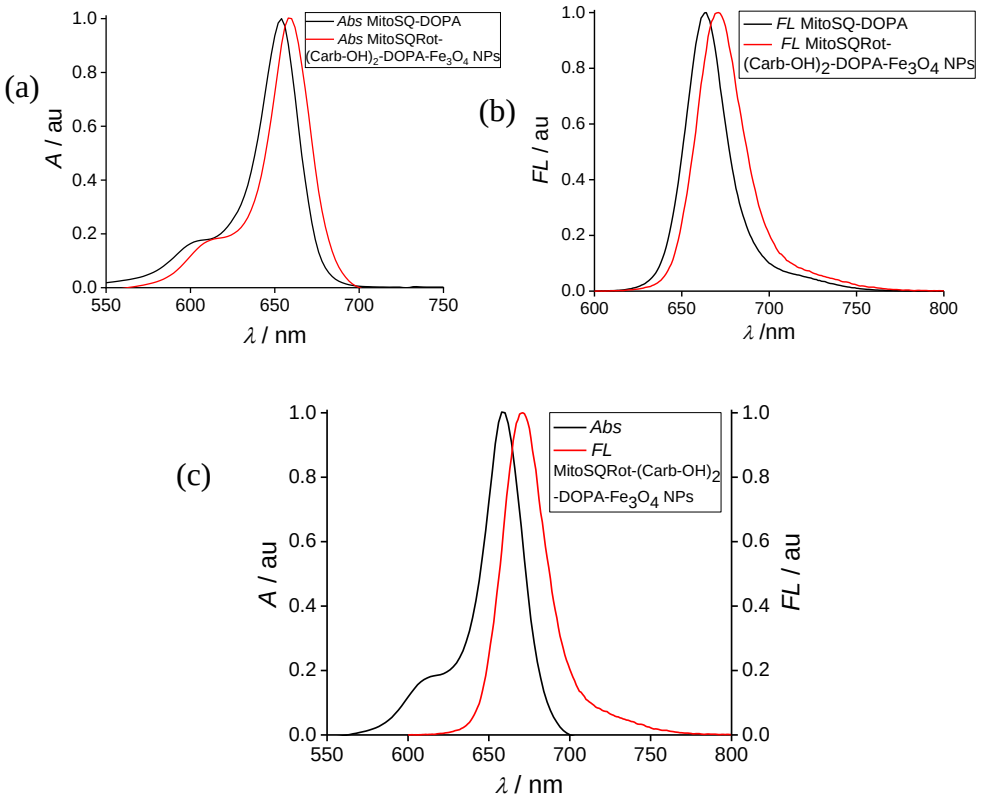

Figure 47. Normalized (a) absorption and (b) fluorescence plots of MitoSQ-DOPA (2 μM) and MitoSQRot-(Carb-OH)$_2$-DOPA-Fe_3O_4 NPs (2 μM) in DMSO. Absorption and emission plots display bathochromic shifts in rotaxane formation. (c) Normalized absorption and emission plot of MitoSQRot-(Carb-OH)$_2$-DOPA-Fe_3O_4 NPs in DMSO.

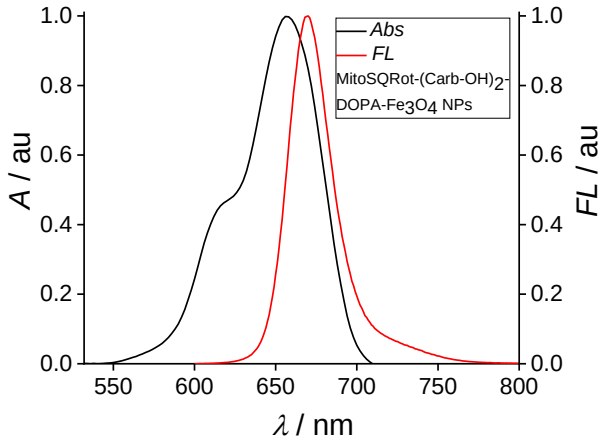

Figure 48. Normalized absorption and emission plot of MitoSQRot-(Carb-OH)$_2$-DOPA-Fe_3O_4 NPs in PBS.

Table 2. Photophysical data

Compound	λ_{max} (nm)	λ_{em} (nm)	Stokes shift ($\Delta\lambda$) nm	$\varepsilon \times 10^5$ (M^{-1} cm^{-1})	QY (F)
MitoSQ-DOPA	653	663	10	1.49	0.23 in DMSO
MitoSQRot-(Alkyne)$_2$-DOPA	660	671	11	1.38	0.58 in DMSO
MitoSQRot-(Carb-OAc)$_2$-DOPA	659	671	12	1.56	0.42 in DMSO
MitoSQRot-(Carb-OH)$_2$-DOPA	659	670	11	1.82	0.37 in DMSO
MitoSQRot-(Carb-OH)$_2$-DOPA-Fe_3O_4 NPs	659	671	12	1.42	0.38 in DMSO
MitoSQRot-(Carb-OH)$_2$-DOPA-Fe_3O_4 NPs	656	670	14	1.32	0.11 in PBS pH=7.2

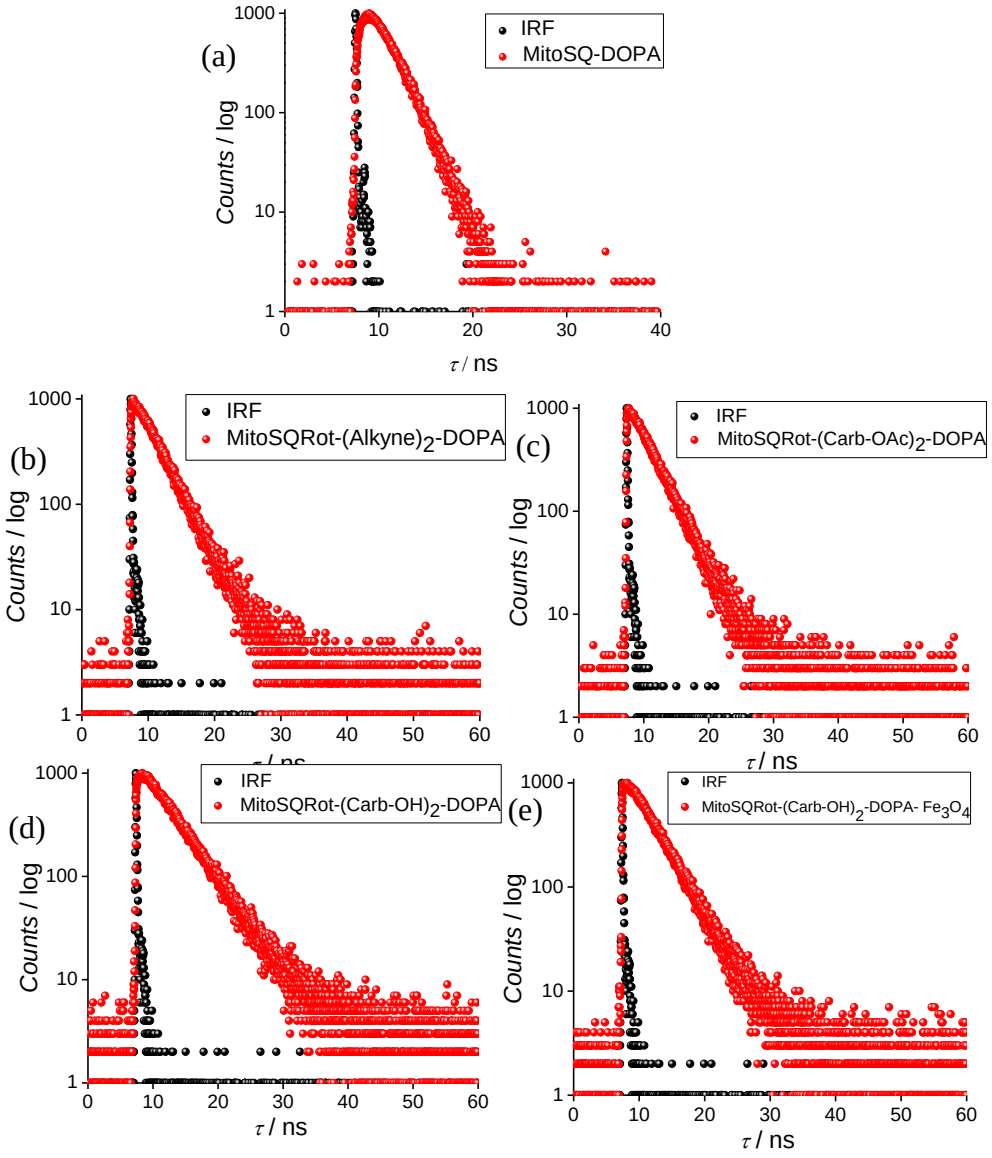

Figure 49. TCSPC plots of (a) MitoSQ-DOPA(b) MitoSQRot-(Alkyne)$_2$-DOPA, (c) MitoSQRot-(Carb-OAc)$_2$-DOPA, (d) MitoSQRot-(Carb-OH)$_2$-DOPA, and (e) MitoSQRot-(Carb-OH)$_2$-DOPA-Fe_3O_4 NPs in DMSO. IRF = Instrument Response Function.

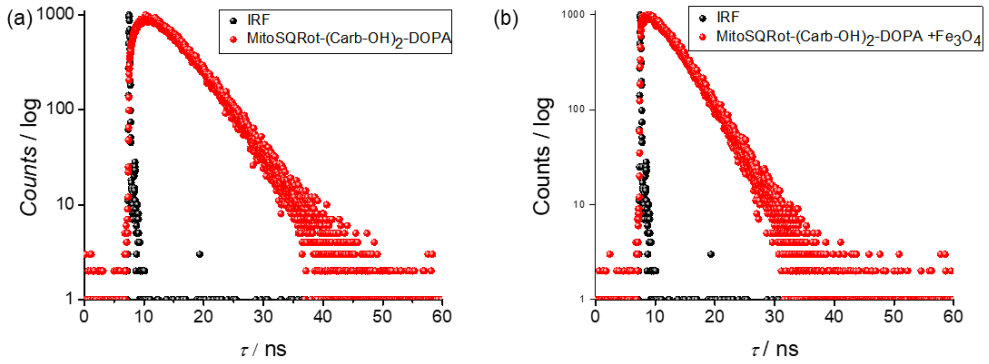

Figure 50. TCSPC plots of (a) MitoSQRot-(Carb-OH)$_2$-DOPA and (b) MitoSQRot-(Carb-OH)$_2$-DOPA-Fe_3O_4 NPs in PBS.

Table 3. Fluorescence lifetime (τ)

Compound	Fluorescence Lifetime (τ)
MitoSQ-DOPA	1.27489±0.354983 ns in DMSO
MitoSQRot-(Alkyne)$_2$-DOPA	3.43917±0.0328704 ns in DMSO
MitoSQRot-(Carb-OAc)$_2$-DOPA	3.32431 ± 0.0332065 ns in DMSO
MitoSQRot-(Carb-OH)$_2$-DOPA	3.60536 ±0.023132 ns in DMSO
MitoSQRot-(Carb-OH)$_2$-DOPA	5.05190 ±0.053329 ns in PBS
MitoSQRot-(Carb-OH)$_2$-DOPA-Fe_3O_4 NPs	3.93932 ±0.031143 ns in DMSO
MitoSQRot-(Carb-OH)$_2$-DOPA-Fe_3O_4 NPs	3.98285 ±0.0560610 ns in PBS

Biocompatibility Study

Dethreading might be a probable pitfall of rotaxane molecules accumulated in the intracellular organelles. ^{1}H NMR experiments at 37 °C for 2 days displayed no dethreading of the axle from the rotaxane. The mechanical stability of the rotaxane coated Fe_3O_4 NPs MitoSQRot-(Carb-OH)$_2$-DOPA-Fe_3O_4 in PBS is also investigated by UV/vis and fluorescence spectroscopy. There is no evidence of the rotaxane dethreading after 2 days at 37 °C.

It confirms that the gem-dimethyl and N-methyl indoline residues, as well as the TPP^+ residue, are bulky enough to prevent rotaxane dethreading. The possibility of GSH interference under physiological circumstances is investigated. In the presence of GSH no notable absorption or emission variations of MitoSQRot-(Carb-OH)$_2$-DOPA-Fe_3O_4 NPs are identified at mitochondrial pH 8.0 for 2 days at 37°C (**Figure 51**). There are no significant changes in the emission of MitoSQRot-(Carb-OH)$_2$-DOPA-Fe_3O_4 NPs (2 μM) at 670 nm in the presence of multiple cations and anions under physiological circumstances (pH 7.2, 37 °C) throughout 24 hours (**Figure 52a-c**). Furthermore, MitoSQRot-(Carb-OH)$_2$-DOPA-Fe_3O_4 NPs is very stable in the presence of bioactive small molecules such as glutathione (GSH, 5 mM) cysteine (Cys, 5 mM) and H_2O_2 (1 mM) under physiological circumstances (PBS, pH 7.2, 37 °C, 48h) (**Figure 52d**).

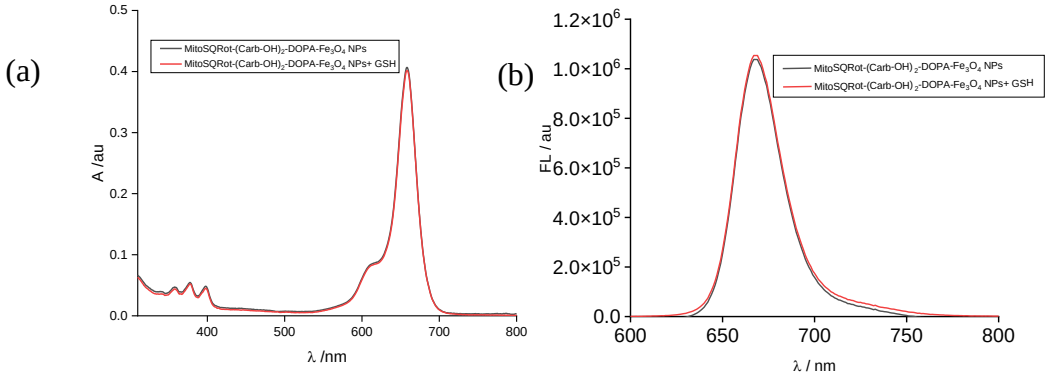

Figure 51. (a) Normalized absorption plot of MitoSQRot-(Carb-OH)$_2$-DOPA-Fe_3O_4 NPs and after the addition of GSH solution (20 μM) at pH 7.4, 37°C, 2 days. (b) Normalized fluorescence spectra of MitoSQRot-(Carb-OH)$_2$-DOPA-Fe_3O_4 NPs and in presence of GSH (20 μM) at pH 7.4, 37ºC, 2 days. No significant changes in absorption and fluorescence intensities of MitoSQRot-(Carb-OH)$_2$-DOPA-Fe_3O_4 NPs are observed in presence of GSH in physiological pH 7.4 over 48 h at 37ºC.

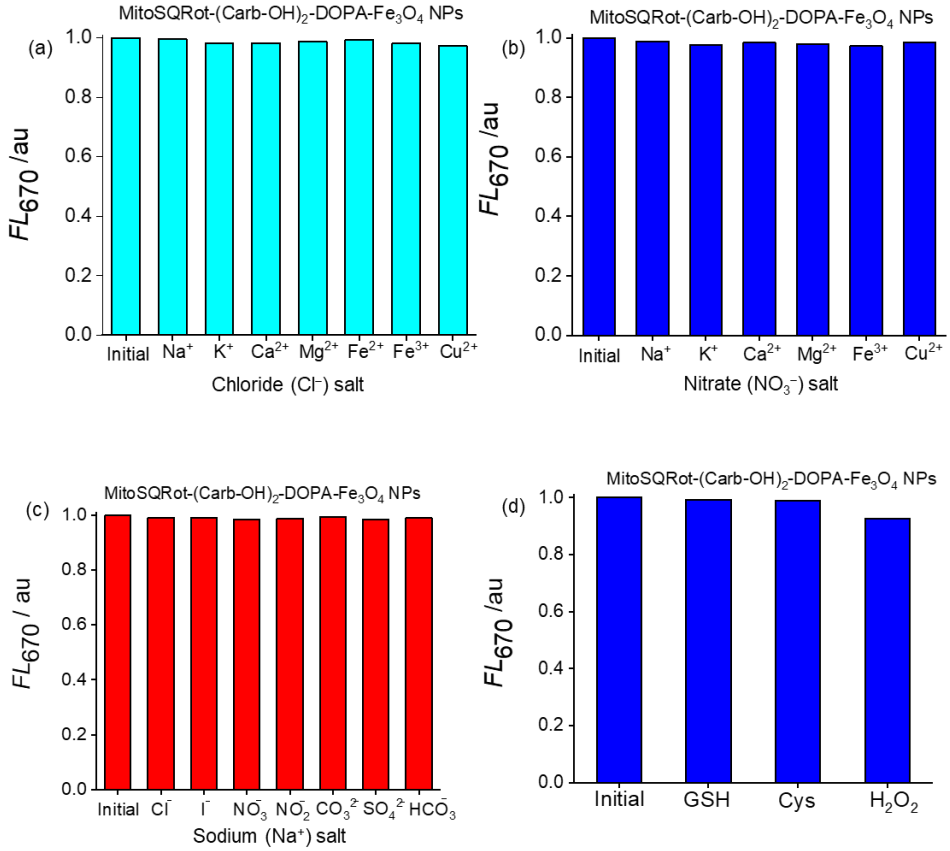

Figure 52. Insignificant fluctuations are perceived in the emission of MitoSQRot-(Carb-OH)$_2$-DOPA-Fe$_3$O$_4$ NPs (2 μM) at 670 nm in addition of innumerable cations [10 mM Na^+, 10 mM K^+ and 200 μM for Ca^{2+}, Mg^{2+}, Fe^{2+}, Fe^{3+}, and Cu^{2+}] as (a) Cl^- and (b) NO_3^- salts; (c) numerous anions (200 μM for Cl^-, I^-, NO_3^-, NO_2^-, CO_3^{2-}, SO_4^{2-}, and HCO_3^-) as Na^+ salts under physiological conditions (pH 7.2, 37°C, 48 h). (d) Trivial fluorescence alterations of MitoSQRot-(Carb-OH)$_2$-DOPA-Fe$_3$O$_4$ NPs (2 μM) at 670 nm are observed in presence of bioactive small molecules e.g. cysteine (Cys, 5 mM), glutathione (GSH, 5 mM), and H_2O_2 (1 mM) under physiological conditions (PBS, pH 7.2, 37°C, 48 h).

Cell viability assay (MTT):

Cell viability studies exhibited that the MitoSQRot-(Carb-OH)$_2$-DOPA-Fe_3O_4 NPs is noncytotoxic to human lung adenocarcinoma A549 and epithelioid cervical carcinoma HeLa cell lines, as well as noncancerous C2C12 cell line (**Figure 53**).

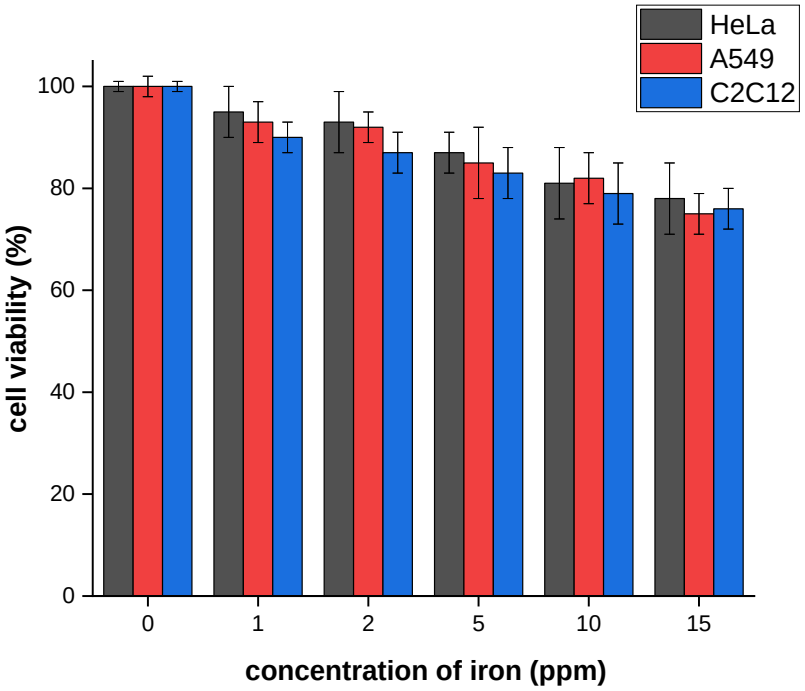

Figure 53. Cell viability assay against A549 and HeLa carcinoma cell lines as well as noncancerous mouse myoblast cell line C2C12 over 24 h at different concentrations of MitoSQRot-(Carb-OH)$_2$-DOPA-Fe_3O_4 NPs.

Confocal laser scanning microscopy (CLSM):

The MitoSQRot-(Carb-OH)$_2$-DOPA-Fe_3O_4 NPs is a great choice for organelle staining because of its excellent biocompatibility, low cytotoxicity, narrow NIR absorption/emission band, and high quantum yield. To determine mitochondrial selectivity, a colocalization assay utilizing MitoSQRot-(Carb-OH)$_2$-DOPA-Fe_3O_4 NPs and a mitochondria-specific marker MitoTracker Green (MTG) is performed in live HeLa and A549 cancer cells. In confocal microscopy, the MitoSQRot-(Carb-OH)$_2$-DOPA-Fe_3O_4 NPs exhibited good colocalization with MTG, with a Pearson's correlation (PC) value of 0.82 for HeLa and 0.84 for A549 cells **(Figure 54 and 55).**

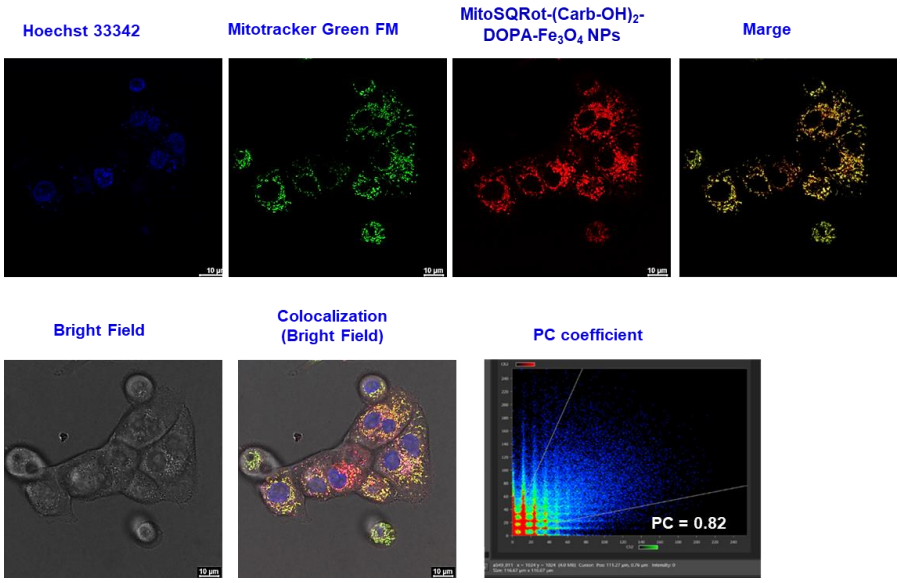

Figure 54. Confocal microscopic images of MitoSQRot-(Carb-OH)$_2$-DOPA-Fe_3O_4 NPs colocalized with MitoTracker Green (MTG) in live HeLa carcinoma cells. Hoechst (blue channel), MTG (green channel), and MitoSQRot-(Carb-OH)$_2$-DOPA-Fe_3O_4 NPs (red channel). Colocalization scatter plot displays Pearson's correlation coefficient (PCC) of 0.82.

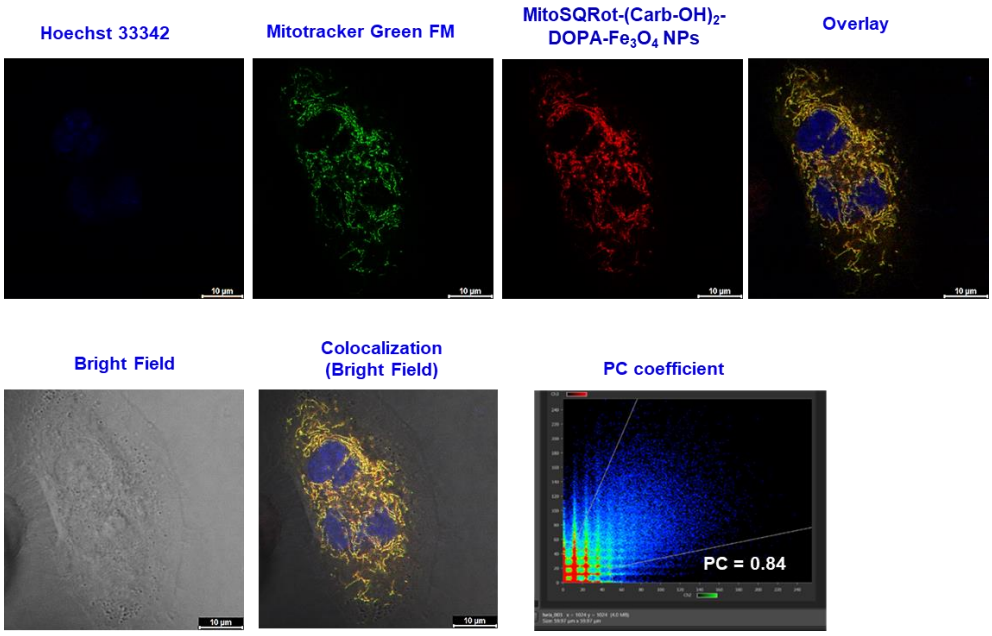

Figure 55. Confocal microscopic images of MitoSQRot-(Carb-OH)$_2$-DOPA-Fe_3O_4 NPs colocalized with MitoTracker Green (MTG) in live A549 carcinoma cells. Hoechst (blue channel), MTG (green channel), and MitoSQRot-(Carb-OH)$_2$-DOPA-Fe_3O_4 NPs (red channel). Colocalization scatter plot displays Pearson's correlation coefficient (PCC) of 0.84.

To get the 3D images of mitochondria, Z-stack images of live HeLa and A549 carcinoma cells labeled with the MitoSQRot-(Carb-OH)$_2$-DOPA-Fe_3O_4 NPs probe are captured by CLSM. For the live cell 3D CLSM image acquisition, the CLSM images are harvested every 0.14 μm on the Z-axis. Several frames (30-40) for individual channels are taken over a time span of 6 minute to acquire the live cell 3D CLSM images (**Figure 56**). In addition, multicolor imaging of live A549 and HeLa cells are obtained using our MitoSQRot-(Carb-OH)$_2$-DOPA-Fe_3O_4 NPs in conjunction with other target-specific probes with different $\lambda_{ex}/\lambda_{em}$ patterns (**Figure 57**).

(a) (b)

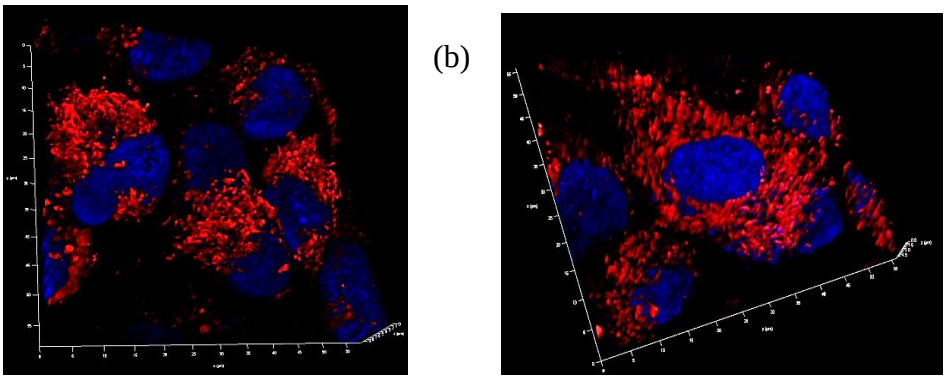

HeLa A549

Figure 56. 3D CLSM image of the living (a) HeLa and (b) A549 carcinoma cells stained with mitochondria targeting MitoSQRot-(Carb-OH)$_2$-DOPA-Fe_3O_4 NPs (red color). Blue color specifies nuclear staining by Hoechst 33342.

(a) (b)

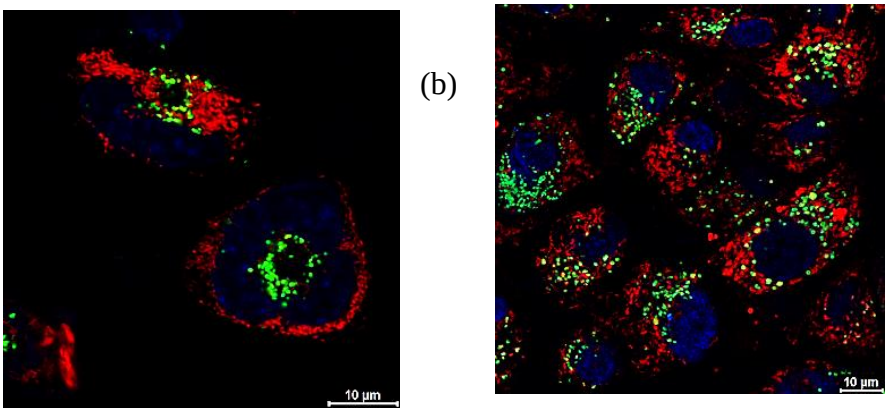

Figure 57. Multicolor CLSM images of live HeLa carcinoma cells stained with blue-fluorescent Hoechst 33342 to target nucleus (blue color), green emitting LTG to stain lysosome (green color), and red emitting MitoSQRot-(Carb-OH)$_2$-DOPA-Fe_3O_4 NPs to selectively track mitochondria (red color). Multicolor imaging of intracellular organelles in the same cell is captured by suitable filter sets using CLSM.

T_2-weighted MR imaging:

Magnetic NPs accelerate spin−spin relaxation of nearby Hs of H_2O by creating a magnetic field, resulting in signal attenuation in T_2-weighted MRI imaging. Amongst the numerous magnetic NPs, Fe_3O_4 NPs are extensively utilized as T_2 MRI contrast agents due to their biocompatibility and benign nature. MRI contrast agents based on iron oxide NPs such as Feridex and Resovist are approved for clinical use.[25] However, their water solubility, delivery, and target specificity are the real concern. Hence, relevant surface coatings are required to enhance the water dispersibility, colloidal stability, biocompatibility, and target selectivity of Fe_3O_4 NPs. In order to determine the performance of the designed MitoSQRot-(Carb-OH)$_2$-DOPA-Fe_3O_4 NPs as MRI diagnostic tool, we have studied MRI on 9.4 T MR scanner. The darkening of the T_2 contrast with the increased concentration of Fe designates a sharp indication of T_2-weighted MRI sensitive contrast effect (**Figure 58a**). Moreover, proton T_2^{-1} relaxation time was gradually increased with Fe concentration and resulted in high relaxation rate (r_2) of MitoSQRot-(Carb-OH)$_2$-DOPA-Fe_3O_4 NPs (r_2 = 180.7 mM^{-1} s^{-1}) (**Figure 58b**) which supports that our designed water soluble rotaxane capped Fe_3O_4 NPs could be useful for T_2 weighted MRI contrast agent in future animal study for diagnosis purpose. Therefore, our designed water soluble biocompatible NIR emitting superparamagnetic MitoSQRot-(Carb-OH)$_2$-DOPA-Fe_3O_4 NPs could be utilized for NIR fluorescence imaging in combination with MRI based multimodal imaging applications.

(a)

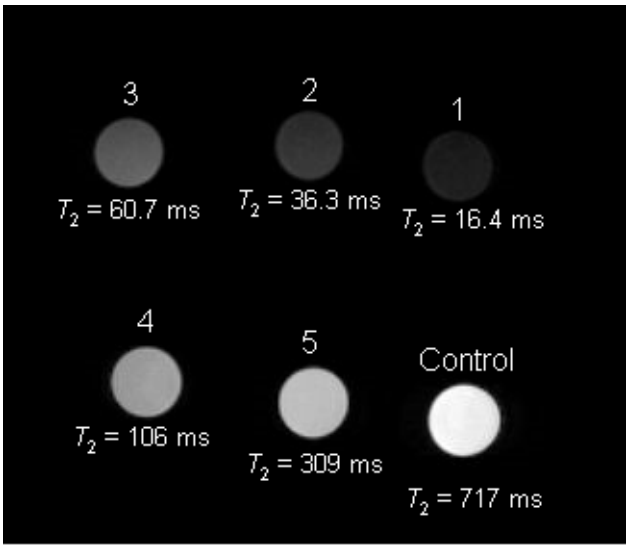

(b)

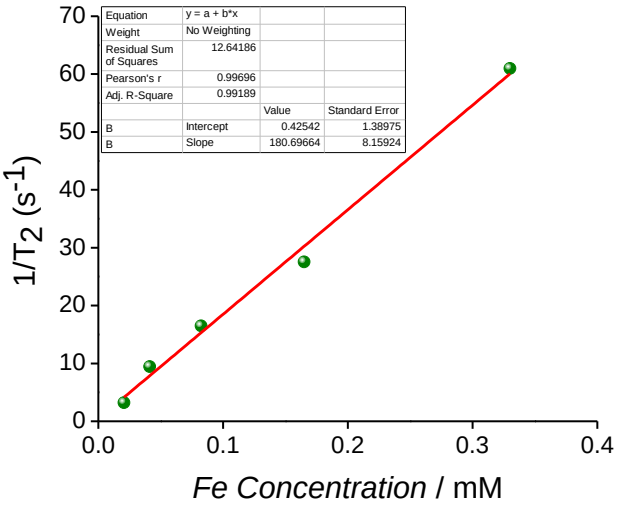

Figure 58. (a) T_2-weighted spinecho images of MitoSQRot-(Carb-OH)$_2$-DOPA-Fe_3O_4 NPs using 9.4 T MR scanner. MRI phantom images of D-PBS (-) solution without (control) and with increased concentration of MitoSQRot-(Carb-OH)$_2$-DOPA-Fe_3O_4 NPs. The darkening of the T_2 contrast with the increased concentration of Fe is observed. (b) $1/T_2$ vs Fe concentration plot exhibited relaxation rate (r_2) of 180.7 mM^{-1} s^{-1}.

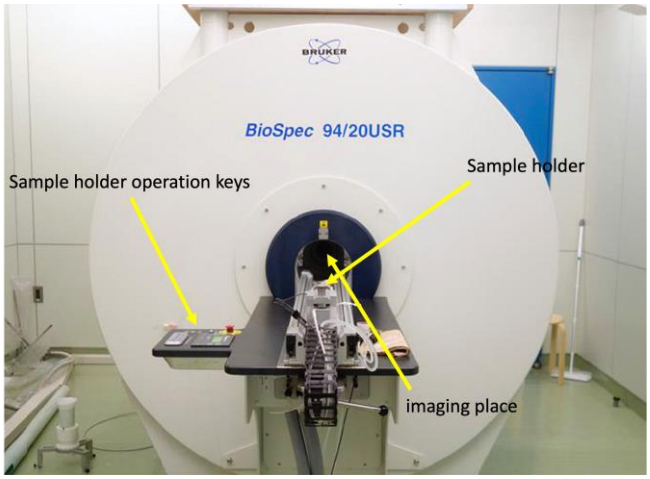

Figure 59: The MRI instrument used for the experiment.

Conclusions:

The dual functional stoppers containing interlocked unsymmetrical squaraine dye inside a sugar conjugated macrocycle to construct the water soluble MIMs has been proven to enhance durability and NIR fluorescence efficiency of the dye. Superparamagnetic Fe_3O_4 NPs surface coated with dopamine conjugated triphenylphosphonium tethered targeted rotaxane help to specifically accumulate the rotaxane capped magnetic NPs inside the mitochondria. The carbohydrate moieties attached with the macrocycle via CuAAC reaction helps in mproving the water solubility of MitoSQRot-(Carb-OH)$_2$-DOPA-Fe_3O_4 NPs. The water soluble rotaxane capped Fe_3O_4 NPs act as a NIR fluorescent imaging agent in combination with T_2-weighted MR contrast agent. NIR rotaxane capped superparamagnetic Fe_3O_4 NPs could be utilized for mitochondria targeted multimodal imaging diagnostics. Moreover, mitochondria targeted NIR rotaxane capped superparamagnetic Fe_3O_4 NPs could generate heat under remotely applied alternating magnetic fields to induce organelle targeted image guided hyperthermia-based cell death which is currently underway in our lab.

REFERENCES:

[1] Zhu, H.; Fan, J.; Du, J.; Peng, X. *Acc. Chem. Res*. **2016**, *49*, 2115−2126.

[2] Yan, R.; Hu, Y.; Liu, F.; Wei, S.; Fang, D.; Shuhendler, A. J.; Liu, H.; Chen, H.-Y.; Ye, D. *J. Am. Chem. Soc.* **2019**, *141*, 10331−10341.

[3] Ducharme, G. T.; LaCasse, Z.; Sheth, T.; Nesterova, I. V.; Nesterov, E. E. *Angew. Chem., Int. Ed.* **2020**, *59*, 8440−8444.

[4] Zhou, B.; Li, Y.; Niu, G.; Lan, M.; Jia, Q.; Liang, Q. *ACS Appl.Mater. Interfaces*. **2016**, *8*, 29899−29905.

[5] Wahsner, J.; Gale, E.M.; Rodriguez-Rodriguez, A.; Caravan, P. *Chem. Rev*. **2019**, *119*, 957−1057.

[6] Jarvis, T. S.; Collins, C. G.; Dempsey, J. M.; Oliver, A. G.; Smith, B. D. *J. Org. Chem.* **2017**, *82*, 5819−5825.

[7] Gassensmith, J. J.; Arunkumar, E.; Barr, L.; Baumes, J. M.; DiVittorio, K. M.; Johnson, J. R.; Noll, B. C.; Smith, B. D. *J. Am. Chem. Soc.* **2007**, *129*, 15054−15059.

[8] Babu, P. S. S.; Manu, P. M.; Dhanya, T. J.; Tapas, P.; Meera, R. N.; Surendran, A.; Aneesh, K. A.; Vadakkancheril, S. J.; Ramaiah, D.; Nair, S. A.; Pillai, M. R. *Sci. Rep.* **2017**, *7*, 42126.

[9] Chen, L. B. *Annu. Rev. Cell Biol.* **1988**, *4*, 155−181.

[10] Arunkumar, E.; Forbes, C. C.; Noll, B. C.; Smith, B. D. *J. Am. Chem. Soc.* **2005**, *127*, 3288−3289.

[11] Chen, H.; Farahat, M. S.; Law, K. Y.; Whitten, D. G. *J. Am. Chem. Soc.* **1996**, *118*, 2584−2594.

[12] Johnson, J. R.; Fu, N.; Arunkumar, E.; Leevy, W. M.; Gammon, S. T.; Piwnica-Worms, D.; Smith, B. D. *Angew. Chem., Int. Ed*. **2007**, *46*, 5528−5531.

[13] Zielonka, J.; Joseph, J.; Sikora, A.; Hardy, M.; Ouari, O.; Vasquez-Vivar, J.; Cheng, G.; Lopez, M.; Kalyanaraman, B. *Chem. Rev.* **2017**, *117*, 10043−10120.

[14] Yu, G.; Wu, D.; Li, Y.; Zhang, Z.; Shao, L.; Zhou, J.; Hu, Q.; Tang, G.; Huang, F. *Chem. Sci.* **2016**, *7*, 3017−3024.

[15] Das, R. S.; Saha, P. C.; Sepay, N.; Mukherjee, A.; Chatterjee, S.; Guha, S. *Org. Lett.* **2020**, *22*, 5839−5843.

[16] Thompson, D. A.; Best, J. S. *IBM Journal of Research and Development*, **2000,** *44*, 311−322.

[17] Laurent, S.; Forge, D.; Port, M.; Roch, A.; Robic, C.; Vander Elst, L.; Muller, R. N. *Chem. Rev*. **2008**, *108*, 2064−2110.

[18] Soenen, S. J.; Himmelreich, U.; Nuytten, N.; De Cuyper, M. *Biomaterials*. **2011**, *32*, 195–205.

[19] Ajayaghosh, A. *Acc. Chem. Res.* **2005**, *38*, 449−459.

[20] Sheldrick, G. M. *Acta Cryst.* **2015**, *A71*, 3–8.

[21] Sheldrick, G. M. *Acta Cryst.* **2015**, *C71*, 3–8.

[22] Dolomanov, O. V., Bourhis, L. J., Gildea, R. J., Howard, J. A. K., Puschmann, H. *J. Appl. Cryst.* **2009**, *42*, 339–341.

[23] Na, H. B.; Palui, G.; Rosenberg, J. T.; Ji, X.; Grant, S. C.; Mattoussi, H. *ACS Nano.* **2012**, *6*, 389−399.

[24] Hsu, J. C.; Tang, Z.; Eremina, O. E.: Sofias, A. M.; Lammers, T.; Lovell, J. F.; Zavaleta, C.; Cai, W.; Cormode, D. P. *Nat Rev Methods Primers* . **2023**, *3*, 30.

[25] Wang, Yi-Xi J. *Quant Imaging Med Surg.* **2010**, *1*, 35-40.

Chapter 6

Summary and Outlook

Development of organelle targeting rotaxane based fluorophores that can selectively target and stain particular cellular compartments such as mitochondria, lysosome, Golgi apparatus, endoplasmic reticulum, etc., has become an emerging field of current research. In this thesis I have mainly focused on the design and synthesis of symmetrical as well as unsymmetrical rotaxane molecules that can selectively target and image cellular mitochondria/lysosomes. Mitochondria are the important target for all cells. For the development of effective mitochondria targeting agents, two important parameters, such as extraordinary biophysical membrane property of mitochondria ($\Delta\Psi_m$ −150 to −180 mV for normal cell and $\Delta\Psi_m$ ~ –220 mV for cancer cell) and the lipophilicity of the targeting rotaxane molecules, have been considered. Among the various intracellular organelles, lysosomes are also the key target for all malignant cells. Lysosomes are the membrane-bound cellular organelles with low pH 4−5. They encompass a variety of degradable enzymes and are liable for the disruption of nucleic acids, fats, proteins, etc. as well as being responsible for exocytosis. Rotaxane-peptide conjugates anchoring with lysosome targeting morpholine moiety have been developed for selective targeting and imaging of malignant lysosomes.

Rotaxane formations have been confirmed by a plethora of spectroscopic techniques (^{1}H NMR, ^{13}C NMR, HRMS, UV/Vis, fluorescence) as well as by single crystal X-ray structure. Mitochondria and lysosome target specificity of the synthesized rotaxane molecules have been established by colocalization experiments carried out with commercially available MitoTracker and LysoTracker using confocal laser scanning microscopy (CLSM).

The novel observations of this thesis are:

- I have used a MW-assisted SPPS protocol for the rapid and effective synthesis of mitochondria targeting NIR unsymmetrical rotaxane

molecule. Herein a microwave-assisted template-directed clipping reaction on low loading 2-chlorotrityl chloride resin is used to develop NIR unsymmetrical squaraine rotaxanes. These rotaxane molecules hold significant potential for selective targeting and NIR imaging of mitochondria.This is the first report of an NIR unsymmetrical 1,3,3-trimethylindoline squaraine-rotaxane-based mitochondria targeting and staining agent. The synthesized rotaxane molecule tethered with TPP^+ functionality could be a promising dye for mitochondrial therapy with NIR imaging diagnostics.

- I have used a MW-assisted SPPS protocol for the rapid and effective synthesis of RGDS peptide and two N_3-RGDS peptides are conjugated at the alkyne containing macrocycle using CuAAC on the Wang resin to synthesize NIR rotaxane/RGDS conjugates. RGDS peptide is incorporated to target the $\alpha_V\beta_3$ integrin which is overexpressed at the tumor site. A morpholine moiety is tethered at the axle to selectively target the lysosome. This dual targeting rotaxane has been used for live cancer cell specific active targeting followed by selective internalization and tracking of malignant lysosomes. The synthesized rotaxane probe can be efficiently used for 3D cellular imaging and real-time monitoring of live cancer cell lysosomes. This is the first report of a water-soluble, red fluorescent, biocompatible, dual targeting mechanically interlocked probe where cancer cell specific RGDS peptide is conjugated at the macrocycle and lysosome targeting morpholine functionality is tethered at the axle for active targeting of live cancer cells followed by selective internalization and imaging of malignant lysosomes along with real-time tracking, 3D and multicolor cellular imaging applications. Moreover, the rotaxane based dye could be utilized for the imaging of lysosomal fusion, lysosome and mitochondrial

cross-talk, early diagnosis of the lysosome related diseases, and targeted image guided surgery.

- In this thesis, I have also reported a multifunctional rotaxane molecule consisting of a lipophilic TPP^+ for targeting mitochondria and a dopamine containing catechol groups for the surface coating of the superparamagnetic Fe_3O_4 NPs. Both the TPP^+ and dopamine residues are tethered at the axle of the NIR rotaxane molecule. To enhance the water solubility of MitoSQRot-DOPA, two carbohydrate moieties are conjugated at the tetralactam macrocycle. The carbohydrate incorporation with the tetralactam macrocycle is achieved by using CuAAC among carbohydrate containing azide and terminal alkyne of the macrocycle. TBDMS protected DOPA of the MitoSQRot-$(Carb\text{-}OH)_2$-DOPA is deprotected using TBAF/THF and capped with our synthesized iron oxide nanoparticle to obtain Fe_3O_4 NPs surface coated with the rotaxane molecules [MitoSQRot-$(Carb\text{-}OH)_2$-DOPA-Fe_3O_4] which is characterized by HRTEM, UV/vis, fluorescence and field dependent magnetization (M-H) at room temperature. catechol functionality of the dopamine residue conjugated at the axle to anchor with the superparamagnetic monodisperse small Fe_3O_4 NPs for the targeted delivery of the magnetic NPs inside the mitochondria as well as T_2-weighted MRI imaging. The rotaxane capped superparamagnetic Fe_3O_4 NPs could be a promising candidate for the targeted multimodal imaging applications.

List of Publications and Research Works Included in the Thesis:

As a First Author:

(1) *Design and Synthesis of Near-Infrared Mechanically Interlocked Molecules for Specific Targeting of Mitochondria.* ***Rabi Sankar Das****, Pranab Chandra Saha, Nayim Sepay, Ayan Mukherjee, Sudipta Chatterjee, and Samit Guha*. Org. Lett.* **2020***, 22,* 5839–5843.

(2) *Construction of Red Fluorescent Dual Targeting Mechanically Interlocked Molecules for Live Cancer Cell Specific Lysosomal Staining and Multicolor Cellular Imagin.* ***Rabi Sankar Das****, Ayan Mukherjee, Samiran Kar, Tapas Bera, Shreya Das, Arunima Sengupta, and Samit Guha*. Org. Lett.* **2022***, 24,* 5907–5912.

(3) *Design of Water-Soluble NIR Rotaxane Capped Superparamagnetic* Fe_3O_4 *Nanoparticles for Mitochondria Targeted Multimodal Imaging.* ***Rabi Sankar Das,*** *Samit Guha*.* ***Manuscript under preparation****.*

List of Publications and Research Works That Not Included in theThesis:

As a Co-Author:

(1) *Acidic pH-Triggered Live-Cell Lysosome Specific Tracking, Ratiometric pH Sensing, and Multicolor Imaging by Visible to NIR Switchable Cy-7 Dyes. Ayan Mukherjee, Pranab Chandra Saha, Samiran Kar, Pampa Guha,* ***Rabi Sankar Das****, Tapas Bera, and Samit Guha*. ChemBioChem.* **2023***, 24,* e2022006.

(2) *Acidic pH-Activatable Visible to Near-Infrared Switchable Ratiometric Fluorescent Probe for Live-Cell Lysosome Targeted Imaging. Ayan Mukherjee, Pranab Chandra Saha,* ***Rabi Sankar Das****, Tapas Bera, and Samit Guha*. ACS Sens.* ***2021****, 6, 2141–2146.*

(3) *Supramolecular β-Sheet Forming Peptide Conjugated with Near-Infrared Chromophore for Selective Targeting, Imaging, and Dysfunction of Mitochondria. Pranab Chandra Saha,* ***Rabi Sankar Das,*** *Tanima Chatterjee, Maitree Bhattacharyya, and Samit Guha*. Bioconjugate Chem.* ***2020****, 31, 1301–1306.*

(4) *Targeting and Imaging of Mitochondria Using Near-Infrared Cyanine Dye and Its Application to Multicolor Imaging. Pranab Chandra Saha, Tanima Chatterjee, Rudradip*

*Pattanayak, **Rabi Sankar Das,** Ayan Mukherjee, Maitree Bhattacharyya, and Samit Guha*. ACS Omega.* **2019**, *4*, 14579–14588.

PRESENTATION/PARTICIPATION IN INTERNATIONAL/NATIONAL/SYMPOSIUM/ CONFERENCES:

1. Poster presentation "***Construction of Near-Infrared Fluorescent Dual Targeting Mechanically Interlocked Molecules for Live Cancer Cell Specific Lysosomal Staining and Multicolor Cellular Imaging"***. Rabi Sankar Das, and Samit Guha*. One Day Symposium in Chemical Sciences, National Conference on Chemistry Organized by Chemical Reserch Society of India (CRSI-2022) held at Indian Association for The Cultivation of Science (IACS), Kolkata, India, 4th June, 2022. (**Best Poster Presentation Awarded**)

2. Poster presentation "***Construction of Near-Infrared Fluorescent Dual Targeting Mechanically Interlocked Molecules for Live Cancer Cell Specific Lysosomal Staining and Multicolor Cellular Imaging"***. Rabi Sankar Das, and Samit Guha*. International Seminar on Recent Advances in Chemistry and Material Science (RACMS-2022) held at Department of Chemistry, Jadavpur University (JU), Kolkata, India, During July 30-31 and August 02-03, 2022. (**Best Poster Presentation Awarded, S S Bhatnagar Young Scientist Awarded).**

3. Poster presentation "***Amyloid-β Peptide Fragment Conjugated with Near-Infrared Chromophore for Selective Targeting and Imaging of Mitochondria*"*.*** Pranab Chandra Saha, Rabi Sankar Das, Ayan Mukherjee, Tapas Bera, and Samit Guha*. National Seminar on Emerging Trends in Chemical Sciences under Centre for Advanced Studies II Program, Organized by Department of Chemistry, Jadavpur University, Kolkata-700032 on January 07, 2020.